

# **Hematite and its Hybrid Nanostructures for Photoelectrochemical Water Splitting: How Do Properties Affect Functionality?**

**Inauguraldissertation**

zur

Erlangung der Würde eines Doktors der Philosophie

vorgelegt der

Philosophisch-Naturwissenschaftlichen Fakultät

der Universität Basel



von

**Debajeet K. Bora**

aus Indien



Basel 2012

Genehmigt von der Philosophisch-naturwissenschaftlichen Fakultät der  
auf Antrag

Von:

Prof. Dr. EdwinC. Constable

Dr. Artur Braun

Prof. Dr. Ernst Meyer

Basel, den 13 December, 2011

Prof. Dr. Martin Spiess  
Dekan der Philosophisch-  
Naturwissenschaftlichen Fakultät

Original document stored on the publication server of the University of Basel  
**edoc.unibas.ch**



This work is licenced under the agreement „Attribution Non-Commercial No Derivatives – 2.5  
Switzerland“. The complete text may be viewed here:  
**[creativecommons.org/licenses/by-nc-nd/2.5/ch/deed.en](https://creativecommons.org/licenses/by-nc-nd/2.5/ch/deed.en)**



## Attribution-Noncommercial-NoDerivativeWorks2.5Switzerland

**You are free:**



to Share — to copy, distribute and transmit the work

**Under the following conditions:**



**Attribution.** You must attribute the work in the manner specified by the author or licensor (but not in any way that suggests that they endorse you or your use of the work).



**Noncommercial.** You may not use this work for commercial purposes.



**No Derivative Works.** You may not alter, transform, or build upon this work.

- For any reuse or distribution, you must make clear to others the license terms of this work. The best way to do this is with a link to this web page.
- Any of the above conditions can be waived if you get permission from the copyright holder.
- Nothing in this license impairs or restricts the author's moral rights.

**Your fair dealing and other rights are in no way affected by the above.**

This is a human-readable summary of the Legal Code (the full license) available in German:  
<http://creativecommons.org/licenses/by-nc-nd/2.5/ch/legalcode.de>

**Disclaimer:**

The Commons Deed is not a license. It is simply a handy reference for understanding the Legal Code (the full license) — it is a human-readable expression of some of its key terms. Think of it as the user-friendly interface to the Legal Code beneath. This Deed itself has no legal value, and its contents do not appear in the actual license. Creative Commons is not a law firm and does not provide legal services. Distributing of, displaying of, or linking to this Commons Deed does not create an attorney-client relationship.

“Science is a wonderful thing if one does not have to earn one's living at it”

-Albert Einstein

**Dedicated to my beloved father –*Late Kosheswar Bora***

He had a dream to see myself as a Scientist.

## **Preface**

The concept of photoelectrochemical water splitting dates back to 1972 when Fujishima and Honda first developed the Titanium based electrode which splits water into hydrogen and oxygen under the presence of light and bias. The water splitting reaction is already well established in nature. For instance, green plants and cyanobacteria used this water splitting machinery to run the very important photosynthetic process. Photosynthesis process involves two systems namely photosystem II and Photosystem I. Photosystem II functionality is very important in the sense that it gives us oxygen which help in the sustainability of all aerobic living organism including humans. On the other hand, the photosystem I main task is to produce carbohydrate and hydrogen. Due to the high demand of clean energy in near future, artificial photosynthesis concept has been developed to provide clean energy in the form of hydrogen. Inspired by these facts, the thesis “**Hematite and its Hybrid Nanostructures for Photoelectrochemical Water Splitting: How Do Properties Affect Functionality?**” has been prepared by giving effort in producing nanostructured hematite thin film and its hybrid nanostructure. Besides these the properties of hematite film are thoroughly studied in order to correlate with the photoelectrochemical functionality of the film. The thesis is divided into three parts.

Part I: Chapter 3 describes the synthesis of hematite nanoparticles by thermal decomposition of fatty acid precursors and hydrothermal treatment of iron salt with amino acid. Chapter 4 represents the structural study of iron oxide nanoparticles with XRD and Fe-K edge X ray absorption spectroscopy. The photocatalytic activity of iron oxide nanoparticles have been described in chapter 5. The synthesis method for producing hematite thin film and Si-Hematite film and their photoelectrochemical properties are described in chapters 6 and 7.

Part II consists of 2 chapters which deal with the ex- situ and in- situ NEXAFS study of a working hematite photoelectrode. Chapter 8 showing the formation of an extra NEXAFS transition in post-photoelectrochemically treated hematite thin film. Chapter 9 describes very promising results about the change in electronic structure of a working photoelectrode under light and applied bias probed with NEXAFS spectroscopy.

Part III has 3 chapters describing the hematite based hybrid nanostructures for photoelectrochemical application. Chapter 10 illustrates a very simple method for obtaining a flower like morphology which boosts the photoelectrochemical performance. Chapter 11 is based on the enhanced photoelectrochemical performance by the surface modification of

semiconductors with light harvesting protein. Chapter 12 finally represents the development of multiple band gap composite electrode of NiO with hematite. The system showed good gas evolution and very high magnitude of current density.

Debajeet K. BORA

EMPA, Dübendorf, Switzerland

Date: 21.11.11

## Acknowledgement

First of all, I would like to acknowledge the great scientific environment as well as infrastructure of *University of Basel* and *Empa. Swiss Federal Laboratories for Materials Science and Technology*, which lead to the completion of this PhD thesis in 2.5 year. After this, my sincere gratitude goes to my supervisor Dr. Artur Braun and to my thesis advisor Prof. Dr. Edwin C. Constable. I am very much grateful to both of them for giving me inspiration, support as well as allowing me to think and built own independent concept to carry out such an innovative project. This thesis was fully funded by the Swiss BfE (project no: 153613/102809) and I am grateful for Dr. Stefan Oberholzer for continued support. I am particularly grateful to Prof. Andreas Luzzi whom I have never met, but who has inspired and support this project. Then I would like to thank Prof. Thomas Graule, Head, Laboratory for High Performance Ceramics, EMPA for the necessary support in order to carry out synchrotron experiments in USA and to attend summer schools, conferences symposium etc. In this regard, my sincere thanks also go to Mrs. Brigitte Schatzmann for the administrative support. Next, I would also like to acknowledge Prof. Dr. Gian- Luca Bona, Director, EMPA for his great inspiration and support to my scientific activity.

In the technical aspect of the thesis work, I would like to thank Mr. Hansjürgen Schindler for the XRD measurement of the samples being developed. For X-Ray absorption spectroscopy work at ESRF, Grenoble, sincere thanks go to Dr. Olga Safonova (Beamline Scientist). I also had an introduction to transmission Electron Microscopy (TEM) during the work. For this I am grateful to Mr. Daniel Schreier for the introduction of Philips 300KeV TEM. For diffuse reflectance spectroscopy of iron oxide nanoparticles, help from Dr. Emma Dunphy at University of Basel is greatly acknowledged. I am indebted to Dr. Stephan Hug, Scientist at eawag who was very patient with me to carry out photocatalytic study with in situ ATR-FTIR. For hematite thin film deposition with spin coating, I would like to thank Dr. William Kylberg, Functional Polymer Lab, for necessary introduction. Thanks go to my students Jean- Pierre Peirog (Master Student from Polytech Montpellier, France) and Romy Löhnert (Bachelor Student from University of Applied Science, Jena, Germany) for their help in optimizing the process parameter for thin film deposition. For morphology study, scanning electron microscopy has been utilized in intensive manner during the PhD thesis study. For this, I would like to appreciate the assistance from Mr. Michael Stiefel, Department of Electronics, EMPA- Dübendorf during the introduction of Hitachi FESEM. Optical property of the hematite thin films has been studied with the proper introduction of UV-

Vis.Spectrometer by Dr. Matthias Nagel, Functional Polymer Lab, EMPA. For X- Ray reflectometry measurement, thanks go to Romy Löhnert. For NEXAFS study at BESSY II, help from Dr. Jejakka Ariffin and Dr. Selma Erat are highly appreciated. For the in-situ operando spectroscopy at Beam Line 7.0.1 in Advanced Light Source (Lawrence Berkeley National Laboratory) I would like to thank Dr. Jinghua Guo, Senior Scientist and Mr. Liang Zhang.

For the hematite nanoflower study, helps from Dr. Rolf Erni and Dr. Giussepino Fortunato for the TEM and XPS characterization are highly appreciated. In the confocal Raman spectroscopy study of hematite / C- Phycocyanin, I would like to appreciate our collaborator Dr. Elena Rozhkova (Scientist, Center for Nanoscale Materials, Argonne National Laboratory) for the necessary support. During the development of hybrid electrode (hematite / C- Phycocyanin), I also got help from Dr. Krisztina Schrantz and Mr. Pradeep P. Wyss and I am very grateful to both of them. For the IPCE measurement and other valuable discussion on photoelectrochemical study with hematite, I would like to thank Dr. Kevin Sivula and Prof. Michael Gratzel at PEC house, EPFL. For the impedance study of hematite film, thanks goes to Ms. Tania Lopez, Helena Aguilar and Prof. Adélio Mendes, Department of Chemical Engineering, University of Porto, Portugal. For the fabrication of cappuccino cell, I would like to thank EMPA machine shop. In this context, other cheerful thanks go to Dr. Fabio Lamattina for the development of novel IPCE measurement set up at EMPA. For the ERDA measurement of NiO- Hematite electrode, I would like to thank Dr. Max Döebli, Ion Beam Physics, ETH Zürich. I also appreciate the assistance acquired from Dr. Magdalena Parlinska and Michael Stifiel for the TEM study of NiO- Hematite electrode. For the atomic force microscopy and XPS depth profile study, help from Dr. Ulrich Müller, Nanoscale Materials Science is highly acknowledged.

Thanks go to group members of “ceramic materials for energy technologies” and fellows of ceramic lab for necessary support and help.

Finally I bow in deep respect and appreciation to my dearest mother, my wife (Krishna), elder brother (Chiranjeet) and his family and entire family members for encourage and necessary support in finishing this thesis.

## Abstract

Hematite nanoparticles and thin films have been synthesized by the thermal decomposition of iron fatty acid precursor solution obtained through non-aqueous materials processing route. The variation in the structural properties of the nano particles with the heat treatment temperature was studied by X-ray diffraction and Fe K shell X-ray absorption spectroscopy. The X-ray diffraction results are paralleled by systematic changes in the pre-edge structure of the Fe K-edge X-ray absorption spectra, in particular by a gradual decrease of the  $t_{2g}/e_g$  peak height ratio of the two leading pre-edge resonances, confirming oxidation of the Fe from  $Fe^{2+}$  towards  $Fe^{3+}$ . Transmission electron microscopy (TEM) on the samples treated at temperatures as high as 900°C showed particles with prismatic morphology along with the formation of stacking fault like defects. The photocatalytic action of hematite nanoparticles are validated with the in-situ ATR-FTIR study of photodegradation of oxalic acid on iron oxide surface. Hematite thin films have been deposited by the dip coating of iron oleate precursor solution on fluorine doped tin oxide (F: SnO<sub>2</sub>) substrate and the morphology and structural properties are characterized well with X-ray Diffractometry and Scanning Electron Microscopy. The final photoelectrochemical properties of the films have been studied by running current vs. potential measurement and it is found that one dip coated layer gives rise to around 250  $\mu A/cm^2$ . The films have also been prepared by the spin coating of polymeric precursor solution but no significant photocurrent density has been observed. The electronic structure of the hematite film has been studied with NEXAFS spectroscopy. Due to electrochemical treatment of hematite ( $\alpha$ -Fe<sub>2</sub>O<sub>3</sub>) nanoparticulate films at 600 mV vs. Ag<sup>+</sup>/AgCl reference in KOH electrolyte, a new species formed at the hematite surface which causes a new transition in the upper Hubbard band between the Fe (3d)-O (2p) state region and the Fe (4sp) - O (2p) region, as evidenced by oxygen near edge x-ray absorption fine structure (NEXAFS) spectra. This transition, not known for pristine  $\alpha$ -Fe<sub>2</sub>O<sub>3</sub> is at about the same x-ray energy, where pristine 1% Si doped -Fe<sub>2</sub>O<sub>3</sub> has such transition. This state coincides with the onset of an oxidative dark current wave as observed in the cyclic voltammogram. Electrochemical oxidation to only 200 mV does not form such extra NEXAFS feature. To take a closer look at the underlying phenomena of water photo oxidation, an in-situ NEXAFS study has been performed with a working photo electrode under ambient condition. From this study, two new extra peaks developed before the pre-edge peak intensity and absent during the dark current measurement. It is believed that these two extra features evolve due to light mediated photooxidative process. After studying the pristine hematite film in detail manner, further attempt have been made to enhance the photocurrent of

pristine hematite film. At the first glance, Si doping have been performed and it is found that 0.5% silicon doped hematite film showing maximum photocurrent density of around 2.4 mA/cm<sup>2</sup>. After this surface modification strategy has been employed in order to get hybrid nanostructure. In this regard, a simple one pot hydrothermal method is described for converting a dip coated hematite nanoparticulate film into an array of nanorodswith superimposed flower like structures suitable for the water splitting in photoelectrochemical cells. The hydrothermal treatment of the dip-coated hematite film with FeCl<sub>3</sub>·6H<sub>2</sub>O and L – Arginine enhances the photocurrent by a factor of two. The photocurrent density of the pristine film reached 218 μA/cm<sup>2</sup>after 48 hours of hydrothermal treatment and this increase was attributed to the higher specific surface area of the modified film and changes in the optical properties pristine film after hydrothermal treatment. Anotherway of increasing the photocurrent of hematite by covalent cross-coupling with phycocyanin has been developed. For this, a hematite – phycocyanin integrated system is assembled by consecutive adsorption and cross coupling of protein molecules separated by an agarose layer and a linker molecule on the top of a mesoporous hematite film. The hematite - phycocyanin assembly shows a two-fold increased photocurrent in comparison with the pristine hematite film. The increase in the photocurrent is attributed to the enhanced light absorption of the hematite film after integration with protein, as is evident from the UV-Vis spectra and from the photocurrent action spectrum. The assembly shows long term stability and thus constitutes a promising hybrid photoanode for photoelectrochemical applications. Finally, a multiple band gap photoelectrode was fabricated by employing the hydrothermal deposition of NiO nanostructure on the top of hematite electrode. This system showed good gas evolution and a current density of around 16 mA/cm<sup>2</sup>and systems works by the redox reaction of Ni and Fe.

## List of Abbreviation

SHE: Standard Hydrogen Electrode

PEC: Photoelectrochemical Cell

THF: Tetra Hydro Furan

TEM: Transmission Electron Microscopy

SAED: Selected Area Electron Diffraction

XANES: X- Ray absorption near edge structure

PIDS: Polarization Intensity Differential Scattering

ATR-FTIR: Attenuated total internal reflectance Fourier Transform Infrared Spectroscopy

BET: Branauer, Emmett and Teller

NEXAFS: Near Edge X-Ray absorption fine structure

FTO: Fluorine doped tin oxide

FIB: Focused Ion Beam Epitaxy

FESEM: Field Emission Scanning Electron Microscopy

RHE: Reversible Hydrogen Electrode.

APCVD: Atmospheric Pressure Chemical Vapor Deposition

CT: Charge transfer band

UHB: Upper Hubbard Band

$E_F$  : Fermi Energy

$\phi$  : Photon Flux

W (v): Width of Depletion Layer

$V_{FB}$  : Flat Band Potential

a: absorption coefficient

$L_p$ : Minority carrier (hole) diffusion length

$D_p$ : Diffusion constant for holes

$W_0$ : depletion layer width constant

$P_0$ : Equilibrium hole density

$S^{CT}$ : Spectral weight

$E_g$ : Energy band gap

AM 1.5: Air Mass

KM: Kubelka- Munk Function

R: Diffuse Reflectance

K: molar absorption coefficient

S: scattering coefficient

$\beta$ : Band Tailing Parameter

$E^\circ$ : Standard Electrode Potential

CV: Cyclic Voltammetry

LH2: Light Harvesting Complex

PBS: Phosphate Buffered Saline

CDI: 1, 1'- Carbonyl diimidazole

EBAC: Expanded Bed Adsorption Chromatography

OER: Oxygen Evolution Reaction

**List of Figures**

**Figure 1.1:** Photoelectrochemical working principle..... 3

**Figure 1.2:** Energy level diagram of semiconductor- electrolyte junction demonstrating a relationship between electrolyte redox couple ( $H^+/H_2$ ), the Helmholtz layer potential drop ( $V_H$ ) and the semiconductor band gap ( $E_g$ ), electron affinity ( $\chi$ ), work function ( $\phi_x$ ), band bending ( $V_B$ ) and flat band potential ( $V_{fb}$ ) [7]..... 3

**Figure 2.1:** Schematic diagram of BL 7 at ALS ..... 12

**Figure 2.2:** A. Cappuccino cell B. Photoelectrochemical work station..... 14

**Figure 3.1:** A. Iron Oxide nanoparticle samples. B. Demonstration of the magnetic behavior of nanoparticles..... 17

**Figure 3.2:** Autoclave used for hydrothermal synthesis..... 20

**Figure 3.3:** A. Low resolution TEM image of iron oxides nanoparticles obtained hydrothermally; B-C. HRTEM image showing the well-developed lattice fringes... 21

**Figure 3.4:** Comparison of XRD pattern of iron oxide nanoparticles obtained by both thermal decomposition and hydrothermal reaction..... 21

**Figure 4.1:** X-ray diffractogram of iron oxide nano particles obtained by heat treatment of precursor complex from (A) 250-500 °C (B) expanded view of (104) and (110) peak in samples synthesized at 250 -500°C..... 28

**Figure 4.2:** X-ray diffractogram of iron oxide nano particles obtained by heat treatment of precursor complex from (A)550-900°C (B) expanded view of (104) and (110) peak in 550-900°C samples..... 29

**Figure 4.3:** TEM images of samples synthesized at (A) 250°C (Inset: SAED pattern) (B) 300°C (C) 600°C and (E) 900°C. (D – F) The corresponding HRTEM images of 600 °C and 900 °C samples..... 31

**Figure 4.4:** (A) Nano particle size distribution measured by particle size analyzer (B) variation of mean and median parameter with synthesis temperature along with crystallite size calculated using the Scherer equation..... 32

**Figure 4.5:** (A) Normalized Fe K-edge X-ray absorption spectra of  $Fe_2O_3$  nano particles synthesized at different heat treatment temperatures. (B) XANES region of the normalized Fe K-edge X-ray absorption spectra. (C) Pre-edge region of the normalized Fe K-edge X-ray absorption spectra. (D) Deconvoluted pre – edge region of spectra from different set of nano particles by varying the temperature..... 34

<b>Figure 4.6:</b> (A) Deconvoluted pre-edge peak of the respective XANES spectra for 250°C. (B) The relative peak area of the normalized peaks (maxima) against different annealing temperature.....	36
<b>Figure 5. 1:</b> The XRD pattern of iron oxides nanoparticles heat treated from 250°C to 550°C .....	42
<b>Figure 5.2:</b> expanded view of (104) and (110) peak in 250-550°C samples.....	42
<b>Figure 5. 3 (A)</b> Diffuse reflectance spectra of iron oxide nanoparticles heat treated at different temperature.....	43
<b>Figure 5.3 (B)</b> Absorbance spectra of iron oxide nanoparticles heat treated at different temperature. Inset shows the variation of energy band gap with heat treatment temperature .....	43
<b>Figure 5.4</b> HRTEM and FFT pattern of iron oxide nanoparticles heat treated from 250°C-550°C.....	45
<b>Figure 5.5 (A)</b> O-K edge NEXAFS spectra of iron oxide nanoparticles heat treated at different temperatures.....	46
<b>Figure 5.5 (B)</b> Variation of the relative peak intensity ( $I_A/I_B$ ) with respect to crystallite size. ....	47
<b>Figure 5.6 (A):</b> The Fe 2p NEXAFS data of iron oxide nanoparticles heat treated at different temperature.....	48
<b>Figure 5.6 (B)</b> Variation of $I_{L3} / I_{L2}$ values with respect to crystallite size.....	49
<b>Figure 5.6 (C)</b> Chemical shift for L3 edge with respect to change in crystallite size... ..	49
<b>Figure 5.7:</b> Sequential ATR-FTIR spectra of oxalate adsorbed onto Iron Oxide nanoparticles heat treated at different temperature in the dark at pH 3.6 and room temperature.....	51-52
<b>Figure 5.8:</b> Sequential ATR-FTIR spectra of oxalate adsorbed onto iron oxide nanoparticle observed after successive period of illumination at a total energy output of 1.0mW./ cm <sup>2</sup> , initial pH 3.60 and room temperature.....	53-55
<b>Figure 5. 9:</b> Variation of rate constant with BET specific surface area and annealing temperatures .....	55
<b>Scheme 6.1:</b> Schematic diagram of synthesis procedure for getting nanostructures hematite thin films.....	59

<b>Figure 6.2:</b> Hematite thin films obtained by the spin coating of polymeric precursor solution and heat treated at different temperature.....	59
<b>Figure 6.3:</b> tridentate ferrous iron-citrate complex: Oxidation and hydrolysis leads to bidentate ferric iron-citrate complex.....	60
<b>Figure 6.4:</b> (A, B, C) FESEM images of the hematite films deposited by spin coating method; (D)FIB imaging of the cross section of hematite film having thickness of 570 nm..	61
<b>Figure 6.5:</b> (A) XRD pattern of hematite nanopowders as well as film deposited on FTO substrate. The (110) plane obtained in both the cases clearly signify the presence of hematite phase.(B) XRD pattern of hematite films annealed at different temperature.....	62
<b>Figure 6.6:</b> Photoelectrochemical set up.....	62
<b>Figure 6.7 A.</b> Current –voltage characteristics of hematite films having a thickness of 570 nm under both dark and light condition. <b>B.</b> Current –voltage characteristics of hematite films annealed at different temperature.....	63
<b>Scheme 6.8:</b> Synthesis procedure for hematite film by dip coating technique.....	65
<b>Figure 6.9:</b> Hematite films obtained by repeated dip coating and annealing of FTO substrate coated with iron fatty acid precursor.....	66
<b>Figure 6.10:</b> XRD pattern of dip coated hematite film.....	66
<b>Figure 6.11:</b> FESEM images of Fe <sub>2</sub> O <sub>3</sub> films grown by dip coating technique on SnO <sub>2</sub> : F coated conducting glass. A. Top view. B. Nanoparticle having different sizes on the top side of the film. C. Cross section of 437 nm thick mesoporous hematite film on 317 nm compact SnO <sub>2</sub> : F.....	68
<b>Figure 6.12:</b> Current –voltage characteristics in darkness and under simulated light at a scan rate of 10 mV/s.....	69
<b>Figure 6.13:</b> Variation of film thickness with different deposited layer.....	70
<b>Figure 6.14:</b> Transmittance spectrum of α-Fe <sub>2</sub> O <sub>3</sub> film having different layer thickness deposited from precursor by dip coating technique.....	70
<b>Figure 6.15:</b> Corresponding XRD profile of hematite films having different layer thicknesses .....	71
<b>Figure 6.16:</b> Morphology of hematite films having different number of layer deposition. ....	71
<b>Figure 6.17:</b> Current –voltage characteristics in darkness and under stimulated light at a scan rate of 10 mV/s for hematite films having different layer thickness.....	72
<b>Figure 6.18:</b> XRD pattern of hematite film heat treated at different temperature.....	73
<b>Figure 6.19:</b> Morphology of hematite film studied by FESEMCharacterization....	73

<b>Figure 6.20:</b> UV-Vis Transmittance spectrum of hematite films deposited at different heat treatment temperature.....	74
<b>Figure 6.21:</b> Photocurrent density of hematite film at different heat treatment temperature under AM 1.5 sun illuminated light.....	75
<b>Figure 6.22:</b> XRD pattern of hematite film dwelled at different time during the deposition.....	76
<b>Figure 6.23:</b> FESEM Investigation of Morphology of Hematite Film with Respect to Dwelling Time.....	76
<b>Figure 6.24:</b> UV-Vis transmittance spectra of hematite films obtained for different dwelling time.....	77
<b>Figure 6.25:</b> Photocurrent density of hematite film dwelled at different time.....	78
<b>Figure 7.2:</b> SEM image of Si/ $\alpha$ -Fe <sub>2</sub> O <sub>3</sub> film prepared by dip coating of silicon wafer in iron fatty acid precursor.....	83
<b>Figure 7.3:</b> Photocurrent and dark current of a one-layer film obtained by dip coating. The inset shows the chopped light response of electrode.....	83
<b>Scheme 7.4:</b> Synthesis scheme for Si doping of hematite film.....	84
<b>Scheme 7.5:</b> Film deposition protocol with TEOS as interfacial layer.....	85
<b>Scheme 7.6:</b> Film deposition protocol at different annealing temperature.....	86
<b>Figure 7.7:</b> X- Ray diffraction pattern of Si-hematite film (0.5%) synthesized at different annealing temperature and TEOS as interfacial layer.....	87
<b>Figure 7.8:</b> Photocurrent vs. voltage curves of Si- Hematite film (0.5%) with TEOS as interfacial layer.....	87
<b>Figure 7.9:</b> Photocurrent vs. voltage curves of Si- Hematite film (A) no interfacial layer; annealed from 500 <sup>0</sup> C to 761 <sup>0</sup> C. (B) With interfacial layer; annealed from 500 <sup>0</sup> C to 761 <sup>0</sup> C (C) no interfacial layer; annealed from 850 <sup>0</sup> C for 2 min (D) with interfacial layer; annealed from 850 <sup>0</sup> C for 2 min.....	88
<b>Figure 7.10:</b> X-Ray diffraction pattern of hematite film doped with different % of Si. The inset shows the evolution of (110) peak with increase in doping %.....	89
<b>Figure 7.11:</b> FESEM images of Si- Hematite film with different doping %.....	90

<b>Figure 7.12:</b> X- Ray photoelectron spectroscopy survey data for the electrodes with different doping % of Si.....	91
<b>Figure 7.13:</b> Left - Photocurrent vs. voltage curves of Si- Hematite film with different doping %. Right – showing the variation of photocurrent density with doping%.....	91
<b>Figure 7.14:</b> Comparison of the photocurrent density of dip coated and APCVD deposited Si-hematite film.....	92
<b>Figure 7.15:</b> Left: Photocurrent density obtained for Si-hematite film deposited on 4 cm <sup>2</sup> FTO substrate (Solaronix). Right: Long term chronoamperometric stability study of Si-hematite film showing good sustainability in photocurrent.....	93
<b>Figure 7.16:</b> Gas evolution from the Si Hematite film on applying bias and illuminating with A.M 1.5 simulated sunlight.....	93
<b>Figure 8.1:</b> a) – Film thickness as a function of layers with linear least square fit; b) – photocurrent and dark current of 1 layer film obtained by dip coating; c) - photocurrent of dip coated films as a function of film thickness, measured at 600 mV; d) – photocurrent and dark current of Si-doped $\alpha$ -Fe <sub>2</sub> O <sub>3</sub> obtained by APCVD.....	99
<b>Figure 8.2:</b> Oxygen NEXAFS spectra of pristine $\alpha$ -Fe <sub>2</sub> O <sub>3</sub> film, film exposed to KOH, and light and dark treated film from 0 mV to 200 mV/SCE in KOH for 2 hours.....	101
<b>Figure 8.3:</b> Left - Oxygen NEXAFS spectra of FTO, pristine Fe <sub>2</sub> O <sub>3</sub> film 4 layers thick (red spectrum), and 1 layer (green) and 10 layer (blue) thin films oxidized to 600 mV in KOH. Middle – deconvolution of 10 layer film spectrum into Voigt functions and arctan function. The extra peak is plotted in red. Right – Oxygen NEXAFS spectrum of oxidized pyrite, as reproduced from Todd et al., ref. [8].....	102
<b>Figure 8.4:</b> Oxygen NEXAFS spectra of $\alpha$ -Fe <sub>2</sub> O <sub>3</sub> nanoparticle powder with 550°C heat treatment (left spectrum) and 1% Si-doped Fe <sub>2</sub> O <sub>3</sub> pristine sample (right).....	105
<b>Figure 8.5:</b> X-ray reflectometry data for the 1 layer $\alpha$ -Fe <sub>2</sub> O <sub>3</sub> film before (pristine) and after electrochemical oxidation at 600 mV for 2 hours.....	106
<b>Figure 9.1:</b> Sketch of cell assembly and film on Si <sub>3</sub> N <sub>4</sub> membrane.....	111
<b>Figure 9.2:</b> Oxygen 1s NEXAFS spectra recorded at 100 mV bias under a) light (left) and b) dark (right) condition.....	111

<b>Figure 9.3:</b> Oxygen 1s NEXAFS spectra recorded at 300 mV bias under a) light (left) and b) dark (right) condition.....	112
<b>Figure 9.4:</b> O1s spectra recorded at 500 mV bias under light (left) and dark (right) condition .....	113
<b>Figure 9.5:</b> Comparison of photocurrent (green line) and spectral weight (orange line with filled squares).....	114
<b>Figure 10.1:</b> Optical properties of pristine and modified hematite thin films A. Absorbance spectrum showing the visible light absorption of hematite at 545 nm, B. Transmittance spectra, C. Evaluation of optical band gap using Tauc plot. D. Variation of scattering coefficient with hydrothermal time calculated by applying the Kubelka- Munk function to diffuse reflectance spectra (inset).....	122-123
<b>Figure 10.2:</b> X-ray diffractograms of pristine film and 48 hour hydrothermal treatment film. ....	126
<b>Figure 10.3:</b> Scheme showing the conversion of pristine hematite film (a) into film with turf like carpet (c) upon hydrothermal after-treatment (b), FESEM images of pristine hematite film (d), total reorganization of the film (e) into stellate structure superimposed on the array of nanorod (f). ....	127
<b>Figure 10.4:</b> TEM studies of newly formed nanostructures after hydrothermal modification. a. The new hematite particles with rice grain shape. b. Superstructures with an exact orthogonality evolve from the nanorods which look like flowers. c. Selected area electron diffraction along with TEM at prominent positions of the multipod structure. d. The higher magnification image showing the nanorods have a substructure comprised of subunits of similarly elongated geometry of 2 nm x 5 nm size.....	128
<b>Figure 10.5:</b> X-ray photoelectron spectra in the valence band (VB) region and Fe 2p core level of pristine, 2 hrs. and 24 hrs. hydrothermal treated films. Black VB theoretical spectrum of hematite.....	129
<b>Figure 10.6:</b> Photocurrent for pristine film and 48 hours hydrothermal treatment film	130
<b>Figure 10.7:</b> Cyclic voltammetry data in the dark and illuminated condition, current versus potential of the Ag/AgCl electrode. Scan rate is 50 mV/s, 1M KOH (pH 13.8) (A) pristine hematite film (B) 48 hour hydrothermally processed film. ....	131

**Figure 10.8:** Long term stability measurement of photocurrent vs. Time at -503 mV (A-B), -253 mV (C-D) and 207 mV (E-F) against Ag/ AgCl electrode for pristine and 48 hour processed film (Inset: chopped light illumination). ..... 133

**Figure 10.9:** The variation of BET surface area and photocurrent of the modified films obtained at different time evolution..... 134

**Figure 10.10:** FESEM images A. Pristine hematite film after treatment with L –Arginine (5mmol); B. Pristine hematite film after treatment with FeCl<sub>3</sub>. 6H<sub>2</sub>O (5 mmol); C.Direct hydrothermal synthesis of FeCl<sub>3</sub>. 6H<sub>2</sub>O and L –Arginine without using hematite film (5:5 mmol) (Inset: hydrothermal treatment of hematite film with only water); D. Pristine hematite film after treatment with FeCl<sub>3</sub>. 6H<sub>2</sub>O and L –Arginine (5:5mmol)..... 136

**Figure 10.11 :** FESEM image of the modified films obtained after (A) 2 hr. (B) 4 hr. (C) 8 hr. (D) 18 hr. (E) 24 hr. (F) 48 hr. of hydrothermal treatment..... 137

**Scheme 10.12:** Illustration of the one pot transformation process in stepwise manner. 138

**Scheme 11.1(A)** The schematic of the conjugation strategy for the fabrication of hematite phycocyanin conjugate. (B) The chemistry involves in the above conjugation process..... 156

**Figure 11.2(I-II)**The FTIR spectra of Hematite – phycocyanin conjugate along with pristine, agarose modified and CDI activated films for probing the conjugation process.... 158

**Figure 11.3 (I):** The X-Ray Diffractogram of pristine hematite (A), Phycocyanin adsorbed on hematite (B), Agarose coated (B1), CDI activated (B2) and Phycocyanin conjugated (B3) films. (II) Expanded view of (104) and (110) reflection along with (101) from substrate. (III) Crystallite size variation of hematite after surface modification calculated using Scherer equation. (IV) Variation in relative Bragg peak intensity ratio [I (104) / I (101)] from the hematite and substrate to see the effect of thickness. (V) Relative Bragg peak ratio [I (104) / I (110)] of hematite and its variation at each surface modification step.... 160-162

**Figure 11.4(I)** UV-VIS absorption spectrums of pristine hematite (A), Phycocyanin adsorbed on hematite (B), Agarose coated (B1), CDI activated (B2) and Phycocyanin conjugated (B3) films. Inset: the change in the absorption maximum of phycocyanin on interacting with the nanoparticle from the film.(II) transmittance spectra of films A - E. Inset :the variation of %T with surface modification step.(III) the energy band gap(E<sub>g</sub>) of pristine film after each surface modification step in all films. Inset showing the trend in the variation of E<sub>g</sub>. 165-166

**Figure 11. 5** Raman spectra of pristine and modified films along with spectra from bare protein on glass and FTO substrate excited with visible and UV light show the integrity of protein after electrochemical treatment. .... 167

**Figure 11. 6** (I) The photocurrent measured for pristine hematite (A), Phycocyanin adsorbed on hematite (B), Agarose coated (B1), CDI activated (B2) and Phycocyanin conjugated (B3) films in 1M KOH electrolyte(pH= 13.6) with three electrode photoelectrochemical cell under the dark and simulated solar illumination (AM 1.5 ). (II)The photocurrent transient responses of pristine hematite (A), Phycocyanin adsorbed on hematite (B), Agarose coated (B1), CDI activated (B2) and Phycocyanin conjugated (B3) films measured during chronoamperometric cycling of all electrodes..... 170

**Scheme 11.7:** Energy band diagram showing the charge transfer from excited state phycocyanin to conduction band of hematite..... 171

**Figure 11.8** Long-term sustainability study of the photocurrent by carrying out the chronoamperometric measurement of the hematite film (A) and the protein functionalized films (B and C) at the oxidation potentials of water (207mV, 1.23 V vs. RHE).(D) The stability of photocurrent over time for pristine and protein functionalized film. (E) Number of moles of electrons obtained during dark chronoamperometric scan after 10 min of operation for samples A, B and B3 (F) IPCE measurement of pristine hematite film(A), phycocyanin adsorbed hematite film (B), Agarose modified phycocyanin adsorbed hematite(B1) and conjugated film (B2).

..... 173-175

**Table 11.9** The number of moles of electrons obtained and corresponding number of moles of evolved oxygen calculated from the chronoamperometric measurement..... 176

**Figure 11.10** (A) transient photorepsonse of the phycocyanin adsorbed FTO substrate and pristine FTO during chronoamperometric cycling to evaluate the individual role of phycocyanin protein in providing extra photocurrent. (B) long term stability measurement of phycocyanin chronoamperometrically for 1 hour under light condition ..... 177-178

**Figure 12.1:** Schematic of a PEC cell with solar conversion and storage capabilities [3]. Under light illumination (B) dark condition..... 189

**Figure 12.2:** Two days conversion and storage characteristics of the AlGaAs/Si/ MH/NiOOH MBPEC cell ..... 190

<b>Scheme 12.3:</b> Represents the architecture of NiO-hematite electrode.....	193
<b>Scheme 12.4:</b> Detail synthesis procedure of NiO –Hematite composite electrode.	193
<b>Scheme 12.5:</b> mechanism depicting the formation of NiO nanostructures on the top of hematite film. ....	194
<b>Figure 12.6 (A):</b> UV-Vis transmittance spectra of NiO- hematite electrode.....	196
<b>Figure 12.6 (B):</b> Evaluation of optical band gap using Tauc plot for indirect transition.	197
<b>Figure 12.6(C):</b> Evaluation of optical band gap for NiO - hematite electrode using Tauc plot for direct transition. ....	198
<b>Figure 12.7:</b> (A) XRD pattern of NiO – Hematite electrode. B) XRD pattern of NiO-Hematite film synthesized for short hydrothermal treatment showing the presence of Ni(OH) <sub>2</sub> .....	198
<b>Figure 12.8:</b> A. FESEM Image represents the morphology of electrode. B. EDX Mapping shows the presence of Fe and Ni elements along with Oxygen.....	199
<b>Figure 12.9:</b> From SEM Image at higher resolution, some wall like nanostructure has been observed on hematite surface.....	200
<b>Figure 12.10:</b> A. FIB Lamellae of NiO - Hematite Electrode; B. TEM Image of cross section of the electrode; C. Bright field image; D. SAED pattern showed the polycrystalline nature of the electrode; E. Dark field image showed the presence of NiO grain; F. HRTEM image showing the lattice fringes of hematite Nano crystallite and NiO corresponding to (110) and (200) plane .....	201
<b>Figure 12.11:</b> A. Area showing the EDX mapping region in the TEM cross section of NiO-hematite electrode. B. EDX mapping shows the presence of Ni (blue) along with Fe (red). C. STEM imaging of cross section of NiO - hematite electrode. D. Annular dark field STEM imaging for the energy filtered mapping of different elements present in the electrode. E, F, G: EF mapping showing the distribution of Fe, Ni and O elements.....	202
<b>Figure 12.12:</b> (A)Two Dimensional ERDA raw data (B)ERDA mass spectrum showed the higher content of Ni on very top surface at 10 nm depth in case of long term hydrothermally treated NiO dispersed on hematite.....	203-204
<b>Figure 12.13:</b> A. XPS survey scan showing the atomic content of Fe, Ni and O. B. XPS depth profile analysis of region 1 showing the atomic distribution of Fe and Ni element across the interface of NiO – Hematite electrode. C. XPS depth profile analysis of different region of NiO – Hematite electrode. ....	205
<b>Scheme 12.14:</b> Mechanism depicting the origin of color transformation.....	208

**Figure 12.15:** A. Cyclic Voltammogram of NiO- Hematite electrode showing around  $16\text{mA}/\text{cm}^2$  dark current. B. Comparison of the photocurrent density of hybrid electrode with pristine hematite electrode. C. Chronoamperometric study of NiO - Hematite electrode D. Phototransient current vs. time for NiO – hematite electrode at 100, 200 and 300 mV respectively. E. Comparison of cyclic voltammogram of samples (A, A1, B, B1) G. Significant gas evolution was observed on the surface of electrode. The exact nature of gas need to be further confirmed with gas chromatography..... 208

**Table of Contents**

Preface I

Acknowledgement IV

Abstract VI

Abbreviation VII

List of Figures IX

<b>Chapter 1: Introduction.....</b>	<b>1</b>
1.1 Photoelectrochemical water splitting .....	1
1.1.1 Basic principle.....	2
1.2 Artificial Photosynthesis.....	4
1.3 Semiconductor thin film as photoanode and way for increasing the efficiency....	4
1.4 Hematite Nanoarchitectures.....	5
1.5 Light harvesting antenna molecule .....	5
1.6 Integrated hybrid system for photoelectrochemical water splitting .....	5
<i>References</i> .....	6
<b>Chapter 2: Experimental Methods.....</b>	<b>9</b>
2.1 General experimental -Chemicals and reagents.....	9
2.2 Synthesis Method.....	9
2.3 Analytical equipment.....	10
<i>References</i> .....	14
 <b>Part 1: Hematite nanoparticle and thin films: properties and functionality</b>	
<b>Chapter 3: Synthesis: a) Thermal decomposition of iron fatty acid composite (b).....</b>	<b>16</b>
Hydrothermal reactions	
3. A.1 Introduction .....	16
3. A.2 Materials and methods.....	16
3. A.3 Results and Discussions.....	17
3. B.1 Introduction.....	18
3. B.2 Materials and methods.....	19
3. B.3 Results and Discussions.....	20
3.4 Conclusion.....	21
<i>References</i> .....	22
<b>Chapter 4: Evolution of structural properties of iron oxide nanoparticles during temperature treatment from 250°C – 900°C: X-ray diffraction and Fe K-shell pre-edge x-ray absorption study .....</b>	<b>24</b>

4.1	Introduction.....	24
4.2	Materials and methods.....	25
4.3	Results and Discussion .....	26
4.4	Conclusion.....	37
	<i>References</i> .....	38
 <b>Chapter 5: In - situ ATR-FTIR study of photocatalytic degradation of dicarboxylic acid on hematite nanoparticle surface.....</b>		
		40
5.1	Introduction.....	40
5.2	Materials and methods.....	41
5.3	Results and discussion.....	41
5.4	Conclusion.....	55
	<i>References</i> .....	56
 <b>Chapter 6: A. Synthesis and Photoelectrochemical Study of Nanocrystalline Pristine Hematite Film Deposited by <i>Spin Coating Method</i> .....</b>		
		57
6. A.1	Introduction.....	57
6. A.2	Materials and methods.....	57
6. A.3	Results and Discussion.....	58
<b>B. Synthesis of hematite thin films by the <i>dip coating method</i> .....</b>		
		64
6. B.2	Materials and methods.....	64
6. B.3	Results and Discussion.....	65
6. B. 3 (I)	Optimization of layer thickness to enhance the value of photocurrent.....	69
6. B. 3 (II)	Optimization of annealing temperature to enhance the value of photocurrent	72
6. B. 3 (III)	Optimization of dwelling time to enhance the value of photocurrent.....	75
6.4	Conclusion.....	78
	<i>References</i> .....	79
 <b>Chapter 7: Synthesis of nanostructured hematite film doped with Silicon for enhanced photocurrent efficiency.....</b>		
		80
7.1	Introduction.....	80
7.2	Materials and methods.....	82
7.3	Results and Discussion.....	83
7.3.1	Effect of different Si -doping % on the photo activity.....	90
7.3.2	Long term stability study of Si- hematite electrode.....	93
7.4	Conclusion.....	94

<i>References</i> .....	95
<b>Part 2: Hematite Electronic Structure Study with Soft X Ray absorption spectroscopy</b>	
<b>Chapter 8: Evolution of an oxygen NEXAFS transition in the upper Hubbard band in <math>\alpha</math>-<math>\text{Fe}_2\text{O}_3</math> upon electrochemical oxidation.....</b>	
8.1 Introduction.....	97
8.2 Experimental section.....	98
8.3 Results and Discussion.....	98
8.4 Conclusion.....	106
<i>References</i> .....	107
<b>Chapter 9: In situ electronic structure study of Si - doped hematite film under photoelectrochemical operation with soft X- ray absorption spectroscopy .....</b>	
9.1 Introduction.....	111
9.2 Materials and methods.....	111
9.3 Results and Discussion.....	112
9.4 Conclusion .....	116
<i>References</i> .....	117
<b>Part 3: Hybrid nanostructures based on hematite for PEC application: properties and functionality</b>	
<b>Chapter 10: Hydrothermal treatment of a hematite Film leads to highly oriented faceted nanostructures with enhanced photocurrents.....</b>	
10.1 Introduction.....	119
10.2 Experimental section.....	119
10.3 Results and discussion.....	121
10.4 Conclusion.....	138
<i>References</i> .....	139
<b>Chapter 11: Functionalization of nanostructured hematite thin film electrodes with the light harvesting membrane protein C-Phycocyanin yields enhanced photocurrent.....</b>	
11.1 Introduction.....	153
11.2 Experimental Section.....	154

11.3	Results and Discussions.....	155
11.3.1	Surface functionalization of hematite thin film with C-phycoerythrin protein.....	155
11.3.1.1	<i>Probing of conjugation reaction with FT-IR Spectroscopy.....</i>	<i>157</i>
11.3.2	Structural properties of hematite-phycoerythrin system.....	159
11.3.3	Optical properties of hematite - Phycoerythrin system.....	163
11.3.3	Probing the integrity of protein structure with Raman Spectroscopy.....	166
11.3.5	Photoelectrochemical properties of hematite - phycoerythrin system.....	168
11.3.5.1	<i>Possible factors influencing the increase in photocurrent.....</i>	<i>170</i>
11.3.5.2	<i>Source of enhanced photocurrent in hematite – phycoerythrin system .....</i>	<i>171</i>
11.3.5.3	<i>Role of phycoerythrin in enhancing the photocurrent and long term operational stability.....</i>	<i>176</i>
11.4	Conclusion.....	179
	<i>References.....</i>	<i>179</i>
<b>Chapter 12: Electrocatalytic Oxidation of Water on Hematite Surface by Hydrothermally Grown NiO Nanostructures.....</b>		
		<b>190</b>
12.1	Introduction.....	190
12.2	Materials and methods.....	193
12.3	Results and discussions.....	194
12. 3.1	Optical Properties of NiO-hematite electrode.....	196
12. 3.2	Structural properties of NiO-Hematite electrode.....	198
12. 3.3	Morphology investigation of NiO - Hematite electrode.....	200
12. 3.4	Surface and Interfacial compositional analysis of NiO - Hematite electrode....	203
12.3.5	Photoelectrochemical study of NiO- Hematite electrode.....	207
12.4	Conclusion.....	209
	<i>References.....</i>	<i>210</i>
	Conclusions and outlook.....	212
	<b>Appendix A: Hematite nanoflower optimization.....</b>	<b>214</b>
	<b>Appendix B: Optimized parameter for the fabrication of NiO – hematite electrode .....</b>	<b>229</b>

## Chapter 1

### Introduction

#### 1.1 Photoelectrochemical water splitting

Due to the increased demand of clean energy in near future, research on the development of alternative energy source is gaining momentum from last decade. Based on the requirement needed hydrogen is considered as eco- friendly green fuel. In nature, plants and cyanobacteria produce this hydrogen gas by utilizing the water splitting machinery of photosynthetic process. A unique method for mimicking the natural photosynthesis process can be realized by the development of photoelectrochemical cell working on the principle of semiconductor photoelectrochemistry concept. Becquerel first discovered the effect of light in electrochemical systems in 1839 [1]. The effect is more prominent in case of semiconductor electrode where energy greater than the band gap of material generate photocurrent and it raised as a result of the formation of electron – hole pair by the absorption of light. In this process, the presence of electric field helps in obtaining the photocurrent or photovoltage once charge carrier of opposite signs are generated [2]. Semiconductor – electrolyte interface determines the occurrence of this step. The potential differences between two phases (semiconductor and liquid) are controlled by the space- charge layer which is considered as part of electrical double layer [2]. It is to be noted that the photocurrent is drive by the electric field in this space charge layer.

The first photoelectrochemical cell was developed by Fujishima and Honda in 1972 [3]. They utilized n- type  $\text{TiO}_2$  electrode for the water electrolysis by shining light on it. However an efficiency of only (0.1%) was estimated at that time. Besides these Calvin [4] also designed another photoelectrochemical cell by sensitizing electrode surface with dye molecules. In the dye – sensitized photoelectrode, the generation of photocurrent is also determined by the space charge layer exist at the interface of semiconductor / dye / electrolyte interface.

The photoresponse effect in the above mentioned photoelectrochemical cell is generally produced by the potential barrier generated at the semiconductor – electrolyte interface by a thermodynamic equilibrium process. This equilibrium is established by the equalization of Fermi levels, where majority charge carrier (for instance, electron in case of n – type semiconductor) from electrode transferred into electrolyte [7]. Gerischer [2] put forwarded the concept of kinetics and energetic of electron transfer across semiconductor - electrolyte junction.

The photoelectrochemical water splitting process is getting paramount importance due to alleviation of energy storage problem by generating hydrogen which is renewable, non –

polluting and flexible in nature. The basic energy conversion of photoelectrochemical process is the transformation of photon energy into chemical energy.

Apart from the physical chemistry of PEC process, significant amount of effort have been given in making highly efficient photoelectrode. Various metal oxide based semiconductor photoelectrodes have been utilized for photoelectrochemical application. Out of these, hematite is found to be suitable for its stability in electrolyte as well as good visible light absorbing capability. During this study, my main focus will be directed towards the development and study of hematite photoelectrode in nanostructured form for photoelectrochemical application. It is noteworthy to mention that; hematite can be prepared at low cost which is considered as an added advantage. The iron (III) oxide or hematite electrode was first investigated by Bard and Hardee [5. *a*]. They found that iron (III) oxide material is very much stable in neutral and alkaline solution under photoelectrochemical operation. The low efficiency observed was interpreted using Gartner theory for semiconductor photoresponse [5. *b*]. They suggested that poor light absorption capability and short minority carrier (hole) diffusion length determine the efficiency of iron (III) oxide. Again, Dare – Edwards et. al [6] found that surface pretreatment of photoelectrode could influence upon the photoelectrochemical performance. They found that photocurrent onset was delayed due to very low Faradic rate constant for water oxidation chemistry. Following this fact, I became motivated to develop hematite based hybrid nanostructure for getting the enhanced photocurrent by the surface treatment of pristine hematite electrode.

### **1.1.1 Basic principle**

The basic principle of the photoelectrolysis of water (Figure 1. 2) consists of multiple steps viz. absorption of light having energy greater than the band gap of semiconductor; photogeneration of charge carrier (electron and holes); separation of charge carrier; diffusion of holes towards the semiconductor- electrolyte interface and oxidation of water; proton transfer across electrolyte towards the cathode and evolution of hydrogen gas with the reduction of proton. The electron required for the reduction process comes from the photoanode through the external circuit.

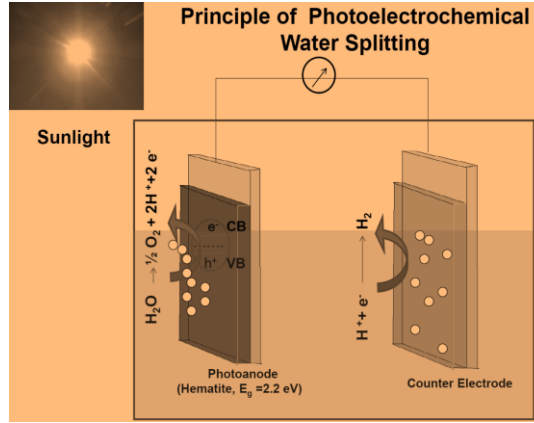


**Figure 1.1:** Photoelectrochemical working principle

**Semiconductor-electrolyte interface:** The formation of semiconductor- electrolyte junction determines all phenomena associated with photoelectrochemical systems [7]. This is formed by the immersion of appropriate semiconductor in appropriate electrolyte. Generally a space-charge layer is build up in a semiconductor upon contact and in equilibrium with another phase unless the chemical potential gradient for electrons is different. The chemical potential is normally given by the Fermi level in the semiconductor. When initial Fermi level in an n-type semiconductor overcome the Fermi level of electrolyte, equilibrium is obtained by the transfer of electrons from semiconductor to electrolyte. As a result of this a positive space charge layer is formed in the semiconductor which is also called as depletion layer as the region is depleted with majority charge carriers. A new potential barrier is established [Figure 1. 2] as a result of the bending of conduction and valence band edges which prevent further electron transfer to electrolyte.

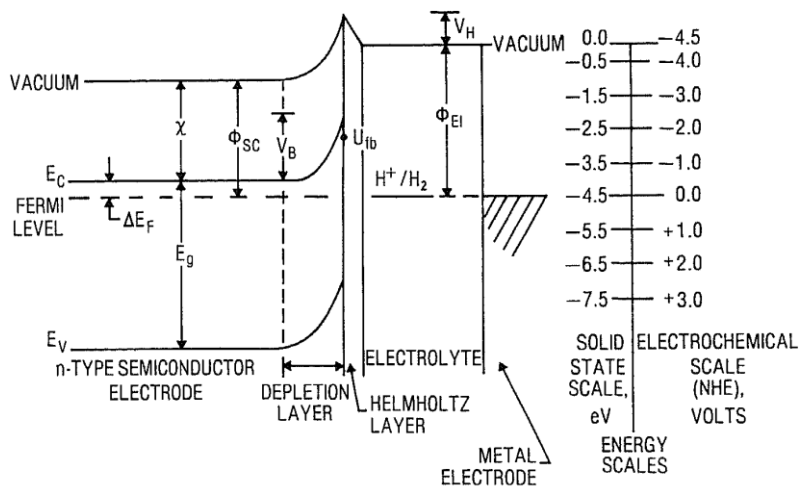


**Figure 1. 2:** Energy level diagram of semiconductor- electrolyte junction demonstrating a relationship between electrolyte redox couple ( $H^+/H_2$ ), the Helmholtz layer potential drop ( $V_H$ ) and the semiconductor band gap ( $E_g$ ), electron affinity ( $\chi$ ), work function ( $\phi_x$ ), band bending ( $V_B$ ) and flat band potential ( $V_{fb}$ ) [7].

## 1.2 Artificial Photosynthesis

Light harvesting is the initial step in the photosynthesis of plants and cyanobacteria, followed by the splitting of water and formation of  $O_2$  by photosystem II [8]. Nature provides thus an early model of light absorption and charge separation structures which can drive fuel forming photochemical reactions. The inorganic analog of this process is the photoelectrochemical water splitting on semiconductor electrodes [2]. Efforts have been made to mimic nature machinery by “artificial photosynthesis” such as by integration of light harvesting protein complexes with inanimate, inorganic material with photovoltaic properties [9]. The charge transfer across protein-solid state junctions has been identified as an important matter in this respect [10]. Integration of the light-harvesting LH2 complex from rhodobacter spheroids to patterned self-assembled monolayers at the micron scale has been demonstrated [11]. This approach is an interesting application in the area of biomimetic photovoltaic devices [12] taking advantage of the interaction of metalloproteins with oxide semiconductors. Another biomimetic light harvesting device concept has been developed using the interaction of cellular organelle such as chlorosomes with  $TiO_2$  [13].

## 1.3 Semiconductor thin film as photoanode and way for increasing the efficiency

Hematite thin films are interesting for photochemical water oxidation [14-18] because of their stability, suitable band gap, and energy band positions, but their reported efficiencies are relatively low. Optimization of their photocurrent densities has been achieved either through doping [19] or by morphological modification. Doping with silicon resulted in the formation of dendritic nanostructures and a significant increase in the incident photon-to-current conversion efficiency of 42% at 320 nm wavelength [20]. The suggested physical rationale for the increased photocurrent is minimization of the distance that the photogenerated electron holes have to overcome to arrive at the semiconductor-liquid interface. Hierarchical nanoarchitectures can also increase the efficiency [21]. The efficiency and photocorrosion stability of photoelectrode materials are also linked to the surface chemistry of crystal facets [22]. In hematite, the surface structure and chemistry of the (001) surface play an important role in the catalytic activity and electronic conductivity [23]. In niobium-doped single-crystal platelets of hematite, the (001) basal plane exposed to the electrolyte exhibits a good efficiency in water oxidation [24]. While substitution and doping can lead to an improved electronic structure and thus enhanced functionality, the influence of the morphology on the performance of the materials should not be underestimated.

## 1.4 Hematite Nanoarchitectures

The development of different hematite-based hierarchical nanoarchitectures such as nanowires, nanobelts, nanotubes, nanorods, flowerlike, urchinlike, and elliptic

superstructures, or dendritic micropines is an emerging strategy for the design of functionalized devices [25-31]. Most of these structures have been fabricated using hydrothermal reactions, chemical vapor deposition, or ionic-liquid-assisted routes. In the case of hydrothermally grown structures, the morphology can be controlled by moderating the aqueous hydrolysis condensation growth onto substrates [32].

### **1.5 Light harvesting antenna molecule**

Phycocyanin is the light-harvesting protein from the phycobilisome family found in the photosynthetic blue-green algae (cyanobacteria), red algae, and the cryptomonads. It absorbs light from the red part of the visible spectrum (620 nm) and then provides a highly efficient exciton migration until the energy arrives at a photochemical reaction center through a funneling mechanism. It belongs to oligomeric proteins which use linear tetrapyrrole chromophores (phycocyanobilins) for light harvesting. The bilins are covalently attached to cysteine residues of the apoprotein by thioether bonds, and are not associated with metal ions [33].

### **1.6 Integrated hybrid system for photoelectrochemical water splitting**

Integration of light harvesting proteins and other photosynthetic molecular machinery with semiconductor surfaces plays an important role in improving their performance as solar cell materials. A biomimetic photonic energy conversion system was developed by immobilizing the photoactive protein complex photosystem I on the surface of nanoporous gold electrodes so as to drive a photoinduced electric current through an electrochemical cell [34]. A detailed study of the photovoltaic activity of a photosystem I based self-assembled monolayer [35] and the interaction of biomolecular assemblies with photoelectrochemical cells [36] has been provided recently. Following this approach, several systems have been developed such as chloroplast photoelectrochemical cell [37], a chlorophyll-lecithin mixed monolayer coated electrode with the aim of designing solar conversion systems based on the photosynthetic primary reactions [38], photoelectrolysis at a chlorophyll - water aggregate coated Platinum electrode as a photocathode [39], immobilization of the bacterial photosynthetic reaction center from *Rhodospirillum rubrum* spheroids on SnO<sub>2</sub> electrode for photoelectrochemical conversion [40], photoelectrochemical cells with chloroplast membranes, chloroplasts, Photosystem I particles, purple membrane fragments containing bacteriorhodopsin [41- 44], to name a few.

Recently, Hybrid systems for energy generation have been developed. For example, TiO<sub>2</sub> nanotube-bacteriorhodopsin hybrid system [45], biomimetic light harvesting device composed of columnar TiO<sub>2</sub> film and chlorosome [13], self-assembled monolayer of light harvesting complex on amino terminated ITO [46], etc. In the biomimetic light harvesting

device, first the chlorosome has been sprayed on the dye adsorbed TiO<sub>2</sub>. The device performance was based on the enhanced current generation due to the interaction of the dye and chlorosome over the entire wavelength region. The photocurrent increased remarkably in the device containing chlorosomes at long wavelength region from 640 nm to near infrared. The presence of chlorosomes in the device increased the photocurrent by over a factor of 30. In the case of the TiO<sub>2</sub> nanotube – bacteriorhodopsin hybrid system, under AM 1.5 illuminations the photocurrent density of hybrid electrode was found to be around 50% over pure TiO<sub>2</sub>. Redox electrolyte increases the photocurrent value to 0.87 mA/cm<sup>2</sup>. The system showed slight increase in photocurrent similar to hematite phycocyanin system in our case. This increase was attributed to the continuous proton pumping mechanism over extended illumination time. For the hybrid device consisting of a self-assembled monolayer of light harvesting complex (LHC) on amino terminated ITO, the photocurrent responses showed a maximum at the wavelength corresponding to the absorption band of the complex when LHC and the reaction center are combined. The enhanced photocurrent was observed especially upon illumination at 880 nm. But in case of the LHC alone, the photocurrent was mainly generated by light absorbed at 770 nm. Again, if only the reaction center is immobilized on amino terminated ITO, photocurrent has not been observed at 880 nm.

The enhanced photocurrent observed at 880 nm in the assembled LH1-RC core complex can be ascribed to energy transfer from LH1 to RC and then electron transfer from the electrode to RC. This indicates that the LH1 RC core complex was well organized on the ITO and the photocurrents were driven by light that was initially absorbed by the light harvesting component. All these strategy based on the chemical modification of electrode surface. The covalent functionalization was originally applied for the surface modification of titanium (IV) oxide electrode to give stable dye sensitization with supersensitizer [47].

## References

- [1] Becquerel, E.; *C. R. Acad. Sci.* **1839**, *9*, 561.
- [2] Gerischer, H.; *Electroanalytical Chemistry and Interfacial Electrochemistry*, **1975**, *58*, 263-274.
- [3] Fujishima, A.; Honda, K. *Nature* **1972**, *238*, 37–38.
- [4] Calvin, M.; *Science*, **1974**, *184*, 375.
- [5] *a.* Hardee, K. L.; Bard, A. J.; *J. Electrochem. Soc.* **1976**, *123*, 1024; *b.* Gaertner, W.; *Phys. Rev* **1959**, *116*, 84
- [6] Dare-Edwards, M. P.; Goodenough, J. P.; Hamnett, A.; Trevellick, P. R.; *J. Chem. Soc., Faraday Trans. 1*, **1983**, *79*, 2027 – 2041.

- [7] Nozik, A. *J. Ann. Rev. phy. Chem.* **1978**, *29*, 189-222.
- [8] Lewis, N. S. *Nature* **2001**, *414*, 589.
- [9] Das, R.; Kiley, P. J.; Segal, M.; Norville, J.; Yu, A. A.; Wang, L.; Trammell, S. A.; Reddick, L. E.; Kumar, R.; Stellacci, F.; Lebedev, N.; Schnur, J. B.; Bruce, D.; Zhang, Baldo, S.; M. *Nano Lett.* **2004**, *4*, 1079.
- [10] Ron, I.; Sepunaru, L.; Itzhakov, S.; Belenkova, T.; Friedman, N.; Pecht, I.; Sheves, M.; Cahen, D. *J. Am. Chem. Soc.* **2010**, *132*, 4131.
- [11] Reynolds, N. P.; Janusz, S.; Escalante-Marun, M.; Timney, J.; Ducker, R. E.; Olsen, J. D.; Otto, C.; Subramaniam, V.; Leggett, G. J.; Neil Hunter, C. *J. Am. Chem. Soc.* **2007**, *129*, 14625.
- [12] Khare, N.; Eggleston, C. M.; Lovelace, D. M.; Boese, S. W. *J. Colloid Interf. Sci.* **2006**, *303*, 404.
- [13] Modesto-Lopez, L. B.; Thimsen, E. J.; Collins, A. M.; Blankenship, R. E.; Biswas, P. *Energ. Environ. Sci.* **2010**, *3*, 216.
- [14] Sartoretti, C. J.; Alexander, B. D.; Solaraska, R.; Rutkowska, I. A.; Augustynski, J. *J. Phys. Chem. B* **2005**, *109*, 13685–13692.
- [15] Watanabe, A.; Kozuka, H. *J. Phys. Chem. B* **2003**, *107*, 12713–12720.
- [16] Duret, A.; Gratzel, M. *J. Phys. Chem. B* **2005**, *109*, 17184–17191.
- [17] Tahir, A. A.; Upul Wijayantha, K. G.; Saremi-Yarahmadi, S.; Mazhar, M.; Mckee, V. *Chem. Mater.* **2009**, *21*, 3763–3772.
- [18] Zhong, D. K.; Sun, J.; Inumaru, H.; Gamelin, D. R. *J. Am. Chem. Soc.* **2009**, *131*, 6086–6087.
- [19] Saremi-Yarahmadi, S.; Upul Wijayantha, K. G.; Tahir, A. A.; Vaidhyathan, B. *J. Phys. Chem. C* **2009**, *113*, 4768–4778.
- [20] Kay, A.; Cesar, I.; Gratzel, M. *J. Am. Chem. Soc.* **2006**, *128*, 15714–15721.
- [21] Rangaraju, R. R.; Pandey, A.; Raja, K. S.; Misra, M. *J. Phys. D: Appl. Phys.* **2009**, *42*, 135303.
- [22] Yang, H. G.; Sun, C. H.; Qiao, S. Z.; Zou, J.; Liu, G.; Smith, S. C.; Cheng, H. M.; Lu, G. Q. *Nature* **2008**, *453*, 638–641.
- [23] Warschkow, O.; Ellis, D. E.; Hwang, J.; Mansourian-Hadavi, N.; Mason, T. O. *J. Am. Ceram. Soc.* **2002**, *85*, 213–220.
- [24] Sabchez, C.; Sieber, K. D.; Somorjai, G. A. *J. Electroanal. Chem.* **1988**, *252*, 269–270.
- [25] An, Z.; Zhang, J.; Pan, S.; Yu, F. *J. Phys. Chem. C* **2009**, *113*, 8092–8096.
- [26] Wen, X.; Wang, S.; Ding, Y.; Lin Wang, Z.; Yang, S. *J. Phys. Chem. B* **2005**, *109*, 215–220.

- [27] Jia, C.; Sun, L.; Yan, Z.; You, L.; Luo, F.; Han, X.; Pang, Y.; Zhang, Z.; Yan, C. *Angew. Chem., Int. Ed.* **2005**, *44*, 4328–4333.
- [28] Chueh, Y. L.; Lai, M. W.; Liang, Q.; Chou, L. J.; Wang, Z. L. *Adv. Funct. Mater.* **2006**, *16*, 2243–2251.
- [29] Tang, B.; Wang, G.; Zhou, L.; Ge, J.; Cui, L. *Inorg. Chem.* **2006**, *45*, 5196–5200.
- [30] Zhu, L. P.; Xiao, H. M.; Liu, X. M.; Fu, S. Y. *J. Mater. Chem.* **2006**, *16*, 1794–1797.
- [31] Cao, M.; Liu, T.; Gao, S.; Sun, G.; Wu, X.; Hu, C.; Wang, Z. L. *Angew. Chem., Int. Ed.* **2005**, *44*, 4197–4201.
- [32] Vayssieres, L. *Appl. Phys. A: Mater. Sci. Process.* **2007**, *89*, 1–8.
- [33] Berns, D. S.; McColl, R. *Chem. Rev.* **1989**, *89*, 807.
- [34] Ciesielski, P. N.; Scott, A. M.; Faulkner, C. J.; Berron, B. J.; Cliffel, D. E.; Jennings, G. K. *ACS Nano*, **2008**, *2*, 2465.
- [35] Carmeli, I.; Frolov, L.; Carmeli, C.; Richter, S. *J. Am. Chem. Soc.* **2007**, *129*, 12352.
- [36] Gratzel, M. *Nature* **2001**, *414*, 338.
- [37] Bhardwaj, R.; Pan, R. L.; Gross, E. L. *Nature* **1981**, *289*, 396.
- [38] Miyasaka, T.; Watanabe, T. *Nature* **1979**, *277*, 638.
- [39] Fong, F. K.; Winograd, N. *J. Am. Chem. Soc.* **1976**, *98*, 2287.
- [40] Jenzen, A. F.; Seibert, M. *Nature* **1980**, *286*, 584.
- [41] Buvet, R.; Allen, M. J.; Massué, J. P. *Living Systems as an Energy Converter: proceedings of the European Conference on Living Systems as Energy Converters*, Elsevier, Amsterdam, **1977**.
- [42] Ochiai, H.; Shibata, H.; Fujishima, A.; Honda, K. *Agr. Biol. Chem. Tokyo* **1979**, *43*, 181.
- [43] Gross, E. L.; Youngman, D. R.; Winemiller, S. L. *Photochem. Photobiol.* **1978**, *28*, 249.
- [44] Skulachev, V. P. *FEBS Lett.* **1976**, *64*, 23.
- [45] Allam, N. K.; Yen, C.; Near, R. D.; El-Sayed, M. A. *Energ. Environ. Sci.* **2011**, *4*, 2909–2914.
- [46] Suemori, Y.; Nagata, M.; Nakamura, Y.; Nakagawa, K.; Okuda, A.; Inagaki, J.; Shinohara, K.; Ogawa, M.; Iida, K.; Dewa, T.; Yamashita, K.; Gardiner, A.; Cogdell, R. J.; Nango, M. *Photosynth. Res.* **2006**, *90*, 17.
- [47] Anderson, S.; Constable, E. C.; Dare – Edwards, M. P.; Goodenough, J. B.; Hamnett, A.; Seddon, K. R.; Wright, R. D. *Nature*, **1979**, *280*, 571 – 573.

## Chapter 2

### Experimental methods

#### 2.1 General experimental -Chemicals and reagents

Following chemicals were used during the entire study of the experiments. All are commercially available with reagent grade and were used without further purification

1. Stearic acid [ $C_{18}H_{36}O_2$ ]
2. Iron (III) nitrate 9-hydrate [ $Fe(NO_3)_3 \cdot 9H_2O$ ]
3. Tetrahydro furan ( $C_4H_4O_5$ )
4.  $FeCl_3 \cdot 6H_2O$  (analytical agent, AR)
5. L-Arginine ( $\alpha$ -amino- $\delta$ -guanidovaleric acid)
6. Deionized water
7. Citric acid [ $C_6H_8O_7$ ]
8. Polyethylene glycol ( $C_2H_6O_2$ )
9. Oleic acid [ $C_{18}H_{34}O_2$ ]
10. TEOS (Tetra ethyl ortho silicate)
11. 1, 4- dioxane
12. Phosphate buffered saline (PBS)
13. C-phycocyanin isolated from *Spirulina* sp. (Sigma-Aldrich, Switzerland, 99.9% purity).
14. 1, 1'-carbonyldiimidazole
15.  $NiCl_2 \cdot 6H_2O$
16. Hexamine

#### 2.2 Synthesis Method

##### *Hematite Nanoparticles*

- Thermal decomposition of iron- fatty acid precursor
- Hydrothermal reaction of iron salt with amino acid

##### *Hematite thin film*

- Spin coating of polymeric precursor solution on FTO substrate
- Dip coating of iron oleate complex on FTO substrate

##### *Hematite nanoflower*

- Hydrothermal treatment with L - Arginine

##### *Hematite/ C-Phycocyanin hybrid electrode*

- Surface functionalization chemistry

##### *NiO – Hematite electrode*

- Hydrothermal treatment with nickel chloride and hexamine.

### 2.3 Analytical equipment

**UV-Vis Spectroscopy:** The optical properties were studied by UV –Vis spectrometer (Carry Scan 50).

**Diffuse reflectance spectroscopy:** Diffuse reflectance has been studied with Cary 5000(V1.12) UV-Vis-NIR Spectrophotometer with an integrating sphere diffuse reflectance accessory. The Integrating sphere was coated with MgO and the spectra were referenced against these white material.

**Field emission scanning electron microscopy:** Field emission scanning electron microscopy was performed on a Hitachi S-4800 model.

**Focused ion beam epitaxy:** TEM lamellae preparation was performed on a FEI dual beam FIB.

**Transmission Electron Microscopy:** A JEOL JEM 2200 FS transmission electron microscope/STEM operating at 200 KeV accelerating voltage was used for TEM analysis.

**X-Ray Diffractometry:** The phase composition of the pristine and modified films was examined by powder X-ray diffraction analysis (PAN analytical X'Pert PRO, Cu K $\alpha$  radiation) measured by Mr. Hansjürgen Schindler.

**X –Ray Reflectometry [1]:** XRR measurement was performed by Ms. Romy Loehnt. For reflectometry measurement a *Siemens D5000* diffractometer with Cu K $\alpha$ 1 radiation was used. To cut off unparallel beam fractions a collimator and LiF-crystal monochromator are installed in front of the detector instead of slits and filters normally used for X-ray diffraction. The sample is fixed to the sample holder by under pressure and a beam-knife is installed above the sample leaving only a small slot between sample surface and beam-knife. In this way the angular divergence of the beam is reduced and sufficient angular resolution is achieved. Prior to the measurement the sample surface has to be aligned exactly to the primary beam direction. By varying the applied voltage and current of the x-ray tube the intensity of the x-ray beam is adjusted to a maximum count rate of 360,000cps in the region of total reflection. The measurement was done in  $\theta/2\theta$ -configuration in a range of  $0.07^\circ \leq 2\theta \leq 2^\circ$  with a scan speed of 2s/step and an increment of  $0.002^\circ$ .

**X-Ray Photoelectron Spectroscopy:** X-ray photoelectron spectra were recorded by a PHI LS5600 spectrometer equipped with Mg K $\alpha$  X-ray source, spectra calibrated using C1s = 285.0 eV.

**BET surface area measurement:** The surface area of nanoparticles and films were obtained by applying the BET technique (Coulter SA3100 Series Surface area and Pore Size Analyzers) on powders, which were scratched from the films.

**Fe-K edge X Ray Absorption Spectroscopy:** X-ray absorption spectra at the Fe K edge were collected at the Swiss-Norwegian beam line (SNBL) at the European Synchrotron Radiation Facility (ESRF), Grenoble, France. The electron energy in the storage ring was 6 GeV with a maximum current of 200mA. A Si (111) double-crystal monochromator was used for energy selection, which was detuned by 20–50% in order to suppress higher harmonic radiation. The intensities of the incident and transmitted X-rays were monitored with nitrogen-filled ionization chambers. The monochromator was scanned from 200 eV below to 800 eV above the Fe K-shell absorption edge (7111 eV). The Fe K-edge XAS were measured in the transmission mode at ambient temperature. A 7- $\mu\text{m}$  thin Fe foil was used as a reference for X-Ray energy calibration. Nano particle powders were mixed with boron nitride in 1:5 ratios and then pressed to pellets for the X-ray absorption measurements. Background subtraction and normalization of the spectra was performed with standard procedures using the software program WinXAS.

**Fe L edge and O K edge near edge X-Ray absorption spectroscopy:** Near edge x-ray absorption fine structure (NEXAFS) spectra were recorded at the undulator beamline UG-56 at BESSY [22], in an UHV recipient with  $2 \times 10^{-10}$  mTorr base pressure or lower. The resolution of this beamline is 0.05 eV (80000 at 64eV) at the soft energy range for oxygen K-edge and Fe L-edges. X-ray reflectometry data were recorded with a Siemens D5000 diffractometer with Cu  $K\alpha_1$  radiation in  $\theta/2\theta$ -configuration in a range of  $0.07^\circ \leq 2\theta \leq 2^\circ$  with a scan speed of 2s per  $0.002^\circ$  step.

**In-situ NEXAFS Spectroscopy of working photoelectrode:** It was performed at Beam line 7.0 in Advanced Light Source, Berkeley. The beam line is equipped with a spherical grating monochromatic, providing resolving power of 5000 in the energy range of 80-1000eV. It is available for studying the fundamental electronic properties of materials in solid, gaseous and aqueous phases. The beamline and end station are capable of performing XAS measurements. The schematic diagram of BL7 at ALS is shown in figure 2.1.

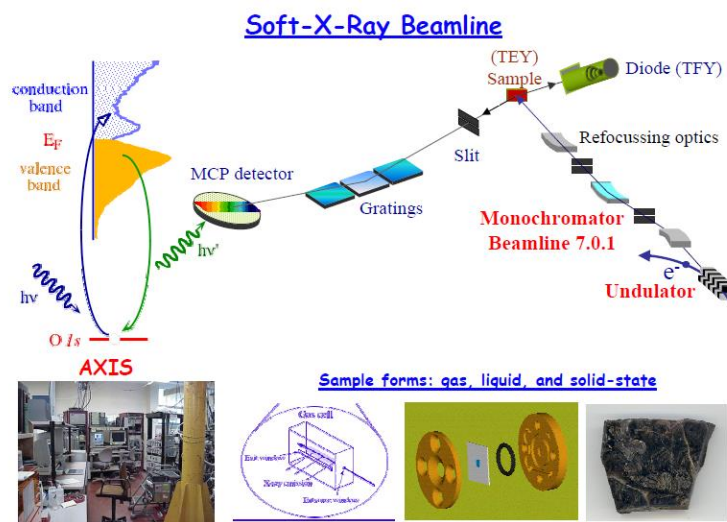


**Figure 2.1:** Schematic diagram of BL 7 at ALS [Courtesy: Dr. Jinghua Guo, Advanced Light Source]

The in situ experiment was carried out by placing the sample in specially designed liquid cell. It has a window for compatibility with the UHV conditions of the spectrometer and beamline. The window is made of silicon nitride with a thickness of 100 nm and it separates the liquid from the surrounding vacuum. It is penetrated both by the incident photon beam and the X-Ray emission. It is commercially available. The test showed that window could hold a nitrogen gas pressure of 18 bars.

**Attenuated total reflectance Fourier transform infrared spectroscopy:** In situ photo catalytic degradation of carboxylic acid on hematite surface was studied with ATR-FTIR. Here, Spectra were recorded on a Bio-Rad FTS 575C instrument equipped with a mercury cadmium telluride detector and a horizontal nine reflection diamond ATR unit with KRS-5 optics (SensIR Technologies, Danbury, CT). Scans were taken from 400 to 4000  $\text{cm}^{-1}$  at 2  $\text{cm}^{-1}$  resolution. Data analysis was performed with Matlab.

**Atomic Force Microscopy:** AFM study has been performed in tapping mode using Nanosurf-AFM, (Mobile S).

**Particle size analysis:** Particle size distribution was determined by LS 230 particle size analyzer from Beckman Coulter by using the PIDS (Polarization Intensity Differential Scattering) signal of 40%. The lower resolution limit of this instrument is 40 nm.

**Profilometry:** Film thickness and roughness of the prepared samples were measured with a mechanical profilometer (*XP-1 Stylus Profiler* by *Ambios Technology*). A stylus with conical diamante tip with diameter of 5  $\mu\text{m}$  is in contact with the sample surface and is moved laterally over it. Changes in thickness and roughness of the sample induce a vertical displacement of the stylus that is recorded and converted to a digital signal.

**Confocal Raman Spectroscopy:** The optical Raman spectra were recorded with a RENISHAW ® in Via Raman Microscope by using blue laser at 442 nm (exposure time of 10.0 s). For characterizing protein samples alone, I used UV excitation at 325 nm (exposure time of 50.0 s, 4 accumulations at 100 % laser power.

**Elastic recoil detection analysis:** The samples compositions of the films were determined by Elastic recoil detection analysis (ERDA). For the ERDA analysis a 12 MeV <sup>127</sup> I beam was used under incidence angle of 18°.

**Photoelectrochemical Study:** To determine the PEC performance of hematite films linear voltammetry was performed under dark and light condition [1]. The sample operates as working electrode in a three electrode configuration. A platinum wire is set as counter electrode and an Ag/AgCl/3-M KCl electrode is used as reference electrode. The electrodes are immersed in 1M KOH electrolyte in a specially developed electrochemical cell called as “cappuccino cell” (figure 2.2.A). Electric contact to the hematite film is made via the FTO coating on the glass substrate and a titanium crocodile clip. In light condition an area of 0.6 cm<sup>2</sup> of the sample is illuminated with simulated sunlight of AM 1.5 global standard solar spectrum [2] generated by a *1 Sun Oriel Lamp* by *L.O.T – Oriel AG*. Wavelengths lower than 280nm and higher than 800nm are removed from the spectra with an Air Mass 1.5 filter. For the measurement a potentiostat (*Voltalab80 PGZ 402* by *Radiometer analytical*) is used. The setup is shown in figure 2.2. B.

For the measurement the open circuit potential of the sample was measured first for four minutes to determine the rest potential. Then the current density  $J$  is measured as a function of the applied voltage  $V$ . The measurement was started at open circuit potential of sample and applied potential was changed up to 600mV at a speed of 10mV/s. The measurement was done in dark condition first and then repeated with illumination of sample. The error of measured current density is 0.2μA/cm<sup>2</sup> below a range of 120μA/cm<sup>2</sup> and above this it is 2μA/cm<sup>2</sup>. The value of achieved photocurrent density is taken at an applied voltage of 0.42V, equal to the voltage of water electrolysis against RHE for the used measurement conditions

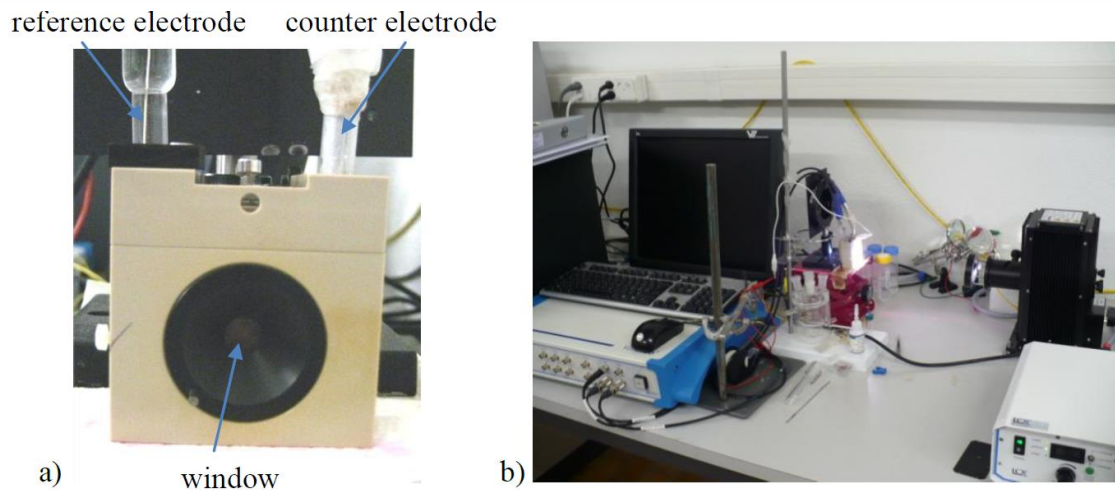


**Figure 2.2.**a) Cappuccino cell b) Photoelectrochemical work station.

**References**

[1] Bachelor Thesis, Romy Löhnart, Synthesis and characterization of hematite nanoparticles and films for photoelectrochemical applications, **2010**, University of Applied Sciences, Jena, Germany.

[2] Standard ISO 9845-1, 1992.

## **Part I-Hematite nanoparticle and thin films: properties and functionality**

## Chapter 3

### **Synthesis: A) Thermal decomposition of iron fatty acid composite**

#### **3. A. 1 Introduction**

Nano sized iron oxide particulates have emerged as versatile materials for different applications due to their, magnetic, electronic, photonic and optical properties. The structure-function relationship of these nano particles have been intensively studied because of the applications in magnetic storage, gas sensing, biomedical, and catalysis applications [1-5]. Iron oxides nano particles have been prepared by a variety of methods such as sonochemical reactions [6], mechanochemical synthesis [7], hydrolysis, thermolysis of precursors as well as co-precipitation technique [8]. Nano particles with a virtually near to monodisperse size distribution can be produced by thermal decomposition of an iron-cupferron complex in octylamine [9]. Organometallic complexes of iron are being used as precursors for the synthesis. For example, iron pentacarbonyl,  $\text{Fe}(\text{CO})_5$ , with oleic acid and trimethyl oxide in octyl ether has been used for maghemite synthesis [10]. Out of various phases of iron oxide nano particle recently great interest has been devoted towards to the synthesis of  $\alpha$ -phase of iron oxide nano particles ( $\alpha\text{-Fe}_2\text{O}_3$ , hematite). These are of technological interest for the use in photoelectrochemical (PEC) water splitting reaction for the production of hydrogen [11-18].

Hematite nano particles can be prepared by several techniques such as hydrothermal approach, catalytic synthesis, flame spray pyrolysis, non-aqueous synthesis, surfactant assisted method such as CTAB etc. [20-25]. Besides these, a versatile and low cost technique was developed to synthesize hematite nano particles through a gentle chemistry route, which has some advantages of its own [26]. Unlike some processes where large aggregates are formed, occurrence of uncontrolled oxidation, and presence of matrix etc. the new technique is free from all of these problems.

#### **3. A. 2 Materials and Methods**

##### **Material used:**

- |  |       |
|--|-------|
| 1. Stearic acid [ $\text{C}_{18}\text{H}_{36}\text{O}_2$ ]                     | 17 gm |
| 2. Iron (III) nitrate [ $\text{Fe}(\text{NO}_3)_3 \cdot 9\text{H}_2\text{O}$ ] | 28 gm |
| 3. Tetrahydro furan ( $\text{C}_4\text{H}_8\text{O}$ )                         | 80ml  |

*Synthesis procedure:* I adopted this synthesis procedure because of my familiarity with it during the master study in India. For the synthesis of iron oxide nano particles high purity (99%) iron (III) nitrate [ $\text{Fe}(\text{NO}_3)_3 \cdot 9\text{H}_2\text{O}$ ] and stearic acid [ $\text{C}_{18}\text{H}_{36}\text{O}_2$ ] in the ratio of 1:2 were used as initial ingredients. The homogeneous solution of the molten mixture was then heated at  $125^\circ\text{C}$  for 90 minutes which then formed a reddish brown viscous mass which was subsequently treated with tetrahydrofuran (THF). The powdery precipitates were collected through centrifugation and dried completely in a furnace supplied with ambient air at  $70^\circ\text{C}$ . The dried precipitates were further subjected to heat treatment at  $250^\circ\text{C}$  for holding time of 30 minute inside the electrically heating furnace to get the nano particles. The remainder of the precursor complex has been synthesized in a similar manner by annealing in systematic fashion from  $300^\circ\text{C}$  to  $900^\circ\text{C}$  to obtain the hematite phase. It was performed in non-isothermal manner by putting the precursor samples in  $\text{Al}_2\text{O}_3$  crucibles in a Ceram-Aix furnace (FHT 175/30) using a heating rate of 300 K/h to the annealing temperature, a holding time of 30 min and a cooling rate of 300 K/h.

### 3. A.3 Results and Discussion

The iron oxide nanoparticles prepared at different heat treatment temperatures are shown in Figure 3.1. The particles shows goof magnetic properties as evident from figure 3.1.B.

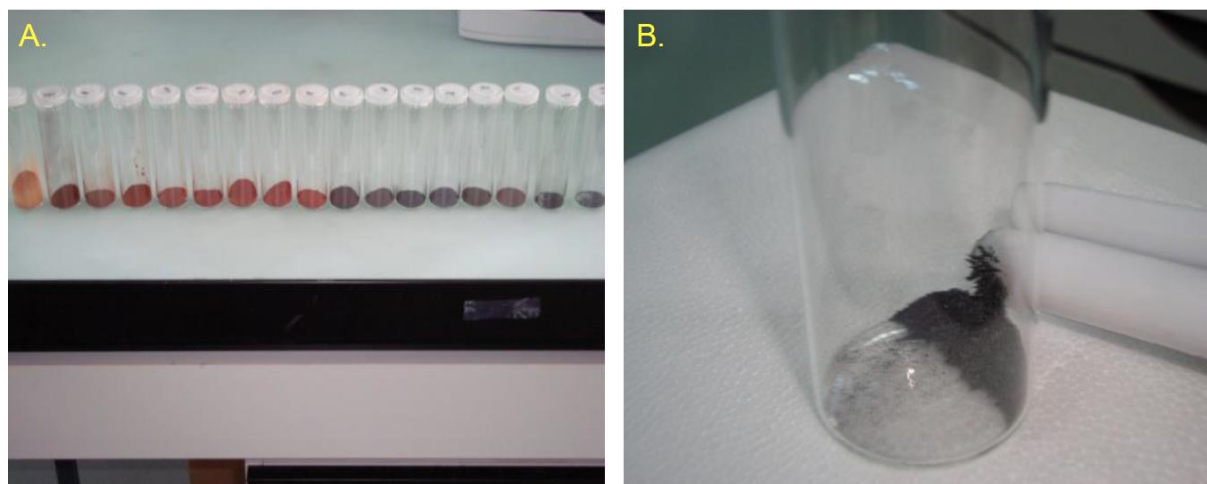


**Figure 3.1:** A. Iron oxide nanoparticle samples. B. Demonstration of the magnetic behavior of nanoparticles.

Heat treatment is basically done in isothermal manner. First the samples are placed in 2 porcelain pots to be inserted into the furnace in such a way that the boat should be in the center point of the furnace. Temperature is set to the desired level. It was seen that after setting the temperature, it goes up rapidly to a very high level but it is maintained at the particular temperature. This is due to the fact that large amount of heat is generated, during the conversion of stearic acid layer over the iron oxide nanoparticle into  $\text{CO}$ ,  $\text{CO}_2$  etc. This is an

exothermic reaction. At above  $200^{\circ}\text{C}$  all stearic acid molecules got decomposed. This was due to the fact that the decomposition temperature of stearic acid molecule is  $200^{\circ}\text{C}$  [26]. In the presence of gases like  $\text{CO}$ ,  $\text{CO}_2$ ,  $\text{H}_2$  etc. After this the  $\text{Fe}_3\text{O}_4$  oxidizes to  $\text{Fe}_2\text{O}_3$  (may be  $\alpha$  or  $\gamma$ ). It might be due to the presence of high  $\text{O}_2$  concentration. After bringing out the samples from the furnace, the color was first black and after sometime (15-20 minutes) when it cools down the color turns reddish brown. This color remained same up to  $650^{\circ}\text{C}$  but after that color got changed from brown to black and finally at  $1000^{\circ}\text{C}$ , little amount of sample showed blue color. When the sample got cooled down, the powders were transferred to a bottle from the boat and checked with a magnet to confirm the presence of magnetic properties. Figure 3.1.B showed the prepared nanoparticles were being attracted by magnet which signifies the retaining of magnetic properties by the same. In this case the role of organic stabilizer such as stearic acid or ligand is usually bind to the surface of the nanocrystals and give rise to a steric barrier to aggregation. This method has widely been used because of the ease and reproducibility of the synthesis, as well as the uniformity, high crystallinity, and monodispersity of the product. Because the catalytic properties of the nanocrystals are size-dependent, significant efforts have been concentrated on the precise control of particle size distribution. The capping group (stearic acid in this case) plays an important role in controlling the particle size. The size and size distribution of  $\text{Fe}_2\text{O}_3$  nanocrystals can be controlled based on choice of ligand, ligand: precursor ratio, and decomposition temperature. The uniformity of the iron oxide nano crystal was controlled by nucleation during the heating process. It was due to the fact that, a homogeneous nucleation was dominant when the heating rate is relatively high, and therefore the nucleation is finished within a short time interval. Here,  $\text{Fe}_3\text{O}_4$  oxidized to  $\text{Fe}_2\text{O}_3$  with additional trace amount of  $\gamma\text{-Fe}_2\text{O}_3$ . At temperature around  $273.20^{\circ}\text{C}$  grain growth of maghemite occurs. Again at temperatures around  $305.76^{\circ}\text{C}$  all the  $\gamma\text{-Fe}_2\text{O}_3$  changes its phase to  $\alpha\text{-Fe}_2\text{O}_3$  as described in the structural study of iron oxide nanoparticles in chapter 4.

## **(B) Hydrothermal reaction: Amino acid assisted synthesis of Hematite Nanoparticles**

### **3. B. 1 Introduction**

The hydrothermal technique is very important method for advanced material synthesis. It has many advantages in the processing of nanostructural materials for wide range of application [27]. It is a most attractive technique for processing nano-hybrid and nanocomposite materials besides monodispersed and highly homogeneous nanoparticles processing. It can be defined as any heterogeneous reaction to dissolve and recrystallize (recover) materials in the presence of aqueous solvents or mineralizers under high pressure and temperature conditions that are

relatively insoluble under ordinary conditions. The physical chemistry of hydrothermal reaction is based on the dealing of solvents with aspects like structure at critical, supercritical and sub-critical conditions, dielectric constant, pH variation, viscosity, coefficient of expansion, density, etc. These all parameters have to be analyzed with respect to temperature and pressure.

Biomolecules are generally considered as effective templates for nanostructures growth and self-assembly, e.g. the template - directed synthesis of nanotubes using tobacco mosaic virus [28]. Hydrothermal treatment of iron salt with amino acid leads to the formation of hematite nanocubes [29].

Following the method described in [29], iron oxides nanoparticles have also been synthesized besides the thermal decomposition of iron - fatty acid complex. The main motivation behind adopting this procedure is to obtain hematite nanoarchitectures with well-defined geometry and modified with some functional part of amino acid. It can be further utilized for functionalization of the nanoparticle surface and thereby fabrication of some novel bioconjugate. The amino acid, with functional groups  $-NH_2$  and  $-COOH$ , is regarded as the key for controlled crystallization of  $\alpha-Fe_2O_3$  nanomaterial.

### **3. B. 2 Materials and Methods**

#### **Materials Used**

- A.  $FeCl_3 \cdot 6H_2O$  (analytical agent, AR, 3 mmol)
- B. L-Arginine ( $\alpha$ -amino- $\delta$ -guanidovaleric acid .pure, 3 mmol)
- C. Deionized water

$FeCl_3 \cdot 6H_2O$  (analytical agent, AR, 3 mmol) was dissolved in 20 ml de-ionized water to form solution A. L-Arginine ( $\alpha$ -amino- $\delta$ -guanidovaleric acid .pure, 3 mmol) was dissolved in 20 ml deionized water to form solution B and was then added drop wise to solution A ,while stirring for 30 min at room temperature. The ratios of  $FeCl_3 \cdot 6H_2O$  to L – arginine were selected as 1:1. The iron salt /amino acid mixture was poured into a 100 ml Teflon lined autoclave [figure 3.2] designed by me and fabricated at EMPA machine shop. The autoclave was then sealed and places inside the furnace. It was then heated to  $180^\circ C$  and maintained at these temperatures for 10 h. After the autoclave was cooled down to room temperatures naturally, the products were collected, and washed with deionized water and then absolute alcohol.



**Figure 3.2:** Autoclave used for hydrothermal synthesis

### 3. B. 3 Results and Discussion

Here the amino acid (L-arginine), with functional group,  $-NH_2$  and  $-COOH$ , has a great influence on the size and shape of the final  $\alpha-Fe_2O_3$  nanocrystal. By reducing the ratio of  $FeCl_3 \cdot 6H_2O$  to L-arginine the number of available functional groups,  $-NH_2$  and  $-COOH$ , increases. This enhances the interaction between the amino acid and the  $\beta-FeOOH$  surface via hydrogen bonds, which suppress the  $\beta-FeOOH$  nuclei assemble and growth. This leads to smaller size of nanocrystals.

The morphology of the nanoparticles obtained by hydrothermal synthesis is studied with transmission electron microscopy. The TEM results as shown in figure 3.2 represent the acicular shape of nanoparticle with size of around 10-30 nm.. The HRTEM image (figure 3.3 B-C) show good lattice fringes indicating the well-defined crystalline behavior of the nanoparticle.

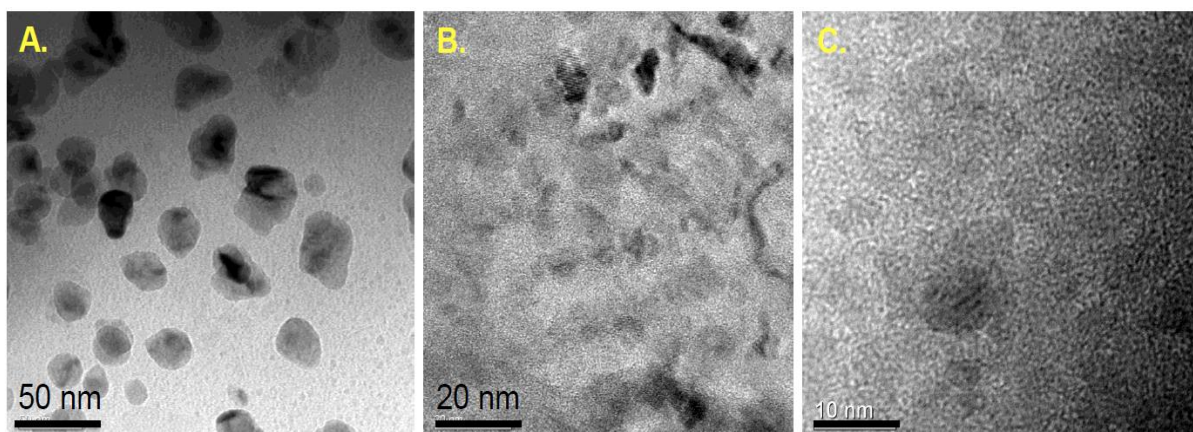


**Figure 3.3:** A. Low resolution TEM image of iron oxides nanoparticles obtained hydrothermally; B-C.HRTEM image showing the well-developed lattice fringes.

The X-ray diffraction pattern of the nanoparticles is shown in figure 3.4. From the XRD pattern it is observed that the entire diffracted peak obtained closely matched with the nanoparticle obtained by thermal decomposition of iron fatty acid precursor at 500 °C as described chapter 4.

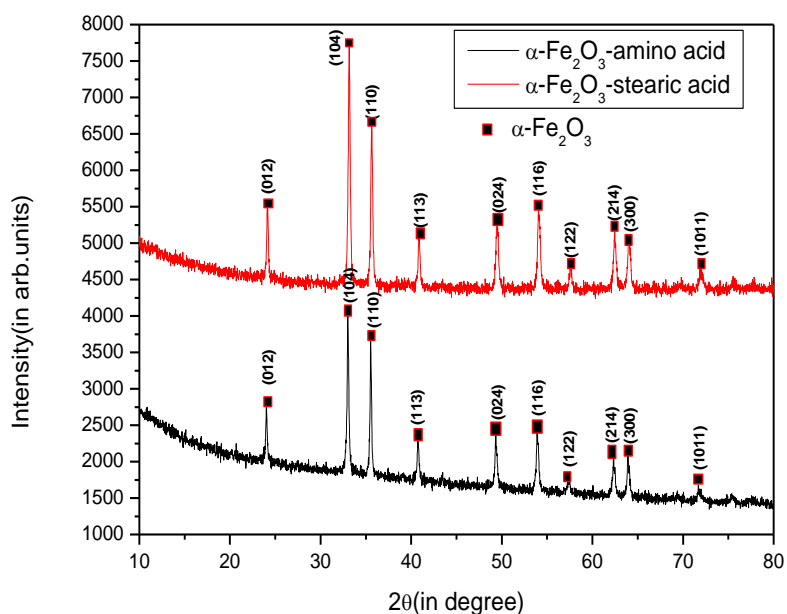


**Figure 3.4:** Comparison of XRD pattern of iron oxide nanoparticles obtained by both thermal decomposition and hydrothermal reaction.

The entire diffracted peak obtained resembles that of hematite phase. The purity of the phase obtained is also confirmed from the XRD result.

### 3.4 Conclusion

The iron oxide nanoparticles obtained by both the method (Thermal decomposition of organic precursor and hydrothermal treatment) have hematite phases which make it suitable for the synthesis of hematite nanoparticles for photocatalytic and photoelectrochemical application.

## References

- [1] Jing, Z.; Wang, Y.; Wu, S. *Sensor Actuat B-Chem.* **2006**, *113*, 177-181.
- [2] Gao, Y.; Bao, Y.; Beerman, M.; Yasuhara, A.; Shindo, D.; Krishnan, M. K. *Appl. Phys. Lett.* **2004**, *84*, 3361.
- [3] Gupta, A. K.; Gupta, M.; *Biomaterials* **2005**, *26*, 3995-4021.
- [4] Bora, D. K.; Deb, P. *Nanoscale Res. Lett.* **2009**, *4*, 138-143.
- [5] Liu, Q.; Cui, Z.; Ma, Z.; Bian, S.; Song, W.; Wan, L. *Nanotechnology* **2007**, *18*, 385605 (5pp)
- [6] Willard, M. A.; Kurihara, L. K.; Carpenter, E. E.; Calvin, S.; Harris, V. G. *Int. Mater. Rev.* **2004**, *49*, 125-170.
- [7] Jovalekic, C.; Zdujic, M.; Radakovic, A.; Mitric, M. *Mater. Lett.* **1995**, *24*, 365-368.
- [8] Lee, S.; Jeong, J.; Shin, S.; Kim, J. *J. Magn. Mater.* **2004**, *282*, 147-150.
- [9] Rockenberger, J.; Scher, E. C.; Alivisatos, A. P. *J. Am. Chem. Soc.* **1999**, *121*, 11595.
- [10] Hyeon, T.; Lee, S. S.; Park, J.; Chung, Y.; Na, H. B. *J. Am. Chem. Soc.* **2001**, *123*, 12798.
- [11] Souza, F. L.; Lopes, K. P.; Nascente, P. P.; Leite, E. R. *Sol. Energ. Mat. Sol. C*, **2009**, *93* 362-368.
- [12] Kay, A.; Cesar, I.; Gratzel, M. *J. Am. Chem. Soc.* **2006**, *128*, 15714-15721.
- [13] Zhong, G. K.; Sun, J.; Inumuru, H.; Gamelin, D. R. *J. Am. Chem. Soc.* **2009**, *131*, 6086-6087.
- [14] Saremi-Yaramahdi, S.; Wijayantha, K. G. W.; Tahir, A. A.; Vaidhyanathan, B. *J. Phys. Chem. C*. **2009**, *113*, 4768-4778.
- [15] Rangaraju, R. R.; Panday, A.; Raja, K. S.; Misra, M. *J. Phys. D: Appl. Phys.* **42**(2009) 135303(10pp).
- [16] Duret, A.; Gratzel, M. *J. Phys. Chem. B* **2005**, *109*, 17184-17191.
- [17] Kiwi, J.; Gratzel, M. *J. Chem. Soc. Faraday T.* **1987**, *83*, 1101-1108.
- [18] Watanabe, A.; Kozuka, H. *J. Phys. Chem. B* **2003**, *107*, 12713-12720.
- [20] Jing, Z.; Wu, S. *Mater. Lett.* **2004**, *58*, 3637-3640.
- [21] Vasquez Mansilla, M.; Zysler, R.; Fiorani, D.; Suber, L. *Physica B: Condensed Matter*, **2002**, *320*, 206-209.
- [22] Strobel, R.; Pratsinis, S. E. *Adv. Powder Technol.* **2009**, *20*, 190-194.
- [23] Liu, H.; Wei, Y.; Li, P.; Zhang, Y.; Sun, Y. *Mate. Chem. Phys.* **2007**, *102*, 1-6.

- [24] Chikate, R. C.; Jun, K.; Rode, C. V. *Polyhedron* **2008**, *27*, 933-938.
- [25] Deb, P.; Basumallick, A.; Sen, D.; Mazumder, S.; Nath, B. K.; Das, D.; *Phil. Mag. Letters*. **2006**, *86*, 491.
- [26] Deb, P.; Basumallick, A. *J. Nanopart. Res.* **2004**, *6*, 527-531.
- [27] Byrappa, K.; Adschiri, T. *Prog. Cryst. Growth. Ch.* **2007**, *53*, 117-166
- [28] Shenton, W.; Douglas, T.; Young, M.; Stubbs, G.; Mann, S. *Adv. Mater.* **1999**, *11*, 253-256.
- [29] Cao, H.; Wang, G.; Warner, J. H. ; Watt, A. A. R. *Appl. Phys. Lett.* **2008**, *92*, 013110.

## Chapter 4

### **Evolution of structural properties of iron oxide nano particles during temperature treatment from 250°C – 900°C: X-ray diffraction and Fe K-shell pre-edge X-ray absorption study<sup>\*1</sup>**

#### **4.1 Introduction**

Hematite is the inexpensive material of interest for PEC application due to its suitable band gap (2.2 eV), valence band edge position, earth abundance and environmentally benign nature [1]. Considering the crystallographic structure of hematite, it is isostructural to a corundum structure wherein oxygen atoms are closely packed with the same density around the Fe<sup>3+</sup> cations, but with a slightly different stacking, which may therefore result in slight distortions from a perfect octahedral environment. There are six formula units per unit cell and possess hexagonal symmetry. Fe<sup>III</sup> ions which are arranged regularly with two filled sites filled two third of the site. In the next step, one vacant site from (001) plane followed the same and ultimately forming the six fold rings. Its structure consists of hexagonally closed packed (hcp) arrays of oxygen ions along the [001] direction whereby (001) plane is parallel with plane of anions [2]. The unique properties of hematite nano particles are mostly associated with the oxidation state and coordination geometry, which can be probed directly from the X-ray absorption spectroscopy. The X-ray absorption near-edge structure (XANES) is sensitive to local geometries and electronic structures of atoms. Both from a theoretical and an experimental point of view, XANES gives information on a specifically local environment and hence is a powerful tool to gain insight into the short- and medium-range structure. These techniques provide information about the oxidation state, the symmetry of the local environment, the partial density of unoccupied states, the coordination number, and the distance to the next neighbor [3-6]. X-ray absorption is a local process in which an electron is promoted to an excited electronic state, which can be coupled to the original core level by the dipole selection rule ( $\Delta l = \pm 1$ ). The pre-edge peaks in XANES spectra are mostly attributed to  $1s$  to  $nd$  quadrupole allowed transitions in the six fold-coordinated cation systems due to distortion [7]. The variation in the pre-edge peak absorption features both in intensity and energy position in the cation  $K$ -edge XANES spectra provides ample evidence for the

---

<sup>1</sup>This chapter is based on the article: Debajeet K. Bora, A. Braun, S. Erat, O. Safonova, E. C. Constable and T. Graule, *Current Applied Physics*, Accepted for Publication (2011).

coordination of transition metal which displays a complex behavior in crystalline and amorphous solids, minerals, biological molecules, and cations adsorbed at surfaces.

The main objective of the study is to understand the evolution in structural properties of iron oxide nano particles formed at different thermal treatment from 250°C – 900°C. For evaluating it, I have synthesized the iron oxide nano particles by the heat treatment of iron fatty acid precursor complex prepared by using a non-aqueous chemical route [as described in chapter 3] at different temperature from 250°C to 900°C. In the next step, nano particles have been characterized by X-ray Diffractometry and Fe K - edge XANES spectroscopy to get information about the structural evolution. During the study, our main focus will be primarily on the hematite nano particles which are considered as a photoactive material in the photoelectrochemical water splitting application. The thermal treatment during the processing of the hematite film has a profound influence on the final photoelectrochemical functionality of the material due to the change in structure of the nano particle in the film [8]. Also, mixing with other phases such as maghemite may effect on the functionality of hematite material as a result of its insulating action [9]. By keeping this in mind, I have applied high heat treatment temperature during the processing stage to get rid of insulating maghemite phase and in order to have fundamental understanding of structural evolution which affects the device performance. On the other hand to get a detail picture on the variation of oxidation state and site symmetry of the material during thermal treatment, I have employed Fe K- edge XANES spectroscopy. Hereby, I am taking into account of the pre edge peak intensity ratio result for probing the oxidation state and site symmetry.

#### **4.2 Materials and methods**

*Synthesis:* Same procedure was adopted for preparing iron oxide nanoparticles as described in chapter 3.

*Characterization:*

X-ray diffraction was carried out using  $\text{CuK}_\alpha$  radiation; wavelength 1.54 Å. The phase composition was examined by analyzing the powder X-ray diffraction pattern with PAN Analytical X'Pert PRO software. Transmission electron micrographs were obtained using a Philips CM30 Transmission electron microscope operated at 300 keV. The temperature of the sample stage was cooled with liquid nitrogen. Particle size distribution was determined by LS 230 particle size analyzer from Beckman Coulter by using the PIDS (Polarization Intensity Differential Scattering) signal of 40%. The lower resolution limit of this instrument is 40 nm. Fe K edge X-ray absorption spectra were measured at the Swiss-Norwegian beam line (SNBL)

at the European Synchrotron Radiation Facility (ESRF), Grenoble, France. The storage ring has the electron energy of 6 GeV with a maximum current of 200 mA. A Si (111) double-crystal monochromator was used for energy selection, which was detuned by 20–50% in order to suppress higher harmonic radiation. The intensities of the incident and transmitted X-rays were monitored with nitrogen-filled ionization chambers. The monochromator was scanned from 200 eV below to 800 eV above the Fe K-shell absorption edge (7111 eV). The Fe K-edge XAS were measured in the transmission mode at ambient temperature. A 7- $\mu\text{m}$  thin Fe foil was used as a reference for X-Ray energy calibration. Nano particle powders were mixed with boron nitride in 1:5 ratio and then pressed to pellets for the X-ray absorption measurements. Background subtraction and normalization of the spectra was performed with standard procedures using the software program WinXAS [10].

### 4.3 Results and Discussion

During the synthesis, magnetite in the dry state is oxidized to maghemite by air. It is known that ultrafine crystals of magnetite change over years from black to the brown of maghemite even at room temperature [3]. At temperature higher than 350°C the transformation further proceeds to hematite. Also, the role of surfactants (also referred to here as ligands) such as stearic acid used in this case usually bind to the surface of the nanocrystals and give rise to a steric hindrance to aggregation [11]. This method has widely been used because of the ease and reproducibility of the synthesis, as well as the uniformity, high crystallinity, and monodispersity of the product. Also, because of the dependence of photocatalytic and photoelectrochemical properties on the nano particle size, significant efforts have been concentrated on the precise control of particle size distribution [12-13]. The capping group plays an important role in controlling the particle size.

The X-ray diffractograms of six samples heat treated at temperatures from 250°C to 500°C (Figure 4.1-A) showed the presence of both  $\alpha$  and  $\gamma$  phases. On increasing heat treatment temperature, the as prepared powder sample at 250°C undergoes complete decomposition of the organic compounds, and the hematite structure evolves along with phases of  $\gamma\text{-Fe}_2\text{O}_3$ . At 350°C, the composition remains same and after that complete phase transformation of nano particles occurred. Above 350°C it is observed that  $\alpha$  phase of the nano particles dominates the diffractogram. From this discussion it is evident that at higher heat treatment temperature  $\gamma\text{-Fe}_2\text{O}_3$  completely transformed into  $\alpha\text{-Fe}_2\text{O}_3$ . This transformation of maghemite to hematite is considered as topotactic with the [111] and [110] axes of maghemite corresponding to the [001] and [110] axes of hematite [14]. The formation of hematite is favored at high temperatures [15]. It has been observed that the reflections coming from low temperature annealed samples were

broadened suggesting the small size of the crystallite. Careful inspection of these reflections shows that they actually become broad non-uniformly in case of samples from 250°C to 350°C. This non-uniform broadening was proposed originally to be due to shape anisotropy of the particles rather than to strains and faults broadening which remains in acicular particles after further heating at 600°C [16]. Initially the particles are smaller and irregular in shape as is evident from electron microscopy data. Upon heat treatment the larger, prismatic shaped nano particles formed in well distributed form at the expense of the smaller particles, likely by diffusion based growth similar to Ostwald ripening. As the temperature increased, the Bragg reflections systematically got sharper and it is significant from increase of the crystallite size along with decrease of full width with half maximum with heat treatment temperature (Figure 4.1-B). In the case of hematite derived from the thermal decomposition of akaganeite, a similar trend was observed [17]. This was due to the increase of crystallization with time and temperature plays a role in obtaining the solid phase. The increase in crystallite size can affect both stoichiometry and structure of the nano particle interior and surface or even can cause local or total phase transformation [18]. The phase transformation with increase in crystallite size generally occurs in order to obtain a stable phase by minimizing the surface energy. From the energetic study of different set of iron oxide it was found that hematite is the most stable phase under aerobic surface condition in comparison to other phases whose enthalpy of formation is higher [19]. The surface energy is nothing but excess energy of the corresponding nano particles with respect to bulk material [20]. It is found to be very high in case of smaller nano particle with higher surface area. On the other hand, from the expanded view of the XRD profile (Figure 4.1-B), it is found that the (104) and (110) Bragg reflections remain at the same position and shape was well maintained on increasing the temperature from 250°C to 500°C. At 300°C the peak got slightly shifted to lower Bragg angle possibly due to the repeated phase transformation of the precursor complex to maghemite and then to hematite during the nucleation and growth process of the nano particle formation. It might also be due to the presence of net lattice disorder as the particle sizes are quite small as evidence from the broad Bragg reflections. However, after 300°C the reflections mainly signify the hematite phase of the nano particle. In this case, the formation of the maghemite like structure is mainly restricted by the kinetic issue during the growth of hematite nano particle by the sintering process. This means that not only particle size but also the growth kinetics determines the structure of the nano particles [21]. The transformation of maghemite to hematite could also be attributed to the fact that with increasing particle size, maghemite ( $\gamma\text{-Fe}_2\text{O}_3$ ) which is a defect spinel polymorph preferentially nucleates and hematite phase obtained on increasing the size. It is worth mentioning here that the spinel phase is thermodynamically less stable due to the higher surface

energy of the nanocrystallites as the particle size got increased. The likely reason is that the spinel phase has a more open lattice

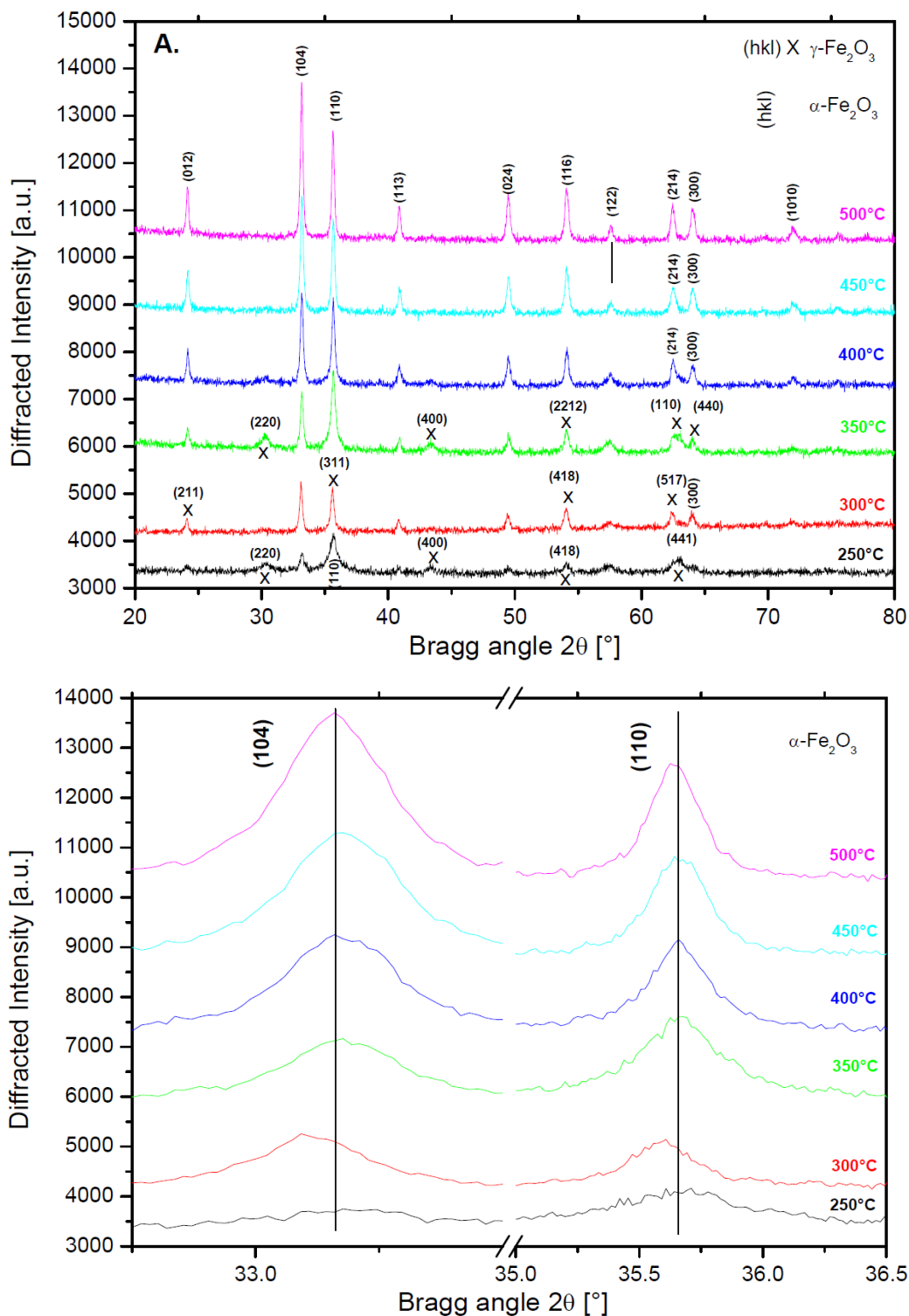


**Figure 4.1:** X-ray diffractogram of iron oxide nano particles obtained by heat treatment of precursor complex from (A) 250-500°C (B) expanded view of (104) and (110) peak in samples synthesized at 250-500°C.

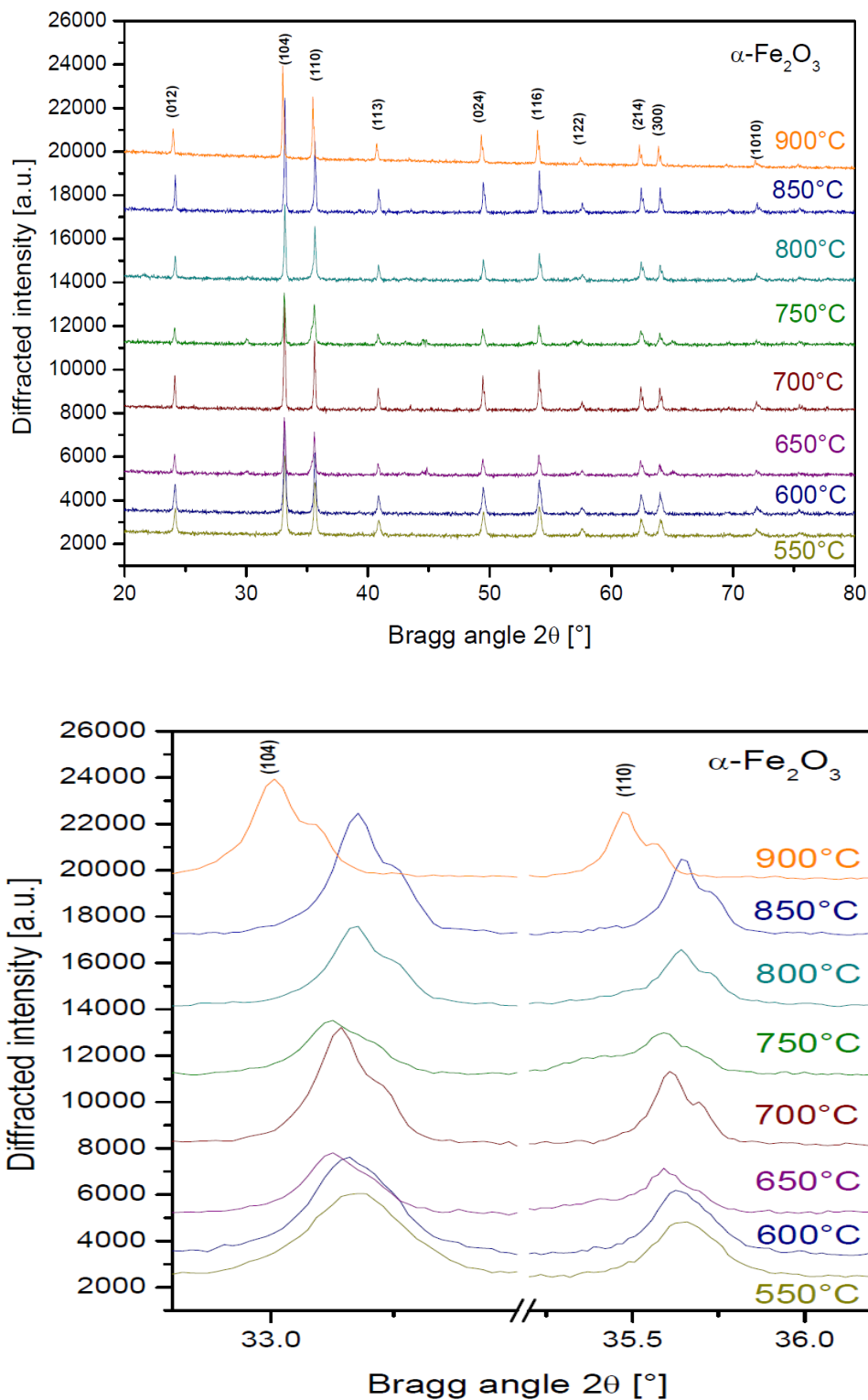


**Figure 4.2:** X-ray diffractogram of iron oxide nano particles obtained by heat treatment of precursor complex from (A)550-900°C(B) expanded view of (104) and (110) peak in 550-900°C samples.

structure, a lower number of broken bonds per unit surface, and lower surface polarity due to increased bond covalence [22]. On the other hand, in case of nano particles heat treated from 550°C to 900°C (Figure 4.2-A) showed the presence of  $\alpha$  phase only. From the expanded view of the peak (110) and (104) as shown in Figure 4.2-B, I observe that the position and shape of the peaks remained identical up to 650°C, but from 700°C up to 900°C the (110) reflections split into two peaks. This peak splitting in case of 550°C to 900°C samples could be due to hexagonal distortion of the usual lattice structure of hematite or might be due to the imposing of compressive stress on the surface of nanostructure by the increasing oxygen content at high temperature. Besides these, at 900°C both peaks finally changed its position to lower angle. This peak shift might be attributed due to formation of defects on the surface of hematite nano particle at high heat treatment. The signature of defect state in nanocrystalline material was well explained from the theoretical calculation of X-ray diffractogram results. From the calculated diffraction pattern, it was proposed that the nanocrystals displays peak shifts and broadening because of the presence of stacking fault as a defect in case of face-centered cubic crystalline geometry. In addition, it was also found that the location of stacking fault has largely influence the magnitude of the peak shifts [23]. In our study, I have observed such kind of stacking fault for 900°C heat treated sample as evident from the TEM image discussed in next section. At 900°C the nanocrystal structure was thought to be transformed from regular octahedral geometry to tetrahedral configuration which mostly signified the presence of magnetite phase at high temperature treated sample. This will be further confirmed with the quantitative analysis of the relative pre edge peak intensity ratio in the Fe – K edge XANES spectra.

In order to get visual information about the nano particles size, its crystallinity and morphology, high resolution transmission electron microscopy (HRTEM) was further applied. Representative images of four samples (250°C, 300°C, 600°C, and 900°C) are shown in Figure 4.3(A-F). I observe that the particle sizes range from 2-50 nm and show good crystalline character. Formation of rings in the selected area electron diffraction pattern (SAED) (Figure 4.3-A) of the sample annealed at 250°C signifies the polycrystalline nature. From the TEM images of 250°C and 300°C sample (Figure 4.3.A-B) it was evident that particles were in disordered state whereas at high temperature (600°C) the particle shape became prismatic, and not round shape, which is standard morphology of small hematite crystals. Besides these from HRTEM image (Figure 4.3-D) I can see the well alignment of crystal plane with  $d_{hkl}$  value of 2.521 Å which corresponds to that of the lattice distance of the (110) plane. Finally in case of sample heat treated at 900°C (Figure 4.3- E), particles preserved the prismatic shape and from the high resolution scale (Figure 4.3-F); I have observed that some step or terrace like pattern

formed over the surface of the nano particle with rhombohedral shape which can be attributed due to the formation of stacking fault like defect. A similar type of stacking fault has also been observed in case of SiC crystal grown by spontaneous nucleation sublimation method [24].

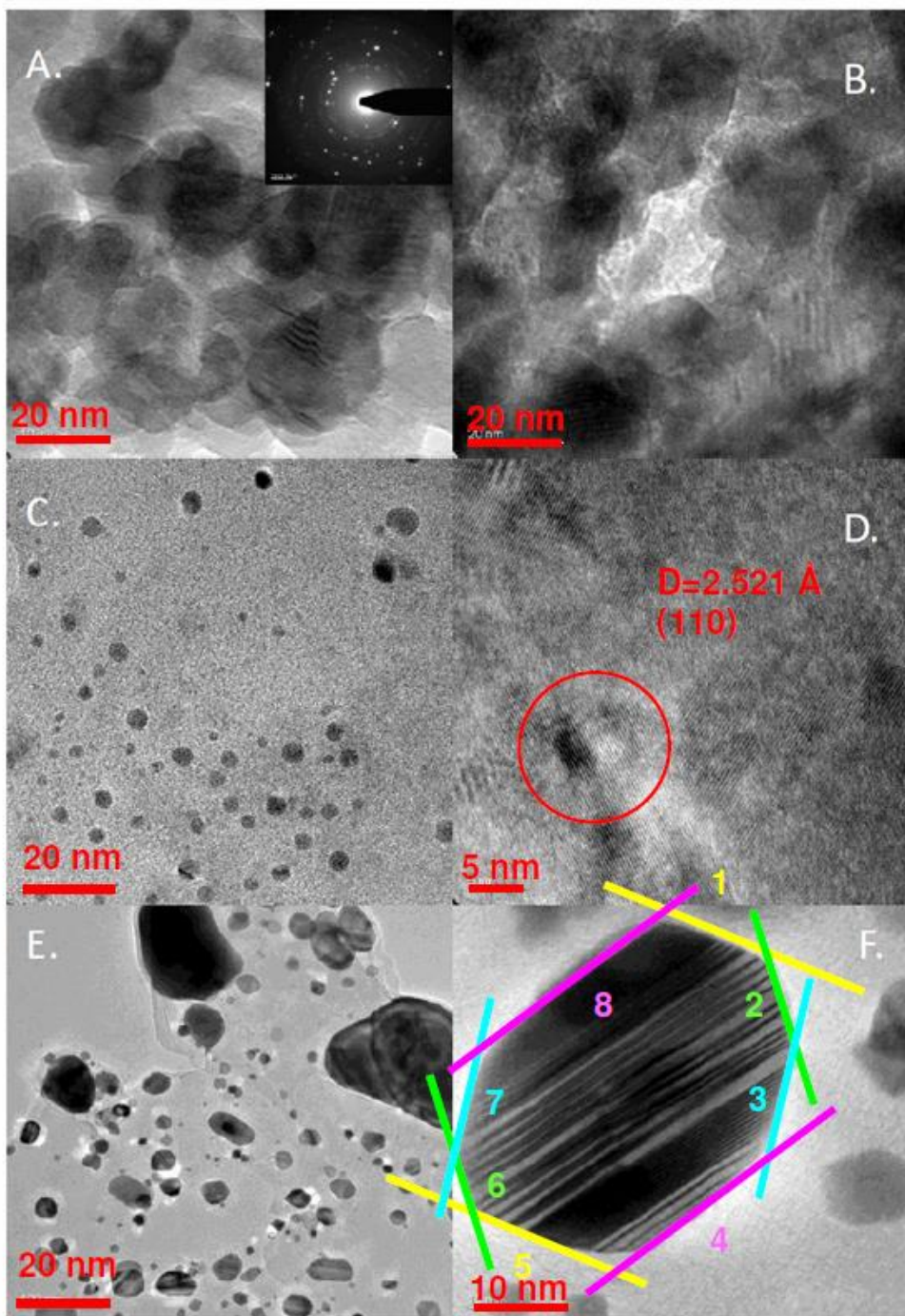


**Figure 4.3:** TEM images of samples synthesized at (A) 250°C (Inset: SAED pattern) (B) 300°C (C) 600°C and (E) 900°C. (D – F) The corresponding HRTEM images of 600 °C and 900°C samples.

Figure 4.4-A shows the mean particle number size distribution of the nano particles synthesized at different annealing temperature. For the annealed samples at 250°C, the width of the

distribution was very broad in comparison to the samples annealed from 300°C to 900°C. This can be explained by taking into account of the formation of two different types of nano particles during the entire heat treatment step. The first type is the large prismatic shaped nano particles for high temperature annealed samples, and the second one is the small disordered particles with lower annealing temperature. Most probably, that the large spherical particles are “mature” ones at the respective conditions of growth, and the small ones are some “immature seeds” from which the large “mature” particles grow. This type of growth process is usually called as diffusion mediated growth or Ostwald ripening. This refers to a dissolution–precipitation based mechanism for particle growth (coarsening) [21]. Hereby small solid nano particles have surface atoms with elevated chemical potential with respect to larger nano particles because of the presence of excess energy associated with the surface. This increases the relative solubility of small particles, and larger particles grow preferentially. It has also to be noted that the seed particles are characterized by larger dispersion than mature particles. On average, the mean and median diameter systematically decreased by about 10% from 250°C to 900°C annealing temperature (Figure 4.4 - A). In particular, no coarsening or growth of particles is observed. Instead, the nano particles actually shrink during heating. In contrast, visual inspection of the Bragg reflexes shows that their full width at half maximum decreases during heat treatment, revealing that the crystallites actually grow (Figure 4.4 - B). Thus a growth of crystallites and shrinking of primary nano particles has been observed. This phenomenon can be explained by the depletion of defects during temperature increasing. Further support for this will be shown by changes in the the pre-edges of the x-ray absorption spectra.

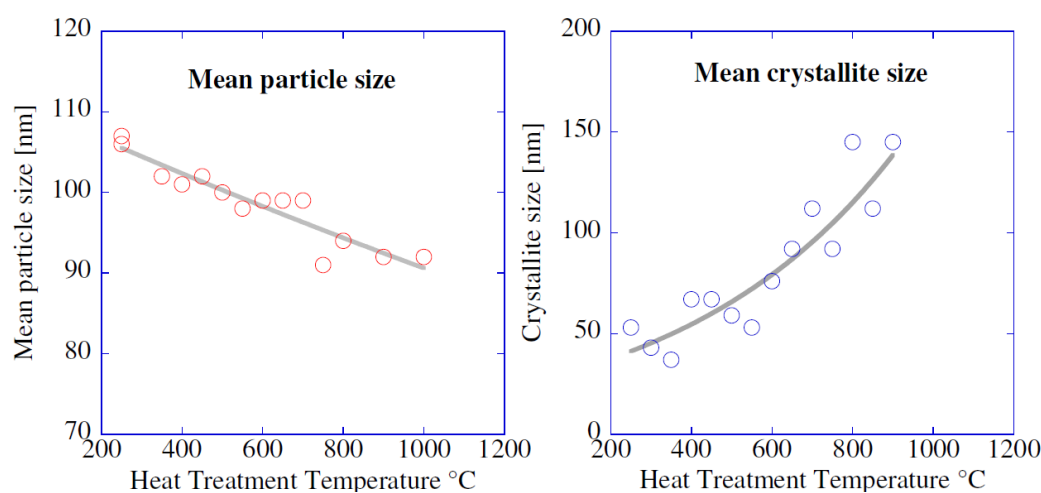


**Figure 4.4:** (A) Nano particle size distribution measured by particle size analyzer (B) variation of mean and median parameter with synthesis temperature along with crystallite size calculated using the Scherer equation [36].

Figure 4.5 shows the normalized Fe - K edge XAS spectra of iron oxide nano particles heat treated at temperatures from 250°C to 900°C. These spectra can be divided into two regions, e.g., the pre - edge and post - edge. The spectra are shown in three different energy resolution scales as in Fig. 4.5 (A-C). The pre-edge features in XANES spectra of transition metal K-edge are attributed to quadrupole transitions from 1s to 3d orbitals, dipole allowed transitions due to the 3d-4p mixing of the metal and 3d-p mixing between the metal atom and ligands through bonding and multiple scatterings involving the same atoms with different scattering paths [25]. Therefore, the positions of the pre-edge peaks directly reflect the crystal field splitting of 3d orbital sub-bands, and intensities of the pre-edge features are sensitive to the local oxygen coordination geometry of the metal atom. The pre-edge shifts with increasing oxidation state to higher energy. The number of transitions in the pre-edge depends on the oxidation state and coordination number [26]. In order to make a systematic and quantitative assessment of the changes in the pre-edge spectra, an accurate background subtraction is necessary, particularly since the pre-edge intensity is very small in comparison to the white line intensity. The adopted routine of smooth baseline interpolation appears reasonable, although one cannot entirely rule out a subjective component [27]. On systematic investigation of the pre-edge peak intensity, we observe that the intensity increases on increasing the annealing temperature. This is due to the change in oxidation state and site symmetry of the crystallite on respective sintered condition. The pre-edge peak intensity decreases with increasing coordination number. In the case of Fe, unlike Ti and Ni species, for example, the pre-edge energy does not shift as a function of coordination number [25].

The sample tempered at 250°C shows a broad pre-edge maximum at about 7113 eV and an intermediate plateau at around 7117 eV. Its relatively high pre-edge intensity suggests that  $\gamma$ -Fe<sub>2</sub>O<sub>3</sub> is the dominant phase, in line with the XRD results. Similar strong pre-edge was observed by Chen et al. [28] in iron oxide nano particles, who also observed that with increasing particle size the pre-edge features resembled more those of  $\alpha$ -Fe<sub>2</sub>O<sub>3</sub>. This is in line with the observations made on maghemite particles in general, i.e. that maghemite typically forms as small nano particles, whereas larger iron oxide particles with Fe<sup>3+</sup> transform to  $\alpha$ -Fe<sub>2</sub>O<sub>3</sub> because of thermodynamical reasons, i.e. a minimization of the free surface energy [29]. Usually the sample annealed from 500°C to 750°C showed Fe in the Fe<sup>3+</sup> oxidation state along with octahedral coordinated geometry for the respective structural pattern of hematite. In the 750°C sample, the structure was trigonal bipyramidal and again at 800°C the pre-peak intensity increased due to distortion of the local structure of the nano particle from trigonal bipyramidal to tetrahedral geometry. It is also worth mentioning that the usual trend of increase in intensity

normally follows the order ferrihydrite > goethite > hematite [30]. This fact is quite obvious

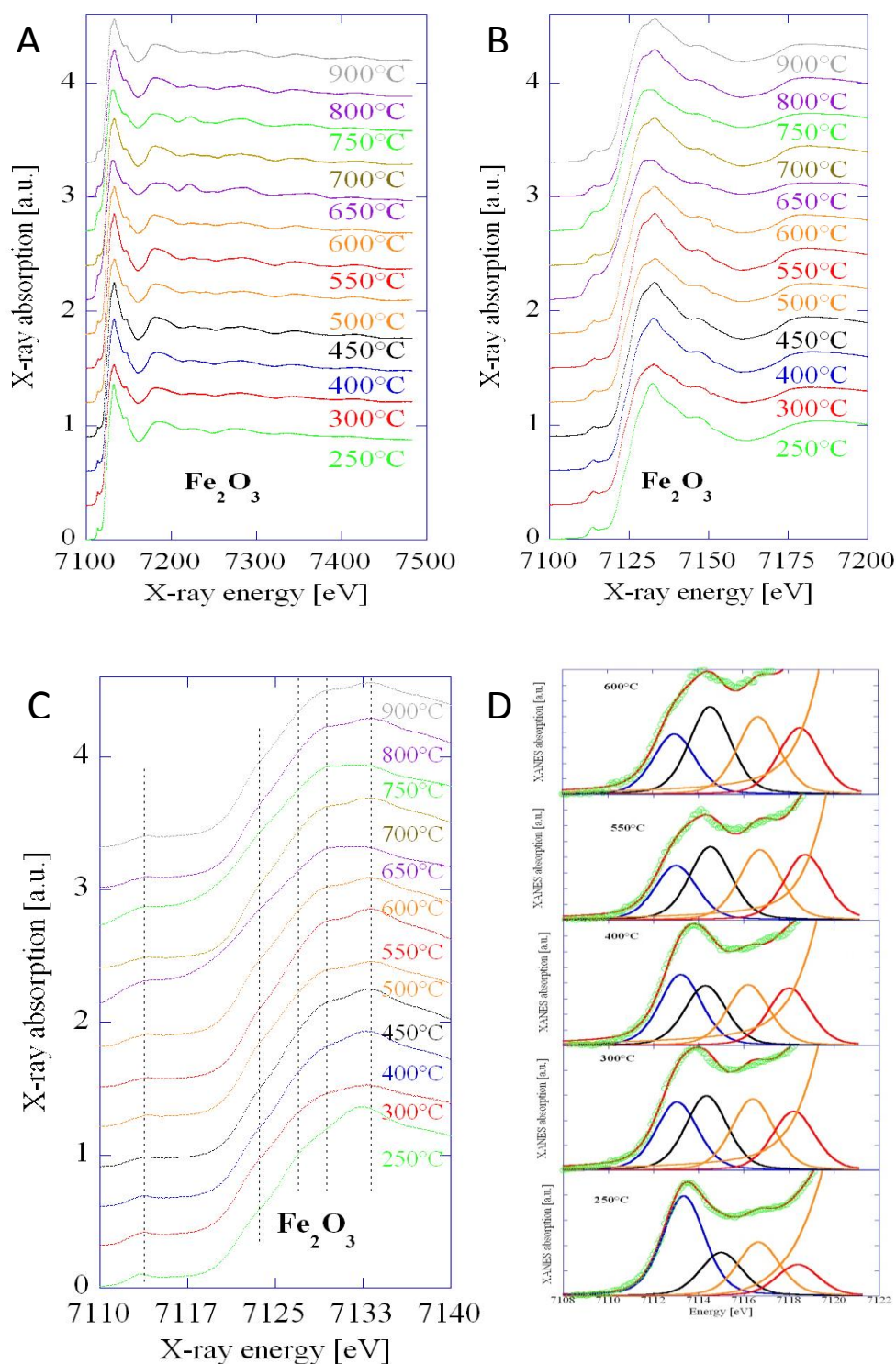


**Figure 4.5:** (A) Normalized Fe K-edge X-ray absorption spectra of Fe<sub>2</sub>O<sub>3</sub> nano particles synthesized at different heat treatment temperatures. (B) XANES region of the normalized Fe K-edge X-ray absorption spectra. (C) Pre-edge region of the normalized Fe K-edge X-ray absorption spectra. (D) Deconvoluted pre – edge region of spectra from different set of nano particles by varying the temperature [36].

from the XRD pattern and might be due to the inverse correlation of the intensity of the pre-edge with the extent of centrosymmetry of the crystallographic site of Fe. Hence the most intense pre-edge peak was found for the sample annealed at 800°C.

On deconvoluting the pre-edge peak of the respective XANES spectra, only two maxima are distinguishable in the pre-edge spectra which might be due to increasing site distortion. In the case of deconvoluted spectra as shown in Figure 4.6 - A (for 250°C), two components obtained were mainly due to the distortion of the octahedron of oxygen atoms around Fe<sup>3+</sup>, which is in agreement with theory. These two components were for high spin Fe<sup>3+</sup> ion with octahedral symmetry related to quadrupolar electronic transition to the t<sub>2g</sub> level. Besides these, pre-edge parameters are much more in agreement with those of the other Fe<sup>3+</sup> compounds including those for ferrihydrite for which high pre-edge intensity was erroneously thought to be related to the presence of tetrahedrally coordinated Fe<sup>3+</sup> [31]. The pre-edge intensity is more sensitive to site centrosymmetry with the most centrosymmetric Fe coordination having lowest intensity. For the Fe K edge, the pre-edge peak intensity is slightly higher in reduced samples for the same composition and there is an energy difference of about 0.5 eV between the edges of the first pre-edge peaks in the oxidized and reduced samples. The edge energy position (7113 eV of the first pre-edge peak for reduced samples is in agreement with that of Fe<sub>2</sub>O<sub>3</sub> having all iron ions in the Fe<sup>3+</sup> oxidation state. The relative peak area of the normalized peaks (maxima) against different annealing temperature has also been studied and the results were shown in Figure 4.6-B. The normalized peak area due to first peak decreases linearly with increasing temperature and the area due to the second peak increases on increasing the sintering temperature. The shape of the pre-edge peak changes from a split to a normal singlet peak. This could be explained by considering the fact that this splitting of the pre-edge feature decreased with lower Fe<sup>2+</sup> coordination. That is with increase in heat treatment temperature both the oxidation state and symmetry of the nano particle changes from Fe<sup>3+</sup> octahedral to Fe<sup>2+</sup> tetrahedral environment. This means that at high heat treatment temperature the crystallite within the nano particle somehow displays faced centered cubic arrangement, which supports the formation of stacking fault defect and XRD peak shifting as discussed in XRD and TEM results. In case, the inversion symmetry of the transition metal is broken, which normally found for maghemite nano particle obtained from 250°C to 300°C as in this case, the pre-edge gains additional intensity due to the local 3d-4p wave function mixing, effectively allowing dipole transitions to the 4p character of the 3d-band. The pre-edge peak also increases slightly in energy with the valence state of the absorbing iron. The distinctive feature of the pre-edge peak that is used in this experiment is the fact that for octahedrally co-ordinated iron, the pre-edge peak is split into

two components with a separation of 1.5 eV [32-33]. This is caused by crystal field splitting of

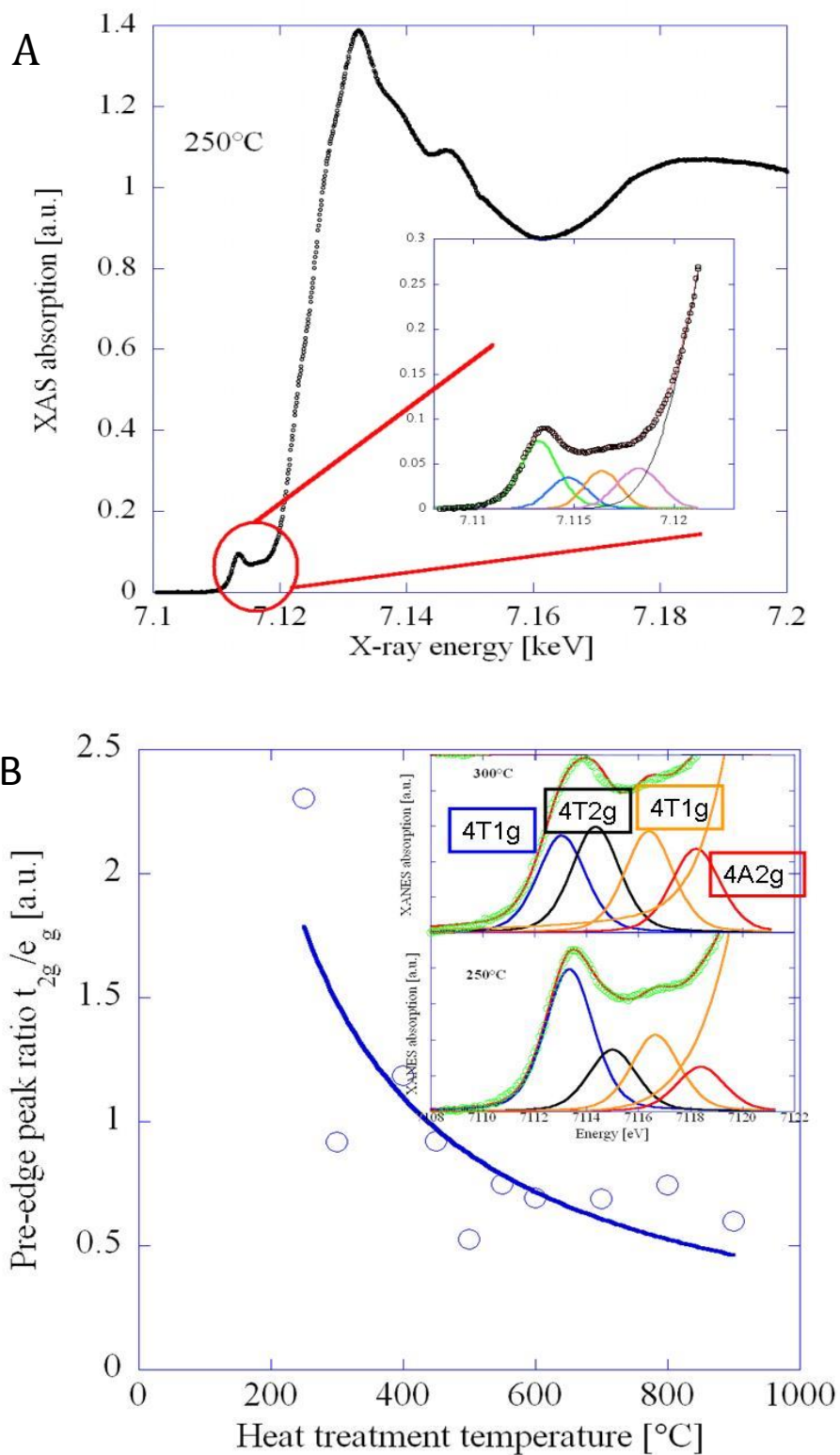


**Figure 4.6:** (A) Deconvoluted pre-edge peak of the respective XANES spectra for 250°C. (B) The relative peak area of the normalized peaks (maxima) against different annealing temperature [36].

the ground state [34]. Peaks are associated with the  $t_{2g}$  and  $e_g$  transitions [35]. For tetrahedral coordination, the crystal field splitting between the  $e_g$  and  $t_{2g}$  levels is much less so they are not resolvable and appear as a single peak [32]. This was found to be the case even when only 60% of the iron ions were tetrahedrally coordinated and the rest were octahedrally coordinated. Detail of the pre-edge peak at the base of the edge shows that the oxides containing tetrahedrally coordinated iron, magnetite ( $Fe_3O_4$ ), and maghemite ( $\gamma-Fe_2O_3$ ) give a single peak whereas hematite ( $\alpha-Fe_2O_3$ ) and the two oxyhydroxides, lepidocrocite ( $\gamma-FeOOH$ ) and goethite ( $\alpha-FeOOH$ ), all of which contain octahedrally coordinated iron, give a split peak.

#### 4.4 Conclusion

In summary, iron oxide particles in the size range of 5-50 nm have been synthesized by a non-aqueous soft chemistry route with different annealing temperature. The systematic analysis of the evolution in structural properties of nano particles synthesized at different heat treatment temperatures was studied by X-ray diffractometry. The XRD results show that at the lower annealing temperature nano particle comprise both the maghemite and hematite phase. As the temperature got increased up to 900°C the maghemite phase seemed to be converted to the hematite phase with the corresponding formation of stacking fault like defect at 900°C which validated the structural transition of hematite particle from regular hcp arrangement to fcc geometry. Also by detailed analysis of the (110) and (104) peak it was found that the peak position gets shifted and split upon increasing the corresponding synthesis temperature. This is primarily because of the local site distortion of the geometry of the nanocrystallite got distorted at the respective higher temperature. TEM results further showed that the samples synthesized at 250 °C, 300 °C, 600 °C and 900 °C were all crystalline in nature with well-developed lattice fringes as evident from high resolution imaging. The shape of the particles synthesized at low temperature was spherical whereas it becomes prismatic on increasing the heat treatment temperature. The selected area electron diffraction pattern of nano particles exhibited its polycrystalline nature. Finally the sample heat treated at 900 °C showed some step like pattern on the surface of the nano particle which is due to the formation of stacking fault like defect as evident from literature study. The particle size distribution study further signified that during the synthesis process two types of nano particle got formed and the distribution got sharper with increase in the heat treatment temperature which was due to the presence of mature particle at that temperature and it becomes quite broad for smaller seed particle from which growth of mature particle took place. Finally, from the pre-edge analysis of the Fe-K edge XANES spectra, it can be concluded that the pre-edge peak intensity increased with respect to the annealing temperature due to change in oxidation state and site symmetry of the nano particle. Quantitative analysis of the relative pre-edge peak area further signified the

Fe<sup>3+</sup> octahedral to Fe<sup>2+</sup> tetrahedral transition in respective nano particle sample on increasing the sintering temperature.

## REFERENCES

- [1] Sartoretti, C. J.; Alexander, B. D.; Solarska, R.; Rutokowska, I. A.; Augustynski, J.; Cerny, R.; *J. Phys. Chem. B* **2005**, *109*, 13685-13692.
- [2] Liu, X.; Fu, S.; Xiao, H.; Huang, C. *J. Solid State Chem.* **2005**, *178*, 2798–2803.
- [3] Cornel, R. M.; Schwertmann, U. *The Iron Oxides. Structure, Properties, Reactions and Uses*, VCH: Weinheim, Germany, **1996**.
- [4] Heijboer, W. M.; Glatzel, P.; Sawant, K. R.; Lobo, R. F.; Bergmann, U.; Barrea, R. A.; Koningsberger, D. C.; Weckhuysen, B. M.; De Groot, F. M. F. *J. Phys. Chem. B* **2004**, *108*, 10002.
- [5] Radu, D.; Glatzel, P.; Gloter, A.; Stephan, O.; Weckhuysen, B. M.; De Groot, F. M. F. *J. Phys. Chem. C* **2008**, *112*, 12409.
- [6] Wong, J.; Lytle, F. W.; Messmer, R. P.; Maylotte, D. H. *Phys. Rev. B* **1984**, *30*, 5596.
- [7] Keller, D. E.; De Groot, F. M. F.; Koningsberger, D. C.; Weckhuysen, B. M. *J. Phys. Chem. B* **2005**, *109*, 10223.
- [8] Wua, Z.; Xian, D. C.; Natoli, C. R.; Marcelli, A.; Paris, E.; Mottana, A. *Appl. Phys. Lett.* **2001**, *79*, 1918.
- [9] Sivula, K.; Zboril, R.; Formal, F. L.; Robert, R.; Weidenkaff, A.; Tucek, J.; Frydrych, J.; Gratzel, M. *J. Am. Chem. Soc.* **2010**, *132*, 7436-7444.
- [10] Crocombette, J. P.; Pollak, M.; Jollet, F.; Thromat, N.; Gautier-Soyer, M. *Phys. Rev. B* **1995**, *52*, 3143.
- [11] Ressler, T. WinXAS: a Program for X-ray Absorption Spectroscopy Data Analysis under MS-Windows, *J. Synchrotron Rad.* **1998**, *5*, 118-122.
- [12] Stolnik, S.; Illum, L.; Davis, S. S. *Adv. Drug Deliver. Rev.* **1995**, *16*, 195-214.
- [13] Calza, P.; Pelizzetti, E.; Mogyorósi, K.; Kun, R.; Dékány, I. *Appl. Catal. B: Environ.* **2007**, *72*, 314-321.
- [14] Torimoto, T.; Tsumura, N.; Nakamura, H.; Kuwabata, S.; Sakata, T.; Mori, H.; Yoneyama, H. *Electrochim. Acta* **2000**, *45*, 3269-3276.
- [15] Feitknecht, W.; Mannweiler, U. *Helv. Chim. Acta* **1967**, *50*, 570-581.
- [16] Cudennec, Y.; Lecerf, A. *J. Solid State Chem.* **2006**, *179*, 716–722.

- [17] Duvigneaud, P.H.;Derie, R. *J.Solid State Chem.***1980**, *34*,323-333.
- [18] Morales, J.;Tirado, J.L.;Macias,M. *J. Solid State Chem.* **1984**, *53*, 303-312.
- [19]Chernyshova,I. V.;Hochella,M. F.;Madden, A. S. *Phys. Chem. Chem. Phys.***2007**, *9* 1736–1750.
- [20] Laberty,C.;Navrotsky.A. *Geochim. Cosmochim Acta* **621998**, *17*,2905 – 2913.
- [21] Gilbert, B.;Zhang, H.;Huang, F.;Finnegan, M. P.;Waychunas , G. A.;Banfield, J. F. *Geochem. Trans.***2003**, *4*, 20–27s.
- [22] McHale,J. M. ;Auroux, A. ;Perrotta, A. J. ;Navrotsky,A. *Science***1997**, *277*,788.
- [23] Makinson,J. D. ;Lee,J.S. ;Magner,S.H. ;De Angelis, R.J. ;Weins,W.N. ;Hieronymus, A.S. *JCPDS-International Centre for Diffraction Data 2000, Advances in X-ray Analysis***2000**, *42*, 407 – 411.
- [24] Hu, X. ;Xu, X. ;Li, X. ;Jiang, S. ;Li, J. ; Wang, L. ;Wang, J. ;Jiang, M. J. *Cryst. Growth***2006**, *292*, 192–196.
- [25] Yamamoto, T. *X-ray Spectrom.***2008**, *37*, 572 – 584.
- [26]Westre,T.E.;Kennepohl, P.;DeWitt, J. G.;Hedman, B.;Hodgson, K. O.;Solomon, E.I. *J. Am. Chem. Soc.***1997**, *119*, 6297-6314.
- [27] Berry,A. J.;O’Neill,H. S.C.;Jayasuriya,K. D.;Campbell,S.J.;Foran,G. J. *Am. Mineral.***2003**, *88*, 967-977.
- [28]Chen, L. X.;Liu,T.;Thurnauer,M.C.;Csencsits,R.;Rajh,T. *J. Phys. Chem B***2002**, *106*, 8539-8546.
- [29] Navrotsky,A. *PNAS*, **2004**, *101*, 12096- 12101.
- [30] Wilke,M.;Farges,F.;Petit,P. E.;Brown,G. E.;Martin,F. *Am. Mineral.* **2001**, *86*,714.
- [31]Zhao,J.;Huggins, F. E.;Feng,Z.;Huffman,G. P. *Clays Clay Miner.***1994**, *42*,737-746.
- [32] Calas,G.;Petiau,J. *Solid State Comm.* **1983**, *48*,625.
- [33] Bajt, S.;Sutton,S. R.;Delaney,J. S. *Geochim. Cosmochim.Acta*, **1994**, *58*, 5209.
- [34] Shuman,G.R.;Yafet,Y.;Eisenberger, P.; Blumberg, W. E. *PNAS***1976**, *73*, 1384.
- [35] Sakane, H.;Watanabe, I.;Ono, K.;Ikeda, S.;Kaizaki, S.;Kushi,Y. *Inorg. Chim.Acta***1990**, *178*, 67.
- [36]Bora,D.K.;Braun,A.; Erat, S.; Safonova,O.; Constable,E.C.;Graule,T. *Current Applied Physics*,Accepted for Publication.(2011).

## Chapter 5

### **In - situ ATR-FTIR study of photocatalytic degradation of dicarboxylic acid on hematite nanoparticle surface**

#### **5.1 Introduction**

Solar energy is used in a photoelectrolysis cell for producing H<sub>2</sub> as a storable fuel and this processes lead to an increase of free energy, *i.e.* (uphill reaction). On the other hand, a photocatalytic reaction where light excitation is used only to speed up a reaction. This is considered as downhill reaction. Examples are the mineralisation or the detoxification of organic waste.

The attenuated total reflection infrared spectroscopy (ATR-FTIR) is a surface sensitive technique which capable of providing information on the individual processes at the mineral-water interface [1]. The photochemical reduction of iron hydroxides in aquatic environments by low molecular weight organic acids finds an important interest. Organic acids have the potential to induce photodissolution of iron oxides and thus to increase the bioavailability of iron in aquatic environments [2-3]. The photodecomposition of carboxylic acids at iron hydroxide surfaces and the concomitant photodissolution of the iron (hydro) oxides may proceed by the oxidation of adsorbed organic acids by photogenerated holes and the photoelectrons reducing surface Fe (III) lattice sites. Adsorption of carboxylic and dicarboxylic acids on mineral oxide surfaces in contact with aqueous solutions is important in several very active research areas, e.g., surface reactions in the environment, application of mineral particles and semiconductors for pollutant degradation and in photoelectrochemical solar energy conversion. Photochemical reactions on mineral surfaces often provide significant degradation pathways for compounds that are resistant to biodegradation [4]. The adsorption of organic pollutants on the TiO<sub>2</sub> surface has been shown to influence the efficiency of degradation [5]. In dye-sensitized TiO<sub>2</sub> solar cells [6, 7] the mode of adsorption of the dyes is of crucial importance to the electron injection efficiency as well as to the photoelectrochemical stability of adsorbed dyes. Due to the strong absorption of IR radiation by water, IR studies of aqueous systems have been limited. With the development of attenuated total reflectance (ATR) techniques and high signal-to-noise Fourier transform infrared (FTIR) instruments; IR studies of mineral particles in the presence of water have become possible [8].

ATR-FTIR has been applied before to the study of various dicarboxylic and polycarboxylic acids in aqueous solutions [9] and on mineral surfaces, e.g., adsorption of oxalate on TiO<sub>2</sub> [10] and on chromium oxides [11], of aliphatic dicarboxylic acids on hematite [12]. The motivation of the current study is to see the photocatalytic oxidation of oxalic acid by recording of

sequential ATR-FTIR spectra of an illuminated iron oxide nanoparticle deposited onto the ATR crystal. Oxalic acid is considered as a simple model system of organic pollutants containing more than one carboxylate group. During its heterogeneous photocatalytic oxidation it is representative for some of the main features of the whole class of organic acids [13]. The interaction of oxalate with photocatalyst surface in the dark is already characterized with ATR-FTIR spectroscopy [14]. Oxalic acid is easily oxidized to  $\text{CO}_2$ , thus minimizing the problem of possible accumulation of intermediate products, its primary oxidation product, the radical anion  $\text{CO}_2^{\bullet-}$  injects its electron into the conduction band and produces a second  $\text{CO}_2$  molecule. In this work, I studied the photocatalytic behavior of a thin  $\text{Fe}_2\text{O}_3$  layer in the presence of aqueous oxalic acid with in situ ATR – FTIR spectroscopy. Also detail optical, structural, electronic property of iron oxide nanoparticle along with morphology has been studied in order to correlate with the final photocatalytic performance. BET study has been done to see the effect of surface area on the rate of photocatalytic process.

## 5.2 Materials and methods

Spectra were taken with Bio-Rad FTS 575C instrument equipped with a mercury cadmium telluride detector and a horizontal nine reflection diamond ATR unit with KRS-5 optics (SensIR Technologies, Danbury, CT). Scans were performed from 400 to 4000  $\text{cm}^{-1}$  at 2  $\text{cm}^{-1}$  resolution. Data analysis was performed with Matlab. An oxide layer was deposited on the ATR crystal and 50 mL of high purity water was added to the liquid cell for the ATR-FTIR photoirradiation experiments. The solutions in the liquid cell were purged with high-purity  $\text{N}_2$  gas to exclude the formation of carbonates by sorption of  $\text{CO}_2$  from air and to stir the solution. After purging the solution above the oxide layer with  $\text{N}_2$  for 45 min, a background spectrum of the water-solid interface was measured (51 co-added scans). Then a small volume of an oxalic acid stock solution was added to reach a concentration of 200  $\mu\text{M}$ , and the pH was adjusted with HCl or NaOH to the desired value. Absorbance spectra were recorded with respect to the background spectrum and it was found that after 30- 40 min, adsorption of the investigated organic acids to iron oxide nanoparticle reached a stable maximum. Subsequently, the mineral water interface was irradiated and absorbance spectra were recorded in time-steps of 1 min (51 co-added scans per spectrum).

## 5.3 Results & Discussion

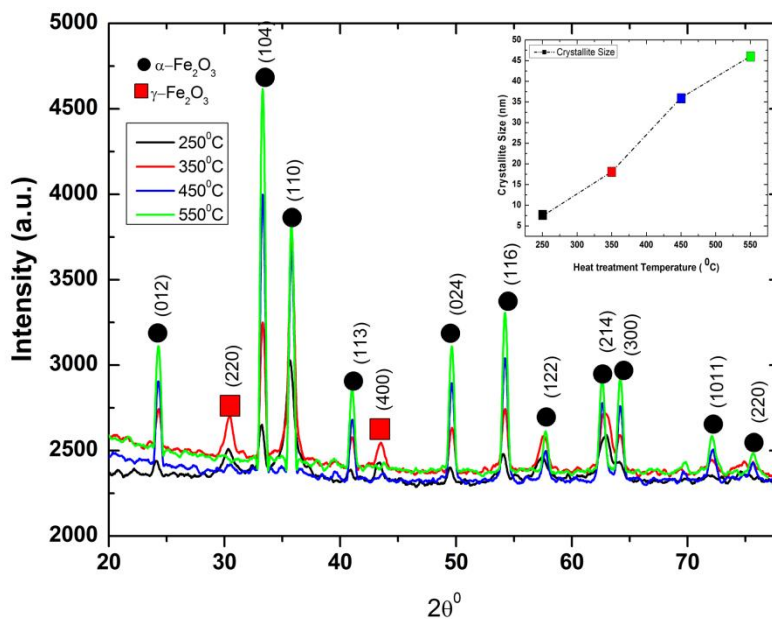


**Figure 5.1:** The XRD pattern of iron oxides nanoparticles heat treated from 250 $^\circ\text{C}$  to 550 $^\circ\text{C}$

The XRD pattern of iron oxides nanoparticles heat treated from 250 $^\circ\text{C}$  to 550 $^\circ\text{C}$  are shown in Figure 5. 1. It has been observed that 250 $^\circ\text{C}$  and 350  $^\circ\text{C}$  had two additional Bragg reflection peak from (220) and (400) planes of maghemite. The other peaks were assigned to hematite phases. In samples heat treated at 450  $^\circ\text{C}$  and 550  $^\circ\text{C}$  only pure hematite phases have been observed. On increasing the heat treatment temperature, the intensity of Bragg peak increases and full width half maximum decreases from 250  $^\circ\text{C}$  to 550  $^\circ\text{C}$  samples. This decrease was due to the increase in the size of the nanocrystallite with heat treatment temperature (as shown in inset of Figure 1) calculated with the help of Scherer equation.

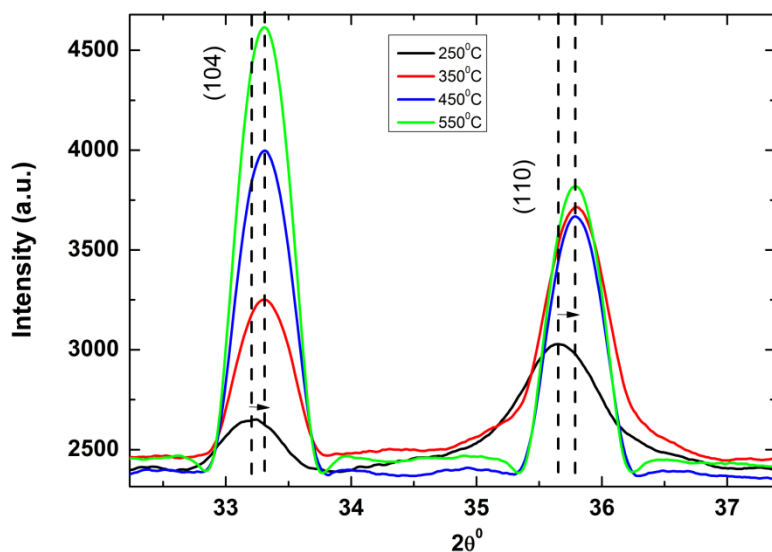


**Figure 5.2:** expanded view of (104) and (110) peak in 250-550 $^\circ\text{C}$  samples.

From the expanded view of the XRD profile (Figure 5.2), it is found that the (104) and (110) Bragg reflections remain at the same position and shape was well maintained on increasing the temperature from 250°C to 550 °C. It is to be noted that the photocatalytic activity of a crystallite also depends on the chemical reactivity of particular facet such as (110) plane in case of hematite [15]. In order to correlate the photo catalytic activity with the growth of Nano crystallite in particular direction, I have calculated the relative Bragg peak ratio (104)/ (110) of heat treated iron oxide nanoparticles. From here I have found that the particles grow along the (104) direction not (110). This renders us to confirm that the particular photo catalytic activity of nanoparticles depends not on the reactivity of crystallographically preferred direction.

The reflectance and absorbance spectra in the range of 350-650 nm of iron oxide nanoparticles heat treated at different temperatures are shown in Figure 5.3 (A) and (B). From Figure 5.3(B), it is observed that the spectra contain several absorption regions.

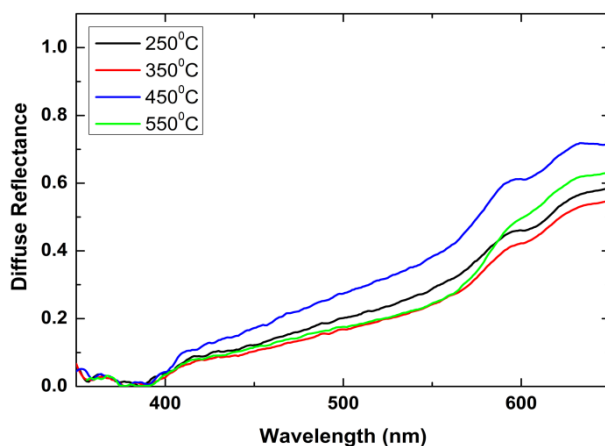


**Figure 5.3 (A)** Diffuse reflectance spectra of iron oxide nanoparticles heat treated at different temperature.

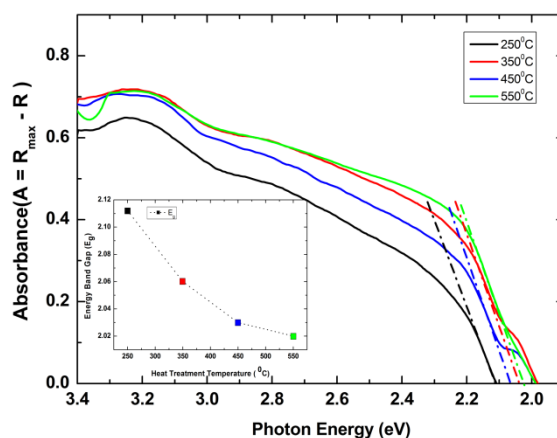


**Figure 5.3 (B)** Absorbance spectra of iron oxide nanoparticles heat treated at different temperature. Inset shows the variation of energy band gap with heat treatment temperature.

The absorption band at 400 nm evolved mainly from the ligand to metal charge transfer reactions. The region between 400-600 nm results from the pair excitation process at 485-500nm [16] which overlapped the contribution of ligand field transitions at 430 nm and charge transfer band tail. The absorption intensity in region 1 (250-400nm) and region 2 (400-600nm) are higher than that in region 3 (above 650 nm) indicating that the absorption from the charge – Transfer transitions and pair excitations is far stronger than that from the ligand field transitions due to the selection rules. It has been also observed that the relative intensities of different regions change with increase in heat treatment temperature which affects the particle size. This change is believed to be due to the pair excitation is enhanced for larger particles together with the charge transfer band redshift. The light absorbing ability of  $\alpha$ -Fe<sub>2</sub>O<sub>3</sub> (550<sup>o</sup> heat treated samples) in long wavelength region is far stronger than that of  $\gamma$ -Fe<sub>2</sub>O<sub>3</sub> (250<sup>o</sup> heat treated samples). The band of  $\gamma$ -Fe<sub>2</sub>O<sub>3</sub> in region 2 blue shifts relative to that of the  $\alpha$ -Fe<sub>2</sub>O<sub>3</sub>. The band of  $\alpha$ -Fe<sub>2</sub>O<sub>3</sub> in region 3 (600–750 nm) obviously broadens as compared with that of the  $\gamma$ -Fe<sub>2</sub>O<sub>3</sub>. These changes in optical properties between  $\alpha$ -Fe<sub>2</sub>O<sub>3</sub> and  $\gamma$ -Fe<sub>2</sub>O<sub>3</sub> is due to the difference in crystal structure. It is to be noted that  $\alpha$ -Fe<sub>2</sub>O<sub>3</sub> is a uniaxial hexagonal crystal with electronic anisotropy and has a corundum structure with distorted FeO<sub>6</sub> octahedra. The octahedra is connected to the nearest neighboring ones via face-sharing bonds in addition to corner and edge-sharing ones. While,  $\gamma$ -Fe<sub>2</sub>O<sub>3</sub> is a cubic crystal and has a cation-deficient spinel Fe<sup>3+</sup> [ $\square_{1/3}$ Fe<sup>3+</sup><sub>5/3</sub>] structure. Here, the parenthesis denotes A site and square bracket denotes B site. In a spinel, the cations in A and B sites have tetrahedral FeO<sub>4</sub> and octahedral FeO<sub>6</sub> coordination with oxygen, respectively, and in the former a central Fe atom is surrounded by the corner-sharing oxygens only and the latter contains both corner and edge-sharing oxygens. The increased absorption for high heat treated sample was in longer wavelength was due to thermal expansion with rising temperature. With increasing temperatures, the absorption edges of O<sup>2-</sup> metal charge transfer show red shifts, with increased absorption in the visible region in high temperature spectra. The degree of red shift for the absorption band due to the Fe<sup>3+</sup> ligand field transition by thermal expansion can be estimated from the reported change of Fe<sup>3+</sup>- O<sup>2-</sup> distance in hematite with temperature [17]. In the case of semiconductors for water splitting, the properties that can potentially estimate from the diffuse reflectance are the band-gap energy (also referred to as the band gap) and the absorption coefficient [18]. Determination of the band gap from the measurement of diffuse reflectance of the powder sample is a standard technique. The powder sample has to be sufficiently thick that all incidents light is absorbed or scattered before reaching the back surface of the sample, 1-3 mm thickness is required.

### Calculation of the band gap from the diffuse reflectance:

Many workers [19] have attempted to obtain the band gap of a semiconductor coating on an opaque substrate directly from diffuse reflectance measurements. They fitted a line to the long-wavelength edge of the dip in the diffuse reflectance (as shown in Figure 5.3 (B)); the band-gap wavelength was taken to be the intersection of this line with a horizontal line corresponding to the maximum reflectance.

In practice, this was done by calculating the absorbance

$$A = R_{\max} - R_{\text{cd}}$$

Where  $R_{\max}$  is the maximum value of  $R_{\text{cd}}$  for wavelengths longer than that of the dip in the diffuse reflectance. This sets the minimum absorbance to zero; the band-gap wavelength is obtained by extrapolating the long-wavelength edge of the peak in absorbance to this zero line. From the band gap determination, it was evident that it does not change with the heat treatment temperature (as shown in inset of figure 5.3 B). It lies between 1.9 - 2.2 eV which is the standard band gap energy of hematite nanoparticle. The observed photocatalytic oxidation of oxalic acid on hematite surface does not corroborate well with the resulting changes in band gap energy.

In order to get visual information about the nano particles size, its crystallinity and morphology, high resolution transmission electron microscopy (HRTEM) was further applied. Representative images of four samples (250°C, 350°C, 450°C and 550°C) are shown in Figure 3(A-F). From these HRTEM images, I can see the well alignment of crystal lattice plane along (110), (024) and (220) respectively further validate the presence of hematite phases in all heat treated samples. The FFT pattern showed the polycrystalline nature of the sample.

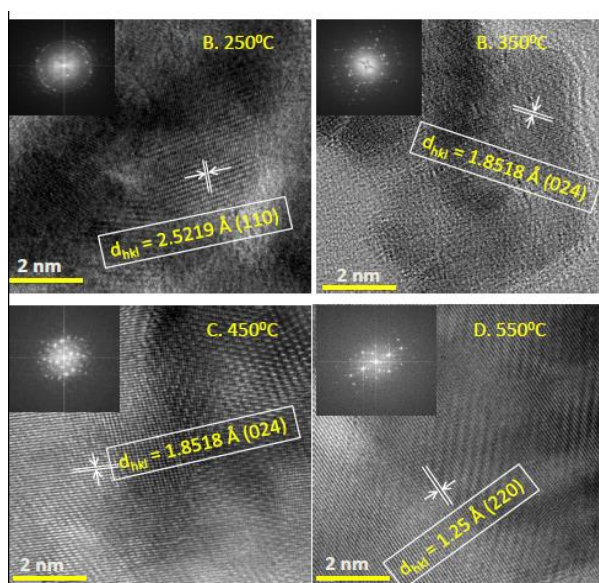


**Figure 5.4** HRTEM and FFT pattern of iron oxide nanoparticles heat treated from 250°C-550°C [TEM Courtesy: Mr. Daniel Schreier]

To get a further insight into the electronic structure of iron oxide nanoparticles, O- K edge and Fe- L edge NEXAFS spectra have been taken. The O- K edge spectra are shown in Figure 5.5 (A). Analysis of the spectrum for the O k edge fine structure can be divided into two regions: the pre - edge and post - edge. The pre edge is defined as the low energy region between the absorption threshold and the absorption jump and the post edge region extends to about 50 eV past the continuum threshold. These regions arise from transition of O 1S electrons to bound excited electronic state and continuum states respectively. For example, near the threshold, the oxygen 2p character is hybridized with the more sharply defined transition metal 3 d band. In the second region, the O 2p character is hybridized with the more weakly structured 4 sp band. The integrated intensity of the 4 sp region is at least equal to that of the 3 d band region, which is indicative of the significance and contribution of metal 4 sp states to the covalent nature of transition-metal oxide.

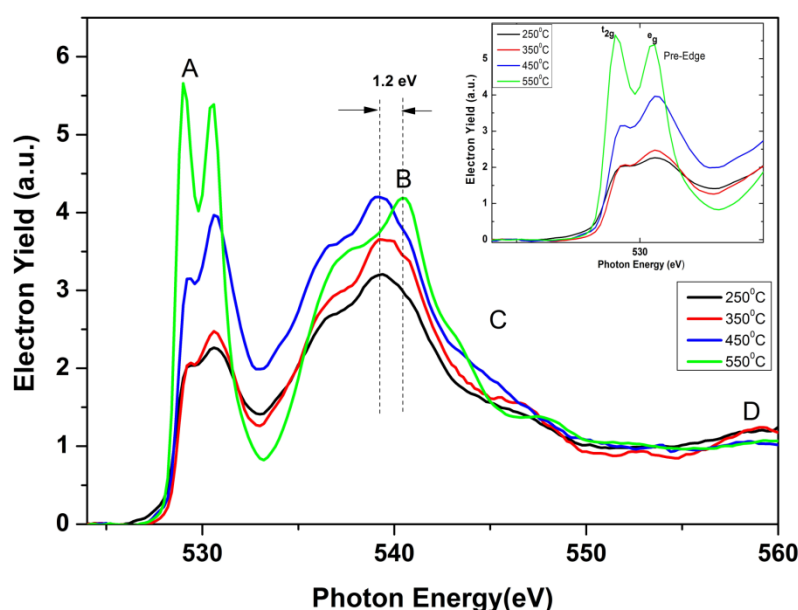


**Figure 5.5 (A)** O-K edge NEXAFS spectra of iron oxide nanoparticles heat treated at different temperatures

From the careful inspection of the O K edge NEXAFS spectra of iron oxide nanoparticles obtained through heat treatment of iron fatty acid precursor at different temperature, the spectra have been divided into two regions, (the pre-edge and post-edge). If I consider the corresponding spectral signature of iron oxide samples, it can be assigned to three regions consisting of 4 features A, B, C and D. In region 1, it has been observed that the shape, intensity and position of the peak changes with increase in heat treatment temperature. The feature A splitted up into two components namely  $t_{2g}$  and  $e_g$  symmetry bands separated by ligand field splitting to a first approximation. This represents a 3:2 ratio in terms of pre edge

intensity. In case of 550<sup>0</sup>C sample, the feature A represents t<sub>2g</sub> and e<sub>g</sub> symmetry bands with identical intensity corresponding to bulk hematite single crystals [20]. To explain the observed 1:1 intensity the effect of orbital hybridization needs to be considered. In theory, the e<sub>g</sub> hybridization is twice as strong as the t<sub>2g</sub> hybridization due to the direction of metal e<sub>g</sub><sup>2</sup> orbitals in O<sub>h</sub> symmetry towards oxygen atoms. This on consequent fashion makes an overlap with the oxygen 2p orbitals. In region 2, the structure of feature B which includes a main peak and a low energy shoulder is related to the O<sub>h</sub> symmetry set up by the nearest oxygen neighbors. The main peak slightly shifted (1.2eV) to higher energy in case of 550<sup>0</sup>C sample. Additional information gained from the spectra concerns the relative peak intensity between peaks A and B that is I<sub>A</sub>/I<sub>B</sub>. The variation of relative peak intensity against crystallite size is shown in **Figure 5.5 (B)**

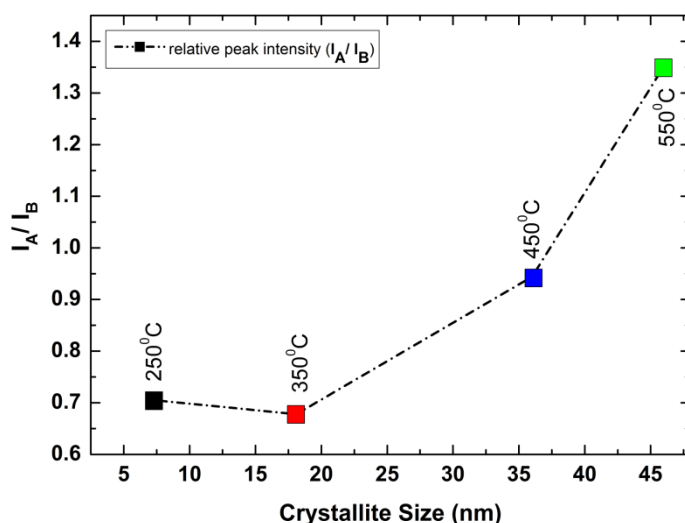


**Figure 5.5 (B)** Variation of the relative peak intensity (I<sub>A</sub>/I<sub>B</sub>) with respect to crystallite size.

The intensity of prepeak A decreases with respect to peak B is related to the decrease in the hole population of the 3d band as compared with that of the 4 sp band. It is in effect a function of the number of unoccupied 3 d states available for hybridization with the O 2p states. Slightly higher values of (I<sub>A</sub>/I<sub>B</sub>) observed for 550<sup>0</sup>C sample in comparison to 250<sup>0</sup>C – 450<sup>0</sup>C samples are indicative of a higher contribution of metal 3 d hybridization in the former [20].

The Fe- L edge NEXAFS spectra can be divided into 2 regions: the L<sub>3</sub> and L<sub>2</sub> edge. The peaks obtained in these regions are due to the transitions of electrons to bound excited electronic states and continuum states respectively. There are two main peaks of L<sub>3</sub> and L<sub>2</sub> edges at ~ 710 eV and ~ 723 eV which are due to electronic transitions of Fe 2p<sub>3/2</sub> and 2p<sub>1/2</sub> core electrons, split by the spin-orbit interaction for the Fe 2p core level, to an unoccupied 3d level highly hybridized with oxygen 2p orbital respectively. According to the dipole selection rule,

Hybridization occurs between the Fe 2p characters with a sharp, highly structured transition metal 3d band. The Fe L<sub>2,3</sub> edges are associated with strong excitations from the 2p<sup>6</sup>3d<sup>n</sup> Fe ground state to corresponding 2p<sup>5</sup>3d<sup>n+1</sup> states, where n = 5 for Fe<sup>3+</sup> and n = 6 for Fe<sup>2+</sup> resulting from multiple effects due to strong columbic and exchange interactions between the 2p core hole and the 3d electrons in the final states. Peak shapes and chemical shifts in the Fe L edge therefore are extremely sensitive to the 3d ground state configuration and to crystal field interactions. The Fe 2p NEXAFS data of iron oxide nanoparticles heat treated at different temperature are shown in Figure 5.6 (A). The spectra for all heat treated iron oxide nanoparticles exhibits rather similar features and consist of two separated white lines centered at ~ 710 eV and ~ 723.3 eV respectively with a spin orbit splitting of ~13 eV respectively.

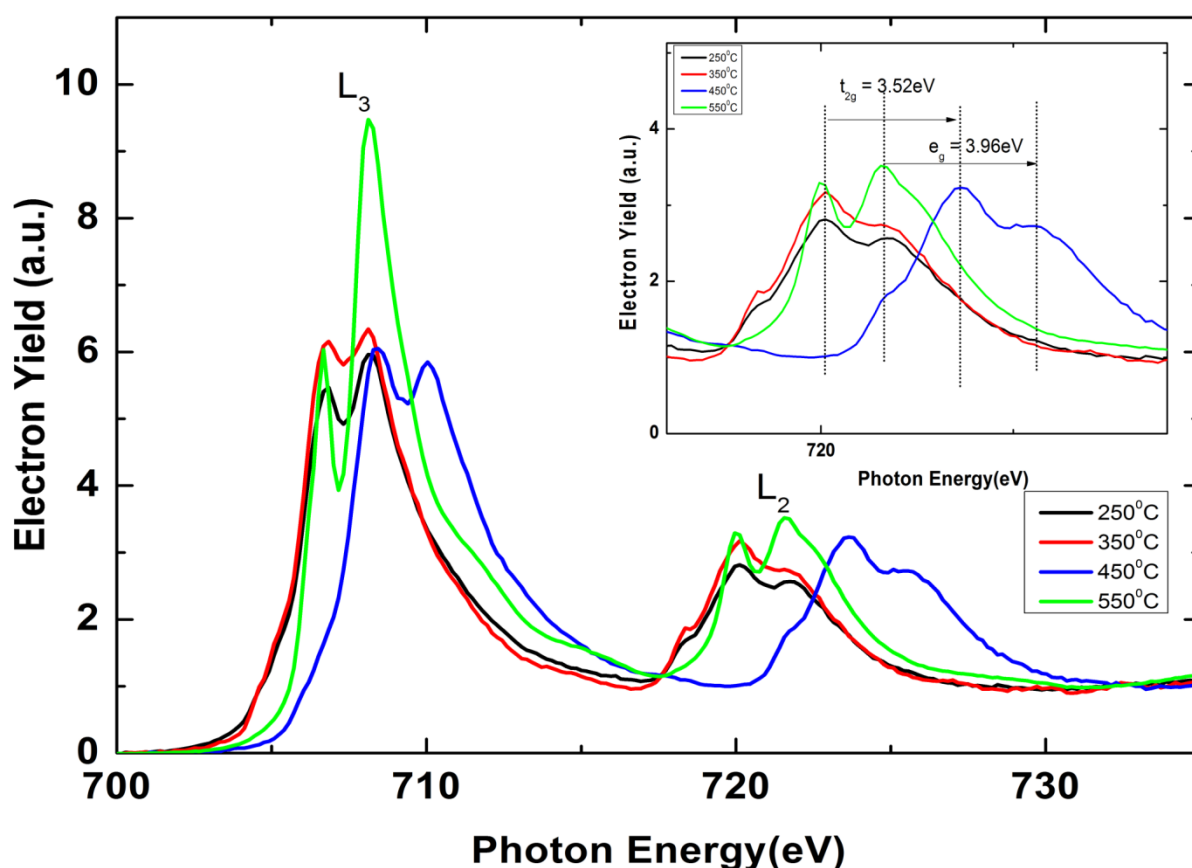


**Figure 5.6 (A):** The Fe 2p NEXAFS data of iron oxide nanoparticles heat treated at different temperature.

Qualitatively it is confirmed that the  $I_{L3} / I_{L2}$  values in our iron oxide nanostructures samples increase with respect to the valence state with increasing d orbital occupancy as shown in Figure 5.6(B). The highest  $I_{L3} / I_{L2}$  value observed in our case is 2.7 for 550°C sample resembles that of hematite rhombohedra (2.8). Since  $I_{L3} / I_{L2}$  ratios are sensitive to the oxidation

states of metals a decrease in  $I_{L3} / I_{L2}$  values can potentially be ascribed to the reduction of  $Fe^{3+}$  to  $Fe^{2+}$  at the surface of iron oxide nanoparticles.

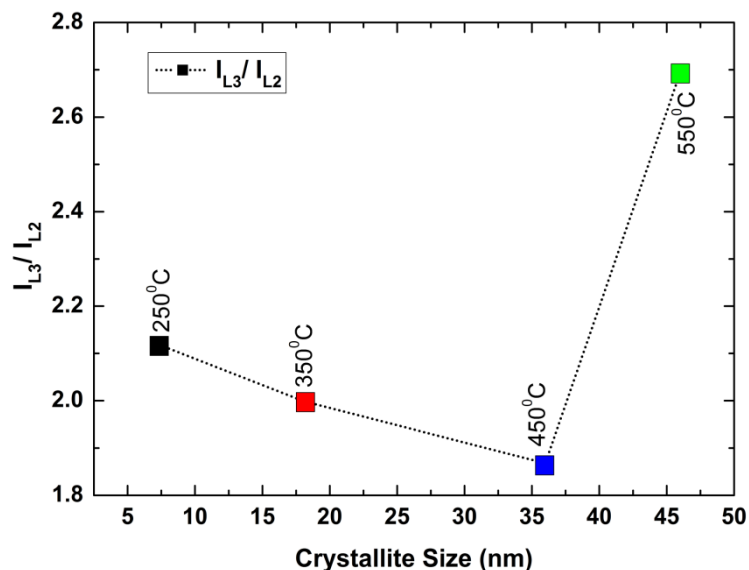


**Figure 5.6(B)** Variation of  $I_{L3} / I_{L2}$  values with respect to crystallite size.

As a qualitative comparison among the all heat treated samples it has been found that the 550°C sample showed maximum chemical shift towards the higher energy region for L<sub>3</sub> and L<sub>2</sub> respectively [see Figure 5.6 (C)]. This increase was supposed to be due to increase in nanoparticle size with heat treatment. The factors responsible for the observed chemical shift are p - d coulomb exchange, and crystal field interactions etc. It can be concluded that nanoscale size effects including surface imperfections, surface confinement effects and surface strain anisotropies influence our observations.

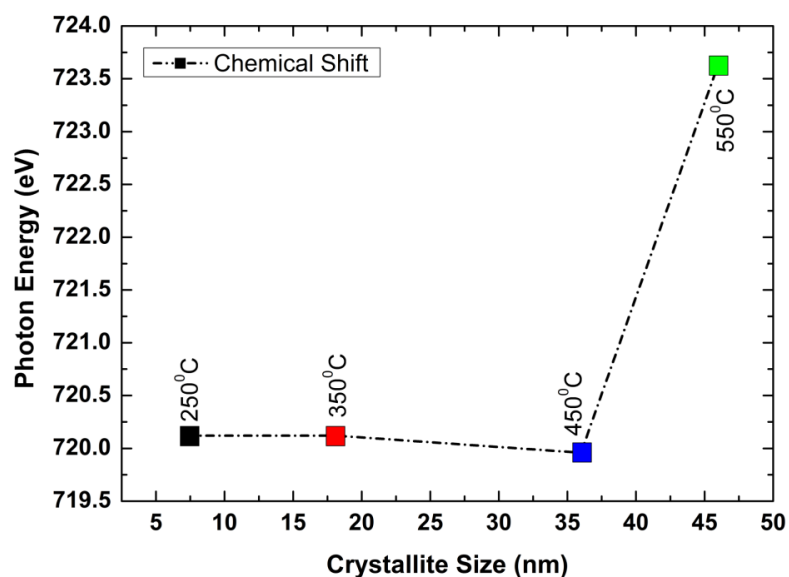
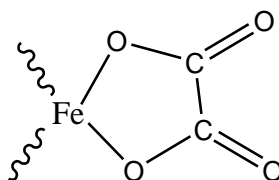
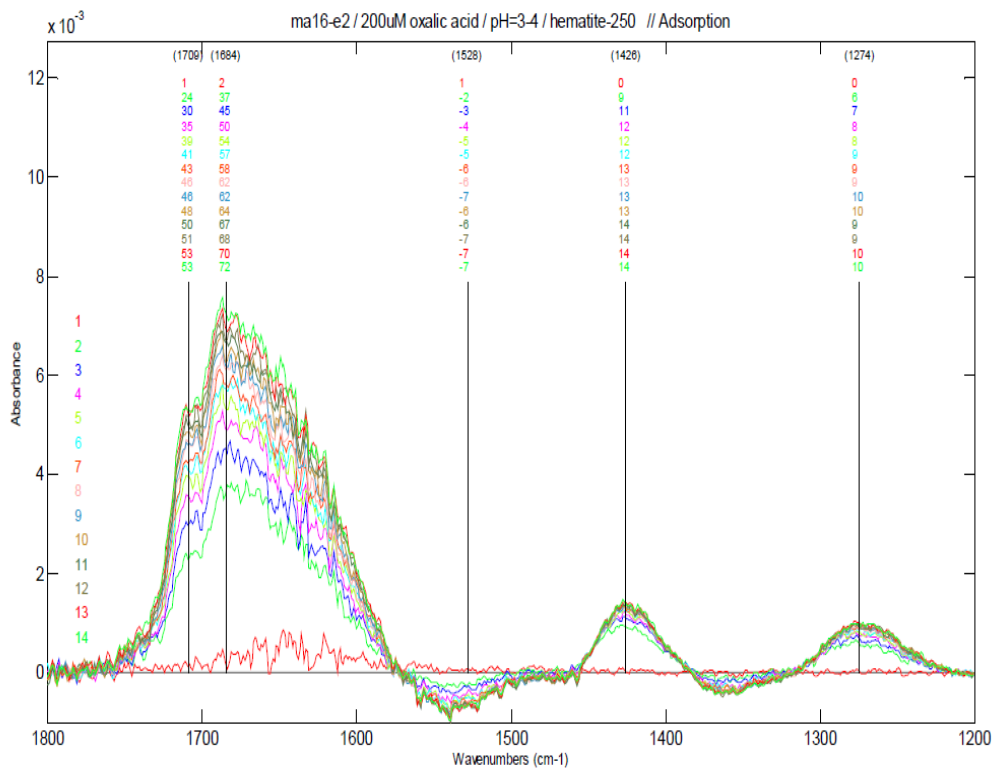


**Figure 5.6 (C)** Chemical shift for L<sub>3</sub> edge with respect to change in crystallite size

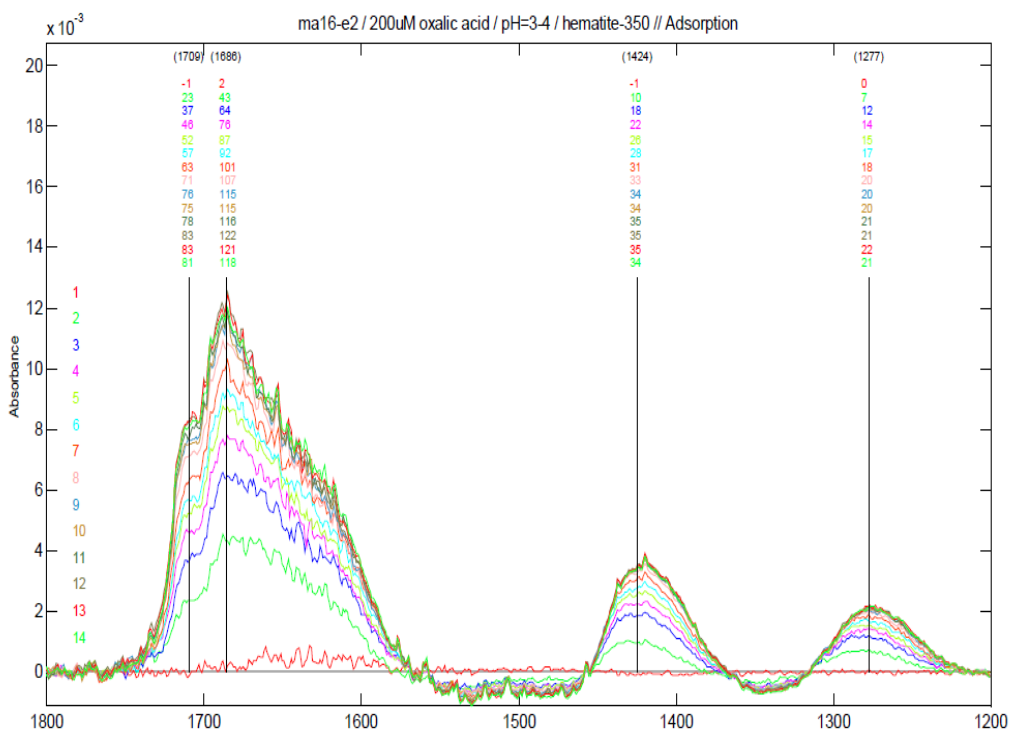
**Figure 5.7** shows the sequential ATR-FTIR spectra of adsorbed oxalic acid on nanoparticle surface heat treated at different temperatures. Here the adsorption process is characterized by two stages. The first step is a rapid one which corresponds approximately 15% of the time required by the system to reach the equilibrium and the absorption peak at  $1710\text{ cm}^{-1}$  gains extra intensity for all the nanoparticles cases. Only adsorbed oxalate exhibits two strong bands above  $1670\text{ cm}^{-1}$ , as expected for a five- (bidentate chelating) or six-membered (bidentate bridging) ring structure with one oxygen of each carboxylic group coordinated to surface sites and two C=O double bonds pointing away from the surface [21]. The final equilibrated spectra correspond to the formation of 3 different complexes of oxalic acid molecule on the iron oxide surface. The position of the absorption band in the spectra of adsorbed oxalic acid signify that the surface complex have the following structures.



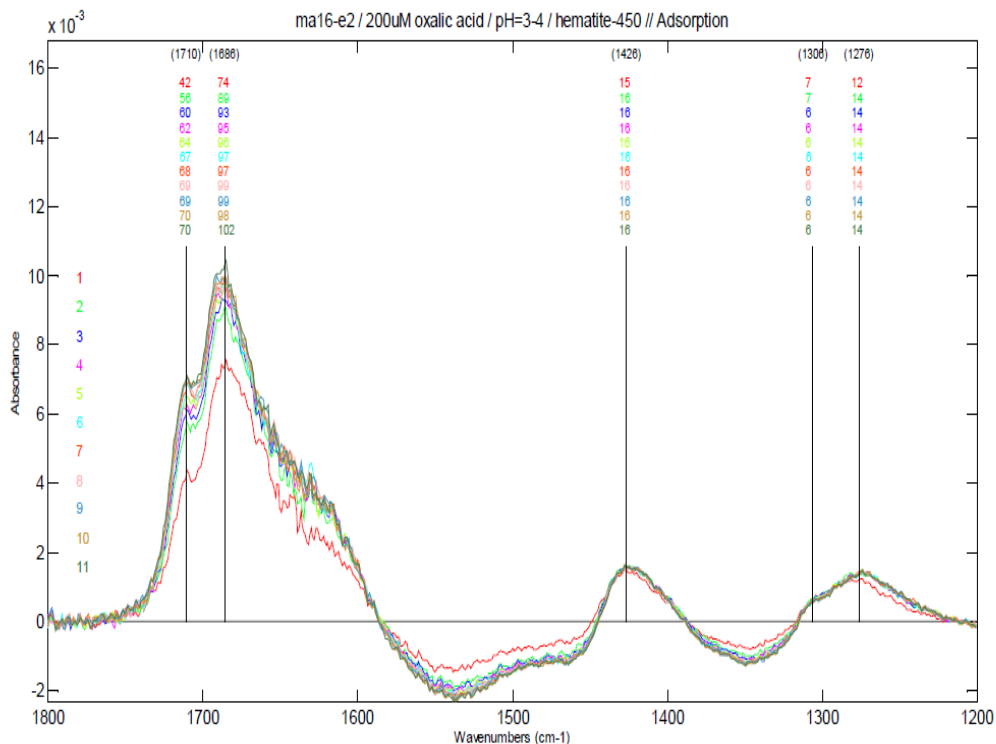
All adsorbed organic acids shows a promising IR-absorption band in this spectral region. Only adsorbed species are detected, as the aqueous concentration of  $200\mu\text{M}$  was too small for the detection of dissolved species. During adsorption of acid, solution concentration seems to be constant, as the amount of the dicarboxylates in solution is far larger than the amount adsorbed by  $30\text{ }\mu\text{g}$  of solid. The spectral changes observed here upon adsorption are correlated with previously reported studies and are consistently interpreted as inner-sphere surface coordination with the formation of ligand-to-metal bonds [21]. The two most prominent peaks of the adsorbed oxalate at  $1715\text{--}1713$  and  $1696\text{--}1679\text{ cm}^{-1}$  are the symmetric and asymmetric combinations of two C=O double bonds ( $\nu_s\text{C=O}$  and  $\nu_{as}\text{C=O}$ ), respectively. The  $1427\text{ cm}^{-1}$  is due to  $\nu(\text{C-O})$  and  $\nu(\text{C-C})$  and  $1272\text{ cm}^{-1}$  is due to  $\nu(\text{C-O}) + \nu(\text{O-C=O})$ . The slight shifting in the absorption band of adsorbed oxalate on nanoparticle surface was caused by changing concentrations of different surface complexes, but also by changing degrees of hydrogen bonding with neighboring hydroxyl groups and water molecules. The change in intensity can also be assigned to the aforementioned fact.



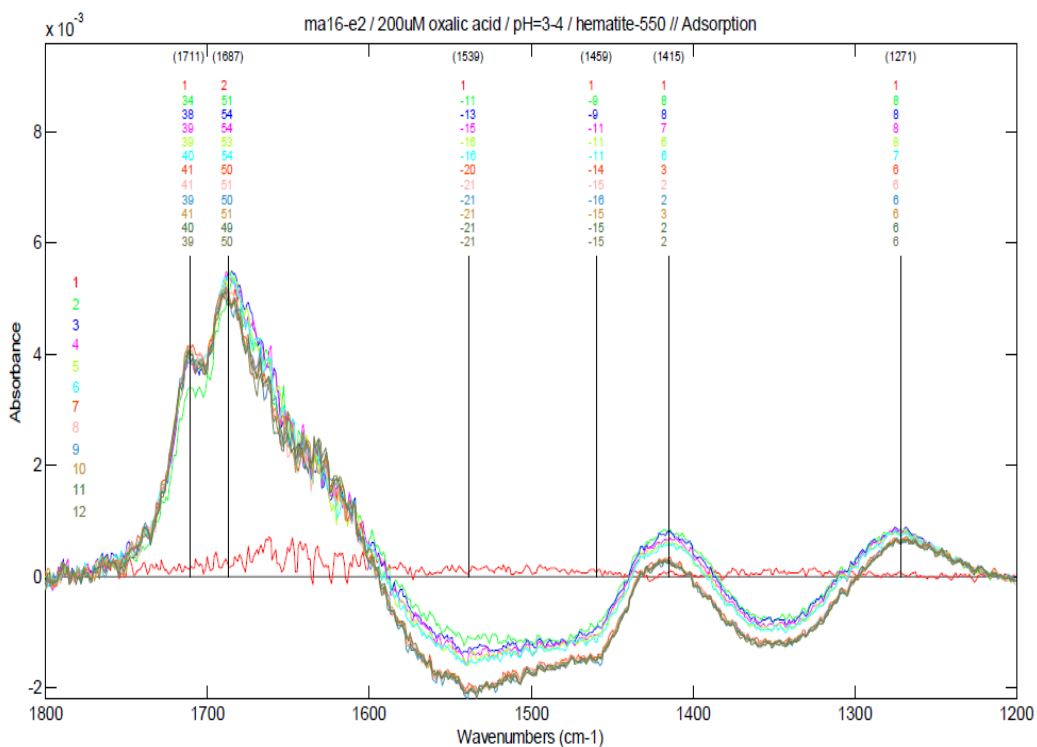
A. 250°C



B. 350°C



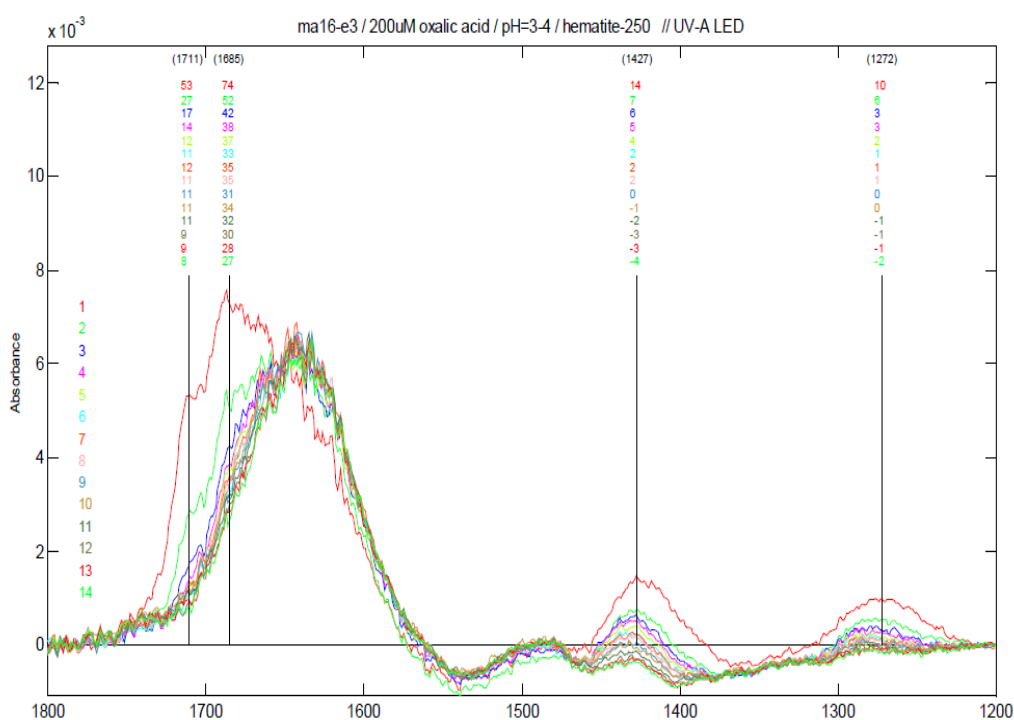
C. 450°C



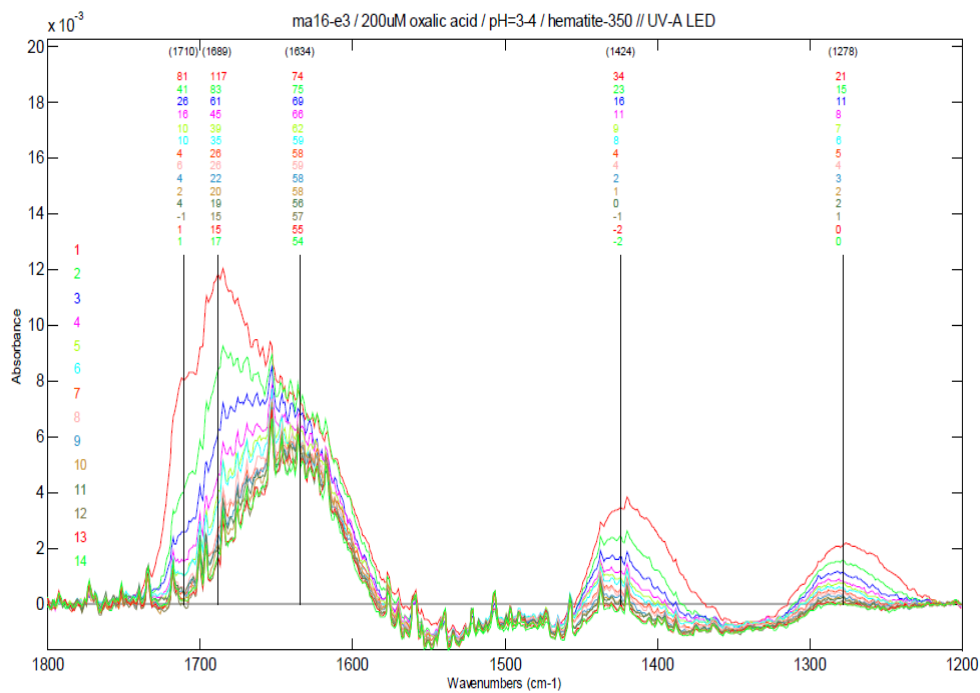
D. 550°C

Figure 5.7: Sequential ATR-FTIR spectra of oxalate adsorbed onto iron Oxide nanoparticles heat treated at different temperature in the dark at pH 3.6 and room temperature.

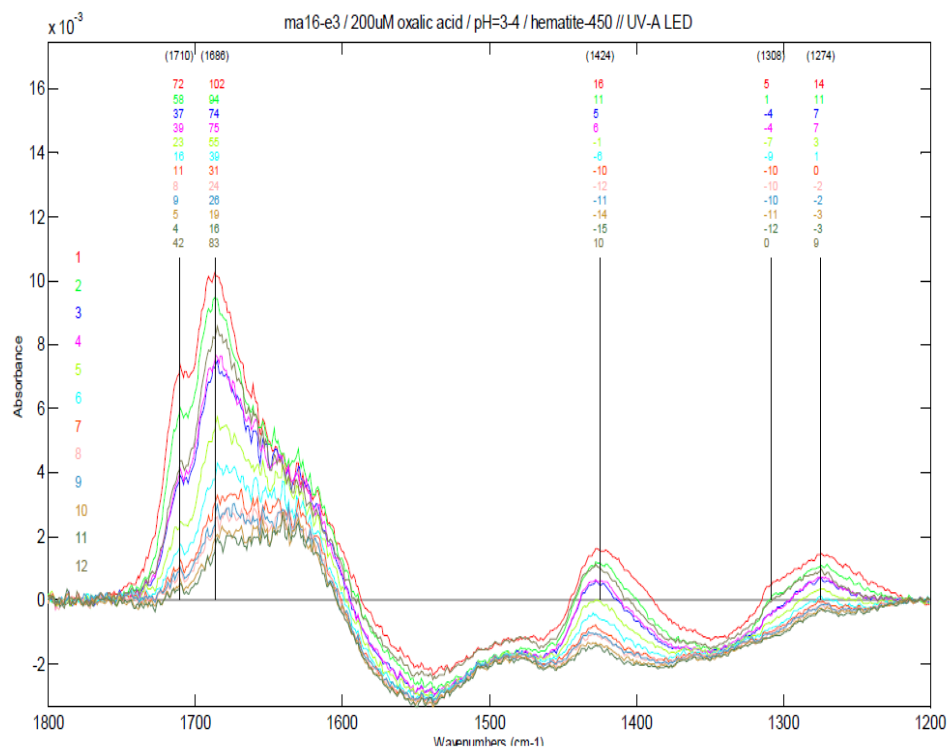
In the next step, the photodecomposition of oxalate has been studied. Figure 5.8 showed the Sequential ATR-FTIR spectra of oxalate adsorbed onto iron oxide nanoparticle observed after successive period of illumination at a total energy output of  $1.0 \text{ mW} / \text{cm}^2$ , initial pH 3.60 and room temperature. Many factors complicated the analysis of photoredox reactions at metal oxide surfaces. For instance, desorption of photo products, competitive adsorption of unaltered ligands and photoproducts by ligand-exchange at the surface, and further (photochemical) decomposition of photoproducts [1]. This holds if the time scale of the photolysis reaction and the subsequent processes are similar. With the application of high light flux, photolysis rates may be achieved that are fast compared to the time scales of the consecutive processes. To resolve the initial photooxidation reaction from the subsequent reactions, the light flux was maximized and the scan time for recording FTIR spectra was minimized. A light flux of  $5 - 10 \text{ W/cm}^2$  (300-500 nm) and a scan time of 1 min per measured spectra (51 co-added scans per spectra) were used to study the photooxidation of oxalate at the surface of iron oxide nanoparticle. Prerequisite for ATR-FTIR photoirradiation studies as described above is that the spectra of the reactants and the photoproducts are distinguishable. The photodegradation of oxalate on iron oxide nanoparticle surface are accomplished within a short span of time. The photodegradation is evidenced by the decrease in absorbance and shifting of the  $1696\text{--}679 \text{ cm}^{-1}$  peaks towards lower wavenumber. It occurs already during the time interval before the first spectrum is recorded. The spectral changes in the following time intervals suggested a change in the surface speciation due to a decrease in the total oxalate surface concentration.



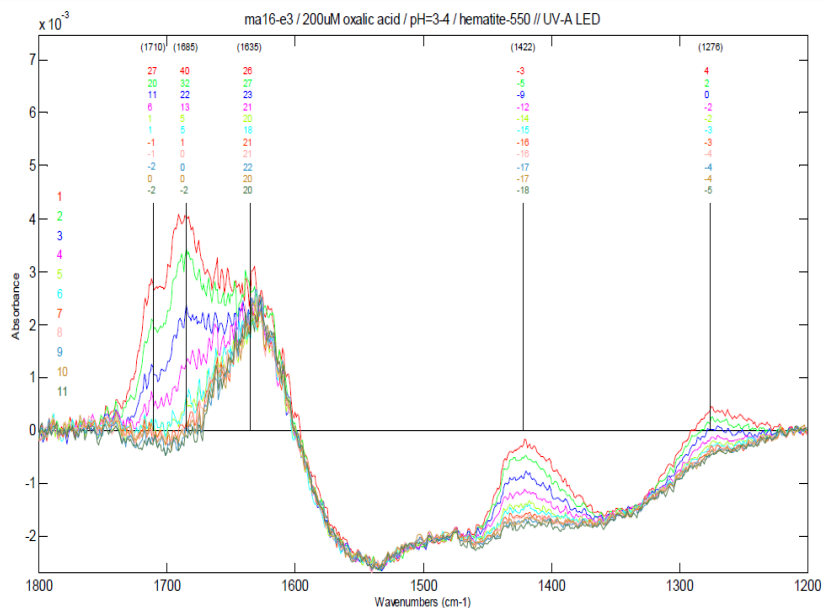
A. 250°C



B. 350 °C



C. 450 °C

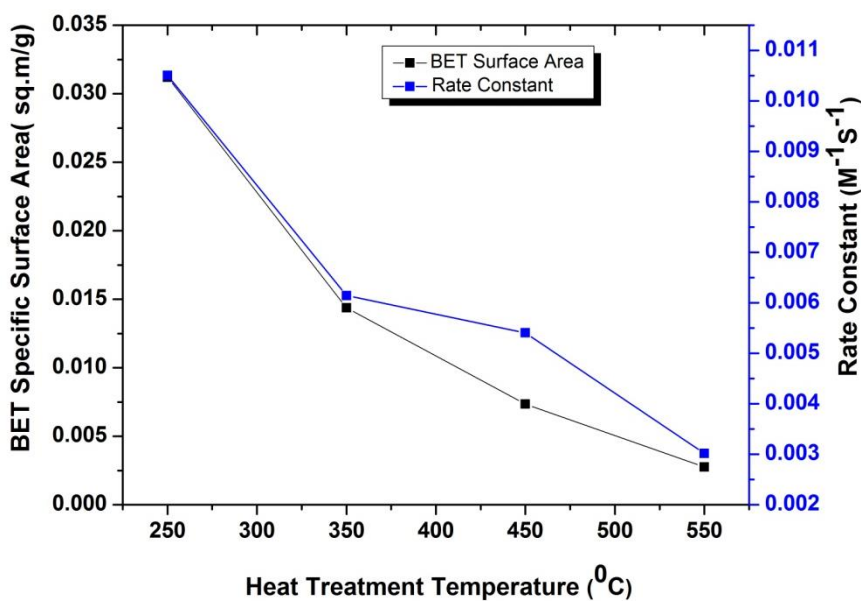


**D. 550°C**

**Figure 5.8:** Sequential ATR-FTIR spectra of oxalate adsorbed onto iron oxide nanoparticle observed after successive period of illumination at a total energy output of 1.0mW. / cm<sup>2</sup>, initial pH 3.60 and room temperature.

Rate constant of the photo catalytic degradation process have been calculated and plotted against BET specific surface area (Figure 5.9). From the resulting trend it can be concluded that igconstant. That means as a result of the increase in particle size due to high heat treatment, the rate of photo catalytic oxidation of oxalic acid on the nanoparticle surface is low.

**Figure 5. 9:** Variation of rate constant with BET specific surface area and annealing temperatures



#### 5. 4 Conclusion

The photocatalytic performance of the entire nanoparticle samples is independent of changes in optical, structural and electronic property and the rate constant changed with the specific surface area of the nanoparticle sample. At this time, it is difficult to correlate them. However, it is evident that all nanoparticles sample showed significant photocatalytic action upto desirable extent which allows us to bring it to the photo electrochemical water splitting application as described in chapter 6.

#### References

- [1] Borer, P.;Hug, S. J.;Sulzberger, B.;Kraemer, S. M.;Kretzschmar, R.*J. Phys. Chem. C* **2007**, *111*, 10560-10569.
- [2] Goldberg, M. C.; Cunningham, K. M.; Weiner, E. R. *J. Photochem. Photobiol. A* **1993**, *73*, 105.
- [3]Waite, T. D.; Morel, F. M. M. *J. Colloid. Interface Sci.* **1984**, *102*,121.
- [4] Sulzberger, B.;Hug, S.J.;Bidoglio,G.;Stumm,W. (Eds.), Chemistry of Aquatic Systems: Local and Global Perspectives, Kluwer Academic Publishers, **1994**, p. 183.
- [5] Cunningham,J.;Sedlak, P. *J. Photochem. Photobiol. A Chem.***1994**, *77*, 255.
- [6] Gratzel, M. *Nature* **2001**, *414*, 338.
- [7] Oregan, B.;Gratzel, M. *Nature* **1991**, *353*, 737.
- [8] Tunesi,S.;Anderson,M.A. *Langmuir* **1992**, *8*, 487.
- [9] Cabaniss,S.E.;Leenheer,J.A.;McVey,I.F. *Spectrochim. Acta Part A Mol. Biomol. Spectrosc.***1998**, *54*, 449.
- [10] Weisz,A.D.;Rodenas, L.G.;Morando,P.J.;Regazzoni,A.E.;Blesa,M.A. *Catal. Today* **2002**, *76*, 103.
- [11] Degenhardt, J. ;McQuillan,A.J. *Chem. Phys. Lett.***1999**, *311*, 179.
- [12] Duckworth,O.W.;Martin,S.T. *Geochim. Cosmochim. Acta* **2001**, *65*, 4289.
- [13] Mendive,C. B.;Bahnmann, D. W.;Blesa,M. A. *Catal. Today* **2005**, *101*, 237–244
- [14] Hug, S. J. ;Sulzberger, B. *Langmuir* **1994**,*10*, 3587-3597.
- [15]Yang, H. G.; Sun, C. H. ; Qiao, S. Z. ; Zou, J. ; Liu, G. ; Smith, S. C.; Cheng, H. M.; Lu, G. Q. *Nature* **2008**, *453*, 638-641.
- [16] He, Y. P.;Miao,Y. M.;Li,C. R.;Wang,S. Q.;Cao,L.;Xie, S. S.;Yang,G. Z. ;Zou, B. S. *Phys. Rev. B* **2005**, *71*, 125411 d.
- [17] Yamanoi, Y.; NakashimaS.;Katsura, M. *Am. Mineral.* **2009**, *94*, 90-97.
- [18] Murphy, A. B. *Sol. Energ. Mat. Sol.C* **2007**, *91*, 1326–1337.
- [19] Khan, S.U.M.; Al-Shahry, M.; Ingler Jr., W.B. *Science***2002**, *297*, 2243–2245.

[20] Park, T.J.; Sambasivan, S.; Fischer, D. A.; Yoon, W.-S.; Misewich, J. A.; Wong, S. S. *J. Phys. Chem. C* **2008**, *112*, 10359–10369.

[21] Hug, S.J.; Bahnemann, D. J. *Electron Spectrosc.* **2006**, *150*, 208–219.

#####

## Chapter 6

### **A. Synthesis and Photo electrochemical Study of Nanocrystalline Pristine Hematite Film Deposited by Spin Coating Method**

#### **6. A. 1 Introduction**

Nano crystalline thin films help in the development of semiconductor electrochemistry and photoelectrochemistry field besides semiconductor single crystals to polycrystalline thin films. It can be obtained in various forms such as membranes, nanoporous or nanophase films, mesoporous films, nanostructured films etc. Nanocrystalline thin films are distinguished from their polycrystalline electrode predecessors by the crystallite size (nm versus  $\mu\text{m}$  in the former) and by their permeability to the electrolyte phase. The development and application of nanocrystalline hematite thin films is a growing interest for the photoelectrochemical water splitting. Hematite is a material of choice for photoelectrochemical application because of its semiconducting behavior, abundance and well matched valence band edge position with water oxidation potential. It is inevitable to mention here that photoelectrochemical water splitting over semiconductor surface is an invaluable method for converting solar energy into clean and renewable hydrogen fuel [1]. Bard and Hardee for the first time prepared hematite thin films using CVD (chemical vapor deposition) method [2]. After this, work has been progressed with different techniques such as, sputtering [3] and thermal oxidation [4], ultrasonic spray pyrolysis (USP) and conventional spray pyrolysis (SP) [5, 6] atmospheric pressure chemical vapor deposition (APCVD) method [7], DC reactive magnetron sputtering [8], sol-gel method [9], potentiostatic anodization [10], as well as sintered disks and single crystals for fabricating  $\alpha\text{-Fe}_2\text{O}_3$  photoanodes [11,12]. Recently, another synthetic route based on a chemical solution deposition method, called complex polymerization route, has been successfully developed for producing thin films of several oxides as  $\text{BaTiO}_3$  [13]. The complex polymerization route helps in the production of appreciable preferred oriented and stoichiometric films with excellent structural and electrical properties. Following a similar complex polymerization technique developed by F. L. Souza et. al [14], nanocrystalline thin film of hematite has been fabricated by the spin coating of polymeric precursor and its photoelectrochemical performance will be studied.

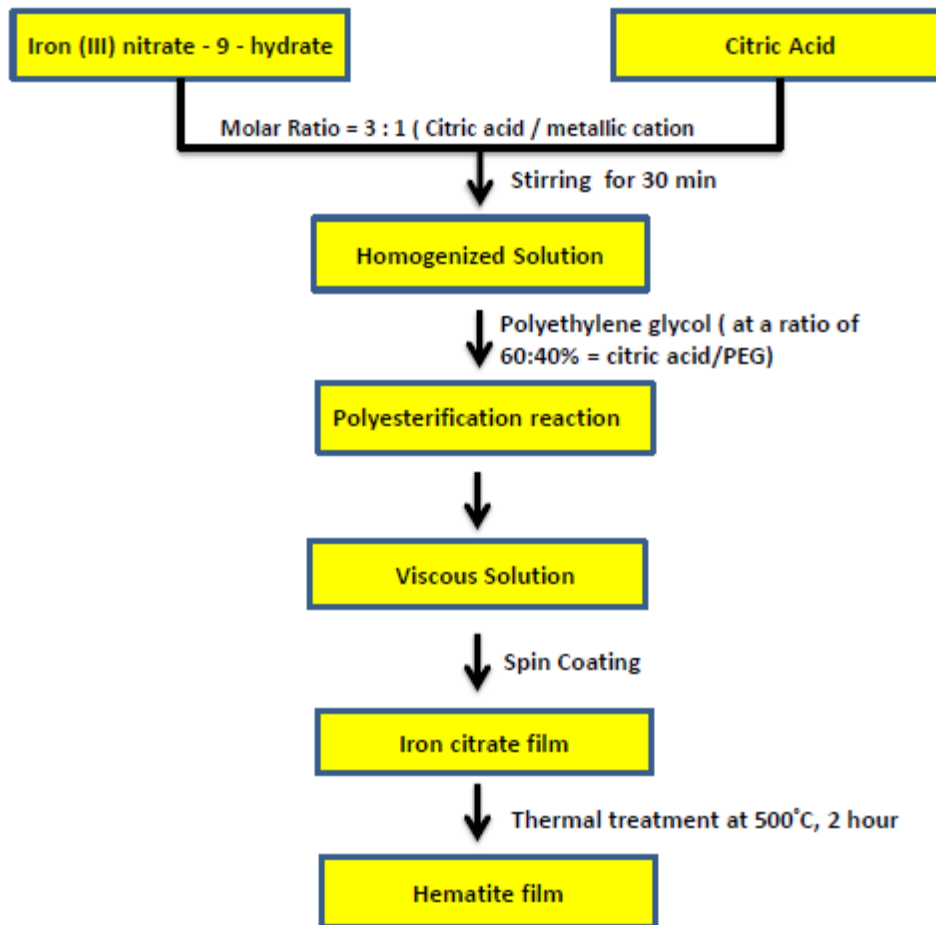
#### **6. A. 2 Material and Methods**

**Synthesis:** The precursors used in this synthesis were citric acid [ $C_6H_8O_7$ ], iron (III) nitrate 9-hydrate [ $Fe(NO_3)_3 \cdot 9H_2O$ ] and polyethylene glycol ( $C_2H_6O_2$ ). This procedure is based on metallic citrate polymerization using polyethylene glycol. To chelate the cation in solution, citric acid was used. Instead of ethylene glycol, I have used polyethylene glycol which leads to the formation of organic ester. Polymerizations, has been promoted when mixture is heated. This result in a homogeneous resin in which metal ions are uniformly distributed throughout the organic matrix. The detail process deals with the solubility of citric acid in deionized water by heating at a temperature between 70 and 90<sup>o</sup> C. Then Iron(III) nitrate 9-hydrate was mixed into the citric acid aqueous solution under constant stirring. The molar ratio used was 3:1 of citric acid / metallic cations. After homogenization of the solution containing  $Fe^{3+}$  cations, polyethylene glycol was added to the mixture in the citric acid/ polyethylene glycol at a ratio of 60:40 wt.%. The resulting solution was stirred and heated until it reached citrate polymerization by the polyesterification reaction. The deposition of thin film on commercial glass substrate coated with fluorine doped tin oxide (FTO), and complied with the following deposition step: a few drops of the resulting solution were placed on top of the substrate which was rotated with a spin coater at a two fixed rotation speed 3 s (500 rpm) and 30 s (1,000 rpm). After the deposition of two layer, the substrate was dried on a hot plate (~ 50<sup>o</sup>C) for a few seconds. For the annealed samples, each layer was heat treated at 500<sup>o</sup> C, for 2 hr., in an electrical furnace with fixed heating and cooling rate of 1<sup>o</sup>C /min.

*Characterization:* the structural property of the hematite films was studied with X-Ray diffraction measurements using  $CuK_{\alpha}$  with a wavelength of 1.54Å (Philips XRD pan analytical pw1830 IMS, rotary anode operating at 150 KV and 40 mA) in the 2 $\theta$  range from 5<sup>o</sup> to 80<sup>o</sup> with a step scan of 0.0170<sup>o</sup>. The XRD pattern of the film was compared with the hematite nanopowders obtained by the non-aqueous chemical route. The morphology of hematite films was characterized by high-resolution field emission scanning electron microscopy (Ultra-high Resolution Scanning Electron Microscope S - 4800, Hitachi at 2 KeV). The films were characterized by top view and cross section (obtained from cleaved samples). The photoelectrochemical performance of the hematite thin film was measured using a three-electrode cappuccino cell fitted with a quartz window (set up was as shown in figure 6.6).

### 6. A. 3 Results & Discussions

The step by step synthesis procedure is illustrated in scheme 6.1.



**Scheme 6.1:** Schematic diagram of synthesis procedure for getting nanostructures hematite thin films

The prepared films were as shown in Figure 6.2. After the deposition of each layer by spin coating technique, hematite film has been obtained by annealing the same at 500°C for 2 hour. The films produced were of reddish brown in appearance and also compact.



**Figure 6.2:** Hematite thin films obtained by the spin coating of polymeric precursor solution and heat treated at different temperature.

The synthesis of precursor involves the formation of a mononuclear bidentate complex,  $[\text{Fe}(\text{III})(\text{OH})_2 \text{cit.}]^{2-}$  by citric acid. With ferric iron the formation of precursor involves two carboxylic acid groups and a tridentate complex,  $[\text{Fe}(\text{II}) \text{cit.}]^-$  and with ferrous iron it involves two carboxylic acid groups and the hydroxyl group [15]. Although the characterization of these complexes is not straightforward, potentiometric and spectrophotometric studies with ferric iron-citrate complexes have shown that a tridentate mononuclear complex is formed below pH 3, and magnetic susceptibility studies have shown the formation of a bidentate dimer complex at neutral pH. Nuclear magnetic resonance studies of ferrous-citrate confirmed the formation of tridentate complex involving the hydroxyl group. In the presence of oxygen during annealing, the ferrous-citrate complex undergoes oxidation and hydrolysis, leading to the formation of ferric iron-citrate complex. The intermediates involved in the conversion of ferrous-citrate to ferric-citrate are presented in Figure 6.3. The degradation of ferrous iron-citrate by the annealing process depended on the rate of oxidation and hydrolysis of the ferrous-citrate complex.

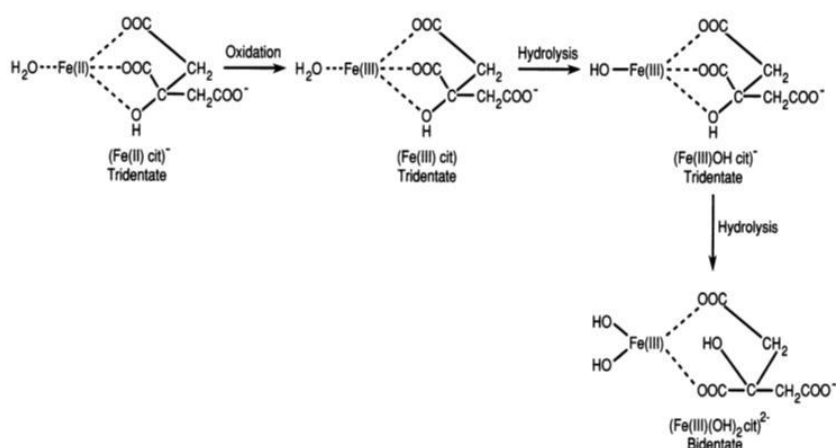


**Figure 6.3:** tridentate ferrous iron-citrate complex: Oxidation and hydrolysis leads to bidentate ferric iron-citrate complex.

The FESEM image of the films has been represented in Figure 6.4. The cross sectional image was taken with Focused Ion Beam Epitaxy Figure 6.4 D. The morphology of hematite films represents nanoporous nature with dumbbell shape interconnected grains. The figure 6.3 A illustrates the top view of hematite films. The good adherence of the film with the FTO substrate is illustrated in the cross sectional image.

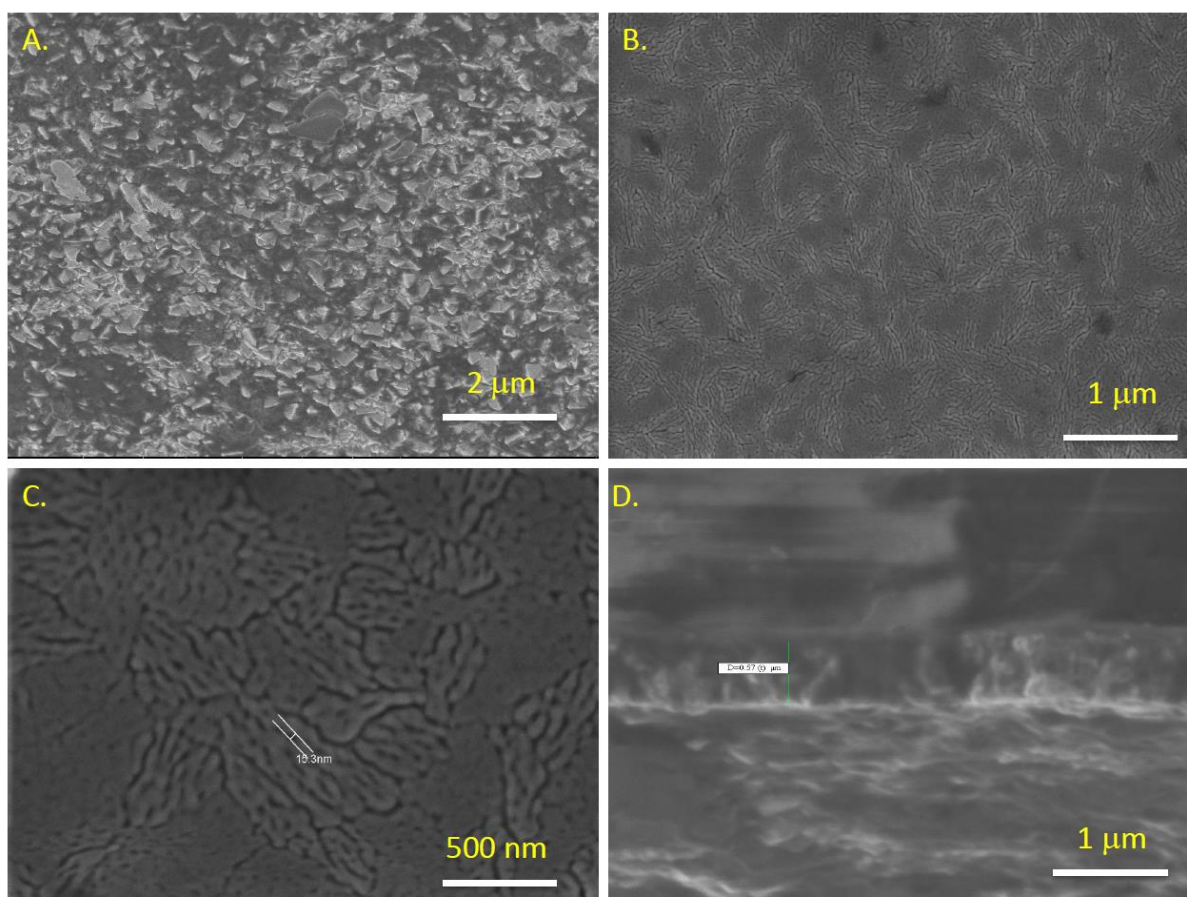


**Figure 6.4:** (A,B,C) FESEM images of the hematite films deposited by spin coating method; (D) FIB imaging of the cross section of hematite film having thickness of 570 nm.

In order to confirm the presence of hematite phase and the crystallinity of the prepared film, XRD measurement has been done and the results were compared with the XRD pattern of hematite nanopowders as shown in Figure 6.5 A. The XRD characterization of the optimized films annealed at different temperature are shown in Figure 6.5 B. From the result obtained, no significant shift in the diffracted peak position has been observed. Also the peaks are quite sharp which verify the well crystallinity as well as larger size of the nanocrystallites forming the hematite film. The relative intensity in the XRD pattern of the hematite film does not exactly correspond to the standard powder pattern of hematite (as shown in fig 7.). The strong peak in standard powder is (104) reflection, however in the film there are apparently two peaks (110) and (116). All the hematite films annealed at different temperatures follow the same X-ray pattern with a strong peak due to hematite, namely the (110) reflection (in rhombohedral coordinates) in addition to much weaker peaks that correspond to the (012), (104), (113), (024), (214) and (300) planes. Another phase of iron oxide or impurity phase had not been observed. A similar presence of the (110) reflection has also been observed for  $\alpha\text{-Fe}_2\text{O}_3$

nanostructure film in studies carried out by Ultrasonic spray pyrolysis (USP) and Atmospheric pressure chemical vapor deposition(APCVD).

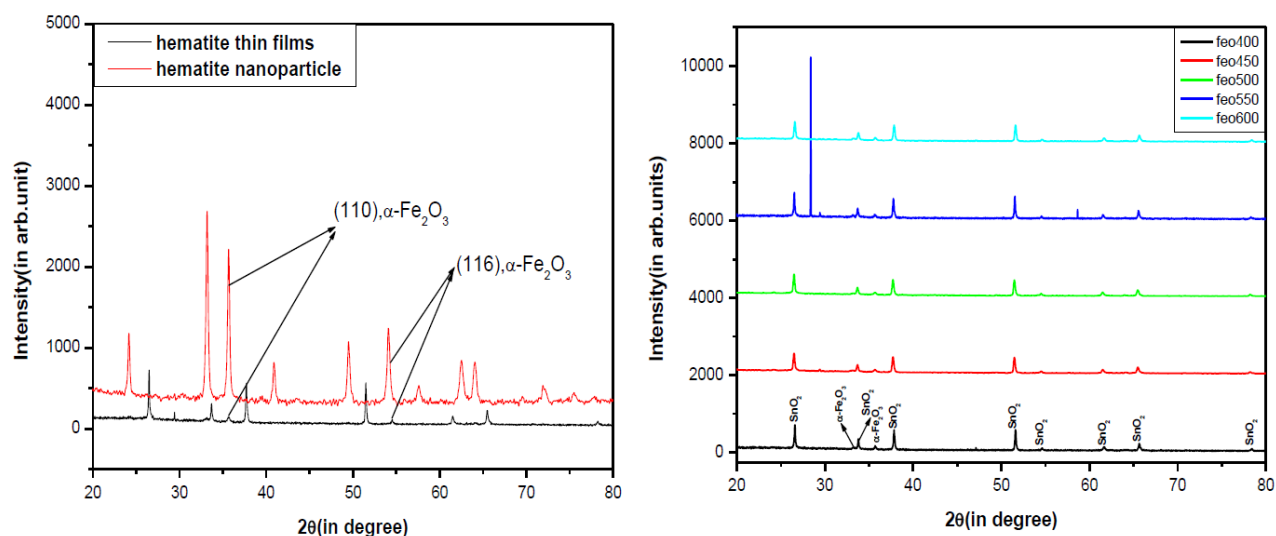


**Figure 6.5:**(A) XRD pattern of hematite nanopowders as well as film deposited on FTO substrate. The (110) plane obtained in both the cases clearly signify the presence of hematite phase.(B) XRD pattern of hematite films annealed at different temperature.

The photoelectrochemical properties of spin-coated hematite thin films are studied by measuring the Current-voltage (I-V) curves in the dark and under AM1.5 simulated light for all the samples using 1 M KOH as electrolyte using the set up as shown in Figure 6.6.

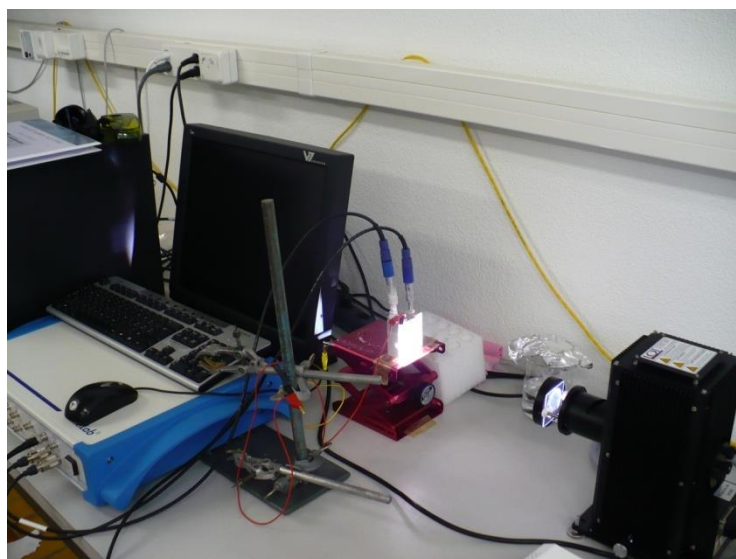


**Figure 6.6:** Photoelectrochemical set up.

Figure 6.7 A. shows the I-V curve of hematite films both under dark and stimulated light condition. The dark current is negligible up to about 0.6 V, where electrocatalytic oxygen evolution starts. Here the photocurrent obtained could not be distinguished from the dark current. The reason behind this might be due to very compact nature of the film or the film has

less porosity which resists the electrolyte to see the nanograin in bulk. Another important point is that the hematite thin films obtained by the spin coating method look very shiny. This will reflect most of the incident light and absorb very less amount. Even on increasing the film thickness I could not able to see the photocurrent. Because the final heat treated layer again looks very shiny. For getting good photocurrent, the films must have roughness in nano or bulk form. The valley like structure helps in trapping more photons due to inter-scattering across the grains in the photoactive layer. After this, the films have been optimized for heat treatment temperature ( $250^{\circ}\text{C} - 600^{\circ}\text{C}$ ) and its photoelectrochemical study was performed as shown in Figure 6.7 B.

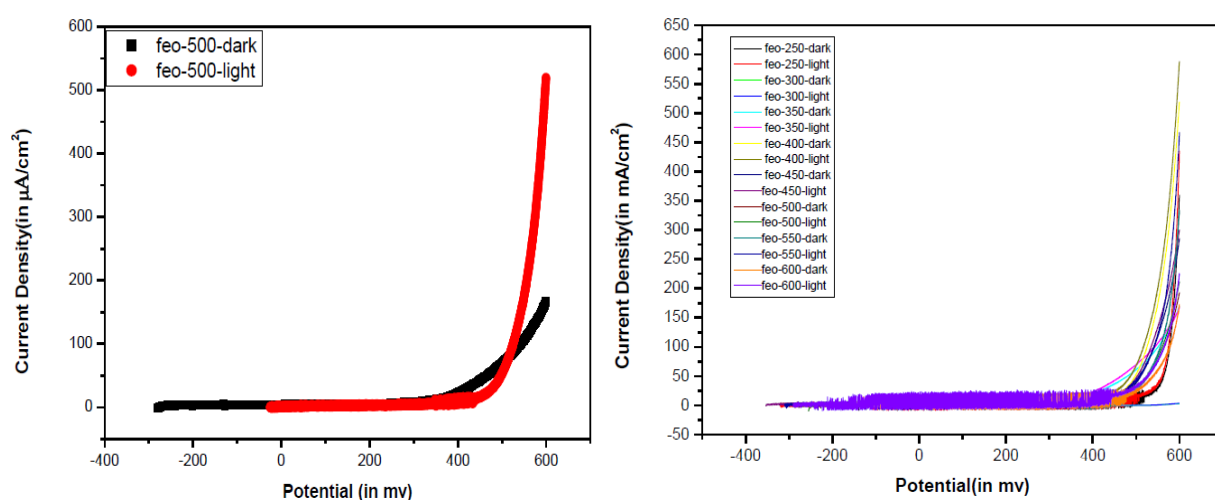


**Figure 6.7 A.** Current –voltage characteristics of hematite films having a thickness of 570 nm under both dark and light condition.**B.** Current –voltage characteristics of hematite films annealed at different temperature.

#### 6. A. 4 Conclusion

On annealing of the iron citrate precursor solution, hematite thin films been obtained due to the oxidation of ferrous ion to ferric ion. The films were homogenous in nature with the well control of the particle nucleation & growth over the FTO substrate for consecutive time of annealing. SEM analysis showed that all the samples with 2 layers deposited (thickness, 570nm) have mesoporous structure, very good homogeneities and nanometric scale grain size. From the XRD study, it is found that hematite films exhibited preferred orientation in the (110) plane perpendicular to the substrate but still showed low photocurrent. It was suggested that strong orientation in the (110) direction, where the basal plane (001) is aligned perpendicularly to the substrate, could facilitate the photoelectron collection by the short diffusion distances from nanostructure to electrolyte. Finally, from the photoelectrochemical investigation, no significant photocurrent has been observed for hematite film deposited by spin coating of the

polymeric precursor. This negative influence is attributed to the less porous character of the film along with very smooth surface. It is to be noted that only film having precise roughness are found to be very photoactive as will be described in the next part.

## **B. Synthesis of hematite thin films by the dip coating method**

**Dip coating** refers to the immersing of a substrate into a tank containing coating material, removing the piece from the tank, and allowing it to drain. The coated piece can then be dried by force-drying or baking.

### **6. B. 2 Materials and Methods**

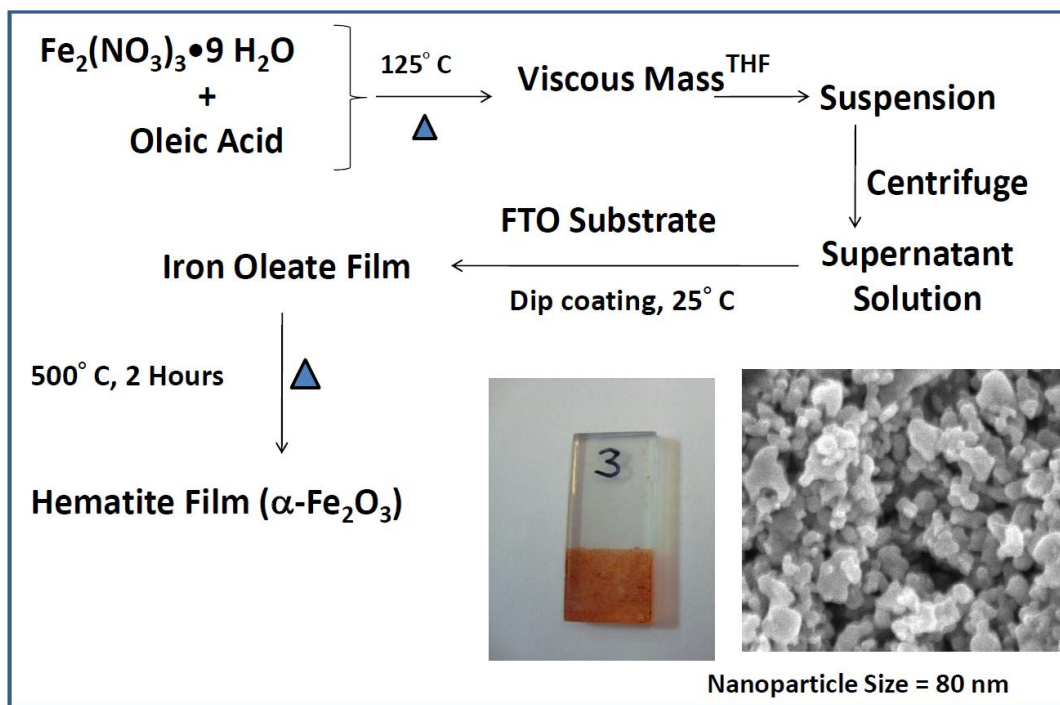
*Synthesis:* The precursor has been synthesized following an earlier protocol developed by P. Deb et. al. [16] with slight modification in the choice of fatty acid. In this case, oleic acid was used case instead of stearic acid used for the synthesis of iron oxide nanoparticle as described in chapter 3.

High purity Iron (III) nitrate [ $\text{Fe}(\text{NO}_3)_3 \cdot 9\text{H}_2\text{O}$ ] and oleic acid [ $\text{C}_{18}\text{H}_{34}\text{O}_2$ ] in the ratio of 1:2 (17 gm. of oleic acid and 28 gm. of iron (III) nitrate) were taken. By putting oleic acid into a beaker, it was initially heated upto  $70^\circ\text{C}$  and then iron nitrate was gradually added to the beaker with consistent stirring to obtain the homogeneous solution. The homogeneous solution is then heated at  $125^\circ\text{C}$  for  $2^{1/2}$  hrs. till all the  $\text{NO}_2$  gas evolve from the solution. The temperature of the reaction system was measured by a thermometer. A reddish brown mass was formed which was cooled at room temperature for 24 hrs. and then treated with 80 ml of THF (tetrahydrofuran). The resultant solution was sonicated for 10 minute to get complete homogeneity of the sample. Further, powdery ppt. from the solution is collected through centrifugation (at a speed of 5000 rpm) for a period of 2-3 minutes. The remaining supernatant solution was used for the deposition process by dip coating technique. Here, FTO substrate was dipped into the solution and hold for 2 min and allowed to dry for 15 minute at a temperature of  $70^\circ\text{C}$  on a hot plate. After drying process, the films were annealed at  $500^\circ\text{C}$  for 2 hr. For depositing different layer same procedure has been adopted (dip coating and annealing for each layer).

*Characterization:* The prepared films are the subjected to XRD characterization, FESEM and photoelectrochemical study. The dip coated films are optimized for thickness, annealing temperature and dwelling time. The thickness determination was determined with a stylus profilometer (Ambios XP-100). Optical absorption and transmittance measurement have been performed using a Varian UV-VIS spectrophotometer to evaluate the optical properties of iron oxide thin films. An FTO glass substrate was first measured to correct the reference background.

### 6. B. 3 Results and Discussion

The detail synthesis procedure for getting the dip coated hematite film is schematically illustrated in scheme 6.8. The prepared films are shown in figure 6.9.



**Scheme 6.8:** Synthesis procedure for hematite film by dip coating technique.

The oleic acid acts here as stabilizer and plays an important role in controlling the size of the particle constituting the film. The uniformity of the iron oxide nano crystal was controlled by the nucleation during the heating process. It was due to the fact that, a homogeneous nucleation was dominant when the heating rate is relatively high, and therefore the nucleation is finished within a short time interval. Here,  $\text{Fe}_3\text{O}_4$  is oxidized to  $\alpha\text{-Fe}_2\text{O}_3$  with additional trace amount of  $\gamma\text{-Fe}_2\text{O}_3$ . At temperature around  $273.20^\circ\text{C}$  grain growth of maghemite occurs. Again at temperatures around  $305.76^\circ\text{C}$  all the  $\gamma\text{-Fe}_2\text{O}_3$  changes its phase to  $\alpha\text{-Fe}_2\text{O}_3$ .

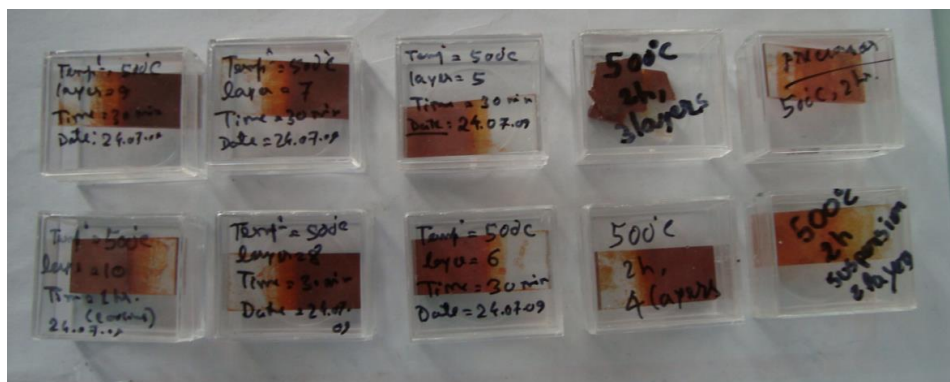


**Figure 6.9:** Hematite films obtained by repeated dip coating and annealing of FTO substrate coated with iron fatty acid precursor.

The XRD pattern obtained for hematite films prepared by dip coating technique was shown in Figure 6.10.

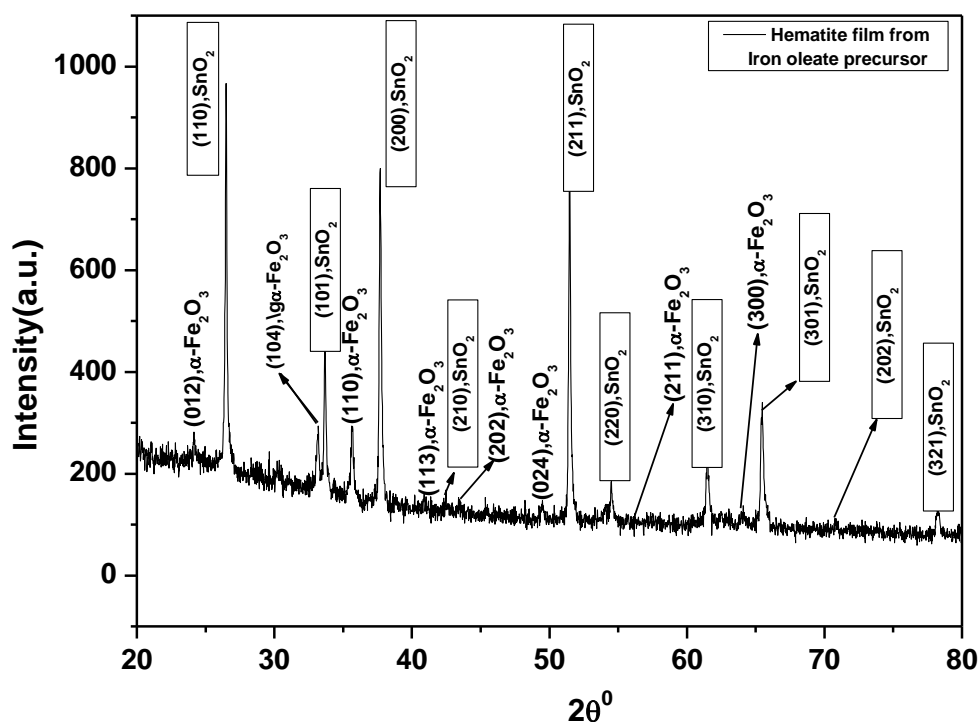


**Figure 6.10:** XRD pattern of dip coated hematite film

The XRD pattern shows mainly diffraction peaks from the dense  $\text{SnO}_2$  coating of the glass substrate ( $0.4\mu\text{m}$  cassiterite). There is only one strong peak due to hematite, namely the (110) reflection (in hexagonal coordinates), besides much weaker peaks corresponding to the (012), (104), (113), (024), and (300) planes. A similar presence of the (110) reflection has also been observed for  $\alpha\text{-Fe}_2\text{O}_3$  nanowires and nanobelts grown by thermal oxidation of iron and this indicated a strong preferential oxidation of the [110] axis vertical to the substrate. Hematite have strong anisotropic conductivity along [110] direction and it is higher within the (001) basal plane upto 4 orders of magnitude. This is due to the crystalline arrangement of hematite. Its lattice can be represented as an alteration of iron bilayers and oxygen layers parallel to the (001) basal plane. Each bilayer has  $\text{Fe}^{\text{III}}$  atoms with parallel spins in contrast to adjacent bilayers which have opposite spins. Electrons can move by hopping through  $\text{Fe}^{\text{II}}/\text{Fe}^{\text{III}}$  valence change within the iron bilayers, while electron exchange between neighboring bilayers is spin forbidden (Hund's rule). The conductivity anisotropy of hematite has been studied quantum mechanically in more detail manner [17]. The valence band hole transfer between adjacent iron double layers can proceed with a higher activation barrier than that within iron planes due to the allowing of spins through  $\text{Fe}^{\text{III}}/\text{Fe}^{\text{IV}}$  valence change. Hematite (001) plane vertically to the substrate is considered as well conducting and preferential orientation along this plane should facilitate collection of photogenerated electrons. Consequently photogenerated holes reach the

electrolyte interface by hopping laterally between (001) planes. On the other hand, Nb doped single crystal platelets of  $\alpha$ -Fe<sub>2</sub>O<sub>3</sub> show good efficiency for water oxidation with only (001) plane exposed to the electrolyte, which implies electron transport vertically to (001) [12]. Apparently in this case the conductivity of Nb-doped  $\alpha$ -Fe<sub>2</sub>O<sub>3</sub> was sufficient even in the [001] direction to allow collection of photogenerated electrons.

The morphology and thickness of hematite films as obtained by FESEM characterization were as shown in figure 6.11. As illustrated in figure 6.11, the surface of the film consists of small larvae shape nanostructures. The average diameter of the particle was 80 nm. Each nanostructure was the result of the incorporation and agglomeration of individual particles and the respective FESEM image clearly signified the same. Individual particles are fused to each other forming an interconnected 3D network with electronic connections to facilitate the photo induced charge transport. The cross sectional image of the film (figure 6.11 C.) further reveals the formation of film with the thickness of 437 nm.

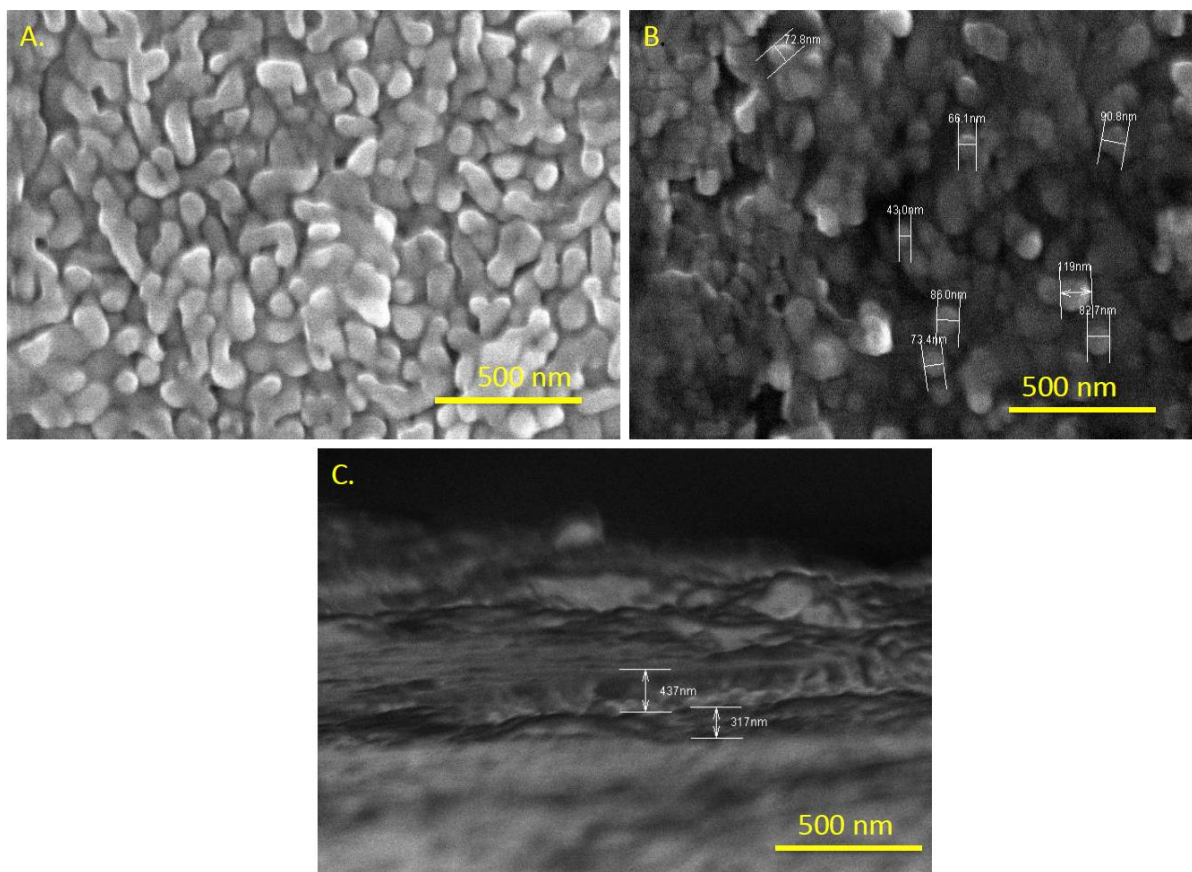


**Figure 6.11:** FESEM images of Fe<sub>2</sub>O<sub>3</sub> films grown by dip coating technique on SnO<sub>2</sub>: F coated conducting glass. A. Top view. B. Nanoparticle having different sizes on the top side of the film. C. Cross section of 437 nm thick mesoporous hematite film on 317 nm compact SnO<sub>2</sub>:F.

The photocurrent density (J) is measured against applied bias potential (V) and shown in figure 6.12. A photocurrent density of  $250 \mu\text{A} / \text{cm}^2$  was achieved at 1.23 V vs. RHE for one layer deposited dip coated hematite film, while no dark current was observed up to about 1.6 V where oxygen evolution normally begins. The photocurrent rises steeply to approximately  $0.25 \text{ mA}/\text{cm}^2$  without reaching the saturation. The significant rise in photocurrent in case of dip coated film is believed to be due to the particular morphology of the film. It can be observed that the film obtained in dip coated manner have good porous character in comparison to spin coated one. Also from the visual inspection, the films are look like more roughened in caparison to spin coated one.

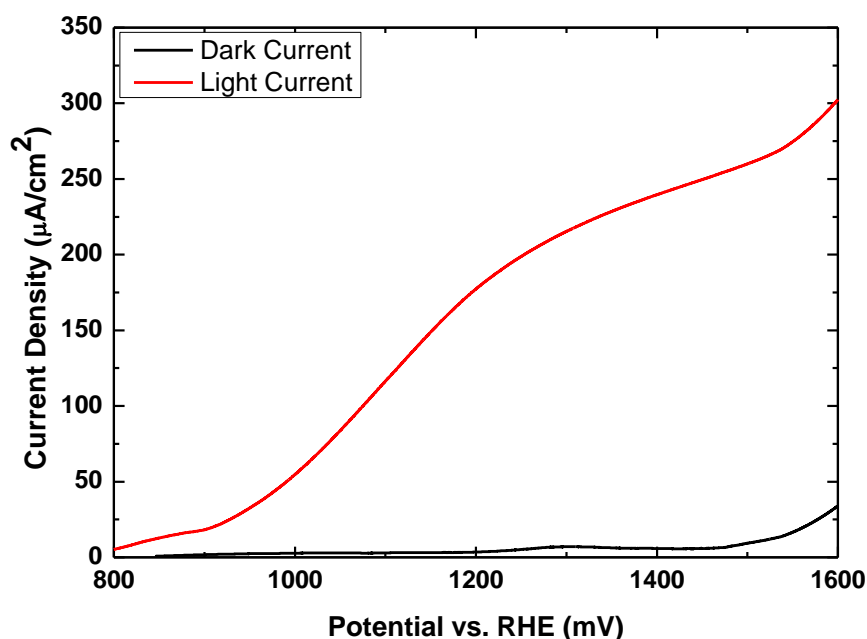


**Figure 6.12:** Current –voltage characteristics in darkness and under simulated light at a scan rate of 10 mV/s.

### 6. B. 3 (I) Optimization of layer thickness to enhance the value of photocurrent

Since the light penetration length in hematite is of the order of 100 nm ( $\alpha = 1.6 \times 10^7 \text{ m}^{-1}$  at 500 nm), most holes created in the bulk and electron will recombine with holes before having reached the surface [6]. Due to this, it was suggested that several very thin films of hematite can be stacked in order to minimize hole transfer distances and still the film can absorb most of the incident light [18]. This approach mimics the stacking of chlorophyll containing thylakoid membranes in the grana or plant chloroplasts [19].

In order to get maximum photocurrent out of Hematite film, films with different thicknesses has been prepared to study the effect of thickness on the observed photocurrent. For this, each layer has been deposited with dip coating and annealed at the desired temperature ( $500^\circ\text{C}$ ) for 2 hour. The total number of layer been studied are from one to ten having different thickness as found by the profilometry technique. For each of the layer deposition, similar protocol was

followed. On plotting the thickness vs. number of layer, it was observed that the thickness increased linearly with the number of deposited layer by dip coating technique as shown in figure 6.13.

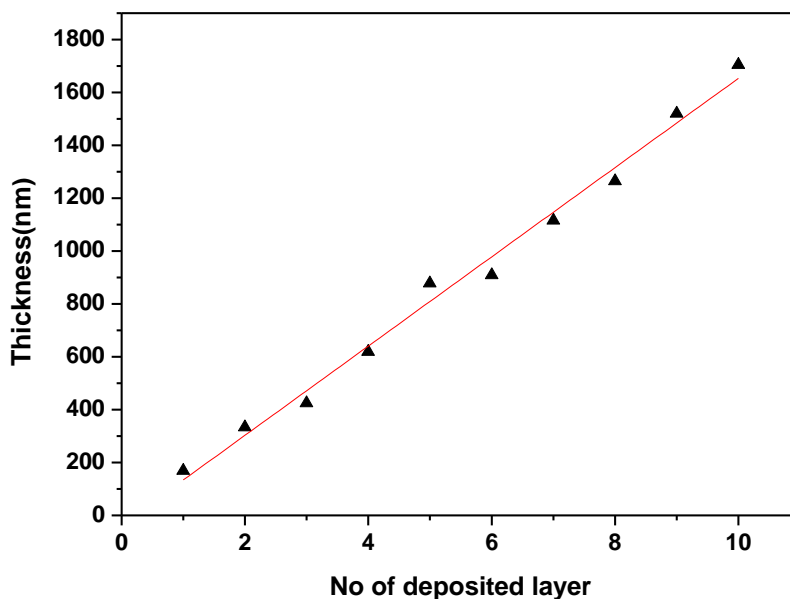


**Figure 6.13:** Variation of film thickness with different deposited layer.

The optical properties of hematite film with different layer thicknesses are studied by UV-Vis transmittance spectroscopy. The results obtained are shown in figure 6.14.

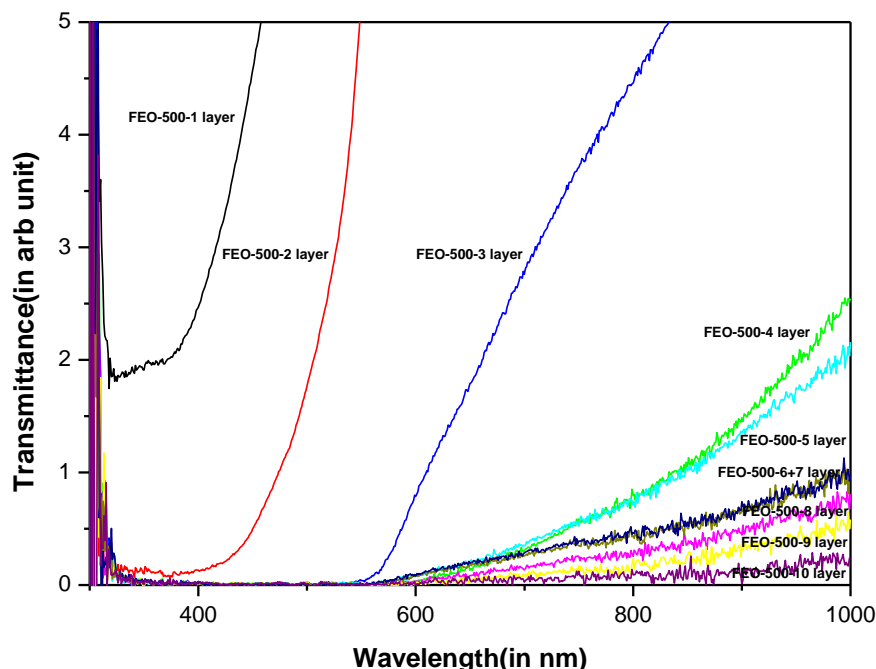


**Figure 6.14:** Transmittance spectrum of  $\alpha\text{-Fe}_2\text{O}_3$  film having different layer thickness deposited from precursor by dip coating technique.

It is observed that with the increasing layer thickness the transmittance decreased in the visible region (400-600 nm) which clearly signified the visible light absorption by the hematite film. All the films with different layer thickness absorb in the visible region.

From the X-Ray diffraction study as shown in figure 6.15, it is observed that with the increase in layer thickness, (104) diffracted peak intensity from hematite increases with the decrease in substrate peak. This further confirms the increase in the thickness of film with consequent layer deposition. It is noted that the intensity of (110) diffracted peak remain constant.

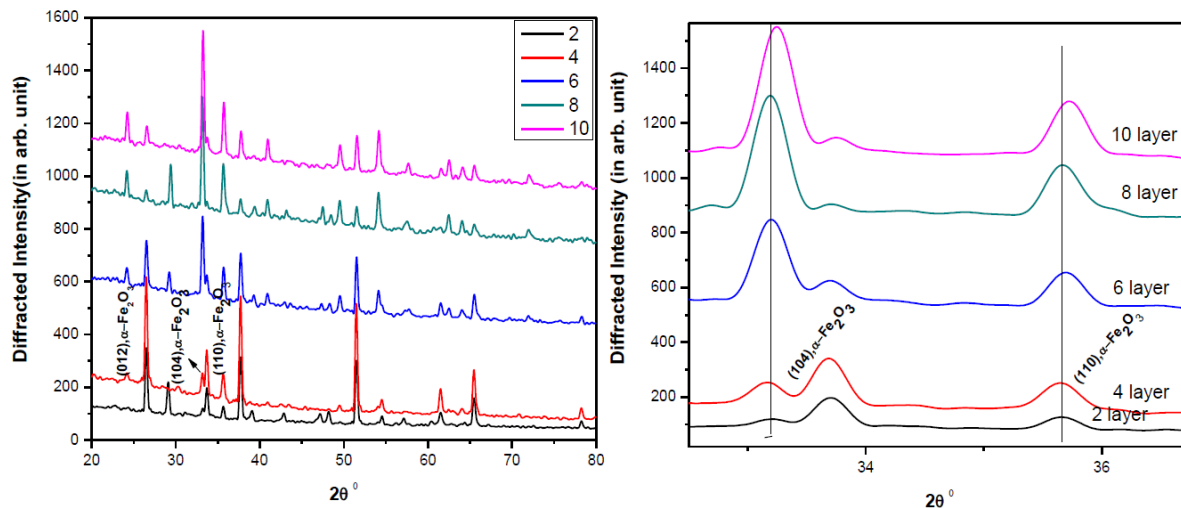


**Figure 6.15:** Corresponding XRD profile of hematite films having different layer thicknesses.

The morphology of the film having different layer thickness is studied with scanning electron microscopy. From the corresponding SEM images [Figure 6.16], it is evident that with the increase in the number of layer the hematite film shows less porosity. Only the 4 layer deposited film have good porosity along with larvae shape nanoparticle.

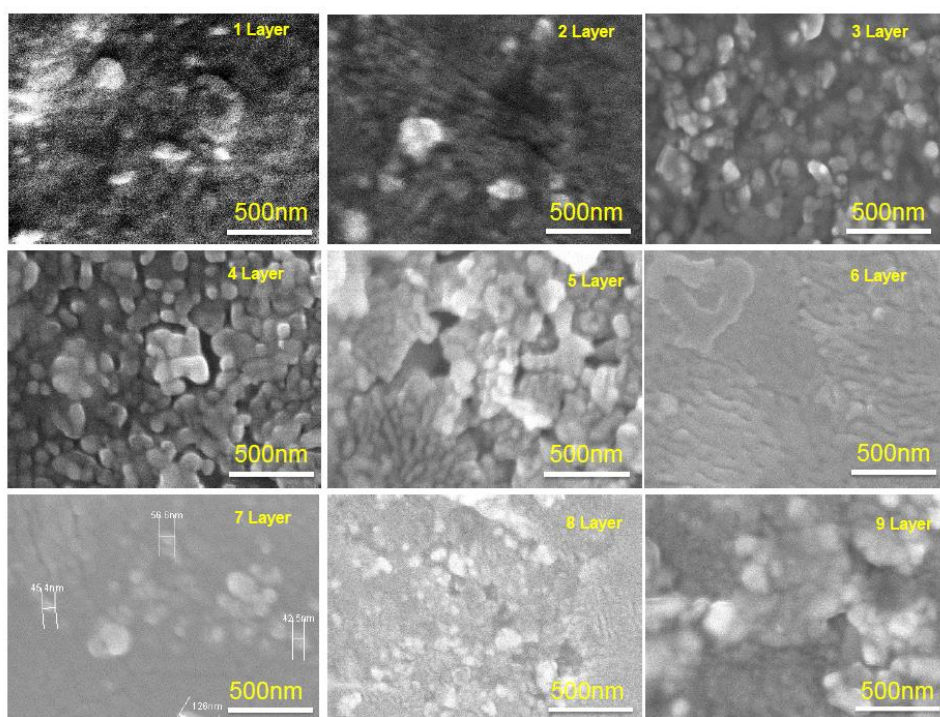


**Figure 6.16:** Morphology of hematite films having different number of layer deposition.

The photoelectrochemical properties have been studied by measuring the photocurrent –voltage curve with the same condition as stated above. The obtained photocurrent curve for different layer was shown in figure 6.17 and it is found that the photocurrent first increases up to a certain point (4 layer gives the maximum photocurrent  $434 \mu\text{A}/\text{cm}^2$ ) and then decreasing towards the low value with the consequent increase in film thickness. This might be due to the increase contribution of bulk effect in comparison to surface counterpart which normally plays an important role in the hole diffusion kinetic process at the semiconductor-electrolyte interface.

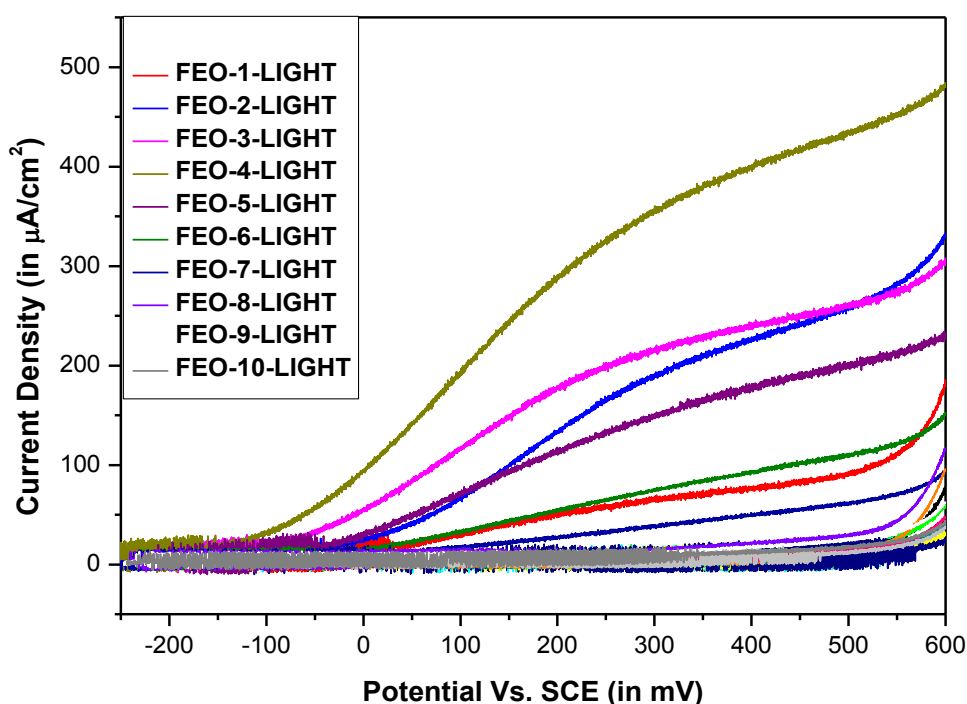


**Figure 6.17:** Current –voltage characteristics in darkness and under stimulated light at a scan rate of 10 mV/s for hematite films having different layer thickness.

### 6. B. 3 (II) Optimization of annealing temperature to enhance the value of photocurrent

To get an idea about the effect of heat treatment temperature on the photocurrent, hematite films have been deposited with different temperature from  $350^\circ\text{C}$  to  $600^\circ\text{C}$  with 4 layer deposition. The X- Ray diffraction pattern of the films deposited at different heat treatment temperature is shown in figure 6.18. From the XRD pattern, it is observed that the (104) and (110) diffracted peak intensity started to evolve with the increase in the heat treatment temperature. Another interesting observation is that both the peak in case of  $600^\circ\text{C}$  shifted to lower Bragg angle. The substrate peak decrease in consistent fashion implying that the nanoparticle constituting the film take a preferential growth along (104) direction.

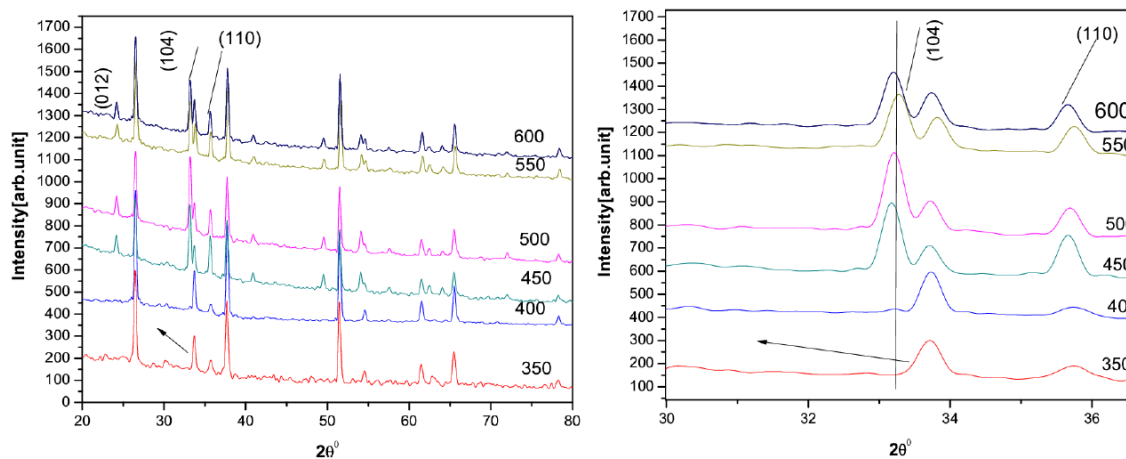


Figure 6.18: XRD pattern of hematite film heat treated at different temperature.

The morphology of the heat treated samples (A-F) is studied with scanning electron microscopy and is shown in figure 6.19. The shape of the particle constituting the film changes from spherical to larvae like and size also increases with the increase in heat treatment temperature.

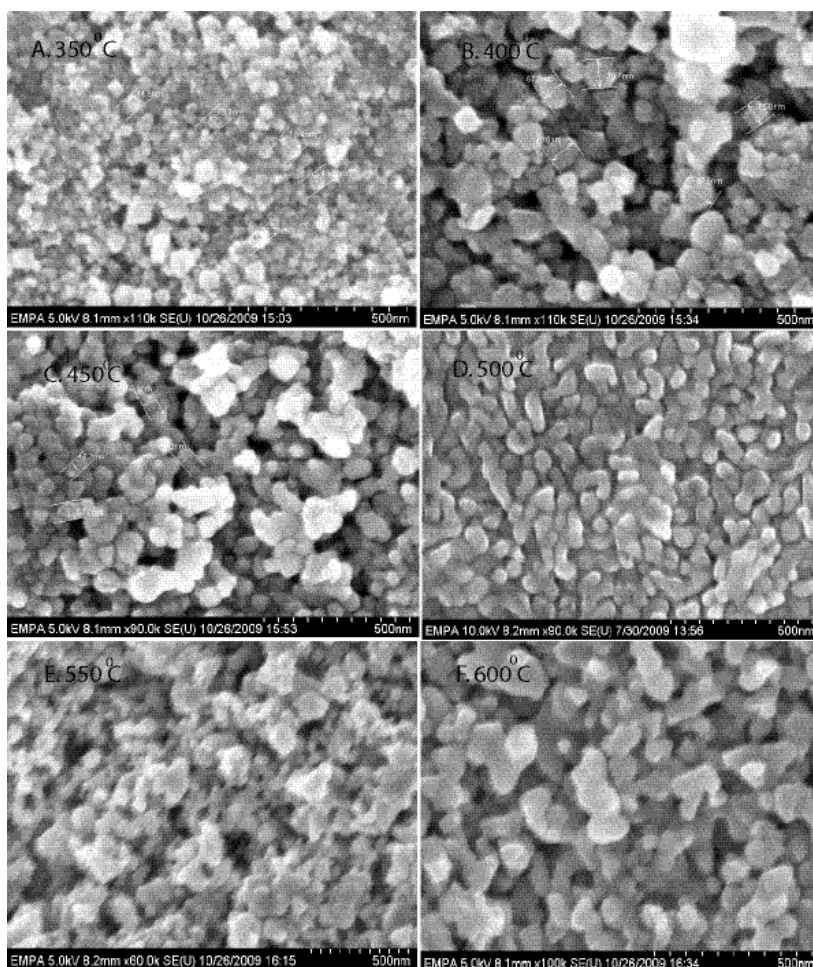
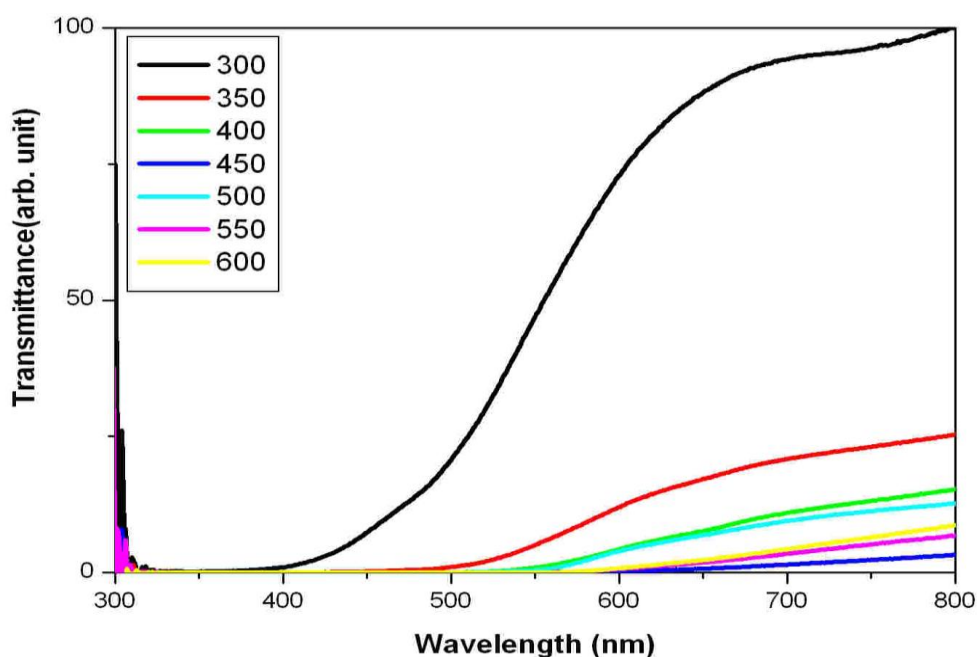


Figure 6.19: Morphology of Hematite Film Studied by FESEM Characterization

It is to be noted that the film heat treated at 400°C, 450°C and 550°C have porous character. While films prepared at 500°C and 600°C have less porosity but somehow 500°C treated samples provided best photocurrent efficiency as discussed in the following section.

The optical properties of the heat treated film are studied with UV-Vis spectroscopy. Figure 6.20 represents the UV-Vis transmittance spectrum of hematite thin films heat treated at different temperatures. From the results obtained, it is observed that the sample heat treated at 350°C started to absorb at 500 nm, while only two samples heat treated at 400°C and 500°C absorb at the absorption edge of hematite (550nm). Interestingly the 450°C treated sample show less transparency in comparison to 300 to 500°C treated samples. This abrupt change might be due to the non-uniform layer thickness even on depositing the same number of hematite layer on FTO substrate. The 550°C and 600 °C heat treated samples also showed less transparency.



**Figure 6.20:** UV-Vis Transmittance spectrum of hematite films deposited at different heat treatment temperature.

From the photoelectrochemical investigation, it is observed that the 500°C treated samples show the maximum photocurrent density with respect to other heat treated samples. The low temperature treated samples shows less photocurrent efficiency due to the existence of surface states and the electrons are trapped mainly by these surface states [21]. The decrease in

photocurrent is caused by the higher charge transfer resistance resulting from the difficulty in transferring the trapped electrons to the oxidized species with respect to the conduction band electron in hematite. The variation of photocurrent with annealing temperature could also be due to the decreased in the internal surface area of the electrode. These factors can lead to a decrease in the grain boundary, as a result of which new surface states appear on the surface of nanoparticles and the density of surface states larger again in low temperature treated samples in comparison to hematite electrodes annealed at 450°C and 500°C.

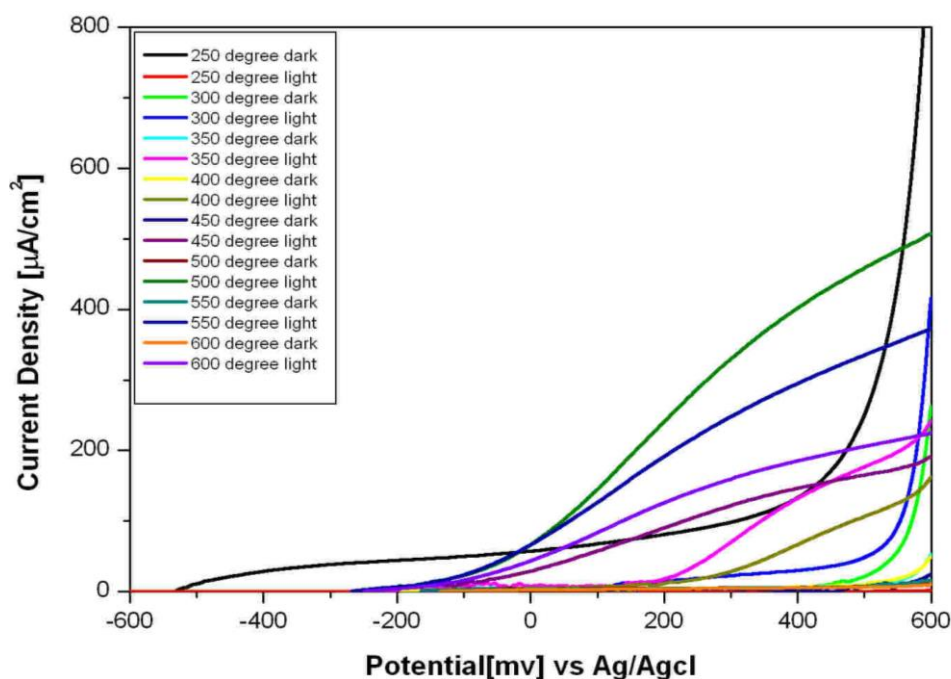


**Figure 6.21:** Photocurrent density of hematite film at different heat treatment temperature under AM 1.5 illuminated light

### 6. B. 3 (III) Optimization of dwelling time to enhance the value of photocurrent

To see the effect of heat treatment time or dwelling time on the photocurrent density, hematite films have been prepared by depositing 4 numbers of layers at 500°C by keeping the each layer at different dwelling time from 30 min to 240 min inside the furnace. After this the structural properties of the films are studied with X- ray diffraction. From the XRD pattern as shown in figure 6.22 all the corresponding diffraction peaks of hematite can be seen. The magnitude of diffracted peak intensity (104) in all the films dwelled for different time changes in normal manner only with the exception of 120 min, 150 min and 240 min. In this case the substrate peak intensity decrease and (104) increase. This non uniform variation in the diffracted peak intensities might be due to the competition of nanocrystallite growth along crystallographically preferred direction for different dwelling period.

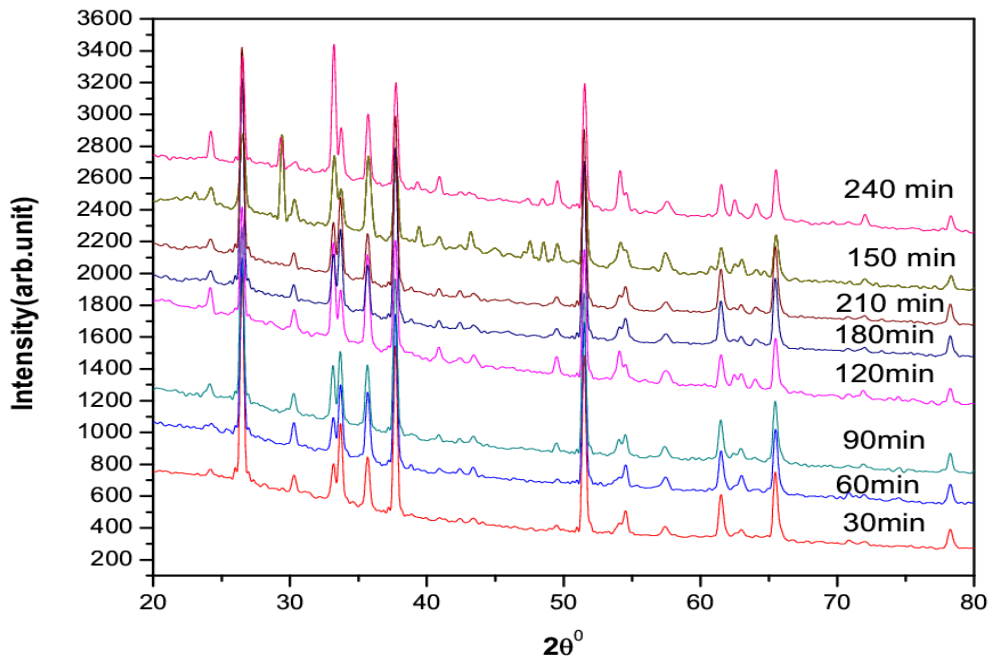


**Figure 6.22:** XRD pattern of hematite film dwelled at different time during the deposition

The morphology of hematite films prepared at different dwelling time is shown in figure 6.23. From the respective SEM images, the sample dwells for 90 min shows good porosity and nanoparticles are spherical in shape. The shape of the nanoparticles varies in different manner from 30 min to 240 min dwelled samples.

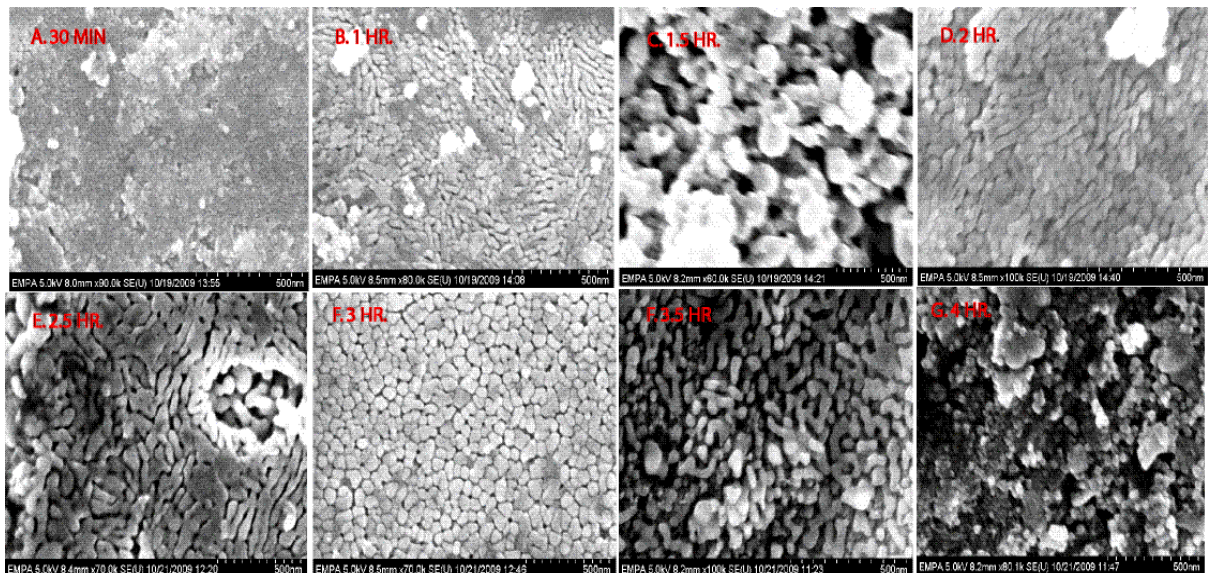


**Figure 6.23:** FESEM investigation of morphology of hematite film with respect to dwelling time.

From the optical property study [figure 6.24], it is observed that all the samples absorb at 550 nm which is the absorption edge of hematite. That is all the samples are photoactive and the

variation in optical property was due to the non-uniform film thicknesses. It is worth to mention that although same layer of film was deposited for all the cases, but due to the non-uniform growth of the crystallite for each deposition the thickness of the finally coated layer changes in inconsistent fashion. Due to this reason, the optical transparency of the hematite films dwelled for different time might be changes in abrupt manner.

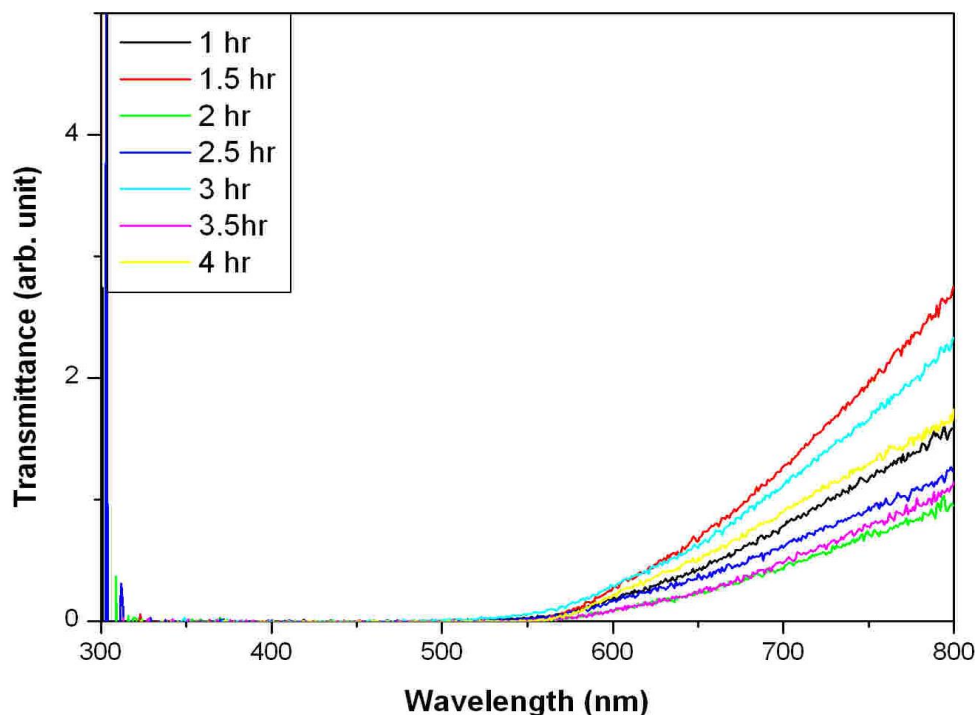


**Figure 6.24:** UV-Vis transmittance spectra of hematite films obtained for different dwelling time.

The photoelectrochemical properties of hematite films are studied to see the effect of dwelling time on the photocurrent density of the film. Figure 6.25 shows the variation in the photocurrent density of hematite films prepared for different dwelling times. From the results obtained, it is found that sample dwelled at 1.5 hour shows the maximum photocurrent. When the effect of dwelling time is considered, it is found that there is an optimum length of time for the best photocurrent density. This is normally attributed to the incomplete diffusion and smaller grains [20]. Also the periodic variation of photocurrent with increase sintering time might be due to the formation of recombination center by the grain boundaries with surface states. The barrier will form a depleted layer in hematite and block the transition of majority carriers, i.e. electrons in this case. Furthermore the grain boundary also reduces the conductivity. With these entire factors, the photocurrent densities for specimens with smaller grains are smaller. This explains why the samples sintered for only 2 hour gave a lower current density than the others. As the dwelling time increased, grains continued to grow and the

photocurrent density also increased. However, prolong sintering would also lead to the formation of additional growth centers and inhibit photocurrent density.

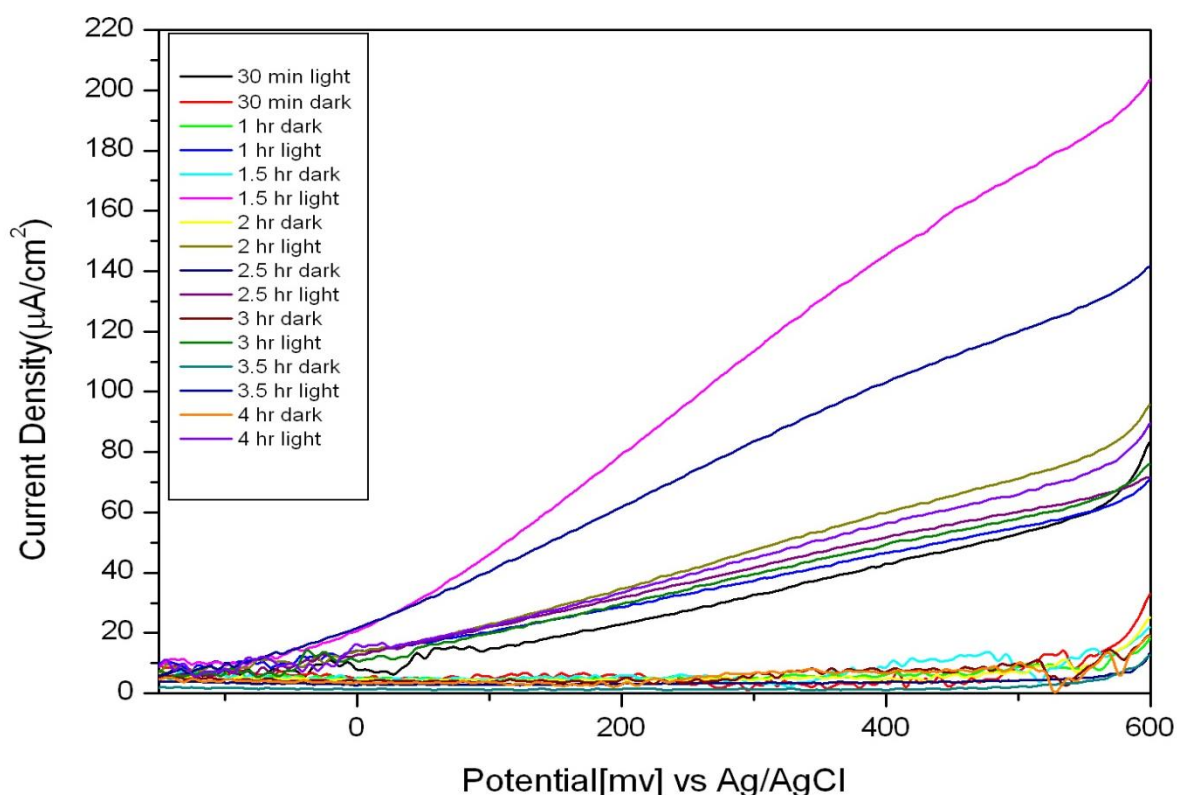


**Figure 6.25:** Photocurrent density of hematite film dwelled at different time.

#### 6.4 Conclusion

Nanocrystalline hematite thin films are fabricated with the help of spin coating and dip coating method. The spin coated samples did not show any significant photocurrent due to the very compact nature of the film. On the other hand, the dip coated film prepared by the deposition of iron oleate precursor on FTO showed promising photocurrent density of around  $250 \mu\text{A} / \text{cm}^2$  for one layer. The photocurrent density follows the well-established trend of benchmark electrode developed by Cesar et. al [6]. Further on optimizing the photocurrent density for different layer thickness, heat treatment temperature and dwelling time; it is found that the hematite film having thickness of 650 nm with 4 layer deposition showed maximum photocurrent density. Similarly samples prepared at  $500^\circ\text{C}$  for 2 hour dwelling time showed maximum photocurrent density. The prepared hematite films were reddish brown in color but with increasing the layer coating the color completely changed to brown after annealing process. SEM analysis showed that the dip coated films have mesoporous structure, very good homogeneities and nanometric scale grain size. From the optical property study it was found

that the film absorbs the visible light which makes it advantageous for utilizing in water splitting chemistry for hydrogen production.

### References

- [1] Sivula, K.; Formal, F. L.; Gratzel, M. *ChemSusChem* **2011**, *4*, 432-449.
- [2] Hardee, K. L.; Bard, A. J. *J. Electrochem. Soc.* **1976**, *123*, 1024-1026.
- [3] Redon, A.M.; Vigneron, J.; Heindl, R.; Sella, C.; Martin, C.; Dalbera, J.P. *Sol. Cells* **1981**, *3*, 179.
- [4] Curran, J.S.; Gissler, W. *J. Electrochem. Soc.* **1979**, *126*, 56.
- [5] Duret, A.; Gratzel, M. *J. Phys. Chem. B* **2005**, *109*, 17184–17191.
- [6] Cesar, I.; Kay, A.; Gonzalez Martinez, J.A.; Gratzel, M. *J. Am. Chem. Soc.* **2006**, *128*, 4582–4583.
- [7] Kay, A.; Cesar, I.; Gratzel, M. *J. Am. Chem. Soc.* **2006**, *128*, 15714–15721.
- [8] Glasscock, J. A.; Barnes, P.R.F.; Plumb, I.C.; Savvides, N. *J. Phys. Chem. C* **2007**, *111*, 16477–16488.
- [9] Miyake, H.; Kozuka, H. *J. Phys. Chem. B* **2005**, *109*, 17951–17956.
- [10] Prakasam, H.E.; Varghese, O. K.; Paulose, M.; Mor, G.K.; Grimes, C.A. *Nanotechnology* **2006**, *17*, 4285–4291.
- [11] Quinn, R.K.; Nasby, R.D.; Baughman, R.J. *Mater. Res. Bull.* **1976**, *11*, 1011–1017.
- [12] Sanchez, C.; Sieber, K.D.; Somorjai, G.A. *J. Electroanal. Chem.* **1988**, *252*, 269–290.
- [13] Lee, E.J.H.; Pontes, F.M.; Leite, E.R.; Longo, E.; Varela, J.A.; Araujo, E.B.; Eiras, J.A. *J. Mater. Sci. Lett.* **2000**, *19*, 1457–1459.
- [14] Souza, F. L.; Lopes, K. P.; Nascente, P. A.P.; Leite, E. R. *Sol. Energ. Mat. Sol. C* **2009**, *93*, 362–368.
- [15] Lensbouer, J. J.; Doyle, R. P. *Crit. Rev. Biochem. Mol.* **2010**, *45*, 453-462.
- [16] Deb, P.; Basumallick, A.; Sen, D.; Mazumder, S.; Nath, B. K.; Das, D. *Phil. Mag. Letters.* **2006**, *86*, 491.
- [17] Iordanova, N.; Dupuis, M.; Rosso, K. M. *J. Chem. Phys.* **2005**, *122*, 144305 d.
- [18] Itoh, K.; Bockris, J. O. *J. Appl. Phys.* **1984**, *56*, 874-876.
- [19] Kay, A.; Gratzel, M. *J. Phys. Chem.* **1993**, *97*, 6272-6277.
- [20] Zhao, D.; Peng, T.; Lu, L.; Cai, P.; Jiang, P.; Bian, Z. *J. Phys. Chem. C* **2008**, *112*, 8486-8494.

## Chapter 7

### **Synthesis of nanostructured hematite film doped with Silicon for enhanced photocurrent efficiency**

#### **7.1 Introduction**

Iron oxide ( $\alpha$ -Fe<sub>2</sub>O<sub>3</sub>, or hematite) is an attractive photoanode due to its abundance, stability, and environmental compatibility, as well as suitable band gap and valence band edge position. The efficiency of pure hematite electrode is relatively very low due to the low rate constant for water oxidation by surface trapped holes [1] and short hole diffusion length (2 - 4nm) [2]. Due to this, holes created close to the electrolyte interface oxidize water. To get rid of the very low photocurrent efficiency of hematite film obtained by dip coating of iron oleate precursor, silicon doping is considered as an alternative strategy. Based on this, several groups used the doping strategy to improve the photocurrent of bare hematite. Kennedy et. al. for the first time showed the photocurrent improvement of hematite electrode doped with silicon [3]. They fabricated the silicon doped electrode by mixing with reagent grade SiO<sub>2</sub> powder, processing and sintering. Sanchez et.al. [4] fabricated the Si doped hematite electrode by mechanical mixing of solid solution of SiO<sub>2</sub>. Recently, thin film of silicon doped hematite was deposited by APCVD method. This showed higher efficiency of 42% at 370 nm and 2.2 mA/cm<sup>2</sup> in A.M 1.5 G sunlight [5]. This remarkable efficiency was attributed to dendritic nanostructure which minimizes the distance the photogenerated holes have to diffuse to reach the hematite / electrolyte interface. These observed feature sizes are found to depend strongly on the temperature and the presence of silicon dopant precursor [6]. Effect of silicon doping on the photoelectrochemical performance of hematite has been studied in detail manner and it was found that incorporation of silicon led to disorder in hematite structure [7]. Besides the APCVD method, other synthetic methods such as ultrasonic spray pyrolysis [8, 9], reactive magnetron sputtering [10], spin coating [11] etc. are utilized. The dip coating process can also be used beside this strategy for making silicon doped hematite thin film.

During the current study, the main goal is to obtain a silicon doped hematite film in a very cheap and consistent manner in order to get enhanced photocurrent efficiency. For validating it, a novel precursor material has been prepared and films have been deposited on FTO substrate by dip coating approach.

## 7.2 Materials and methods

*Synthesis of Si-Hematite thin films by two different approaches:*

*The first approach* involves the dip coating of a Si wafer in iron oleate precursor complex used for the synthesis of hematite film. The dip coated Si wafer was the heat treated at 500°C for 2 hour and followed by room temperature cooling.

*The second approach* consists of modification of the iron fatty acid precursor complex with TEOS (Tetra ethyl ortho silicate). The precursor complex was synthesized by heating a mixture of Fe (NO<sub>3</sub>)<sub>3</sub> · 9H<sub>2</sub>O (28.0 g), oleic acid (17.0 g) and TEOS (differ in atomic % with respect to salt amount) to 70°C to give a homogenous liquid phase. For example, in case of 3.7% and 1.5% doping, 1.00 gm. and 0.42 gm. of TEOS has been used. Before putting the salt into the oleic acid matrix, desired amount of TEOS was added. This homogeneous mixture was then heated at 125°C for 90 minutes to give a reddish brown viscous mass which was then cooled to room temperature, left for 24 hr. and subsequently treated with 80 ml of tetrahydrofuran (THF). The resultant solution was stirred with a glass rod for 30minutes and the powdery precipitate separated from the solution by centrifugation (5000 rpm) for 2-3 min. After centrifugation, the supernatant (precursor complex) was recovered for the dip coating of the film. FTO was used as a substrate. The dip coating process involves many different parameters and is tabulated as shown in Table 7. 1.

**Table 7.1:** Si-Hematite film deposition parameter.

Doping Wt.%	Temperature	Layer	TEOS interfacial layer
0.5%	500 <sup>0</sup> C	5	SiO <sub>2</sub> (500 <sup>0</sup> C)
	900 <sup>0</sup> C	3	SiO <sub>2</sub> (900 <sup>0</sup> C)
1%	do	do	do
1.5%	do	do	do
3.7%	do	do	do

The detail process of precursor synthesis and film deposition has been illustrated in Scheme 7.4. The process starts with the deposition of 1 layer of precursor (each precursor have definite doping % of Si, as stated in table 7.1) on FTO substrate and then annealed at 500<sup>0</sup>C for 30 min. The number of deposited layer is increased following the same protocol to get a desired thickness. Each of the layers has been deposited with a pre-deposited interfacial layer of TEOS

[scheme 7.5]. The TEOS containing hematite layer was dried at  $70^{\circ}\text{C}$  for 2 minute. After high heat treatment at  $500^{\circ}\text{C}$ , TEOS gets converted to  $\text{SiO}_2$ . In the next step, the film was deposited at different annealing temperature,  $900^{\circ}\text{C}$  for 2 minute following the same protocol.

In another series of synthesis, 2 layer of hematite was deposited with TEOS as interfacial layer. Hereby second layer with TEOS annealed for 30 min at  $500^{\circ}\text{C}$ . This was further annealed from  $500^{\circ}\text{C}$  to  $760^{\circ}\text{C}$  in non-isothermal manner for 30 min as shown in scheme 7.6. Similarly, same protocol was repeated with applied temperature of  $850^{\circ}\text{C}$ .

#### *Characterization:*

The phase composition of the pristine and modified films was examined by powder X-ray diffraction analysis (PAN analytical X'Pert PRO,  $\text{Cu K}\alpha$  radiation). . Field emission scanning electron microscopy was performed on a Hitachi S-4800 model. The dark current and photo current was recorded with a Voltalab® potentiostat in a three electrode configuration with 1M KOH (pH=13.6) as electrolyte, Ag/AgCl/sat. KCl as reference and a platinum wire as counter electrode. The  $\text{Fe}_2\text{O}_3$  film was illuminated on a  $0.45\text{ cm}^2$  area of electrolyte and a fused silica window with a  $0.5\text{ cm}^2$  circular mask, the total geometric area immersed in electrolyte was approximately  $2.6\text{ cm}^2$ . Sunlight was simulated with a filtered xenon lamp from LOT Oriel®. The light intensity was adjusted to AM 1.5 simulated light. X-ray photoelectron spectra were recorded by a PHI LS5600 spectrometer equipped with Mg  $\text{K}\alpha$  X-ray source, spectra calibrated using  $\text{C1s} = 285\text{ eV}$ .

### **7.3 Results and discussion**

The dip coating of silicon wafer in iron oleate precursor complex results in a very rough film and it does not stick to the substrate in gentle manner like as that of pristine hematite film deposited on FTO substrate. Here silicon wafer was used for doping silicon in the hematite lattice by the high temperature mediated diffusive action. This is believed to be take place by the inter diffusion of silicon due to high heat treatment. The morphology of the film deposited on silicon wafer has been studied with FESEM. From the SEM image as shown in figure 7.2, it has been observed that the film deposited on the silicon wafer have nano grains with good porosity. The main disadvantage of the technique is that the film deposited is very thin which prevent it to absorb sufficient amount of light need to get reasonable photocurrent.

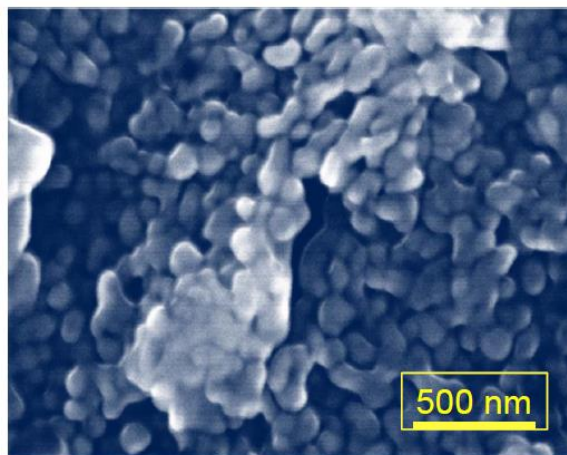


**Figure 7.2:** SEM image of Si/ $\alpha$ -Fe<sub>2</sub>O<sub>3</sub> film prepared by dip coating of silicon wafer in iron fatty acid precursor.

The photoelectrochemical activity has been studied by placing the film in a 3 electrode cell called as “cappuccino cell” having Ag/AgCl reference electrode and counter electrode. From the current vs. potential curve, a small difference between dark and photocurrent has been seen and a photocurrent of around 30  $\mu\text{A} / \text{cm}^2$  is obtained for one layer deposited hematite film on silicon wafer. To get more insight into the photoresponse action of the electrode, chopped photocurrent has also studied. This validated the photoactivity of the film. Since the photoactivity of the film is quite low in this synthesis route, another route has been adopted in order to get enhanced photocurrent.

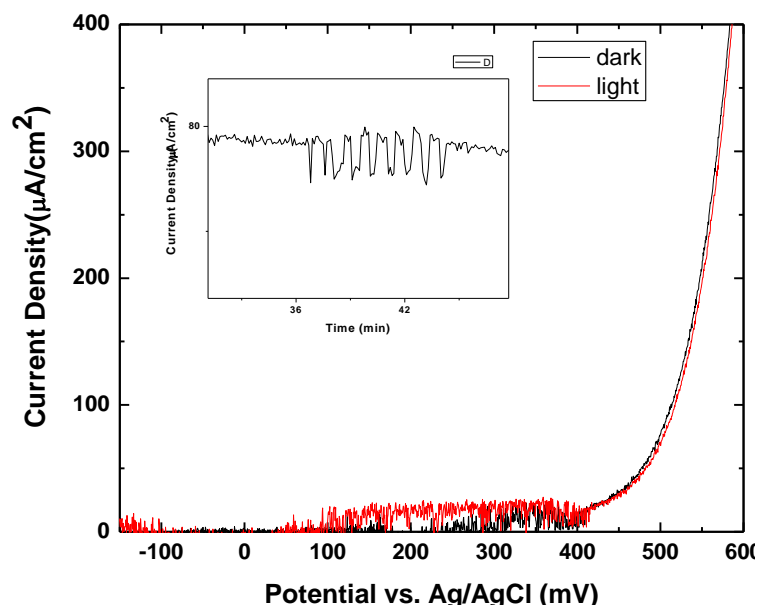
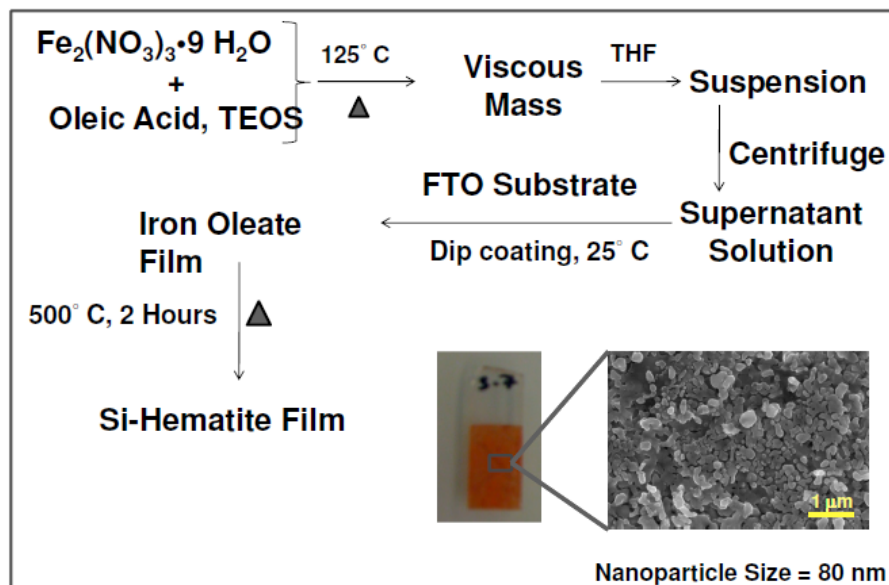


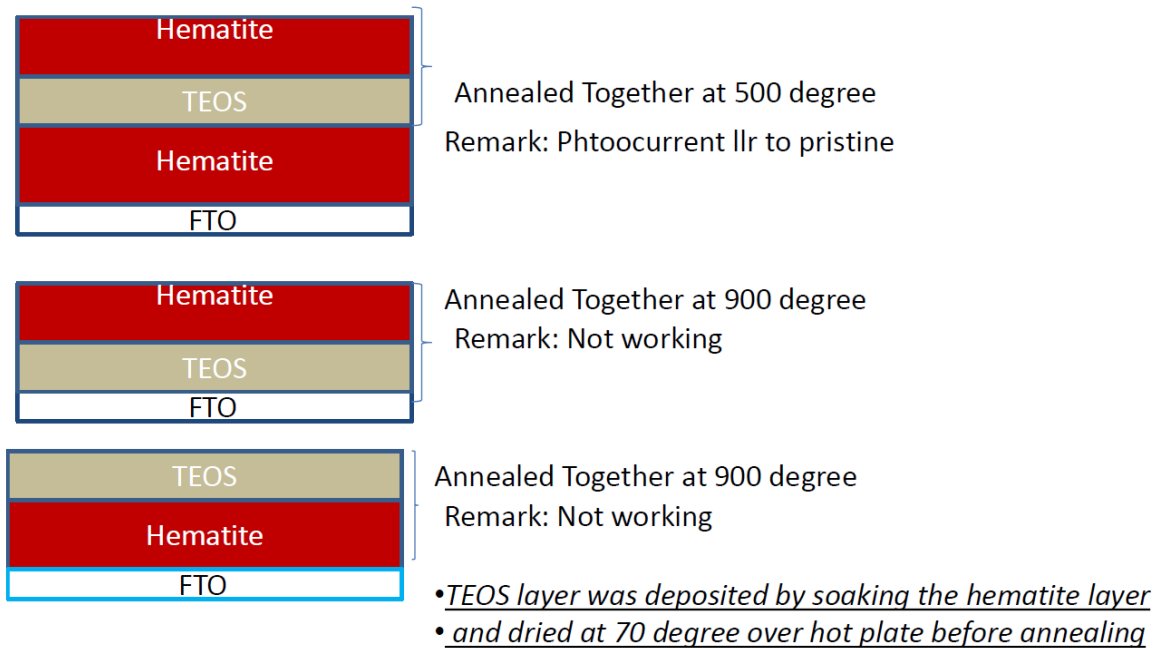
**Figure 7.3:** Photocurrent and dark current of a one-layer film obtained by dip coating. The inset shows the chopped light response of electrode.

The other synthetic route is as shown in scheme 7.4. It involved the film deposition with TEOS modified iron oleate complex.



**Scheme 7.4:** Synthesis scheme for Si doping of hematite film.

The samples are look like as shown in scheme 7.4 and from morphology study, the size of the nanoparticle constituting the film is found to be around 80 nm. In this case, the films are deposited at different heat treatment condition ( $500^\circ\text{C}$  and  $900^\circ\text{C}$ ) with alternative deposition of TEOS between pre deposited hematite layers and between hematite and FTO as depicted in scheme 7.5. The idea of applying high heat treatment was to do intentional doping of Si from the TEOS interfacial layer into hematite which helps in getting the enhanced photocurrent. In the case of Si- hematite film deposited at  $500^\circ\text{C}$ , it is found to be photoactive. On the other hand,  $900^\circ\text{C}$  treated sample does not show any photoactivity. It is believed that at  $900^\circ\text{C}$  the size of the crystallite become larger and the film become granular which made it reflective based on visual inspection. Since most the light get reflected back, it seems to be less photoactive and also formation of lots of defect across grain boundary create recombination center which will finally decrease the efficiency.

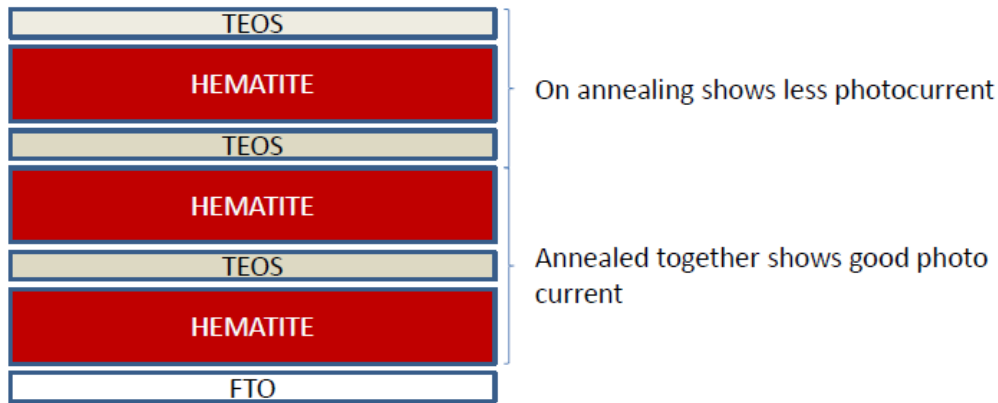


**Scheme 7.5:** Film deposition protocol with TEOS as interfacial layer

In another study, 0.5% doped Si- Hematite film has been fabricated by applying different heat treatment condition as shown in scheme 7.6. Here, temperature was applied in a non-isothermal manner. That is the heat treatment temperature is increased from 500 °C up to 760 °C and the sample is dwell during this temperature gradient for 30 min. Another important observation is that when the number of TEOS layer on the top of hematite increase by the heat treatment, the photocurrent decrease in drastic manner. When a TEOS layer is deposited on the top of 2 hematite layer, photocurrent drastically decreases. The reason behind it is not clear yet. The experiment has been repeated also without an interfacial layer. Similar strategy has been adopted for different heat treatment condition at 850°C but the sample is less photoactive in comparison to sample synthesized in non-isothermal manner.

**Synthesis strategy:**

1. **500 – 760 degree** :First layer deposited at 500 degree for 30 min  
Second layer and TEOS layer were annealed first at 500 degree and then non isothermally heated upto 760 degree for 30 min
2. **850 degree**. same



**Scheme 7.6:** Film deposition protocol at different annealing temperature.

The X-Ray diffractogram of the samples (pristine hematite, film prepared at 760<sup>0</sup>C without interfacial layer, with interfacial layer, film synthesized at 850<sup>0</sup>C without interfacial layer, and with interfacial layer) as shown figure 7.7 represent the main diffraction peaks (101) from the substrate (FTO). For simplicity, I just focused on the diffraction peaks of hematite (104) and (110) in hexagonal coordinates. It is to be noted that all other peak in case of all silicon doped hematite sample closely matched with that of pristine hematite lead us to conclude that film deposited have only hematite phases. From the expanded view of the (104) and (110) peak of hematite in Si-hematite films, it is observed that the (104) diffracted peak intensity is higher in case of sample prepared at 760<sup>0</sup>C with TEOS with respect to other sample. Also the substrate peak and (110) peak due to hematite remain in the same magnitude. This significant change in the magnitude of (104) peak intensity might be due to the influence of TEOS as interfacial layer in case of 760<sup>0</sup>C heat treated sample.

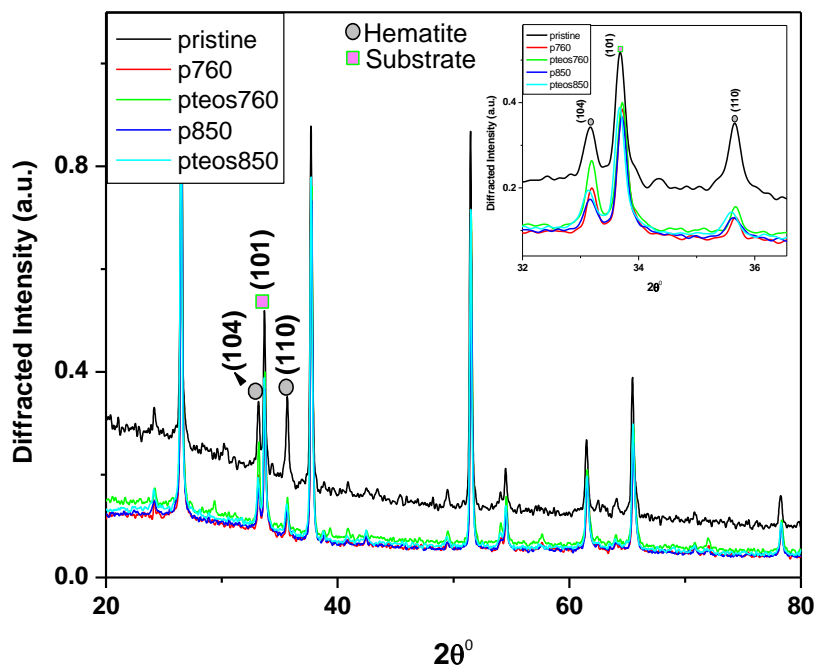


**Figure 7.7:** X- Ray diffraction pattern of Si-hematite film (0.5%) synthesized at different annealing temperature and TEOS as interfacial layer

The Photocurrent – voltage curve of the samples with and without TEOS layer are shown in figure 7.8. From this study, it is observed that the photocurrent density of 0.5% Si- Hematite layer without TEOS layer is slightly higher in comparison to sample with interfacial layer. Although the photocurrent obtained at onset potential is higher for sample with interfacial layer. The reason behind this dramatic change is difficult to make during the current investigation.

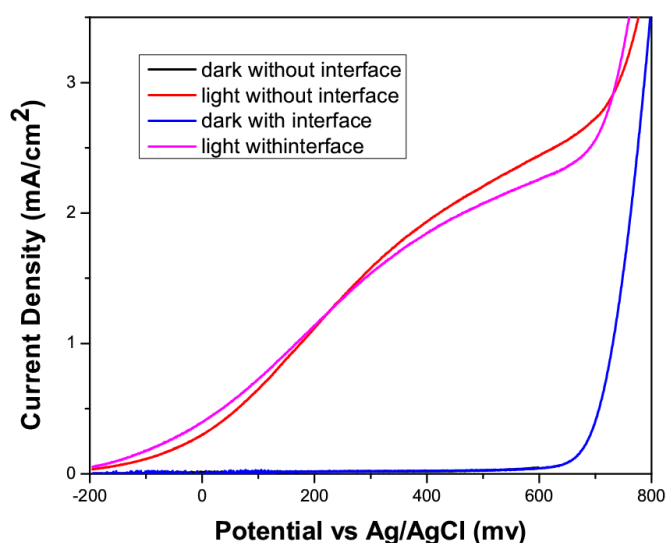


**Figure 7.8:** Photocurrent vs. voltage curves of Si- Hematite film (0.5%) with TEOS as interfacial layer.

In the next part, the photocurrent density of 0.5% Si-hematite film with 2 layer are measured and it is found that the presence of SiO<sub>2</sub> interfacial layer (formed as a result of the thermal decomposition of TEOS at high heat treatment temperature, 500 - 760<sup>0</sup>C) does not have any effect on photocurrent density (2.5 mA/ cm<sup>2</sup>) as shown in figure 7.9 (A) and (B). But in case of 850<sup>0</sup>C treated sample, I have seen differences in photocurrent density with and without SiO<sub>2</sub> interfacial layer. In case of sample without any SiO<sub>2</sub> layer, the photocurrent seems to be high. The SiO<sub>2</sub> layers are generally used in metal-insulator-semiconductor devices such as MIS solar cells [12]. In this type of junctions, electron tunneling from hematite thin film occurs through the insulating SiO<sub>2</sub> layer. The advantage of putting a thin insulating layer could be due to an improved energy level alignment at the interface. Another important point is that, the SiO<sub>2</sub> layer may also affect the nucleation of hematite on the substrate [5]. The increase in photocurrent at higher sintering temperature for Si- Hematite film without having interfacial layer may be due to diffusion doing of Si into hematite lattice [13].

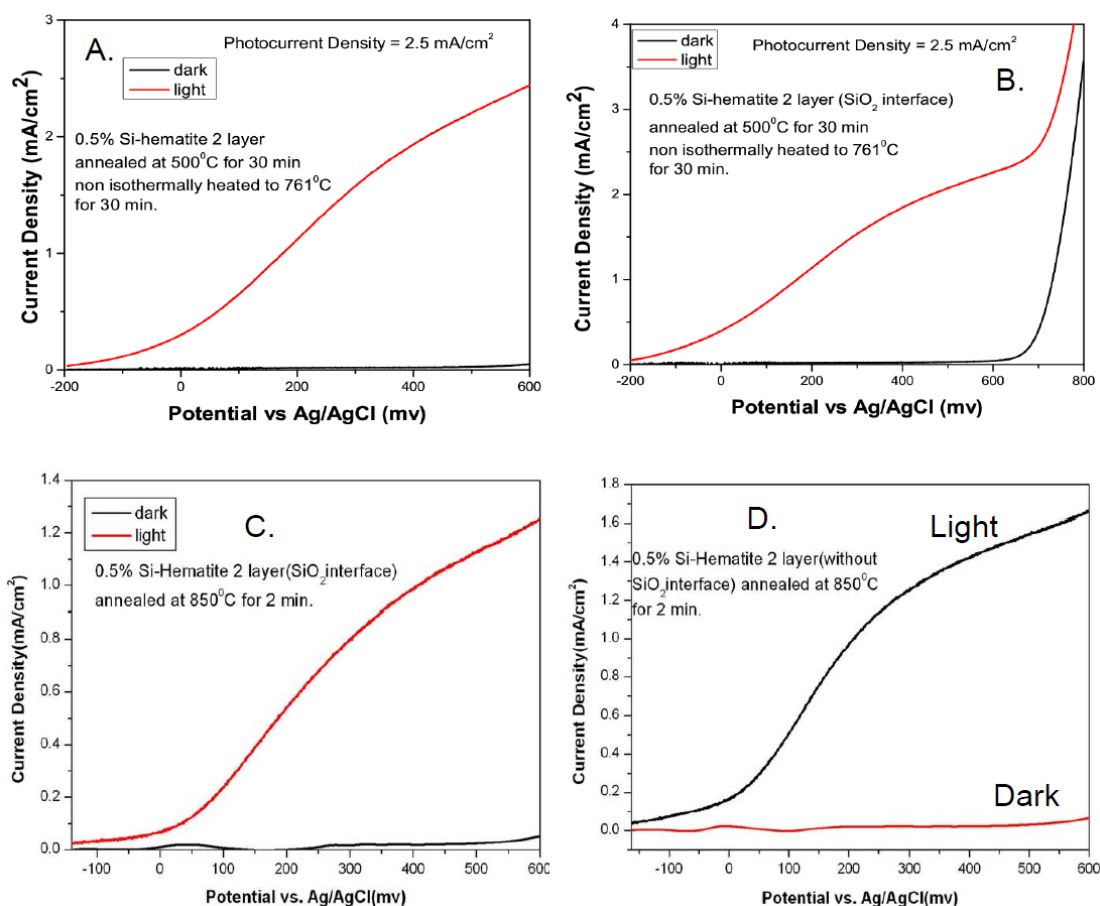


**Figure 7.9:** Photocurrent vs. voltage curves of Si- Hematite film (A) no interfacial layer; annealed from 500<sup>0</sup>C to 761<sup>0</sup>C. (B) With interfacial layer; annealed from 500<sup>0</sup>C to 761<sup>0</sup>C (C) no interfacial layer; annealed from 850<sup>0</sup>C for 2 min (D) with interfacial layer; annealed from 850<sup>0</sup>C for 2 min.

### 7.3.1 Effect of different Si -doping % on the photo activity

To study the effect of doping concentration of Si, films have been prepared with different concentration of TEOS containing precursor by following the protocol as mentioned in scheme 7.6. It is to be noted that, no TEOS interfacial layer was deposited in between hematite layers during this synthesis strategy.

The X-Ray diffraction pattern of Si-Hematite film prepared with different doping concentration of silicon is shown in Figure 7.10. From the XRD pattern, it is observed that the diffracted peak intensity of (104) and (110) from hematite crystalline plane varies. The variation of peak intensity is maximum in case of (104) plane for 1.5% Si containing film and in case of (110) plane, 3.7% shows maximum value. On normalizing these peak intensity with the maximum value of peak intensity from the substrate due to (101) plane, it is found that the substrate peak intensity also varies in contrast with the rest of the peak from hematite. This led us to believe that the variation in (104) and (110) diffracted peak intensity from hematite is just due to the non-uniform increase in film thickness. From the profilometric measurement, no definite thickness has been obtained as the film is very rough due to high heat treatment. Another important point to be mentioned is that only the rough film can give the best performance.

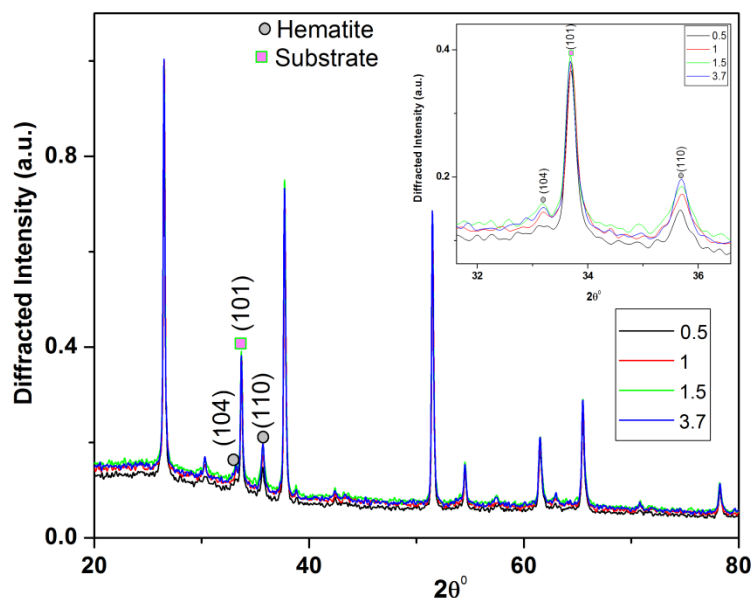


**Figure 7.10:** X-Ray diffraction pattern of hematite film doped with different % of Si. The inset shows the evolution of (110) peak with increase in doping %.

The morphology of the Si- hematite film with different concentration of Si is studied with FESEM and is shown in figure 7.11. From the SEM study, the porous nature of film can be

seen and it is systematically increase with higher doping %. Also the shape of the particle change from dumb bell shape to spherical one from 0.5% to 3.7%.

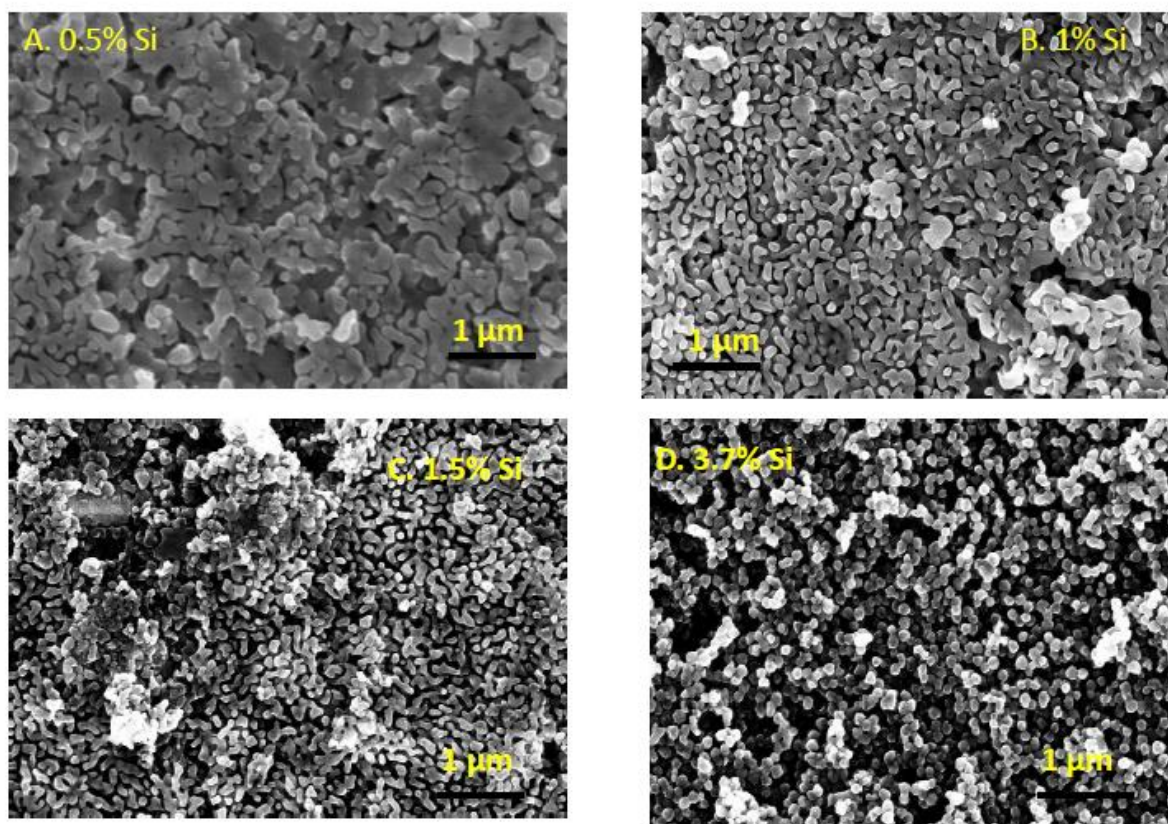


**Figure 7.11:** FESEM images of Si- Hematite film with different doping %.

The composition of the films is studied with X-ray photoelectron spectroscopy. XPS survey scan [figure 7.12] shows the presence of Si 2p peak at 102.5 eV for all samples excluding 0.5% Si-Hematite film. Two distinct peaks are also obtained at 531 and 533 eV. These peaks are assigned to O 1s peak attributed to SnO<sub>2</sub> and SiO<sub>2</sub> [14]. The high heat treatment temperature may also help in diffusion of Sn from substrate. But from the XPS result, no corresponding peak due to Sn binding energy has been seen in all the cases. Sivula et. al. [13] has found the corresponding Sn peak in the 800°C annealed hematite films. It was suggested that the Sn atoms could be diffusing from the substrate into the Fe<sub>2</sub>O<sub>3</sub> and acts like electron donating substitutional impurities (Sn<sup>4+</sup>). In this case, it can be concluded that the heat treatment temperature from 500°C to 760°C is not enough to make the diffusion of Sn into the lattice.

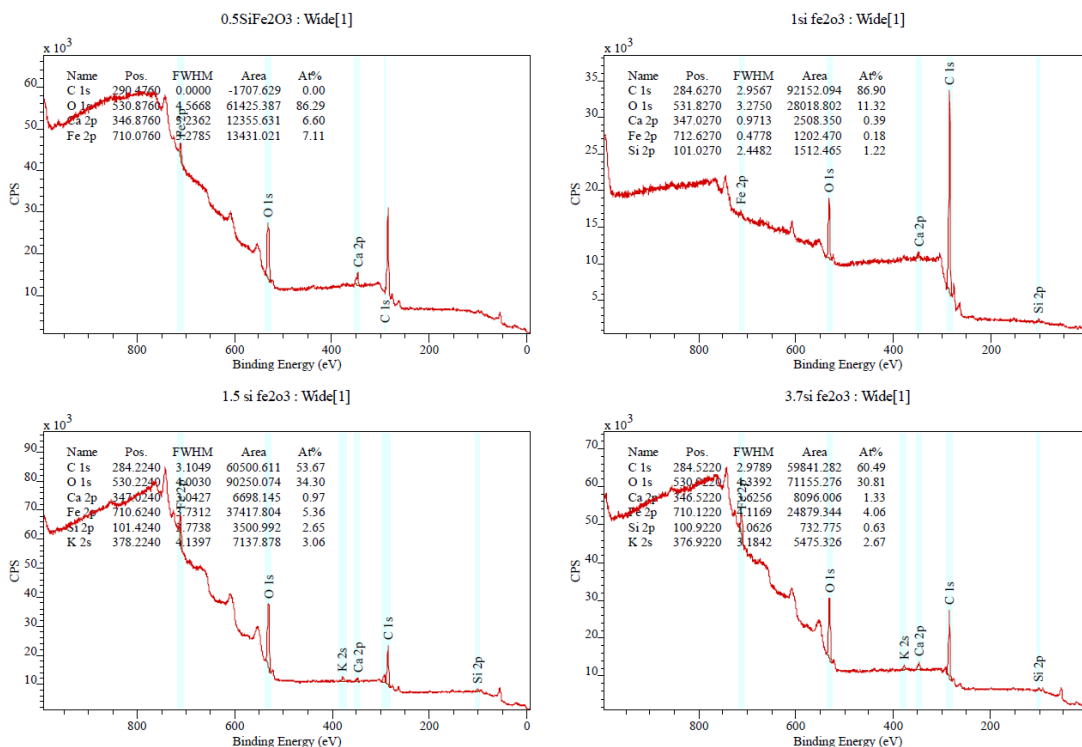


**Figure: 7.12:** X- Ray photoelectron spectroscopy survey data for the electrodes with different doping % of Si. [Courtesy: Dr. Fortunato Giuseppino, EMPA St. Gallen]

From the photoelectrochemical study [figure 7.13], the photocurrent density of 0.5% Si-Hematite film is found to be highest in comparison to other doping concentration. The doping concentration has been fixed for this value (0.5%) for depositing further sets of film. The thickness of the film is not uniform even after depositing the same number of layers, so photocurrent density trend might be ascribed to inconsistent variation in film thickness. To exactly quantify the influence of doping concentration, some other studies are necessary but it is beyond the scope of the present work. Here, optimization has been made in order to get the maximum efficiency of hematite film with the help of Si doping.

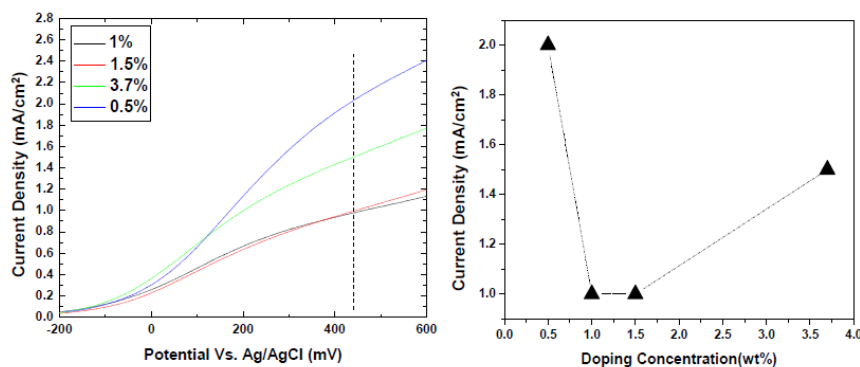


**Figure 7.13:** Left - Photocurrent vs. voltage curves of Si- Hematite film with different doping %. Right – showing the variation of photocurrent density with doping%.

The photocurrent density of dip coated Si - Hematite film after correction of light intensity is compared with that of APCVD (Atmospheric pressure chemical vapor deposition) film and is illustrated in figure 7.14. It is found that the APCVD deposited film [5] showed 3 fold increases in photocurrent (around  $2.2 \text{ mA} / \text{cm}^2$ ) in comparison to dip coated Si-hematite film. Note that the APCVD deposited hematite film at EPFL is the benchmark working electrode for PEC application.

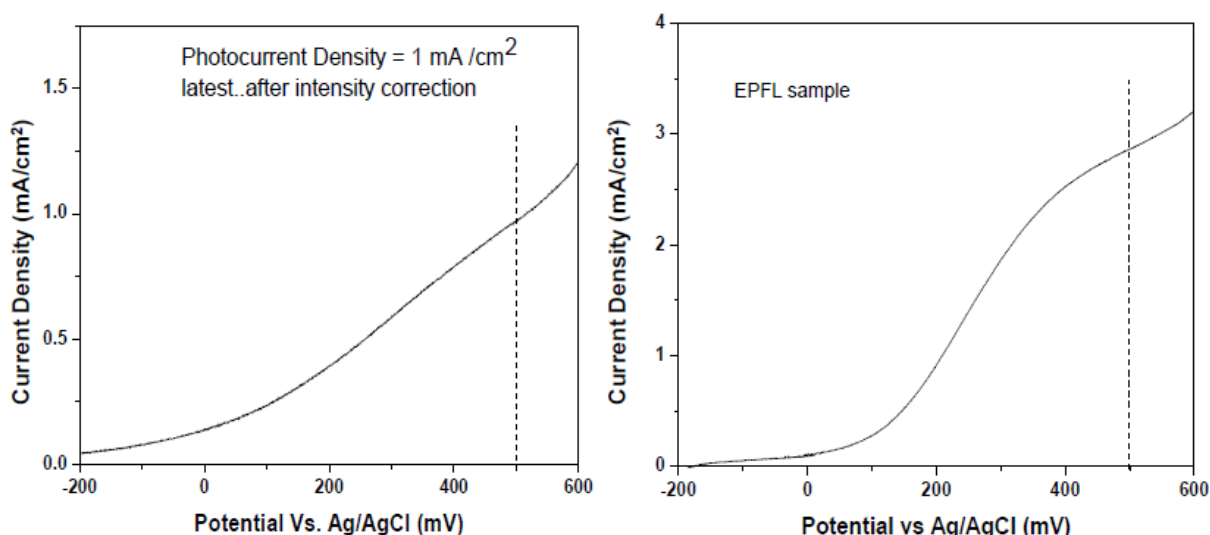


**Figure 7.14:** Comparison of the photocurrent density of dip coated and APCVD deposited Si-hematite film.

### 3.2 Long term stability study of Si- hematite electrode

The stability of the electrode is also studied by the long term chronoamperometric study. For this Si - Hematite film (0.5%) was deposited on a big FTO substrate ( $4 \text{ cm}^2$ ) supplied from Solaronix, Switzerland. The photocurrent density of the electrode was found to be around  $3 \text{ mA} / \text{cm}^2$  as shown in figure 7.15 (left). From the long term chronoamperometric study [figure 7.15 (right)], the photocurrent density was found to be very sustainable which allow the electrode to be used for long term operability. The long term measurement has been done by applying an anodic bias of 200 mV [water splitting potential when Ag/AgCl scale converted to reversible hydrogen electrode (RHE) scale]. During the chronoamperometric measurement, significant gas evolution has been observed from the electrode surface as shown in figure 7.16.

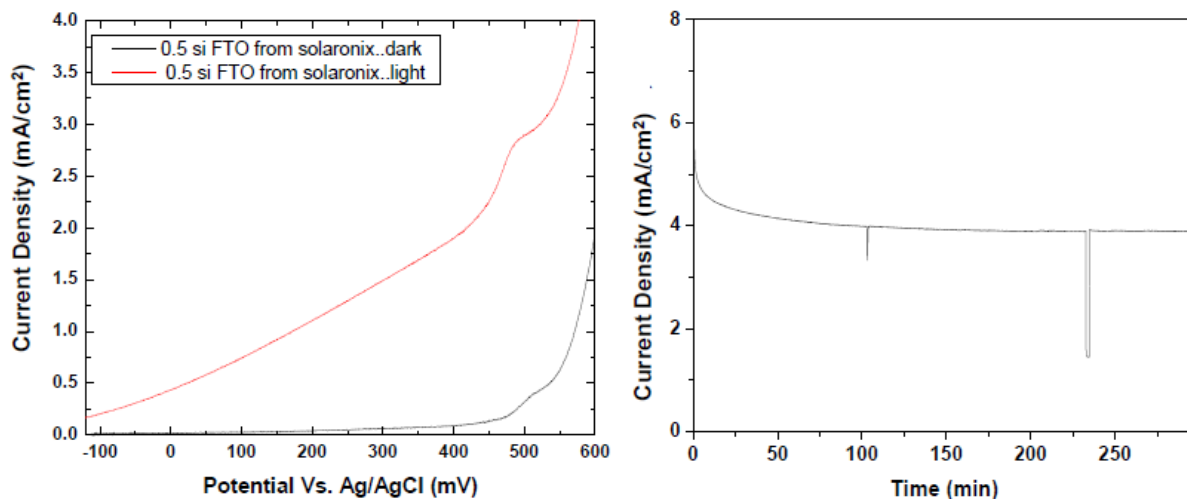


**Figure 7.15:** Left: Photocurrent density obtained for Si-hematite film deposited on 4 cm<sup>2</sup> FTO substrate (Solaronix). Right: Long term chronoamperometric stability study of Si-hematite film showing good sustainability in photocurrent.

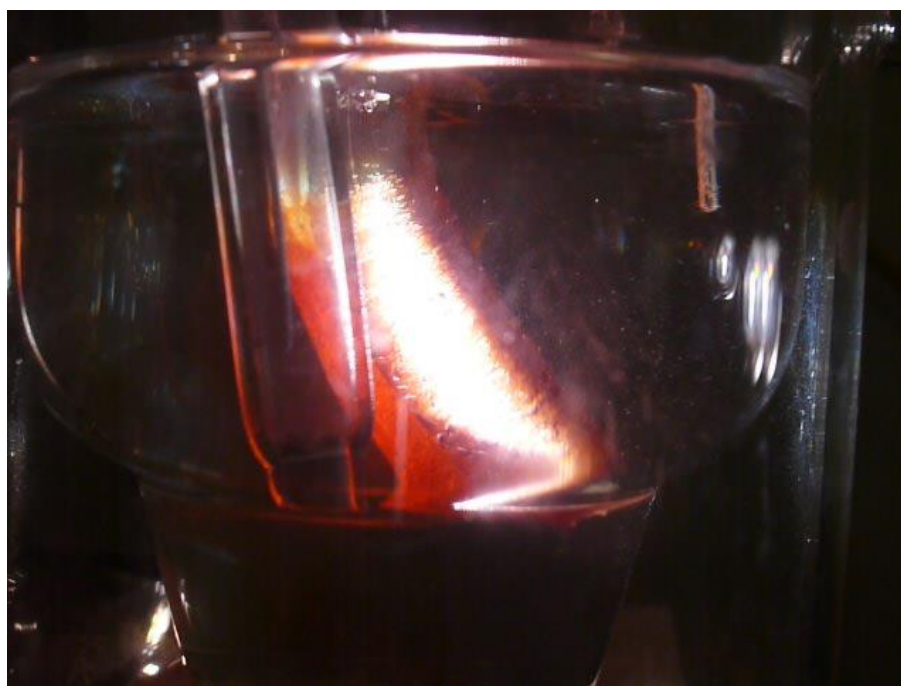


**Figure 7.16:** Gas evolution from the Si Hematite film on applying bias and illuminating with A.M 1.5 simulated sunlight.

#### 7.4 Conclusion

Silicon doped nanocrystalline hematite thin film is fabricated by the dip coating of FTO substrate in a TEOS modified iron fatty acid precursor. From the optimization study, it is found that many parameters such as annealing temperature, SiO<sub>2</sub> interfacial layer plays a role in the enhanced photoactivity of hematite thin film. From the dopant concentration dependent study,

0.5% silicon doped hematite film showing maximum photocurrent density of around 2.4 mA / cm<sup>2</sup>. The electrode also shows good operational stability with clear sign of gas evolution.

## References

- [1] Dare-Edwards, M. P.; Goodenough, J. B.; Hamnett, A.; Trevellick, P. R. *J. Chem. Soc., Faraday Trans. I* **1983**, 79, 2027-2041
- [2] Kennedy, J. H.; Frese, K. W. *J. Electrochem. Soc.* **1978**, 125, 709-714.
- [3] Kennedy, J. H.; Shihar, R.; Ziegler, J. P. *J. Electrochem. Soc.* **1980**, 124, 2307-2309.
- [4] Sanchez, H. L.; Steinfink, H.; White, H. S. *J. Solid State Chem.* **1982**, 41, 90-96.
- [5] Kay, A.; Cesar, I.; Gratzel, M. *J. Am. Chem. Soc.* **2006**, 128, 49.
- [6] Cesar, I.; Sivula, K.; Kay, A.; Zboril, R.; Gratzel, M. *J. Phys. Chem. C* **2009**, 113, 772-782.
- [7] Saremi-Yarahmadi, S.; Upul Wijayantha, K. G.; Tahir, A. A.; Vaidhyanathan, B. *J. Phys. Chem. C* **2009**, 113, 4768-4778.
- [8] Cesar, I.; Kay, A.; Gonzalez Martinez, J. A.; Gratzel, M. *J. Am. Chem. Soc.* **2006**, 128, 4582-4583.
- [9] Zhang, M.; Luo, W.; Li, Z.; Yu, T.; Zou, Z. *Appl. Phys. Lett.* **2010**, 97, 042105.
- [10] Glasscock, J. A.; Barnes, P. R. F.; Plumb, I. C.; Savvides, N. *J. Phys. Chem. C* **2007**, 111, 16477 – 16488.
- [11] Souza, F. L.; Lopes, K. P.; Nascente, P. A. P.; Leite, E. R. *Sol. Energ. Mat. Sol. C* **2009**, 93, 362–368.
- [12] Fonash, S. J. *J. Appl. Phys.* **1976**, 47, 3597-3602.
- [13] Sivula, K.; Zboril, R.; Formal, F. L.; Robert, R.; Weidenkaff, A.; Tucek, J.; Frydrych, J.; and Gratzel, M. *J. Am. Chem. Soc.* **2010**, 132, 7436-7444.
- [14] NIST XPS database: <http://srdata.nist.gov/XPS>.

## **Part II: Hematite Electronic Structure Study with Soft X Ray absorption spectroscopy**

## Chapter 8

### **Evolution of an oxygen NEXAFS transition in the upper Hubbard band in $\alpha$ -Fe<sub>2</sub>O<sub>3</sub> upon electrochemical oxidation**

The following analysis of NEXAFS spectra and scientific rational is provided and derived by A. Braun in ref. [33]

#### **8.1 Introduction**

Hematite,  $\alpha$ -Fe<sub>2</sub>O<sub>3</sub> is the most common iron oxide mineral in nature, and a detailed understanding of its electronic structure and transport properties is of particular interest for its functionality in device applications. Particularly for photo electrochemical applications,  $\alpha$ -Fe<sub>2</sub>O<sub>3</sub> is attractive as a photoanode due to its suitable durability, abundance, and valence band edge position with respect to water oxidation potential [1-5]. Hematite is also regarded as the cheapest semiconductor that absorbs substantial amounts of visible light, and is therefore a candidate component of inexpensive, inorganic artificial photosynthesis systems for generating chemical fuels from sunlight [6]. Its electronic structure has been studied with x-ray and electron spectroscopy in its pristine state as well as after exposure to gases and, because of its importance to geosciences, exposure to water. In so far, a cross fertilization between materials science and geological science has taken place in the last ten years. When hematite is used in a photoelectrochemical cell, the interaction of aqueous electrolyte with hematite under the applied potential may have an influence on its electronic structure especially at the semiconductor liquid junction. Even in the absence of such an external potential, the electrolyte and electrode may interact in a way that, for example, a chemically induced surface potential gradient across crystallites, together with sufficiently high bulk electrical conductivity dissolution of edge surfaces, is balanced with simultaneous growth of the crystallographically distinct (001) basal plane [7]. The crystallographic structure of the [0001] hematite surfaces in aqueous media has been studied by scanning tunneling microscopy [8]. Particularly soft x-ray spectroscopy at the oxygen K-edge has proven useful for the analysis of the electronic structure [9, 10, 11, 12, 13, 14]. The surface oxidation phase on pyrite FeS<sub>2</sub> reacted in aqueous electrolytes at pH 2-10 and with air under ambient condition was studied using synchrotron-

based O K-shell near edge x-ray absorption fine structure (NEXAFS) spectroscopy [15,16]. NEXAFS spectroscopy at the O K edge was also utilized to reveal band edge electronic structure of bulk and nanoscale hematite [17]. The band gap widening in nanoscale iron oxide is potentially important for its application in solar cells [18, 19]. Thin film of single crystal iron oxides,  $\text{Fe}_x\text{O}$  (111),  $\text{Fe}_3\text{O}_4$  (111) and  $\alpha\text{-Fe}_2\text{O}_3$  (001) prepared by oxidizing the Fe films evaporated on a Pt (111) surface, have been studied recently using NEXAFS [20]. NEXAFS investigation of the electronic structure and chemistry of iron based metal oxide nanostructured materials was studied to show the correlation between electronic structure and surface chemistry [13]. The O K edge NEXAFS spectrum of hematite originates from transition from the O (1s) core orbitals to the empty Fe (3d)-Fe (4s) - and Fe (4p) - like bands or molecular orbitals that have some O (2p) character.

The motivation of this work is to study the influence of electrochemical oxidation of hematite on its electronic structure, because such kind of oxidation is an operational step in the functionality of photoelectrochemical cells. For this O K edge NEXAFS spectroscopy have been carried out for hematite films having different thicknesses cycled under applied bias of 200 mV and 600 mV in 1M KOH. The spectra are compared with spectra obtained from Si doped hematite films prepared by atmospheric chemical vapor deposition. To the best of our knowledge, hematite before and after electrochemical treatment has not yet been studied with NEXAFS spectroscopy.

## 8.2 Experimental Section

**Reagents and Materials.** Hematite  $\alpha\text{-Fe}_2\text{O}_3$  thin films were synthesized by dip coating of a precursor complex on a fluorinated tin oxide (FTO, TEC-8 Pilkington from Hartford Glass, MA) coated glass substrate, followed by annealing at  $550^\circ\text{C}$  for 2 hr. in air. The precursor complex was synthesized by heating a mixture of  $\text{Fe}(\text{NO}_3)_3 \cdot 9\text{H}_2\text{O}$  (28.0 g) and oleic acid (17.0 g) to  $70^\circ\text{C}$  to give a homogenous liquid phase. This homogeneous mixture was then heated at  $125^\circ\text{C}$  for 90 minutes to give a reddish brown viscous mass which was then cooled to room temperature, left for 24 h and subsequently treated with 80 ml of tetrahydrofuran. The resultant solution was stirred with a glass rod for 30 minutes and the powdery precipitate separated from the solution by centrifugation (5000 rpm) for 2-3 min. After centrifugation, the supernatant (precursor complex) was recovered for the dip coating of the film. FTO was used as a substrate. By repeated dipping and annealing at  $500^\circ\text{C}$  for 30 minutes for each layer, films with layer thicknesses from 1 to 10 layers were obtained. This deposition technique is reproducible and allows making porous films with well-defined thickness by repeated dip coating. The thickness of a number of films was determined with a stylus profilometer (Ambios XP-100). 4 dip coated layers resulted in an approximately 600 nm thick film with optimized

photoelectrochemical properties. Phase purity was confirmed by x-ray diffraction. Thicker films had overall larger crystallite sizes, as evidenced by the evolution of widths of Bragg reflections. 1 at.% Si doped  $\alpha$ -Fe<sub>2</sub>O<sub>3</sub> films were deposited on the same FTO substrates with ambient pressure chemical vapor deposition (APCVD) after a previously described protocol [21]. Photocurrent and dark current were measured using a spectro-electrochemical cell containing 1 M KOH as electrolyte, Ag<sup>+</sup>/AgCl reference electrode and a Pt. counter electrode. Chronoamperometry was applied at 200 mV for 2 hours for the electrochemically oxidized films. Near edge x-ray absorption fine structure (NEXAFS) spectra were recorded at the undulator beamline UG-56 at BESSY [22], in an UHV recipient with  $2 \times 10^{-10}$  mTorr base pressure or lower. The resolution of this beamline is 0.05 eV (80000 at 64eV) at the soft energy range for oxygen K-edge and Fe L-edges. X-ray reflectometry data were recorded with a Siemens D5000 diffractometer with Cu K $\alpha$ 1 radiation in  $\theta/2\theta$ -configuration in a range of  $0.07^\circ \leq 2\theta \leq 2^\circ$  with a scan speed of 2s per  $0.002^\circ$  step.

### 8.3 Results and Discussion

The evolution of the film thickness upon repeated dip coating and subsequent annealing is shown in Figure 8.1– a. The linear increase as a function of coated layers, with an average thickness of  $164 \pm 3$  nm per layer as determined by least square regression, demonstrates reproducibility of the deposition method. Note, that the first layer in a 10 layer thick film has been exposed 10 times to 500°C for 30 minutes, whereas the top layer has been exposed only once. The film should thus have graded structure across the thickness. This is indicated by the average crystallite size, which ranges from 30 nm for the 1 layer film to 80 nm for the 10 layer film according to x-ray diffraction. Phase purity as hematite has been confirmed by x-ray diffraction [23].

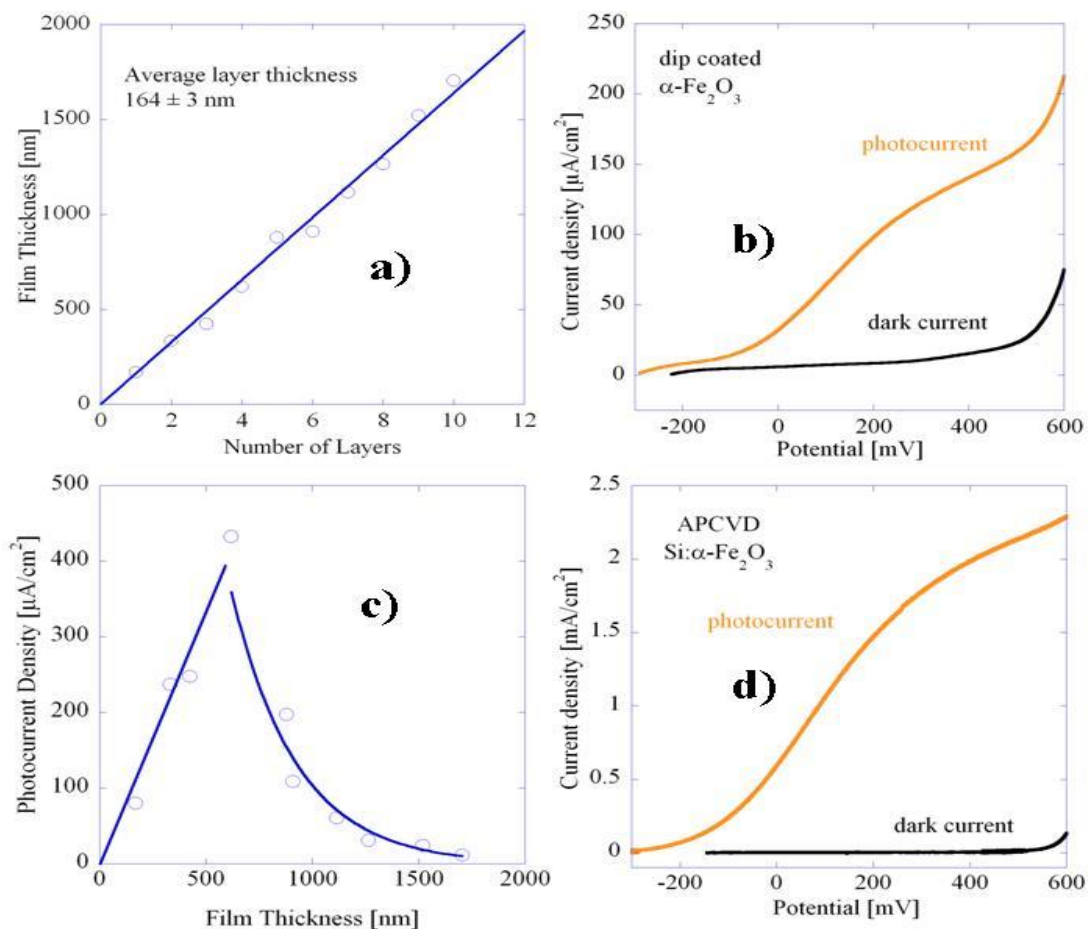


**Figure 8.1:** a) – Film thickness as a function of layers with linear least square fit; b) – photocurrent and dark current of 1 layer film obtained by dip coating; c) - photocurrent of dip coated films as a function of film thickness, measured at 600 mV; d) – photocurrent and dark current of Si-doped  $\alpha\text{-Fe}_2\text{O}_3$  obtained by APCVD [33].

The current/voltage diagram in Figure 8.1-b shows a strong onset of photocurrent for a 1 layer film with 164 nm thickness at around 0 mV/SCE, whereas the dark current maintains a flat slope of around  $15\mu\text{A}/\text{cm}^2$  until 500 mV. At the same potential also the photocurrent has a strong additional onset of an oxidative current wave. For films with 1 to 9 layers, the current was determined at 600 mV and plotted versus the film thickness, see Figure 8.1-c. The photocurrent is obviously dependent on the thickness of the film. The total current measured at 600 mV includes a substantial dark current, which has not been subtracted in Figure 8.1-c). For films with thicknesses up to 4 layers, the photocurrent increases linearly. The maximum photocurrent was found for a film with 4 layer thickness, i.e.  $430\mu\text{A}/\text{cm}^2$ . For films thicker than 4 layers, the photocurrent decreases with a profile that can be modeled with an exponential. Thus, the photocurrent can be optimized in terms of film thickness. For comparison, Figure 8.1-

d shows dark current and photocurrent of a Si-doped hematite film at about the same potential like the one shown in Figure 8.1-b.

Figure 8.2 shows the oxygen NEXAFS spectra of four differently treated  $\alpha$ -Fe<sub>2</sub>O<sub>3</sub> films with 4 layer thickness deposited on FTO glass. The spectra have been normalized to the intensity tail at energies larger than 550 eV. One spectrum corresponds to the pristine film, one spectrum to such film exposed to KOH electrolyte, and two films electrochemically oxidized under dark and under light condition from 0 mV to 200 mV. The dark/light experiment was carried out because hematite has a charge-transfer band gap (about 2.2 eV) smaller than the cutoff of solar radiation in the troposphere (about 4.3 eV) and is thus able to participate in photochemical reactions [24]. At first glance we see no major differences in these four spectra. Particularly all resonances are virtually at the same energy positions. The spectra show a well developed double peak in the pre-edge region at 530 eV, see upper right inset in Figure 8.2, which originates from transitions of hybridized Fe(3d)-O(2p) states with  $t_{2g}$  and  $e_g$  orbital symmetry [8,9,12,13]. Oxygen edge profiles are sensitive to the local bonding and symmetry properties of the excited oxygen. The features of the pre peak are governed by the 3d components in the hybridized unoccupied pd wave functions [13]. A potential difference is the intensity at around 533-534 eV, the range between the Fe (3d)-O (2p) doublet and the Fe (4sp)-O (2p) resonances. It is low for the pristine sample (red color spectrum), whereas the spectra of the samples exposed to KOH and oxidized to 200 mV have a higher intensity in this energy region, as well as in the region where the doublet is found.

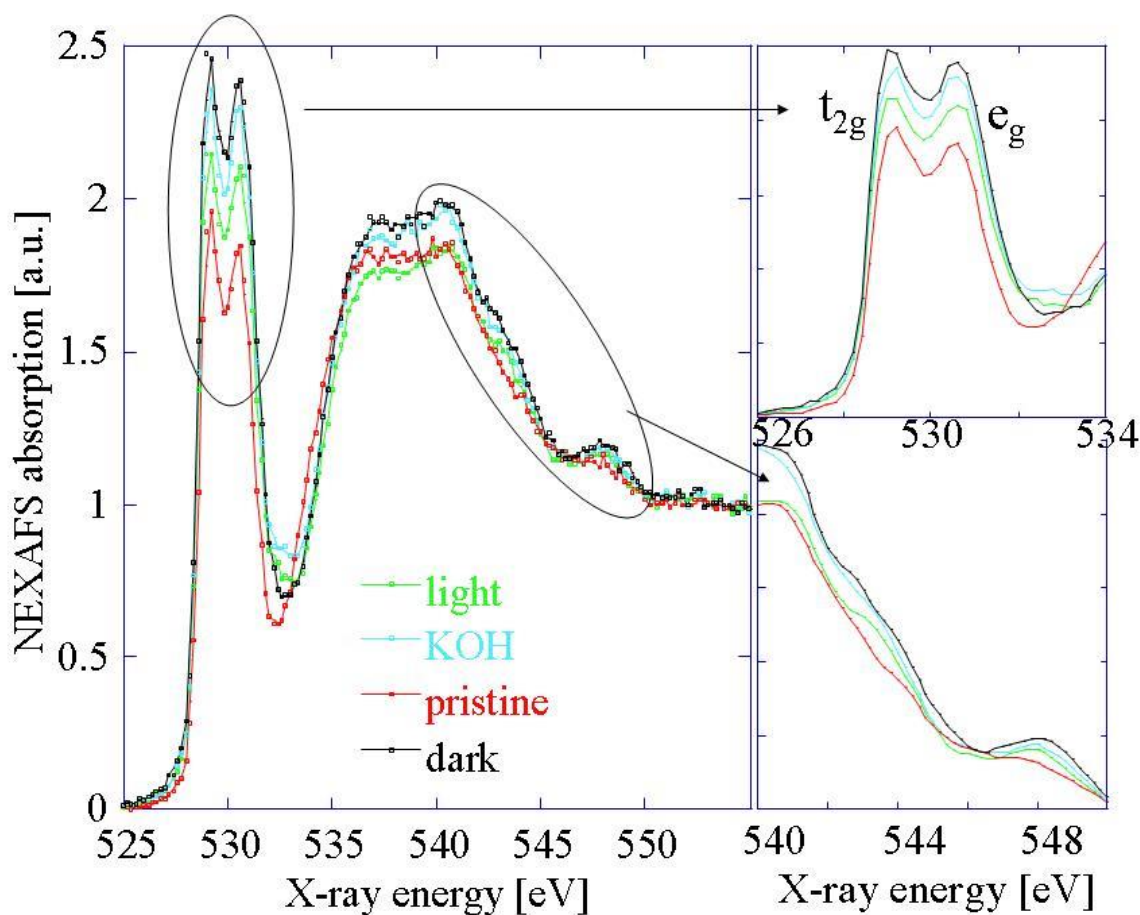


**Figure 8.2:** Oxygen NEXAFS spectra of pristine  $\alpha$ - $\text{Fe}_2\text{O}_3$  film, film exposed to KOH, and light and dark treated film from 0 mV to 200 mV/SCE in KOH for 2 hours [33].

Close inspection and comparison of all four spectra in Figure 8.2 suggests that upon KOH exposure, a weak broad structure readily present in the pristine sample at around 542 eV to 544 eV evolves a little more upon contact with KOH and oxidation to 200 mV. The spectral range for this structure is shown in the magnified lower inset in Figure 8.2. In addition it appears that the spectra of the samples exposed to KOH have a slight noticeable shift in the energy range at 524 eV towards higher energy. Another peculiarity is that the pre-edge peaks of the KOH treated samples are relatively larger than those of the pristine sample.

Besides the above findings, during the beamtime I made the following interesting observation. I find more peculiar details in the films that were oxidized at a voltage 600 mV. These films reached the potential of 600 mV only during the photocurrent and dark current measurement, i.e. only for several seconds. Figure 8.3 shows the oxygen NEXAFS spectra of a pristine 4 layer film, and films with 1 layer and 10 layers, both of which were oxidized to 600 mV, and the oxygen spectrum of a clean FTO glass for reference.

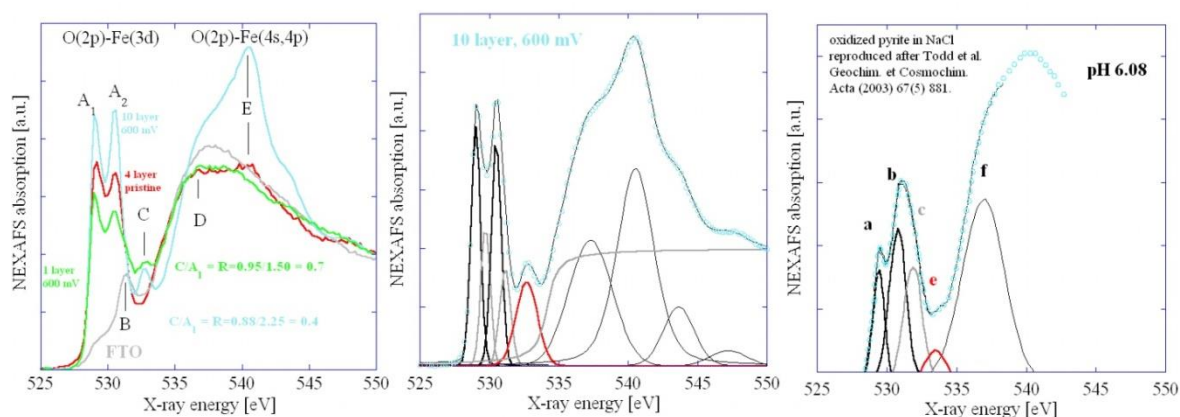


**Figure 8.3:** Left - Oxygen NEXAFS spectra of FTO, pristine  $\text{Fe}_2\text{O}_3$  film 4 layers thick (red spectrum), and 1 layer (green) and 10 layer (blue) thin films oxidized to 600 mV in KOH. Middle – deconvolution of 10 layer film spectrum into Voigt functions and arctan function. The extra peak is plotted in red [33]. Right – Oxygen NEXAFS spectrum of oxidized pyrite, as reproduced from Todd et al., ref. [8].

The spectrum of the FTO glass has only minor intensity in the range where the hematite has a typical strongly developed doublet – around 530 eV. FTO has a relatively strong resonance at 531.4 eV. These spectral details are important in order to judge which details in the spectra originate from  $\text{Fe}_2\text{O}_3$ , and which are from the FTO underneath. Therefore it is also important to know about the information depth and x-ray attenuation depth of the x-rays in the  $\text{Fe}_2\text{O}_3$  sample. For  $\text{Fe}_2\text{O}_3$  with an assumed  $5.3 \text{ g/cm}^3$  density, the theoretical attenuation depth for x-ray energies of around 530 eV is around 600 nm, this is, the x-ray intensity of 530 eV electrons has decayed to  $1/e$  of its original intensity [25]. According to Figure 1, the 1-layer film has a thickness of 164 nm. Therefore, the oxygen spectrum of the 1 layer film is significantly contaminated with spectral intensity from the FTO underneath. This is clearly visible at around 531.75 eV for the 1 layer film, where a shoulder is observed which coincides with the aforementioned peak of the FTO sample in the same energy range. The films with 4 layers and 10 layers, 650 nm and 1650 nm thickness, respectively, do not show such shoulder.

We now take a closer look at the energy range of around 532.4 eV, Figure 8.3 left panel, where the pristine  $\text{Fe}_2\text{O}_3$  and the FTO spectrum have a relative intensity minimum. We notice that the 10 layer film has a relatively strong transition (peak feature denoted C) in this region. Also, the 1 layer film has a transition in this region. This transition “C” at around 532.7 eV has not been observed previously in spectra of hematite. X-ray spectroscopy classifies hematite as a charge transfer or intermediate type insulator [8]. We believe that the extra peak C is due to a transition probably to the conduction band, i.e. to the upper Hubbard band with mainly Fe (3d) character. A potential scenario is transitions to on-site Fe empty 4p states hybridized to empty

3d states of next-to-nearest neighbor Fe atoms. Possibly, the C peak is thus determined by inter-site Fe 4p-3d mixing via strong Fe 3d-O 2p hybridization and thus a direct probe of the upper Hubbard band in this highly oxidized Form of Fe; compare ref. [26]. The pristine Fe<sub>2</sub>O<sub>3</sub>, Fe<sub>2</sub>O<sub>3</sub> films exposed to KOH, and Fe<sub>2</sub>O<sub>3</sub> oxidized to 200 mV, as discussed before, do not show this C peak. Hence, the electrochemical oxidation to 600 mV is a clear condition for the formation of this transition. Little is known about the redox chemistry and higher redox states of Fe at the iron oxide solid/aqueous liquid interface [27]. A representative energy diagram of the  $\alpha$ -Fe<sub>2</sub>O<sub>3</sub>/KOH junction is sketched in [28]. Cummings et al. hypothesize the presence of Fe with higher oxidation states, i.e. Fe<sup>4+</sup> at the iron oxide interface with neutral electrolytes, in addition to readily established Fe<sup>4+</sup> at alkaline electrolytes [27, and references therein].

The pre-edge doublet in the oxygen NEXAFS spectra of FeOOH has been considered as a convolution of a pair of t<sub>2g</sub>-e<sub>g</sub> states from the oxygen in FeOOH O (2p)-Fe (3d) transitions, and a conjugate pair of the hydroxyl group, latter of which is slightly shifted towards higher energy [29]. Comparison with the literature spectrum of FeOOH suggests that the extra peak that we observe at 532.7 eV is not commensurate with the peak labeled “d” in Figure 2-b) in ref. [14]. However, Figure 6-a) in [14] shows three spectra obtained at high pH with a peak labeled “e”, which remains unassigned in [14], in the same relative energy position like the extra peak at 532.7 eV. Todd et al. speculate this peak cannot be assigned to a bound state, but could be a multiple scattering feature [15]. This spectrum has been reproduced in the right panel in Figure 3 and highlighted feature “e” by deconvolution of the relevant part of the spectrum into a series of Voigt functions. In a follow up paper, Todd et al. [15] assign a similar structure in oxidized chalcopyrite to an O(1s) in OH<sup>-</sup> → O(2p)-H(1s) antibonding molecular orbital in OH<sup>-</sup>, possibly from adsorbed water. We believe this peak is representative to a highly oxidized surface species, slightly more so than from FeOOH because it is found at a higher energy than the feature specific to FeOOH, and potentially resembles an electron hole feature which transfers from O (2p) to Fe (3d). Increased spectral weight in the range around 534 eV, this is where the NEXAFS spectra have a relative minimum intensity, is also found in a size dependent study on hematite nanoparticles with O(1s) NEXAFS spectroscopy [16]. The spectra of nanoparticles have in this relative intensity minimum a larger spectral weight, than bulk hematite (see Figure 5-b) in [15]). The spectrum of hematite exposed to KOH only, Figure 8.2, suggests a similar increased intensity in this energy range, though not to the extent that a distinct peak is formed.

Comparison of the spectra from the 1-layer and 10-layer films in Figure 8.3 suggests that the 1 layer film has a relatively higher intensity of the extra transition C compared to the intensity of the doublet A<sub>1</sub>, A<sub>2</sub>, in contrast to the 10 layer film. This becomes clear in the relative peak

height ratios between the newly formed peak C and the height of  $A_1$  in the doublet. For the 1 layer film the relative ratio of the peak C is  $R = C/A_1 = 0.95/1.50 = 0.7$ , and for the 10 layer film it is  $R = C/A_1 = 0.88/2.25 = 0.4$ . One explanation is that the spectra which we compare here resemble not only the electronic structure of the surface but also the electronic structure of the bulk. We recall that the 10 layer film has larger hematite crystallites (average 80 nm) than the 1 layer film (average 30 nm) because of the extended exposure to 500°C. This implies that the 1 layer film with the relatively larger extra peak has relatively more surface contribution from that film than the 10 layer thick  $\text{Fe}_2\text{O}_3$  film, where more of the information comprises the bulk properties. After all, the electrochemical oxidation in KOH should particularly impact the surface, and not the bulk. Impedance studies on electrochemical passivation of Fe metal [30, and references therein] point to an interconversion of p-type Fe (II) and n-type Fe (III) in the course of forming and dissolving a surface passive film. Specifically, within a potential range from -300 mV to +1000 mV an n-type Fe (III)-oxide layer is formed [30]. Moreover, between 500 mV and 700 mV, the tunneling exchange current increases by three orders of magnitude with the valence band, and the apparent tunneling current transfer coefficient decreases by a factor of ten [30]. From oxidation of pyrite it is known that at high pH iron (III) oxyhydroxide forms at the surface, and under most alkaline conditions the oxygen NEXAFS spectrum resembles that of goethite  $\text{FeOOH}$  [14]. When we compare feature E in the spectra at 540.5 eV (Figure 8.3), its clear absence in the 1 layer film, which represents a larger surface-volume ratio than the thicker films and also has smaller crystallites. The 4 layer film has a noticeable intensity for feature E, and the 10 layer thick film has an overwhelmingly dominant E structure. we thus conclude the transition labeled E at 540.5 eV is a bulk hematite feature.

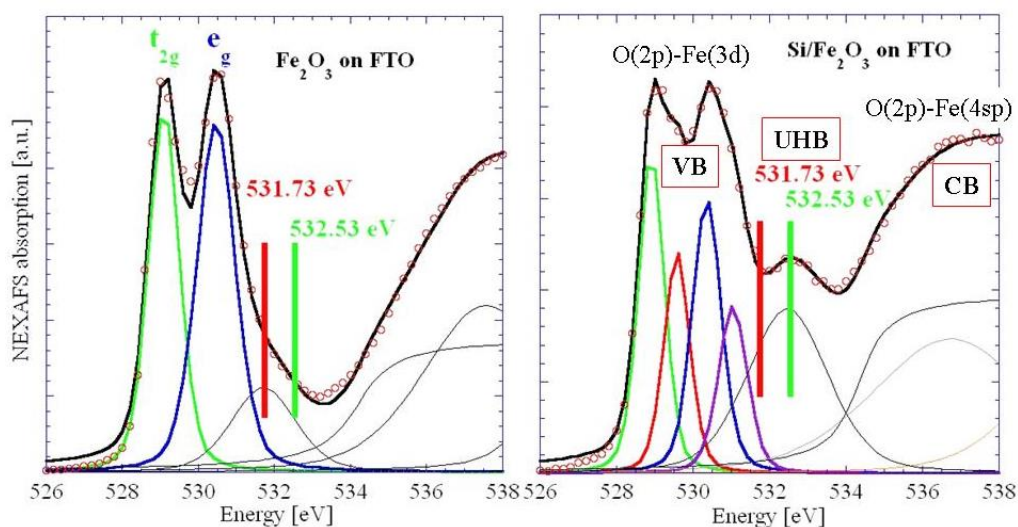


**Figure 8.4:** Oxygen NEXAFS spectra of  $\alpha\text{-Fe}_2\text{O}_3$  nanoparticle powder with 550°C heat treatment (left spectrum) and 1% Si-doped  $\text{Fe}_2\text{O}_3$  pristine sample (right) [33].

When we return to the  $t_{2g}$ - $e_g$  doublet features  $A_1$  and  $A_2$  at about 529 and 530 eV, we notice that the relative height of  $A_1$  and  $A_2$  is equal for the 10 layer film, whereas for the thinner films feature  $A_1$  is larger than  $A_2$ . The likely reason for this is that the 10 layer film has been exposed 10 times to thermal treatment, whereas the 4 layer and 1 layer films have been exposed only 4 times and 1 time only, respectively. Thus, the hematite phase in the thick film is crystallographically more developed, as was found by peak width analysis of the x-ray diffractograms, which manifests in the oxygen NEXAFS spectra pre-edge doublet, which has equal height in Fe six fold coordinated by oxygen [10]. Figure 8.4 shows the oxygen NEXAFS spectra of pristine  $\alpha$ - $Fe_2O_3$  powder (i.e., no FTO underneath) and a 1% Si-doped  $\alpha$ - $Fe_2O_3$  film synthesized by APCVD. Both spectra are reminiscent of  $\alpha$ - $Fe_2O_3$  as far as the  $t_{2g}$ - $e_g$  doublet at 529 eV – 531 eV is concerned. Interestingly, the spectrum of the Si doped hematite shows an extra peak at around 532.4 eV, - the same energy where in Figure 3 the feature C peak was found in the 600 mV oxidized samples - although the 1% Si-doped  $\alpha$ - $Fe_2O_3$  film was not electrochemically treated. We have then cycled such film several times in KOH (not shown here), including exceeding 600 mV. Both spectra, the pristine and the electrochemically treated 1% Si-doped  $\alpha$ - $Fe_2O_3$  film, show the feature C peak. The vertical bars (red and green at 531.7 and 532.5 eV) in the spectra in Figure 4 indicate the position of C, and a side band observed in the spectrum of the powder. Comparison shows clearly that the sideband of  $\alpha$ - $Fe_2O_3$  does not coincide with our newly observed peak C, and both should not be mistaken for each other. Also other ferrous or ferric oxides do not show such extra peak in the oxygen NEXAFS spectra before or after exposure to water [31].

Peculiarities in the doublet structure of the APCVD 1% Si-doped  $Fe_2O_3$  film spectra, particularly their width, made us believe that each peak in the doublet could be actually comprised of two peaks, so that the doublet shows actually four peaks in total. Awareness of potentially more transitions in the pre-edges of the oxygen spectra on doped oxides arises from experience with nitrogen doped  $TiO_2$  [32]. Close inspection of the energy range from 531 eV to 534 eV shows that the pristine  $\alpha$ - $Fe_2O_3$  powder spectrum has a shoulder at around 531.7 eV which cannot be accounted for by the doublet in the deconvolution of the spectrum. We have therefore included an additional, broad Voigt function for its deconvolution at this energy.

The question naturally arises as to which influence has the electrochemical oxidation at 600 mV on the hematite surface, in contrast to oxidation to 200 mV or mere exposure to KOH. Does oxidation at 600 mV increase the hematite surface area? Upon visual inspection, the electrochemically oxidized films looked smoother than the pristine one. The Si-doped hematite films looked smoother even before electrochemical treatment. This suggestion is quantitatively

confirmed by profilometer data (not shown here), telling that larger spikes became reduced in size upon 2 hours oxidation at 600 mV. The x-ray reflectograms in Figure 8.5 also show that the reflectivity of the oxidized film exceeds that of the pristine film.

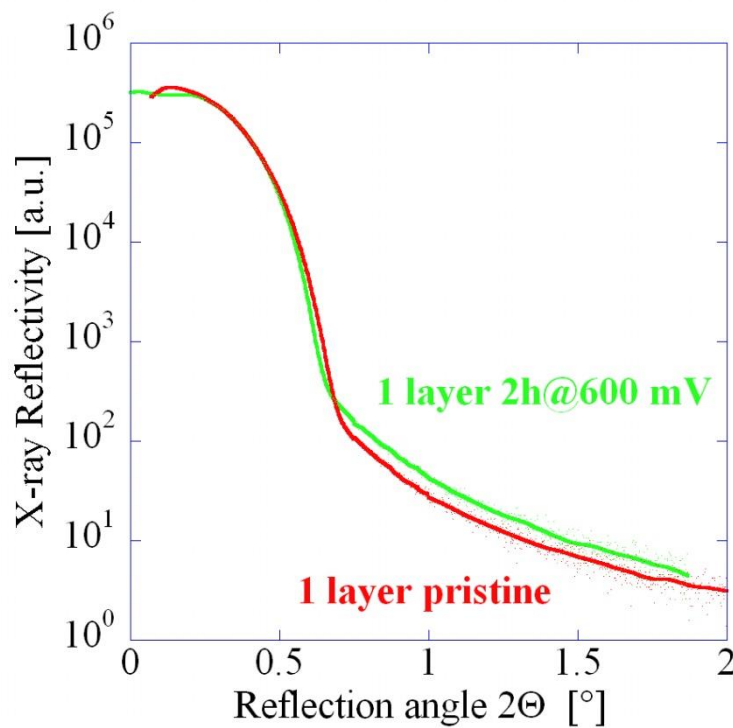


**Figure 8.5:** X-ray reflectometry data for the 1 layer  $\alpha$ -Fe<sub>2</sub>O<sub>3</sub> film before (pristine) and after electrochemical oxidation at 600 mV for 2 hours [33].

Hence, there is no or little support for the suggestion that the electrochemical oxidation to 600 mV would increase the surface roughness, at least not at the sensitivity scale for reflectometry. An alternative explanation is that the Si-doping and the electrochemical oxidation at 600 mV cause morphological changes in a way that a surface is created, such as facets, which promote the formation of highly oxidized Fe species at the surface of the hematite.

#### 8.4 Conclusion

A new transition has been identified in the oxygen NEXAFS spectra on Si doped hematite and on electrochemically oxidized hematite. The energy position of this transition at around 532.7 eV relative to the top of the valence band and suggests that this transition arises from O (2p) orbitals to the Hubbard band with a strong Fe (3d) character for both. While exposure to KOH seems to cause slight increase of spectral weight in this region, it needs a potential of around 600 mV to form this transition, the potential of which reportedly causes the tunneling exchange current to increase by three orders of magnitude with the valence band whereas a potential of 200 mV only is not sufficient for that. The electrochemical origin of this transition suggests that

is related with a surface state. In such alkaline environment, formation of highly oxidized Fe species is likely to occur, which may go along with electron hole states from the O (2p) orbitals. Without further experiments, a similar statement cannot be made on the Si doped hematite, which, interestingly, bears this electronic structure in absence of KOH or electrochemical potential. All films with this transition look visually smoother and have also, in the case of the 600 mV oxidized film, a higher x-ray reflectance, ruling out that increased surface roughness is a precondition for this peak. The fact that films with larger crystallites have relatively less spectral weight for this extra peak than those with smaller crystallites leads to the suggestion that surface faceting could be related with the extra transition to the Hubbard band. Support for this hypothesis comes from the suggestion that doping with Si acts as a hematite structure directing agent.

### References

- [1] Sartoretti, C.J.; Alexander, B.D.; Solarska, R.; Rutkowska, I.A. ; Augustynski, J. *J. Phys. Chem. B* **2005**, *109*, 13685-13692.
- [2] Watanabe, A.; Kozuka, H. *J. Phys. Chem B* **2003**, *107*, 12713-12720.
- [3] Duret, A.; Grätzel, M. *J. Phys. Chem. B* **2005**, *109*, 17184-17191.
- [4] Tahir, A.A.; Upul Wijayantha, K.G.; Saremi-Yarahmadi, S.; Mazhar, M.; Mckee, V. *Chem. Mater.* **2009**, *21*, 3763–3772.
- [5] Zhong, D. K.; Sun, J.; Inumaru, H.; Gamelin, D. R. *J. Am. Chem. Soc.* **2009**, *131*, 6086-6087.
- [6] M. Grätzel, *Nature* **2001**, *414*, 338.
- [7] Yanina, S. V.; Rosso, K. M. *Science* **2008**, *320*, 218.
- [8] Eggleston, C.M.; Stack, A.G.; Rosso, K.M.; Higgins, S.R.; Bice, A.M.; Boese, S. W.; Pribyl, R.D.; Nichols, J.M. *Geochim. Cosmochim. Ac.* **2003**, *67*, 985-1000.
- [9] Ma, Y.; Johnson, P.D.; Wassdahl, N.; Guo, J.; Skytt, P.; Nordgren, J.; Kevan, S.D.; Rubensson, J.E.; Böske, T.; Eberhardt, W. *Phys. Rev. B* **1993**, *48*, 2109-2111.
- [10] Park, T.; Sambasivan, S.; Fischer, D. A.; Yoon, W.; Misewich, J. A.; Wong, S. S. *J. Phys. Chem. C* **2008**, *112*, 10359–10369.
- [11] Pollak, M.; Gautier, M.; Thromat, N.; Gota, S.; Mackrodt, W. C. ; Saunders, V.R. *Nucl. Instrum. Methods* **1995**, *B97*, 383-386.
- [12] Povazhnaya, N.A.; Yalovega, G.E.; Soldatov, A.V. *Phys. Stat. Sol. (b)* **1996**, *195*, K1.

- [13] Wu,Z.Y. ; Gota,S. ; Jollet,F. ; Pollak,M. ; Gautier-Soyer, M. ; Natoli,C.R. *Phys. Rev. B***1997**, *55*, 250-2577.
- [14] Colliex,C. ;Manoubi,T. ;Ortiz, C. *Phys. Rev. B***1991**, *44*, 11402-11411.
- [15] Todd,E.C.;Sherman,D.M.;Purton, J.A. *Geochim.Cosmochim. Ac.***2003**, *67*, 881-893.
- [16] Todd,E.C.;Sherman,D.M.;Purton, J.A.*Geochim.Cosmochim. Ac***2003**, *67*, 2137-2146.
- [17] Gilbert,B.;Frandsen,C.;Maxey, E.R.; Sherman,D. M. *Phys. Rev. B***2009**, *79*, 035108.
- [18] Khan S.U.M.;Akikusa.J.J. *Phys. Chem B***1999**, *103*, 7184.
- [19] Vayssieres, L.; Sathe, C.; Butorin, S. M.; Shuh, D. K.; Nordgren, J.; Guo, J. H., *Adv. Mater.* **2005**,*17*, 2320.
- [20] Schedel-Niedrig, T.;Weiss,W.;Schlögl, R. *Phys. Rev. B***1995**, *52*, 17449.
- [21] Sivula, K.; Le Formal, F.; Gratzel, M., *Chem. Mater.* **2009**, *21*, 2862-2867.
- [22] Sawhney,K.J.S. ;Senf,F. ;Scheer,M. ;Schäfers,F. ;Bahrtdt,J. ;Gaupp,A. ;Gudat,W. *Nucl. Instr. Meth.* **A1997**, *390*, 395-402.  
<http://www.bessy.de/upload/bitpdfs/mustang.pdf>[http://www.bessy.de/upload/bitpdfs/ID\\_05\\_1.pdf](http://www.bessy.de/upload/bitpdfs/ID_05_1.pdf)
- [23] D. K. Bora,A. Braun, R. Erni, G. Fortunato, T.Graule, E. C. Constable, *Chem. Mater.***2011**, *23*, 2051.
- [24] Toledano D. S. ; Henrich,V. E. *J. Phys. Chem. B***2001**, *105*, 3872-3877.
- [25] X-ray attenuation depth in the oxygen NEXAFS energy range for  $\alpha$ -Fe<sub>2</sub>O<sub>3</sub>. At around 600 nm, which corresponds to 4 layers, the X-ray intensity is attenuated to 1/e of its original intensity. Calculation after [[http://henke.lbl.gov/optical\\_constants/](http://henke.lbl.gov/optical_constants/)];Henke, B.L.;Gullikson, E.M.;Davis, J.C. X-ray interactions: photo absorption, scattering, transmission, and reflection at E = 50 eV - 30000 eV, Z=1-92, *Atomic Data and Nuclear Data Tables* 1993,*54*, 181-342.
- [26] Gougoussis, C. ;Calandra, M.;Seitsonen, A.;Brouder, C.;Shukla, A.;Mauri, F. *Phys. Rev. B***2009**, *79*, 045118.
- [27] Cummings,C. Y.;Bonné,M. J.;Edler, K. J.; Helton,M.;McKeeb,A.;Marken, F.;*Electrochem. Comm.***2008**, *10*, 1773-1776.
- [28] Boudjemaa,A.;Boumaza,S.;Trari,M.;Bouarab, R.;Bouguelia, A. *Int. J. Hyd.Energ.***2009**, *34*, 4268 – 4274.

- [29] Gilbert, B.;Kim, C.S.;Dong, C. L.;Guo, J.;Nico, P. S.; Shuh, D.K. *AIP Conf. Proc.* **2007**, 882, 721-725, X-ray absorption fine structure - XAFS13: 13th International Conference; doi:10.1063/1.2644643
- [30] Díez-Pérez, I.; Sanz, F.; Gorostiza P.*Electrochem. Comm.***2006**, 8, 1595-1602.
- [31] Kendelewicz,T.;Liu,P.;Doyle,C.S.;Brown Jr.G.E., Nelson,E.J.;Chambers, S.A. *Surf. Sci.* **2000**, 453, 32–46.
- [32] Braun,A.;Akurati,K.K.;Fortunato,G.;Reifler, F.A.; Ritter,A.;Harvey,A.S.;Vital, A.;Graule,T. *J. Phys. Chem. C* **2010**, 114 , 516–519.
- [33] Bora, D. K.;Braun, A.;Erat, S.; Ariffin, A. K.; Löhnert, R.; Sivula, K.; Manzke, R.; Töpfer, J.;Grätzel,M.;Graule,T.;Constable,E. C. *J. Phys. Chem. C* **2011**, 115, 5619.

## **Chapter 9**

### **In situ electronic structure study of Si - doped hematite film under photoelectrochemical operation with soft X- ray absorption spectroscopy**

The following analysis of NEXAFS spectra and scientific rational is provided and derived by A. Braun in ref. [14, to be submitted/or in preparation]

#### **9.1 Introduction**

The motivation is to study the electronic behavior of the hematite electrode in a working photo-electrochemical cell with in situ soft x-ray absorption spectroscopy under bias and illumination.

#### **9.2 Materials and methods**

The films were deposited on Si frames of 5mm x 5 mm area, 0.5 mm thickness, with a 1 mm x 0.5 mm wide  $\text{Si}_3\text{N}_4$  window of 100 nm thickness (Silson Ltd., JBJ Business Park, Northampton Road, Blisworth, Northampton NN7 3DW, England). Prior to deposition, 1 nm Cr and 10 nm Au layers were evaporated on the  $\text{Si}_3\text{N}_4$  window in order to provide an adhesive metallic current collector between  $\text{Fe}_2\text{O}_3$  and  $\text{Si}_3\text{N}_4$ . The 1% Si doped hematite was deposited by ambient pressure chemical vapor deposition as described in [1]. The non-doped hematite was deposited by distributing a sol-gel solution over the window and heating the assembly for 30 minutes at  $500^\circ\text{C}$  in an air vented furnace. Synthesis and composition of the precursor solution is described in chapter 6 or elsewhere [2]. Using a specifically designed soft X-ray in-situ/operando cell as outlined in [3], it was possible to carry out the photo-electrochemical experiment under potentiostatic and galvanostatic conditions (FemtoStat FAS2, Gamry Instruments, Warminster, PA 18974, USA) with 1m NaOH electrolyte. The electrolyte was continuously exchanged during the experiment using a peristaltic pump. Figure 1 displays a schematic sketch of the substrate-film-cell assembly in contact with the NaOH electrolyte.

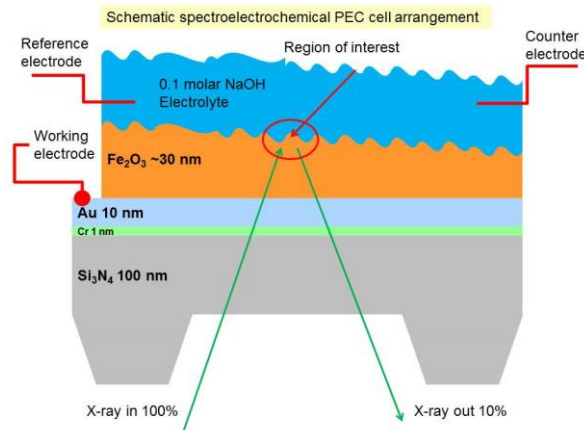


**Figure 9.1:** Sketch of cell assembly and film on Si<sub>3</sub>N<sub>4</sub> membrane [Courtesy: Dr. Artur Braun].

## Results and Discussion

Oxygen K-edge spectra are sensitive to the local bonding and symmetry properties of the excited oxygen atom. The oxygen (1s) pre-peak structure of 3d metal oxides is governed by the 3d components in the hybridized unoccupied *pd* wave functions [4]. The O1s NEXAFS spectrum of hematite is known to have a well-developed doublet in the pre-edge region at 530 eV, which originates from transitions of hybridized Fe(3d)-O(2p) states with  $t_{2g}$  and  $e_g$  orbital symmetry [5,6].

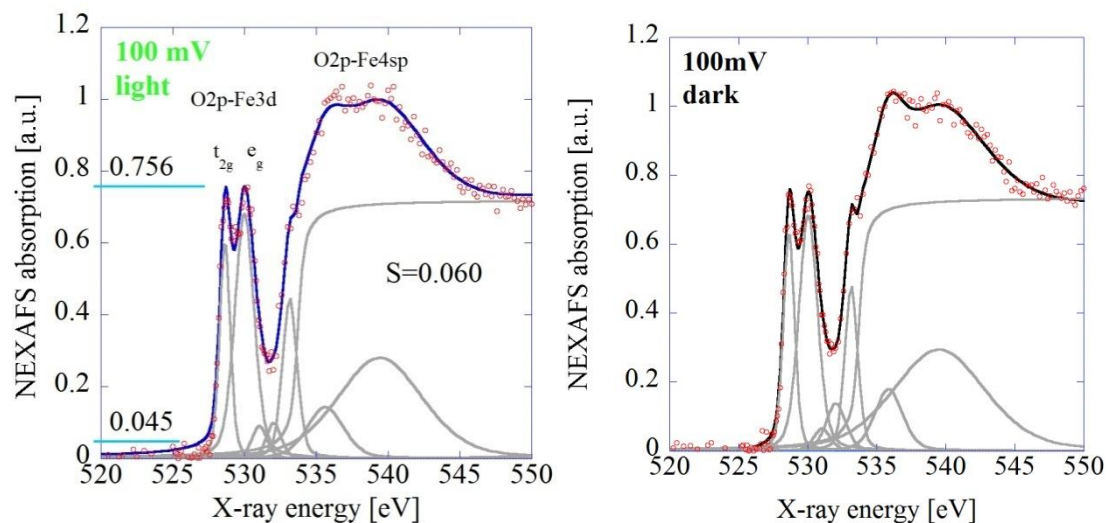


**Figure 9.2:** Oxygen 1s NEXAFS spectra recorded at 100 mV bias under a) light (left) and b) dark (right) condition [Courtesy: Dr. A. Braun].

The oxygen NEXAFS spectrum in Figure 9.2 (a) shows such pre-edge doublet at around 530 eV and the Fe4sp-O2p derived resonances at 535 eV to 545 eV. Note that this spectrum is obtained from the Si doped hematite film in contact with the NaOH electrolyte under a reverse bias potential of 100 mV vs. Ag<sup>+</sup>/AgCl. At first glance, there are no obvious spectral

differences with the film exposed to 1.5 AM light, as shown in Figure 1-b. However, when I increased the potential to 300 mV and point light on the electrode, I noticed that the pre edge region is increased in intensity. This is obvious in Figure 9.3, where the spectra at 300 mV under dark and light condition are plotted together for convenient and direct comparison.

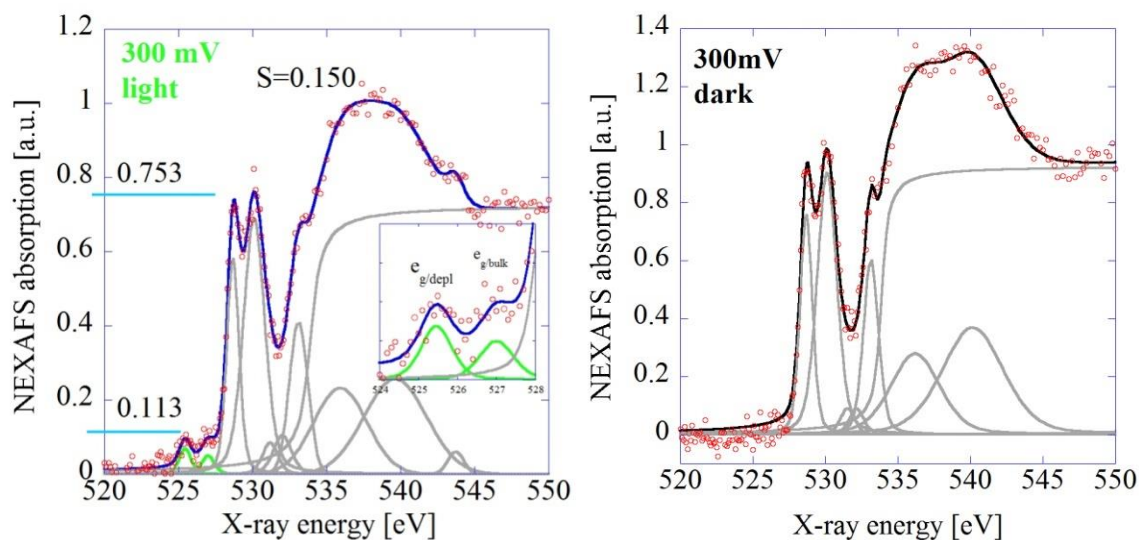


**Figure 9.3:** Oxygen 1s NEXAFS spectra recorded at 300 mV bias under a) light (left) and b) dark (right) condition [Courtesy: Dr. A. Braun].

This new feature has been observed clearly for the bias potentials of 300 mV, 500 mV, and 700 mV, when under illumination. At 900 mV a slightly enhanced intensity before the pre-edge could be made out, though it was difficult to precisely quantify its small relative spectral weight. The occurrence of new transitions before the pre-edge doublet of oxygen NEXAFS spectra in metal oxides has been associated with electron holes incurred by doping on the A-site of perovskites [7], and also with holes from B-site doping [8]. While a correspondence between electric conductivity and hole doping peak has been postulated, a clear quantitative relationship has been found only recently [9]. In particular it was shown for A-site and B-site substituted  $\text{LaFeO}_3$  that its relative spectral weight of such hole transitions and the pre-edge doublet scales exponentially with the electronic conductivity and linear with the relative hole concentration [10]. Given the fact that these new transitions only occur under bias plus illumination, it is reasonable to assume that they originate from the same electron hole transitions which cause the photocurrent.

In the spirit of the approach exercised in [9], the oxygen spectra into specific transitions has been deconvoluted so as to be able to quantitatively determine the relative spectral weight of the new pre-edge peaks and the  $t_{2g}$ - $e_g$  doublet. Closer inspection of the spectrum collected at 300 mV under illumination shows that the hole peak intensity can hardly be represented by one

transition only. In fact, inclusion of two transitions represents this range of the spectrum better; identify thus a transition at around 525.46 eV and at around 527.00 eV, with a peak separation of 1.55 eV. The same holds for the spectra recorded under illumination at 500 mV (525.80 eV, 527.06 eV; 1.26 eV) and 700 mV (525.30 eV, 527.15 eV; 1.85 eV) [Figure 9.4]

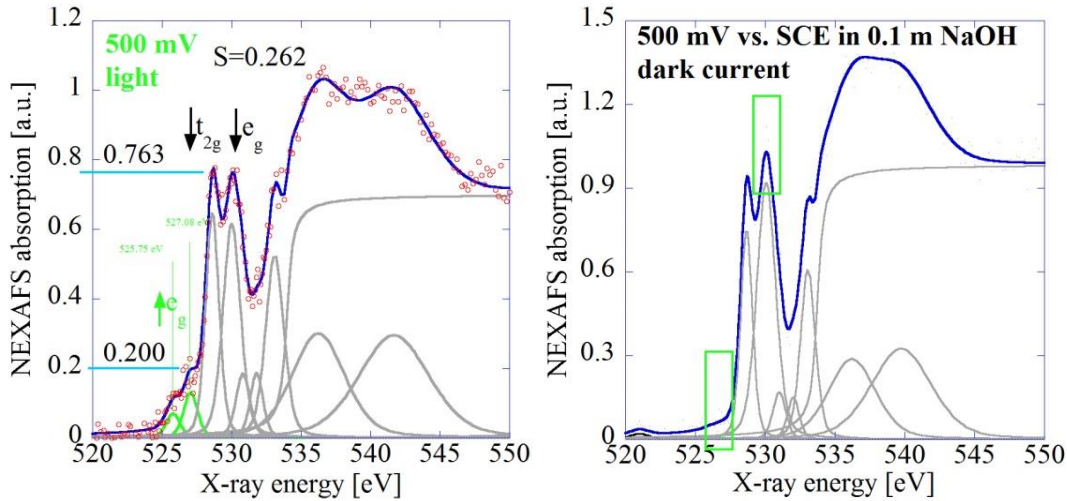


**Figure 9.4:** O1s spectra recorded at 500 mV bias under light (left) and dark (right) condition [Courtesy: Dr. A. Braun].

Because the photocurrent flowing through the hematite is known to be caused by holes generated in the depletion layer and by the holes generated in the bulk [11, 12], it is believed that the two new hole peaks in the O1s NEXAFS spectra can be specifically assigned to the photocurrent from the depletion region and from the bulk diffusion region. It tentatively associates the leading peak at around 525.50 eV with the electron hole generated in the depletion layer ( $e_{g\uparrow}^{CT}$ ), and the following peak around 527 eV as the electron hole peak generated in the bulk ( $e_{g\uparrow}^{UHB}$ ). A similar case where two different types of electron holes have been observed in the O1s NEXAFS spectra is the Sr-substituted  $\text{La}_2\text{CuO}_4$  high temperature superconductor [13]. The low-energy peak had been assigned to an O2p-type electron hole transition into the charge transfer (CT) band, whereas the high energy peak was attributed to a more Fe3d-type electron hole transition into the upper Hubbard band (UHB). In this context, the O2p-type electron hole  $e_{g\uparrow}^{CT}$  is assigned and it goes into the charge transfer band the relative spectral weight  $S^{CT} = \frac{e_{g\uparrow}^{CT}}{t_{2g\downarrow} + e_{g\downarrow}}$ , and the Fe3d-type electron hole  $e_{g\uparrow}^{UHB}$  into the upper Hubbard band the relative spectral weight  $S^{UHB} = \frac{e_{g\uparrow}^{UHB}}{t_{2g\downarrow} + e_{g\downarrow}}$ . For 300 mV bias, the peak  $e_{g\uparrow}^{CT}$  has clearly higher intensity than the  $e_{g\uparrow}^{UHB}$  peak, see inset in Figure 9.3.a. The spectral weights  $S^{CT}$  and  $S^{UHB}$  from all spectra recorded under illumination versus the bias potential V have been plotted and it is noticed that

$S^{CT}$  (for the depletion layer holes) have their maximum around 400 mV, whereas  $S^{UHB}$  (for the bulk holes) have the maximum at around 500 mV. The sum of both  $S = \frac{e_{g\uparrow}^{CT} + e_{g\uparrow}^{UHB}}{t_{2g\downarrow} + e_{g\downarrow}}$  has the maximum at around 500 mV.

When compare the evolution of the hole peak heights with the photocurrent, see Figure 9.5, we notice a striking parallelism. It shows the experimentally obtained current obtained in dark (black line) and 1.5 AM illumination condition (grey line). The photocurrent (green line) was obtained by subtraction of both currents. The dark current is negligible up to 500 mV and evolves substantially at 600 mV. The photocurrent increases exponentially for -20 mV to 200 mV. For -20 mV to 200 mV, the photocurrent follows a linear characteristic. For 300 mV to 520 mV, the photocurrent can be approximated by a linear curve, but with by a factor 6 smaller slope than in the previous potential range. Above 570 mV, the photocurrent decreases as sharply as it increases between -20 mV and 200 mV. These characteristic ranges are indicated by dotted lines and highlighted by color panels in Figure 9.5. The sum of the spectral weight of the both types of holes  $S = \frac{e_{g\uparrow}^{CT} + e_{g\uparrow}^{UHB}}{t_{2g\downarrow} + e_{g\downarrow}}$  is also plotted in Figure 9.5 (square symbols with orange line).

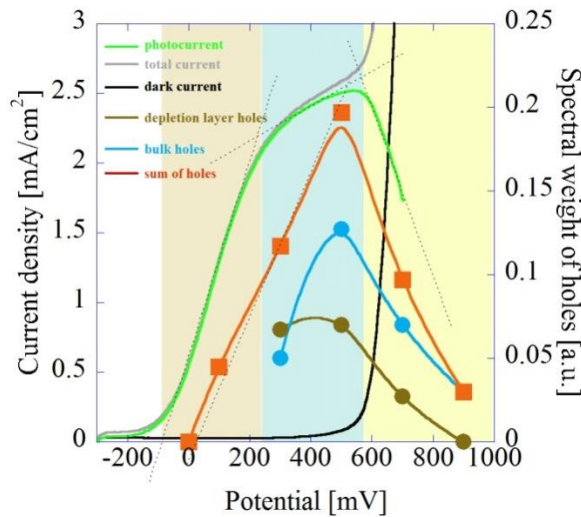


**Figure 9.5:** Comparison of photocurrent (green line) and spectral weight (orange line with filled squares) [Courtesy: Dr. A. Braun].

Re-inspection of the spectrum recorded under light at 100 mV shows that there is a slight enhanced intensity of 0.045 at around 525 eV, which also include as data point for the spectral weight of holes at 100 mV. For the potentials of 300 mV and 500 mV, the spectral hole weight increases to 0.12 and 0.2. The maximum spectral weight for holes coincides with the

photocurrent maximum at around 500 mV, as well as the steep increase of both from 0 mV to 500 mV. Above 500 mV, the spectral weight decreases as rapidly as the photocurrent.

The hematite film in the NaOH electrolyte has been interpreted in the framework of the Schottky barrier theory and includes here also the carrier formation in the depletion layer after [11]. The width of the depletion layer  $w(V)$  extends from the semiconductor-electrolyte junction into the bulk of the semiconductor, and scales with the square root of the potential  $V$  and is pinned by the flat band potential  $V_{FB}$ :  $w(V) \sim w_0 \sqrt{V - V_{FB}}$ . Following the discussion, the equation for the total photocurrent density under monochromatic illumination is derivatized; which is given by

$$J_{TOT} = -q\Phi \left[ \frac{1 - e^{-aw}}{1 + aL_p} \right] - \frac{qp_0 D_p}{L_p}$$

and depends on the photon flux  $\phi$ , absorption coefficient  $a$ , minority carrier (hole) diffusion length  $L_p$  and diffusion coefficient for holes  $D_p$ , depletion layer width constant  $W_0$ , equilibrium hole density  $p_0$  according to Gärtner's derivation [11].  $J_{TOT}$  contains the current generated in the depletion layer and in the diffusion layer. Note that in our experiment we have used 1.5 AM solar simulated light, and not monochromatic light. When we look in Figure 5 at the variation of the spectral weight  $S^{CT} = \frac{e_{g\uparrow}^{CT}}{t_{2g\downarrow} + e_{g\downarrow}}$  with the bias potential  $V$ , we notice a square-root like trend for the potentials up to 500 mV, and after that a decay. This, together with the fact that the depletion layer  $w$  also scales square-root like with the bias potential as  $(V) \sim w_0 \sqrt{V - V_{FB}}$  [Gärtner 1959, Butler 1977], leads us to assume that  $e_{g\uparrow}^{CT}$  is the hole formed in the depletion layer. Then,  $e_{g\uparrow}^{UHB}$  is the hole formed in the bulk diffusion layer.

#### 9.4 Conclusion

The oxygen 1s soft x-ray absorption spectra of hematite and 1% Si doped hematite thin films in solid-liquid junction with 0.1 molar NaOH electrolyte have been recorded *operando* under electrochemical polarization from 0 mV to 900 mV vs.  $Ag^+/AgCl$  reference. Under 1.5 M illumination and at between bias potentials of 300 mV and 900 mV, new spectral signatures evolve at the oxygen pre-edge before the  $t_{2g\downarrow} - e_{g\downarrow}$  doublet, which we assign to  $e_g$  spin up symmetry transitions due to photo-generated electron holes in the valence band. The relative spectral weight  $S$  of the new transition depends on the electrochemical potential applied and has its maximum at 500 mV. Quantitative analysis of the spectra clearly shows that  $S$  scales quantitatively with the photocurrent, revealing that the photocurrent is a consequence of the

electron hole generation under light and energy band bending by the applied bias potential. Without 1.5 AM illumination, no pre-edge feature was detected, irrespective of the applied potential. Without Si doping, also no pre-edge feature was detected, irrespective 1.5 M illumination or applied potential. Close inspection and analysis of the spectra show that the new pre-edge features originate from two different transitions. The one at lower x-ray energy is an O2p electron hole transition in the charge transfer band (CT), whereas the subsequent one is a Fe3d type transition into the upper Hubbard band (UHB). The variation of their corresponding S ratios  $S^{CT} = \frac{e_{gl}^{CT}}{t_{2gl} + e_{gl}}$ , and  $S^{UHB} = \frac{e_{gl}^{UHB}}{t_{2gl} + e_{gl}}$  with bias potential shows that the leading pre-edge peak gains intensity at a lower bias potential than the following one. The sigmoidal curvature of the CT transition, i.e. a square-root like characteristic, suggests that the electron holes for  $S^{CT}$  are created in the depletion layer, whereas the holes from  $S^{UHB}$  are created in the bulk diffusion layer

## References

- [1] Sivula, K.; Le Formal, F.; Grätzel, M. *Chem. Mater.* **2009**, *21*, 2862–2867.
- [2] Bora, D. K.; Braun, A.; Erat, S.; Ariffin, A. K.; Löhnert, R.; Sivula, K.; Manzke, R.; Töpfer, J.; Grätzel, M.; Graule, T.; Constable, E. C. *J. Phys. Chem. C* **2011**, *115*, 5619.
- [3] Jiang, P.; Chen, J.; Borondics, F.; Glans, P.; West, M. W.; Chang, C.; Salmeron, M.; Guo, J. *Electrochem. Comm.* **2010**, *12*, 820-822.
- [4] Pollak, M.; Gautier, M.; Thromat, N.; Gota, S.; Mackrodt, W.C.; Saunders, V.R. *Nucl. Instrum. Methods* **1995**, *B97*, 383-386.
- [5] Wu, Z.Y.; Gota, S.; Jollet, F.; Pollak, M.; Gautier-Soyer, M.; Natoli, C.R. *Phys. Rev. B* **1997**, *55*, 2570-2577.
- [6] Colliex, C.; Manoubi, T.; Ortiz, C. *Phys. Rev. B* **1991**, *44*, 11402-11411.
- [7] Abbate, M.; de Groot, F. M. F.; Fuggle, J. C.; Fujimori, A.; Strebel, O.; Lopez, F.; Domke, M.; Kaindl, G.; Sawatzky, G. A.; Takano, M.; Takeda, Y.; Eisaki, H.; Uchida, S. *Phys. Rev. B* **1992**, *46*, 4511.
- [8] Erat, S.; Braun, A.; Ovalle, A.; Piamonteze, C.; Liu, Z.; Graule, T.; Gauckler, L.J. *Appl. Phys. Lett.* **2009**, *95*, 174108.
- [9] Braun, A.; Bayraktar, D.; Harvey, A.S.; Beckel, D.; Purton, J.A.; Holtappels, P.; Gauckler, L. J.; Graule, T. *Appl. Phys. Lett.* **2009**, *94*, 202102.

[10] Braun, A.; Akurati, K.K.; Fortunato, G.; Reifler, F.A.; Ritter, A.; Harvey, A.S.; Vital, A.; Graule, T. *J. Phys. Chem. C* **2010**, *114*, 516–519.

[11] Gärtner, W. *Phys. Rev.* **1959**, *116*, 84–87.

[12] Butler, M.A. *J. Appl. Phys.* **1977**, *48*, 1914–1920.

[13] Chen, C. T.; Sette, F.; Ma, Y.; Hybertsen, M. S.; Stechel, E. B.; Foulkes, W. M. C.; Schuler, M.; Cheong, S. W.; Cooper, A. S.; Rupp, Jr., L. W.; Batlogg, B.; Soo, Y. L.; Ming, Z. H.; Krol, A.; Kao, Y. H. *Phys. Rev. Lett.* **1991**, *66*, 104–107.

[14] Artur Braun, Kevin Sivula, Debajeet K. Bora, Liang Zhang, Jinghua Guo, Michael Grätzel, Edwin C. Constable Direct observation of two different electron holes in hematite during the photo-electrochemical water splitting process, to be submitted/or in preparation.

## **Part III: Hybrid nanostructures based on hematite for PEC application: properties and functionality**

## Chapter 10

# Hydrothermal Treatment of a Hematite Film Leads to Highly Oriented Faceted Nanostructures with Enhanced Photocurrents

### 10.1 Introduction

The development of different hematite based hierarchical nano-architectures such as nanowires, nanobelts, nanotubes, nanorods, flower-like, urchin-like and elliptic superstructures or dendritic micropines is an emerging strategy for the design of functionalized devices [1–7]. Most of these structures have been fabricated using hydrothermal reactions, chemical vapor deposition or ionic liquid-assisted routes. In the case of hydrothermally grown structures, the morphology can be controlled by moderating the aqueous hydrolysis-condensation growth onto substrates [8]. Also with the application of hydrothermal strategy, different morphologies of hematite were fabricated besides from those mentioned above [9–18]. Solvothermally grown rod-like and flower-like hematite nanostructures have been used in gas sensors and batteries, and as photocatalysts [19, 20]. Hydrothermal synthesis in highly basic medium has been used to obtain nanorods [21] and the solution pH has a profound influence on the morphology [22]. With the aim to increase the photocurrent of undoped hematite films, I have developed a very simple and effective hydrothermal procedure for modifying the structures of hematite nanoparticles in the pristine film into array of nanorods, on which flower like superstructure evolve upon hydrothermal treatment, as shown in Figure 10.3. This was achieved by the hydrothermal after treatment of the pristine hematite thin film in a closed vessel filled with iron (III) chloride and L-arginine. The amino acid was found to play a decisive role in directing the morphology of the nanostructures. The amino acid assisted hydrothermal method has already been demonstrated for the synthesis of SnO<sub>2</sub> nanocrystals and hematite nanocubes [23, 24]. The modified nanostructure grows in a hierarchical fashion from single nanorods to stellate objects. Such sequential growth of nanostructures follows the same pattern as that observed on WO<sub>3</sub> [25] and besides this supports the idea that biomolecules act as effective templates for the growth and self-assembly of nanostructures [26, 27].

### 10.2 Experimental Section

#### *10.2.1 Synthesis of pristine hematite film and corresponding hydrothermal treatment*

Iron salts, oleic acid and tetrahydrofuran (THF) used in the synthesis of hematite film were of reagent grade obtained from Sigma-Aldrich. The amino acid (L-Arginine) used was obtained

from Sigma- Aldrich, Switzerland (99. 9% pure). Nanostructured Hematite ( $\alpha$ - $\text{Fe}_2\text{O}_3$ ) thin films were synthesized by the dip coating of a precursor complex on an FTO-coated glass substrate with a withdrawal speed of 1mm/sec, followed by annealing in air at  $500^\circ\text{C}$  for 2 hr. The dip coating is a steady process and here the film thickness is determined by the competition of different forces such as viscous force, capillary force and gravity [28]. Faster withdrawal yields generally thicker films. The precursor complex was synthesized by heating a mixture of  $\text{Fe}(\text{NO}_3)_3 \cdot 9\text{H}_2\text{O}$  (28. 0 g) and oleic acid (17. 0 g) to  $70^\circ\text{C}$  to give homogenous liquid phase [29]. The homogeneous mixture was then heated at  $125^\circ\text{C}$  for 1. 5 hrs. to give a reddish brown viscous mass which was then cooled to room temperature, left for 24 h and subsequently treated with 80 ml of tetrahydrofuran. The resultant solution was stirred with a glass rod for 30minute and the final powdery precipitate separated from the solution by centrifugation (5000 rpm) for 2-3 min. After centrifugation the supernatant containing the precursor complex was used for the dip coating of the film. The thicknesses of these pristine hematite films were measured with profilometry and optimized at 600 nm after four layer deposition.

The flower like superstructure along with array of nanorod were synthesized over the intact hematite film by an amino acid assisted hydrothermal reaction. The pristine hematite film above was first immersed in a solution of  $\text{FeCl}_3 \cdot 6\text{H}_2\text{O}$  (5 mmol) and L-arginine (5 mmol) in water (35ml) in closed vessel and allowed to react for 48 h at a temperature of  $95^\circ\text{C}$ . After 48 hr., the film was removed, washed with distilled water and dried at room temperature overnight. The dried films was then further characterized by UV–Vis spectroscopy, XRD, FESEM, TEM, XPS, BET and current density was recorded in a photoelectrochemical workstation.

### **10.2.2 Characterization**

The optical properties of the pristine hematite and hydrothermally modified films were studied by UV –Vis spectrometer (Cary Scan 50). Diffuse reflectance spectroscopy of pristine and modified films has been studied with Cary 5000 (V1. 12) UV-Vis-NIR Spectrophotometer with an integrating sphere diffuse reflectance accessory. The Integrating sphere was coated with MgO and the spectra were referenced against these white material. The film thickness was determined with a stylus profilometer (Ambios XP-100). The phase composition of the pristine and modified films was examined by powder X-ray diffraction analysis (PAN analytical X'Pert PRO,  $\text{Cu K}_\alpha$  radiation). A JEOL JEM 2200 FS transmission electron microscope/STEM operating at 200 keV accelerating voltage was used for TEM analysis. Field emission scanning electron microscopy was performed on a Hitachi S-4800 model. The dark current and photo current was recorded with a Voltalab® potentiostat in a three electrode configuration with 1M KOH (pH=13. 6) as electrolyte, Ag/AgCl/sat. KCl as reference and a platinum wire as counter

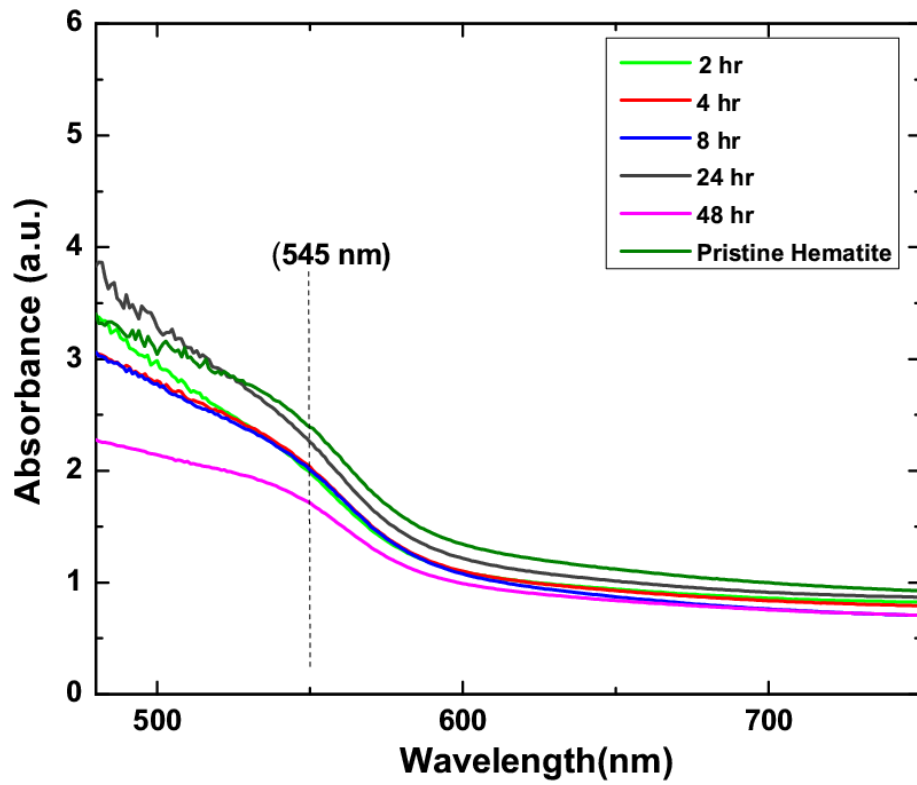
electrode. The  $\text{Fe}_2\text{O}_3$  film was illuminated on a  $0.45 \text{ cm}^2$  area of electrolyte and a fused silica window with a  $0.5 \text{ cm}^2$  circular mask, the total geometric area immersed in electrolyte was approximately  $2.6 \text{ cm}^2$ . Sunlight was simulated with a filtered xenon lamp from LOT Oriel®. The light intensity was adjusted to AM 1.5 simulated light. X-ray photoelectron spectra were recorded by a PHI LS5600 spectrometer equipped with Mg  $K\alpha$  X-ray source, spectra calibrated using  $\text{C}1s = 285.0 \text{ eV}$ . The surface area of the pristine film and hydrothermally treated films was obtained by applying the BET technique (Coulter SA3100 Series Surface area and Pore Size Analyzers) on powders, which were scratched from the films.

### 10.3 Results and Discussion

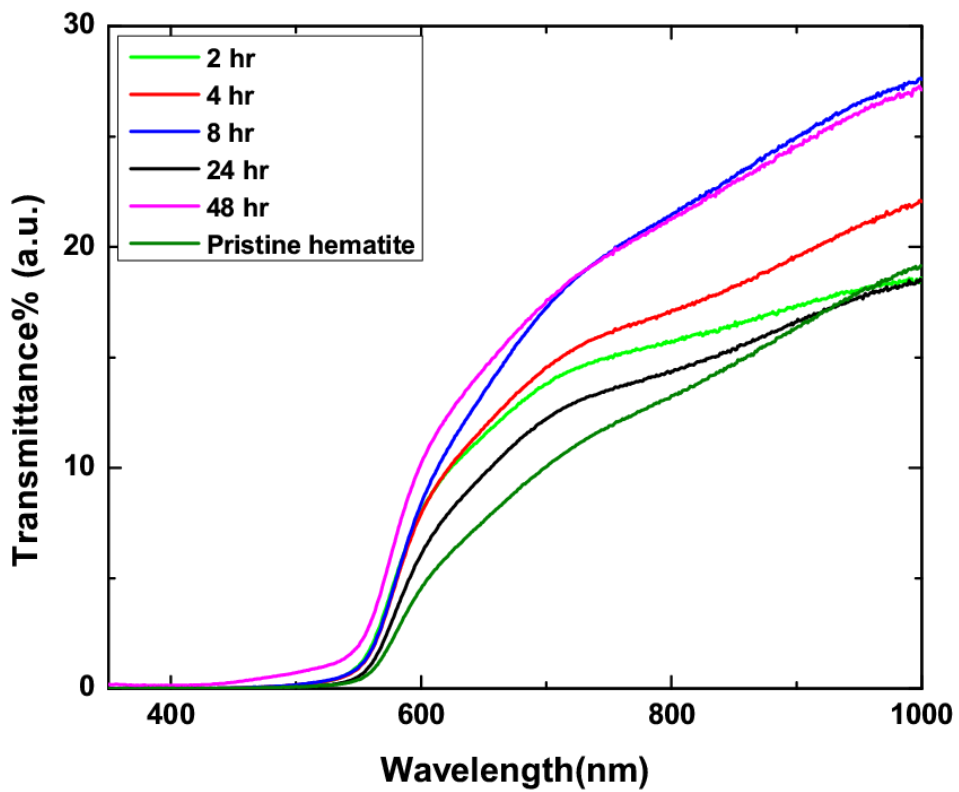
Due to the importance of optical absorption properties and electronic nature of the band gap in hematite on the solar energy conversion I have studied changes in optical property of hematite with UV-Vis spectroscopy after hydrothermal modification. The absorbance spectra (Figure 10.1-A) shows that hydrothermally modified films absorb at  $545 \text{ nm}$  which is the absorption edge of pristine hematite. Here, the absorption intensity decreases from pristine to 48 hr. treated film with increasing hydrothermal time. In the case of sample hydrothermally treated from 2-8 hr., it remains constant. The 24 hour treated sample shows some unusual behavior. It exhibits the same absorption characteristics as that of pristine film. These variations in absorption value of pristine and hydrothermally treated films can be explained by considering the effect of scattering contribution. To obtain quantitative information about the scattering contribution I have applied Kubelka-Munk (KM) function to the diffuse reflectance spectra (as shown in inset of Figure 10.1- D) of hematite and modified films with following equation

$$f(R) = \frac{(1-R)^2}{2R} = \frac{k}{s} \quad (1)$$

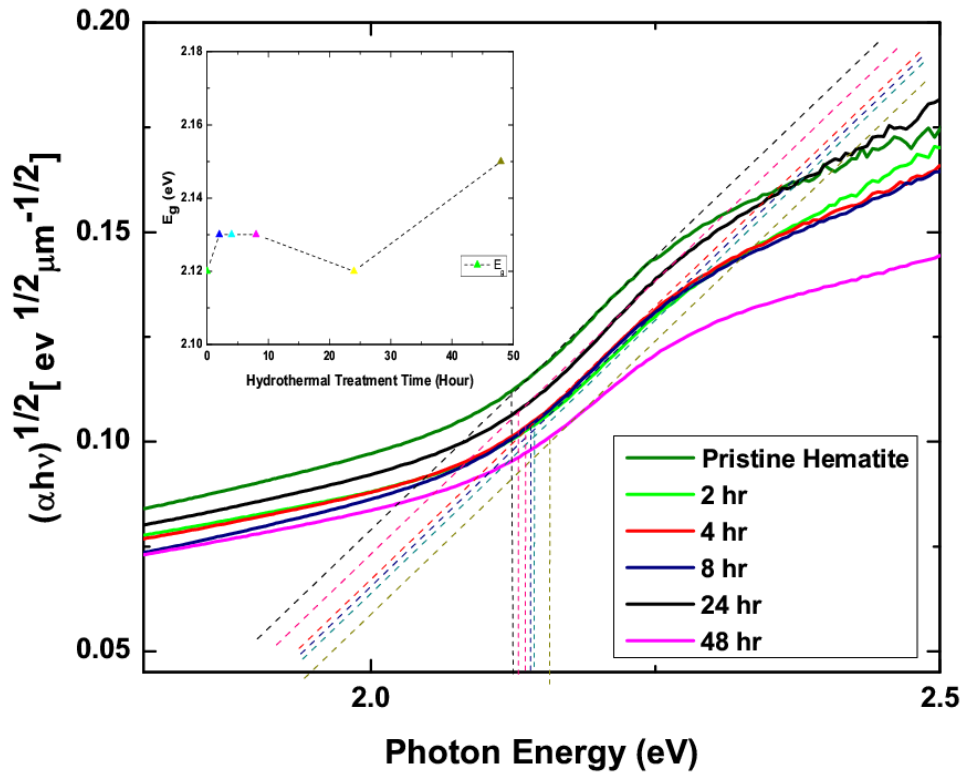
R is the diffuse reflectance of the layer relative to standard such as magnesium oxide, “k” is the molar absorption coefficient and “s” is the scattering coefficient of the sample. The respective diffuse reflectance spectrum can be seen in inset of figure 10.1- D. On analyzing the reflectance spectra; I have found that scattering coefficient (Figure 10.1- D) varies in a significant manner from pristine to 48 hour film. The effect is more prominent for 2, 4 and 8 hour sample between  $300 - 600 \text{ nm}$ . In the long term hydrothermally treated samples, the scattering coefficient also changes with the wavelength. The light scattering properties of the films thus changes with morphology and the observed optical changes are associated with these changes in scattering coefficient. This change in scattering coefficient is basically due to the variation in the crystal size and morphology as a result of hydrothermal treatment. In this case



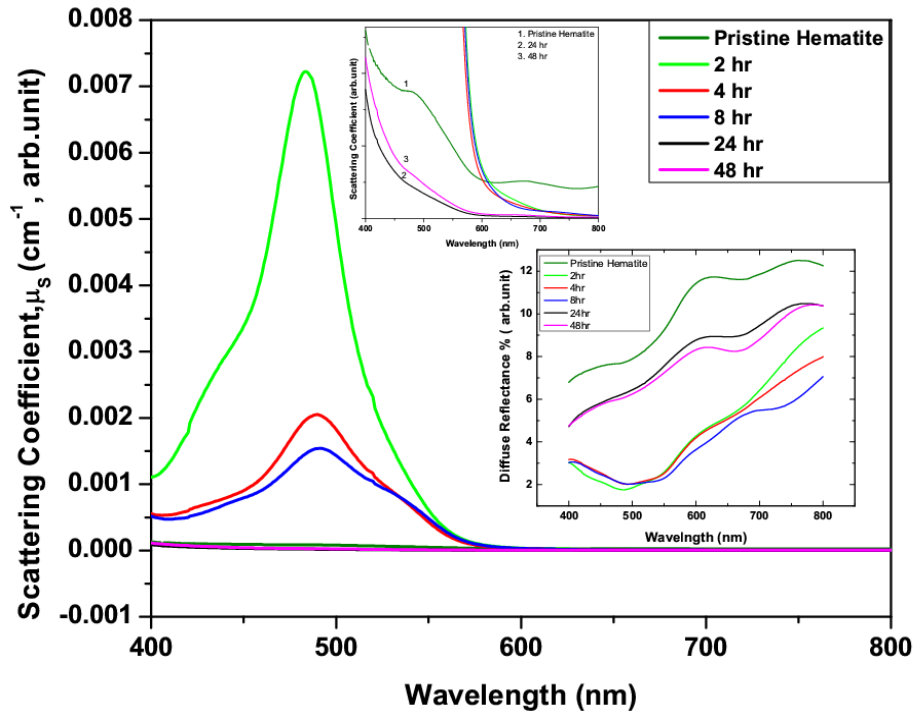
A.



B.



C.



D.

**Figure 10.1:** Optical properties of pristine and modified hematite thin films A. Absorbance spectrum showing the visible light absorption of hematite at 545 nm, B. Transmittance spectra, C. Evaluation of optical band gap using Tauc plot. D. Variation of scattering coefficient with

hydrothermal time calculated by applying the Kubelka- Munk function to diffuse reflectance spectra (inset).

The crystallite size changes as a result of increasing hydrothermal treatment time as evident from crystallite size calculation (Table S1, supporting information). It was originally found that variations in crystal size and morphology [30] altered the scattering and absorption coefficients of goethite and hematite. Another possible reason for increase in the magnitude of scattering coefficient is the roughening of the nanoparticle surface after hydrothermal treatment which affects the mean path length of the rays though the particle, thus decreasing the amount of light absorbed [31].

From the transmittance spectra (Figure 10.1-B) of pristine hematite and modified films, I have not found any precise variation in film transmittance with the corresponding increase in hydrothermal time. Although the transmittance gets decrease as evident by looking into spectra of modified films with respect to pristine film in the region  $\lambda = 400$  to  $800$  nm. It is observed that the film become more transparent after 2 hr. treatment and it getting enhanced up to 8 hr. It becomes again less transparent after 24 hr. treatment which might be due to increase in layer thickness from the larger density of globular flower as evident from the FESEM image (Figure 11). Again at 48 hr., transmittance gets increased and coincides with the 8 hr. processed film. These changes in film transmittance can be explained on the basis of contribution of different factors. In pristine and hydrothermally treated films, the change in the spectral transmission occurs by an increase in the particle dimensions which affected by interplay of two factors. These are respectively the decrease in the number of scattering centers and an increase in the coefficient of attenuation of light by a single particle [32]. In the region of strong absorption (for hematite ,  $\lambda \sim < 600$  nm), it was evident from other study that the second factor well prevailing than first one which leads to a decrease in the spectral transmission with increasing particle dimensions. But in our case, I have not observed similar trend. It increases with increase in the dimension of the particle from the pristine to hydrothermally modified film. In the region  $\lambda > 600$  nm there is no any definite tendency in the variation of spectral transmission with increase in the mean particle dimensions. This can also be related to the uncontrolled variations in the structure of the hematite layer with increase in the mean particle dimensions and morphological change due to hydrothermal treatment. In the next part, I have considered the shape of the flower to have some effect on the optical properties. It was already reported that absorption properties of hematite changes as a result of change in the shape up to  $400$  nm [33]. To get an idea about the changes occurs, I have calculated the band gap of pristine and modified film using Tauc plot [34] for indirect transition (Figure 10.1-C), which states that

energy bands are parabolic with respect to the crystal momentum. Hematite have an indirect phonon assisted band gap transition around 1.9-2.2 eV [35]. Band gap varies slightly with the increase in hydrothermal treatment time as observed from the figure. All the films showing the band gap around 2.12-2.15 eV using similar Tauc fit and falls within the hematite band gap range. This pointed out that I have no changes in the electronic structure of pristine hematite film after hydrothermal treatment. Another interesting observation that can be seen is the change in the slope of the transition with respect to hydrothermal time and is maximum in case of 48 hour sample. A similar result was also observed in case of annealed mesoporous hematite and correlated this with nanoparticle size and detailed structural investigation [36]. The slope is proportional to band tailing parameter ( $\beta$ ) [37] which relates the distribution of energy states near the valence and conduction bands. It is consistently increase with increase in crystalline order and a larger particle size [38] and validated further from the calculation of the nanocrystallite size with increase in hydrothermal time as discussed in the following section.

The X-ray diffractogram of the pristine film shows an overall lower incoherent scattering background than that of the modified film (Figure 10.2) which signifies that the new flower like superstructures and array of nanorod constitute a larger roughness on the nanoscale than the pristine film. The modified film shows more prominent Bragg reflections than the pristine film. Closer inspection of the diffractograms shows that the intensities of the (104) Bragg reflection in the modified film diffractogram becomes relatively enhanced when compared with the same reflection in the pristine hematite diffractogram, suggesting an increase of preferential orientation. This becomes particularly clear when comparing the relative intensities of the (104) reflection with that of the (110) reflection; initially in the pristine film the (104) peak is the same as that of (110) peak, see magnification of the diffractogram in the right part of Figure 10.2. In the modified film the (104) peak is larger than the (110) peak. In the pristine film, the (012) and (220) peaks are barely visible, whereas they are well developed in the modified film. The same holds for the (211) and (310) peaks. From the diffractograms of the intermediate modified films (Figure S1; supporting information), I have observed that the intensity of the (110) and (104) peak from hematite varies with the treatment time whereas the substrate peak change slightly. In the case of (104) peak intensity, the 2 hour and 8 hour treated film shows minimum and maximum value. The intensities of the 18 and 24 hour treated films remain almost constant. On the other hand, the (110) peak intensity remain constant for 8, 18 and 24 hour treated films and its minimum for 2 hour film. This change in intensity could be due to the changing film thickness, as suggested from the optical spectra (Figure 10.1-B). But careful comparison of the transmittance spectra with with the diffraction data (Figure S1-B) shows this

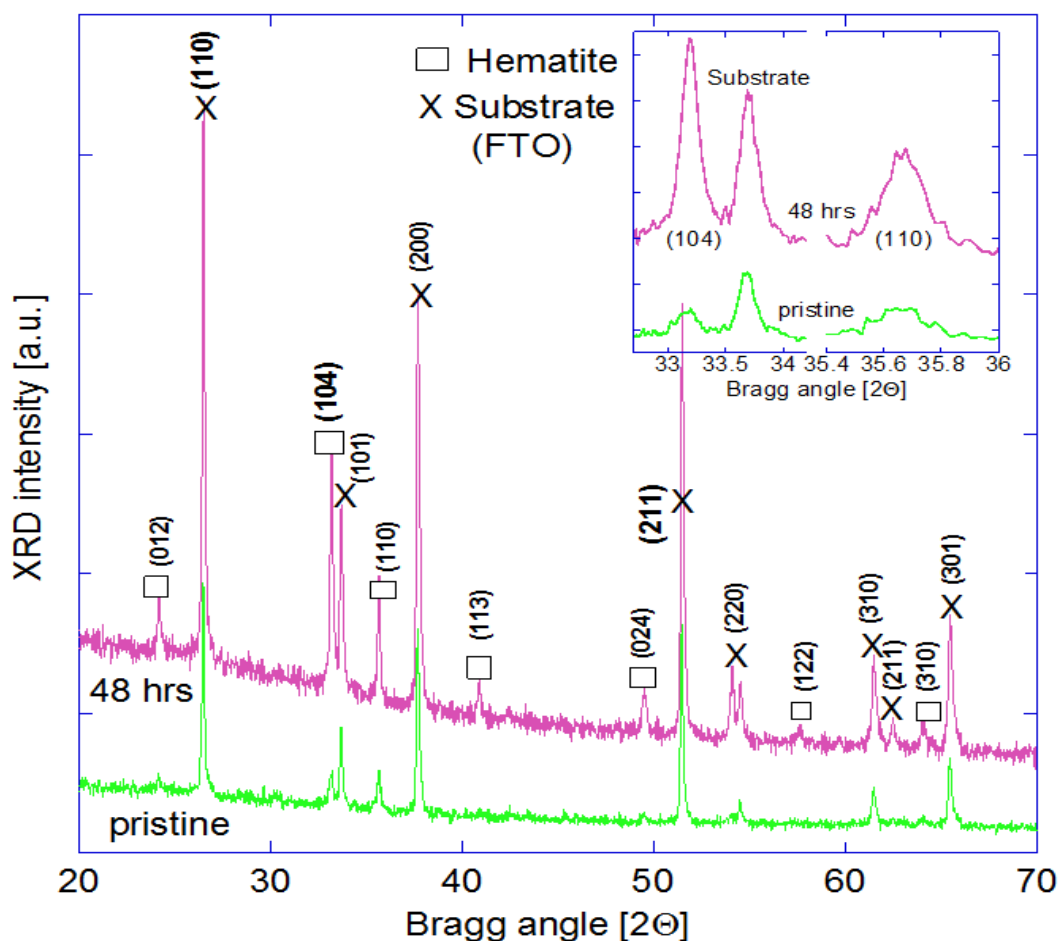


**Figure 10.2:** X-ray diffractograms of pristine film and 48 hour hydrothermal treatment film [54].

is not exactly the case. From here it can be seen that the 8 hr. treated film is more transparent than the 24 hour films, but its (104) peak intensity reached maximum in XRD diffractograms and (110) peak intensity remain constant which supports the suggestion of the preferential growth and transformation of nanoparticle into nanorod assembly and superstructure. The crystallite size, as determined with the Scherrer equation [39], is increasing during hydrothermal processing (Table S1) along with the primary particle size. From this I can justify the increase in band tailing parameter as observed in the optical properties of films. Summarizing, we can say that, while the structural peculiarities of the hematite film as evidenced by the electron diffraction pattern are representative only for the modified nanostructures, the x-ray diffractograms provide significant support that the structure of the pristine film undergoes considerable transformations towards the flower shape morphology with preferential orientation and a distinct texture different from those of the pristine hematite, in line with the visual observations on the morphology made by microscopy.

In the morphology study, Figure 10.3-d displays the field emission electron micrograph of a typical pristine hematite film with an apparent porosity between the primary particles. The primary particles look like larvae with a smooth surface and have sizes of approximately 50 nm x 100 nm.

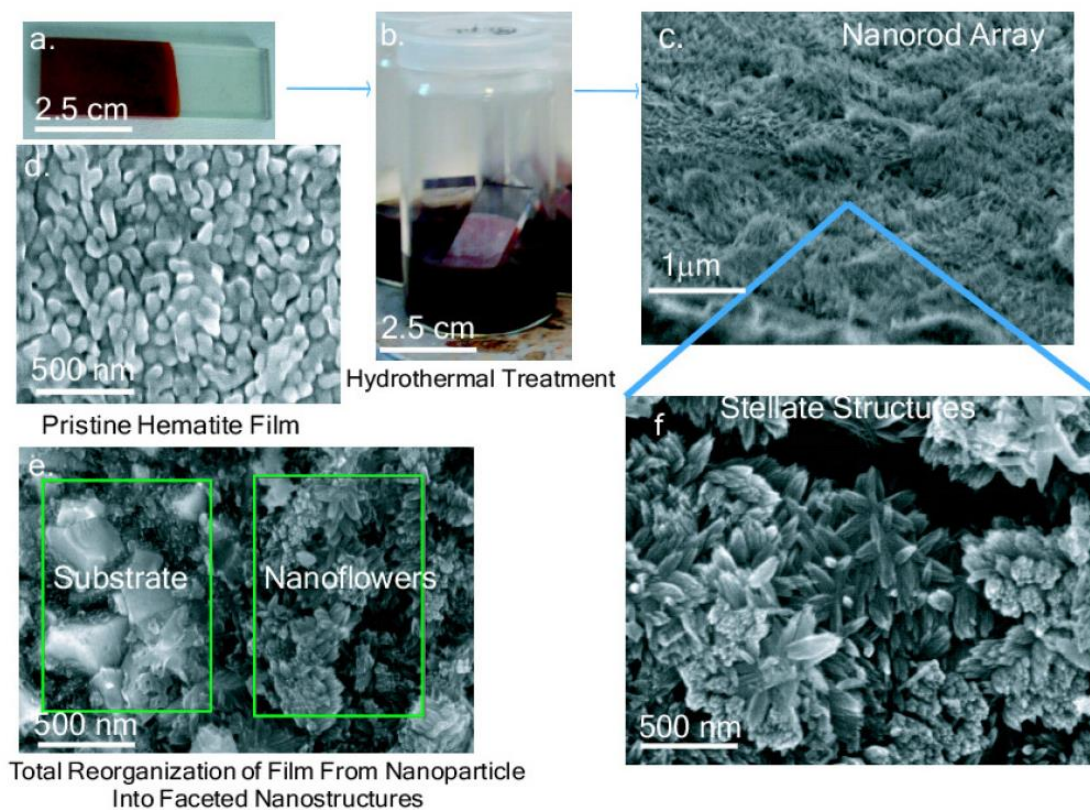


**Figure 10.3:** Scheme showing the conversion of pristine hematite film (a) into film with turf like carpet (c) upon hydrothermal after-treatment (b), FESEM images of pristine hematite film (d), total reorganization of the film (e) into stellate structure superimposed on the array of nanorod (f).

In the electron micrograph of the film after 48 hours of hydrothermal treatment, Figure 10.3-e, I notice several alterations: The smoothness known from the pristine particles has disappeared; the modified particles have a more prismatic geometry. Transmission electron microscopy provides further insight into the structure and orientation of the building blocks of the modified hematite film. The particles look more elongated and thinner, like rice grains with size of around 40 nm x 200 nm, as demonstrated in Figure 10.4-a. The rod-like structures are arranged in morphology reminiscent of a turf like carpet. Interestingly, superstructures evolve from the nanorods which look like flowers. Close inspection shows that the superstructures are hexapods with an absolute orthogonality, and that their branches are faceted parallel to their long axis, Figure 10.4-b. Employing selected area electron diffraction along with TEM (Figure 10.4-c) at prominent positions of the hexapods, we found an interesting diffraction pattern

which we could crystallographically index with good accuracy. Here, all the indicated reflections coincide with the ones from the corresponding high-resolution micrographs. The green spots stem from the green rod direction and the red from the other wing. There are quite a few spots not indexed that nevertheless show quite some intensity. Since these additional reflections do not correspond to real (possible) hematite crystal spacings, it is likely that they can be attributed to a complex way of dynamic diffraction within the center of the crossed flower. The lowest order reflections plus the one along the rod direction were thus only indexed. As pointed out, the rods are inclined, which implies that there can be some intensity mismatch between the different spots compared to a zone-axis aligned hematite film. Moreover, one also needs to consider that there might be small sub grains, as observable in the HRTEM micrographs, which are not properly aligned in respect to the main texture. The splitting of the spots along the y-direction of the diffraction pattern in Figure 10.4-c can be explained by the fact that the horizontal wings are slightly inclined in respect to each other. The incident beam direction is  $[-221]$ . It looks like the projection of the rod direction as it is seen in the image and the diffraction pattern is 118, which means that the 110 planes run along the rod direction. The higher magnification image in Figure 10.4-d shows that the nanorods have a substructure comprised of subunits of similarly elongated geometry of 2 nm x 5 nm size.

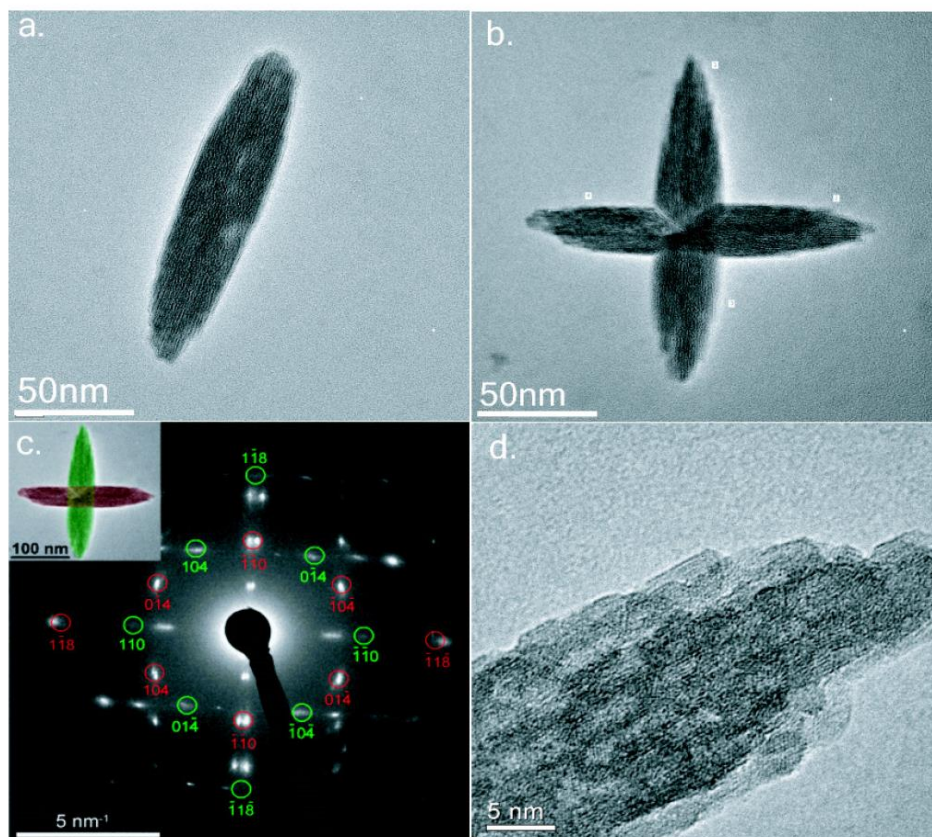


**Figure 10.4:** TEM studies of newly formed nanostructures after hydrothermal modification. a. The new hematite particles with rice grain shape. b. Superstructures with an exact orthogonality evolve from the nanorods which look like flowers. c. Selected area electron diffraction along with TEM at prominent positions of the multipod structure. d. The higher magnification image showing the nanorods have a substructure comprised of subunits of similarly elongated geometry of 2 nm x 5 nm size [54].

The XPS survey scans (Figure S2) show that the relative carbon concentration on the surface of the films decreases rapidly from 64% to below 35 % upon hydrothermal treatment, whereas the relative iron concentration increases from below 6% to above 10%, and the chlorine concentration to just below 5% . The valence band range of the XPS spectra (Figure 10.5) shows a depletion of spectral intensity near the Fermi energy from pristine to hydrothermal films. This intensity arises from shoulders at 1.5 eV which are likely due to a state with  $e_g$  orbital symmetry from iron with  $3d^5L$  electronic structure in octahedral coordination, when compared with the theoretical VB spectrum of hematite [40]. This structure is diminished upon hydrothermal treatment, when the Fe is becoming more reduced at the surface, thus probably affecting the photoelectrochemical properties. This is corroborated by a chemical shift of around 1 eV in the Fe (2p) core level spectra, revealing a partial reduction of the Fe at the surface during hydrothermal treatment. An oxygen depleted surface would fit with the recently proposed suggestion that oxygen chemisorption could play a central role in the photoresponse<sup>52</sup> and the modified films avoid the deleterious effects of grain-boundary recombination.

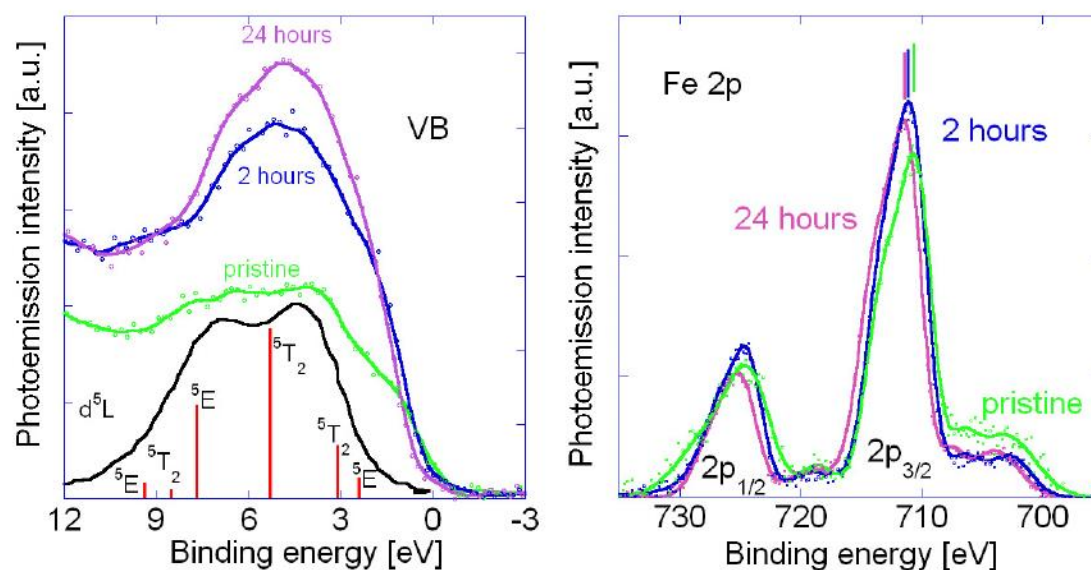


**Figure 10.5:** X-ray photoelectron spectra in the valence band (VB) region and Fe 2p core level of pristine, 2 hrs. and 24 hrs. hydrothermal treated films. Black VB theoretical spectrum of hematite [54].

I have measured the photocurrent of the hematite films under AM 1.5 solar light simulation. The pristine film has a saturated photocurrent of  $140 \mu\text{A}/\text{cm}^2$  at  $450 \text{ mV}$  vs. Ag/AgCl scale. Upon hydrothermal treatment, the photocurrent decreases for treatment times of up to 18 hours to a value of around  $67 \mu\text{A}/\text{cm}^2$ . After further treatment time, the photocurrent increases to  $157 \mu\text{A}/\text{cm}^2$  after 24 hours and  $218 \mu\text{A}/\text{cm}^2$  after 48 hours. Thus, a two day hydrothermal treatment can increase the photocurrent by about 50% (Figure 10.6).

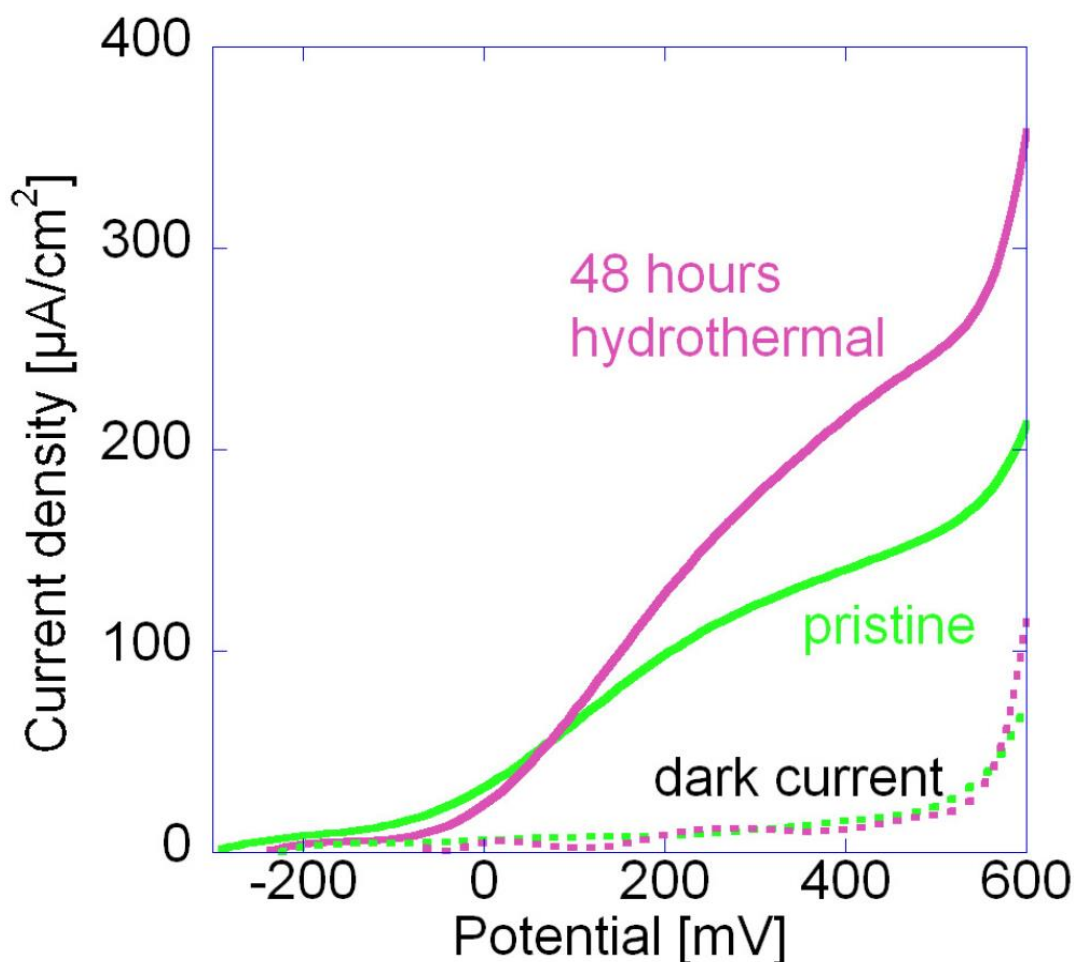


**Figure 10.6:** Photocurrent for pristine film and 48 hours hydrothermal treatment film [54].

The photocurrent results of the intermediate modified films are shown in the figure S3 (supporting information). In all cases, the photocurrent onset is observed at  $-90 \text{ mV}$  and is saturated after  $450 \text{ mV}$  followed by the oxidative dark process. The photocurrent generally originates from the water oxidation by the photogenerated holes. But in this case it might also come from other oxidative process such as oxidation of residual carbon and  $\text{Fe}^{2+}$  at the film surface, as suggested by the XPS data. The residual carbons were come from the heat treatment of iron fatty acid complex during the synthesis of pristine hematite film and post hydrothermal modification with L-Arginine. So in order to verify the contributions from carbon and  $\text{Fe}^{2+}$  oxidation, I have performed a cyclic voltammetric study of pristine and 48

hour treated film both under dark and light condition at a scan rate of 50 mV/Sec. From the CV scans of both the pristine and hydrothermally treated film (Figure 10.7 A and B) I have not observed any extra anodic or oxidative peak in the range of carbon and  $\text{Fe}^{2+}$  oxidation potential. Note that the standard electrode oxidation potential ( $E^\circ$ ) for carbon and  $\text{Fe}^{2+}$  oxidation are 503mV and 770mV vs. SHE [42, 43].

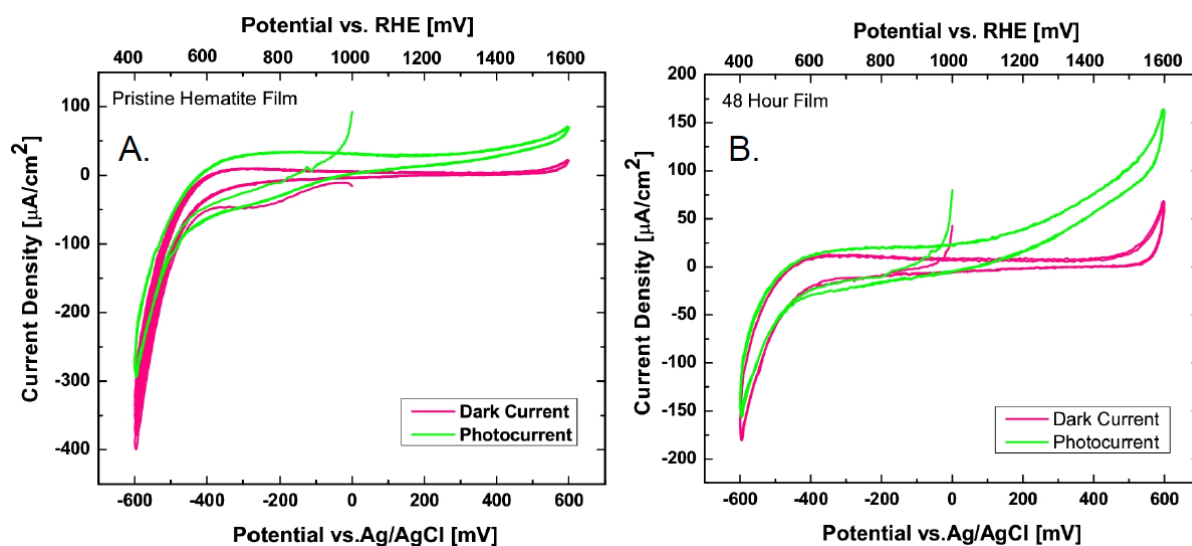


**Figure 10.7:** Cyclic voltammetry data in the dark and illuminated condition, current versus potential of the Ag/AgCl electrode. Scan rate is 50 mV/s, 1M KOH (pH 13.8) (A) pristine hematite film (B) 48 hour hydrothermally processed film.

In our case the potential of the photoelectrode is reported against the reversible hydrogen electrode (RHE) <sup>7</sup>

$$E_{RHE} = E_{AgCl} + 0.059 \text{ pH} + E_{AgCl}^\circ; E_{AgCl}^\circ = 0.208 \text{ V at } 25^\circ \text{ C.} \quad (2)$$

by considering pH of 1M KOH (~ 13.83), the electrolyte used during photoelectrochemical study. Next, during the reverse CV scan, one oxidative peak should come at +0.35 V vs. SCE (or 0.59 V vs. Ag/AgCl), which deciphers the removal of the residual carbon species on hematite surface left due to processing step [44]. If I express this potential vs. Ag/AgCl by applying the above equation, then it should be around -434 mV. Also in another study dealing with the interaction of hydroquinone with hematite surface [45], an extra oxidative peak showed the presence of residual carbon which was not removed during the cleaning process. The cathodic and anodic peak at the extreme potentials in the CV illustrates the decomposition of the solvent such as reduction and oxidation of water species. In the illuminated condition, the anodic peak increases in both the pristine and hydrothermal condition. Similarly, in case of  $\text{Fe}^{2+}$  oxidation I have not also observed any extra anodic current near  $\text{Fe}^{2+}$  oxidation potential.

Following this, I have checked the long term sustainability of photocurrent by carrying out the chronoamperometric measurement of hematite film and 48 hour processed film at each of the oxidation potential of carbon,  $\text{Fe}^{2+}$  and water for suitable period of time. From figure 10.8 (A-B, C-D) it is evident that on applying the respective carbon and  $\text{Fe}^{2+}$  oxidation potential, I have not seen any photoanodic current with respect to time in both the pristine and 48 hour film. Only in case of pristine film by applying bias of -253 mV, I have observed little amount of photocurrent but it is absent in case of 48 hour film. Finally on applying the water oxidation potential of 207 mv (1.23 V vs. RHE), I found reasonable photocurrent in both pristine and 48 hour film and it is stable upto 1 hour and 2 hour periods of time (Figure 10.8. E-F). In Figure 10.8. F, I observe a small increase in the dark current for the hydrothermally treated film (48 hour) at 0.207 V for the first 20 minutes of chronoamperometric operation. Note, however, that these dark current decays relatively fast over time. To learn about the origin of this dark current, I have calculated the total number of moles of electrons generated after 120 minutes of chronoamperometric operation. This was done by following the procedure described elsewhere (S5; see the supporting information). From this calculation I find that roughly 102 nano-moles of electrons get produced by oxidation process at the surface of the 48 hour modified film. This might arise from the oxidation of  $\text{Fe}^{2+}$  and residual carbon on the surface of the pristine and modified films, but this oxidation is finished after 20 minutes. Note that during recording the CV I did not observe any extra current wave due to  $\text{Fe}^{2+}$  and carbon oxidation as the CV operation was run for short period. From the preceding discussion I do accept that the photocurrent was a combination of oxidation of residual  $\text{Fe}^{2+}$  and carbon oxidation along with water photo oxidation. The source of photocurrent from water oxidation was established by the stability in photocurrent obtained in both the pristine and hydrothermally modified film (Figures 10.8. E and F). From here, it is also evident that the hydrothermal modification of original pristine film yields enhanced photocurrent. Next, in the inset of (Figure 10.8. E and F) I demonstrates the chopped light illumination of both the film where the falling transients (spike) clearly represent the photogeneration of an electron acceptor such as  $\text{OH}^\bullet$  radical. When light is absorbed, electrons are moved from the valence band to the conduction band and photocurrent is recorded on moving down a potential gradient. The valence band holes move to the surface to oxidize  $\text{OH}^-$  ion from electrolyte to make  $\text{OH}^\bullet$  [46]. The cathodic transient spike arise when  $\text{OH}^\bullet$  at the surface continues to scavenge conduction band electrons due to light turned off and  $\text{OH}^\bullet$  is used up. Finally oxygen yield has been calculated from the collected charge during the chronoamperometric measurement of hematite film and 48 hour processed film under dark and light condition (for pristine film:  $0.12773\text{C} \equiv 1.3237 \mu\text{mol}$  of electron

which corresponds to  $0.331 \mu\text{mol}$  of oxygen and for 48 hour film:  $0.40021\text{C} \equiv 4.1478 \mu\text{mol}$  of electron which corresponds to  $1.0369 \mu\text{mol}$  of oxygen; see S5 in supporting information).

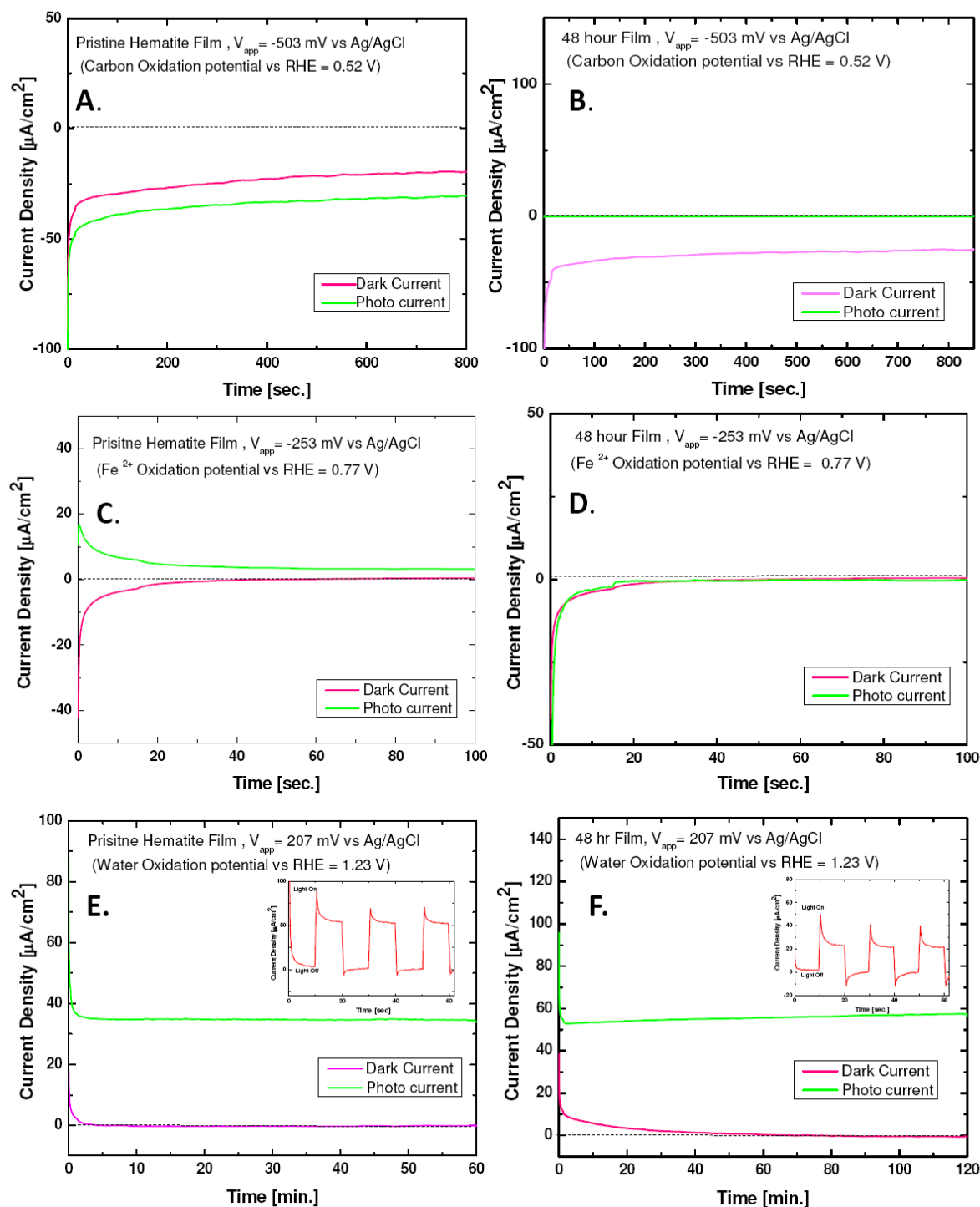


**Figure 10.8:** Long term stability measurement of photocurrent vs. time at  $-503 \text{ mV}$  (A-B),  $-253 \text{ mV}$  (C-D) and  $207 \text{ mV}$  (E-F) against Ag/AgCl electrode for pristine and 48 hour processed film (Inset: chopped light illumination).

The next question naturally arises as to what causes the changes, and particularly the increase of the photocurrent for the long time hydrothermally treated films. Potential origins may be of

chemical, morphological or structural nature. A complementary rationale for the increased photocurrent upon long term hydrothermal treatment comes from a comparison of the surface areas of the films. To answer this, I have carried out the BET measurement of pristine and modified film hydrothermally treated at different time interval. The BET surface areas for pristine and modified film treated for 48 hr. are  $140 \text{ m}^2/\text{g}$  and  $210 \text{ m}^2/\text{g}$ , respectively, which means a 50% increase of surface area, and which quantitatively corresponds to the 50% increase in photocurrent. Also from the BET analysis of corresponding intermediate products (Figure 10.9), I have found that the BET surface areas of films decrease from 2 hr. to 8 hr. with the consequent increase from 18 hour to 48 hour. Although the 24 hour processed film shows the almost same surface area in comparison to 18 hr., while the photocurrent of 24 hr. processed film quite higher. The reasons behind this still not clear. After all, on comparing the BET surface area trend with the corresponding photocurrent data as shown in Figure 10.9, I have found that photocurrent data varies in similar fashion up to some extent with the BET surface areas of the modified film. From this study, it is evident that the drop in photocurrent is due to the reduction of surface area at middle stages and then an improved surface area at the end of the process. This validated the improved photocurrent performance of the modified film as a result of the effect of increased surface area, measured by BET after long hydrothermal processing time (48 hour).

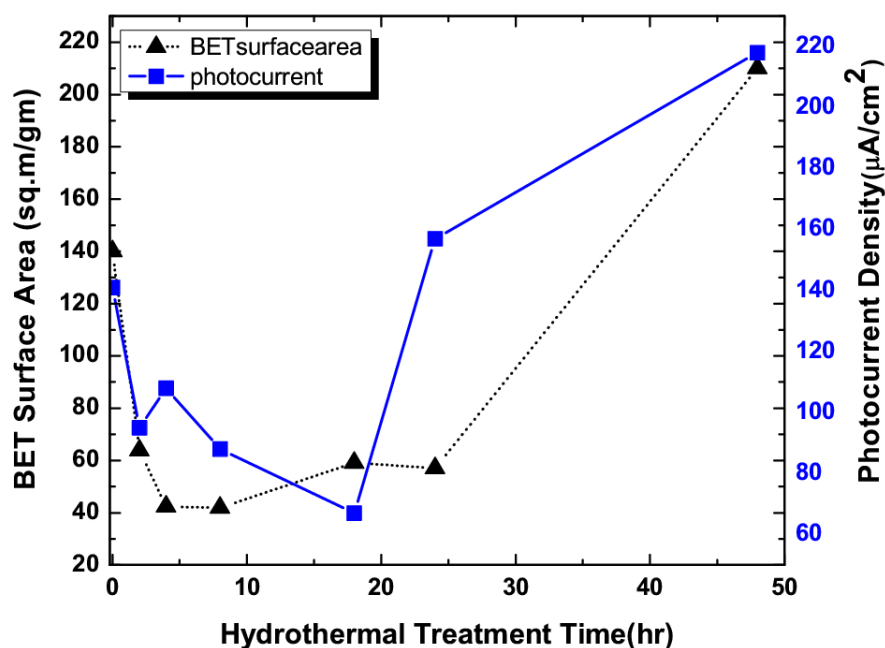


**Figure 10.9:** The variation of BET surface area and photocurrent of the modified films obtained at different time evolution.

I have further studied the influence of amino acid in forming the flower like superstructures and the morphology evolution of modified films at different time. The hematite nanocrystals that form the modified film are produced through a two-step phase transformation. In the first step, the hematite nanoparticles of the pristine film act as seeds for the formation of nanorods which form a self-assembled layer having array of nanorod. In the second step, the nanorods partially transform in a stepwise manner into stellate structures as shown in Figure 10.3-f. Also, it has been observed that the pristine film morphology completely reorganized into the stellate structure upto the substrate as evident in Figure 10.3-e. It is in this process that the amino acid can exert a decisive influence on the size and shape of the hematite nanocrystals [24]. To really understand the role of the presence of both iron precursor and amino acid, I have performed additional control experiments. From the FESEM results of the corresponding hematite films treated individually with iron salt, amino acid and both I have found that only amino acid (L – Arginine) (Figure 10.10. A) have not transformed the film to flower like form which renders it to be ineffective for driving the reaction. Also on treating the film with  $\text{FeCl}_3 \cdot 6\text{H}_2\text{O}$  for 48 hour (Figure 10.10. B), I have seen some rod like pattern but it just lying on the surface of the pristine hematite film. A blank experiment has also been performed by the hydrothermal treatment of hematite film with water for 48 hour at  $95^\circ\text{C}$  (Inset; Figure 10.10. C). Here I have not observed any changes in the morphology of the hematite film. Again direct hydrothermal reaction of  $\text{FeCl}_3 \cdot 6\text{H}_2\text{O}$  with L - Arginine in the absence of pristine hematite film (Figure 10.10. C) results into some rod like structure agglomerated together along with nanoparticle; but no flower like morphology obtained. Finally on treating with both the precursor, the original pristine film transformed into faceted structures with the consequent formation of hexapod flowers (Figure 10.10. D). The amino acid L - Arginine acts here as a structure directing agent and its functional group  $-\text{NH}_2$  and  $-\text{COOH}$  is the key part for controlled crystallization of hematite nanostructures [47]. Biomolecules are recently exploited as structure directing agents in the synthesis of nanomaterials. For instance,  $\text{Bi}_2\text{S}_3$  flowerlike patterns with well aligned nanorods were fabricated using L - Cysteine where amino acid acts a both sulphur source and structure directing molecule [48]. Peptide such as Glutathione was used as the assembling molecule and sulfur source to synthesize the highly ordered snowflake structure of bismuth sulphide nanorods under microwave radiation [49]. A Biostabilized CdS nanoparticle has been prepared using cystine and glutathione whereby the band gap energies adjustable with the variation of the pH value, the biomolecules and the corresponding concentrations [50].

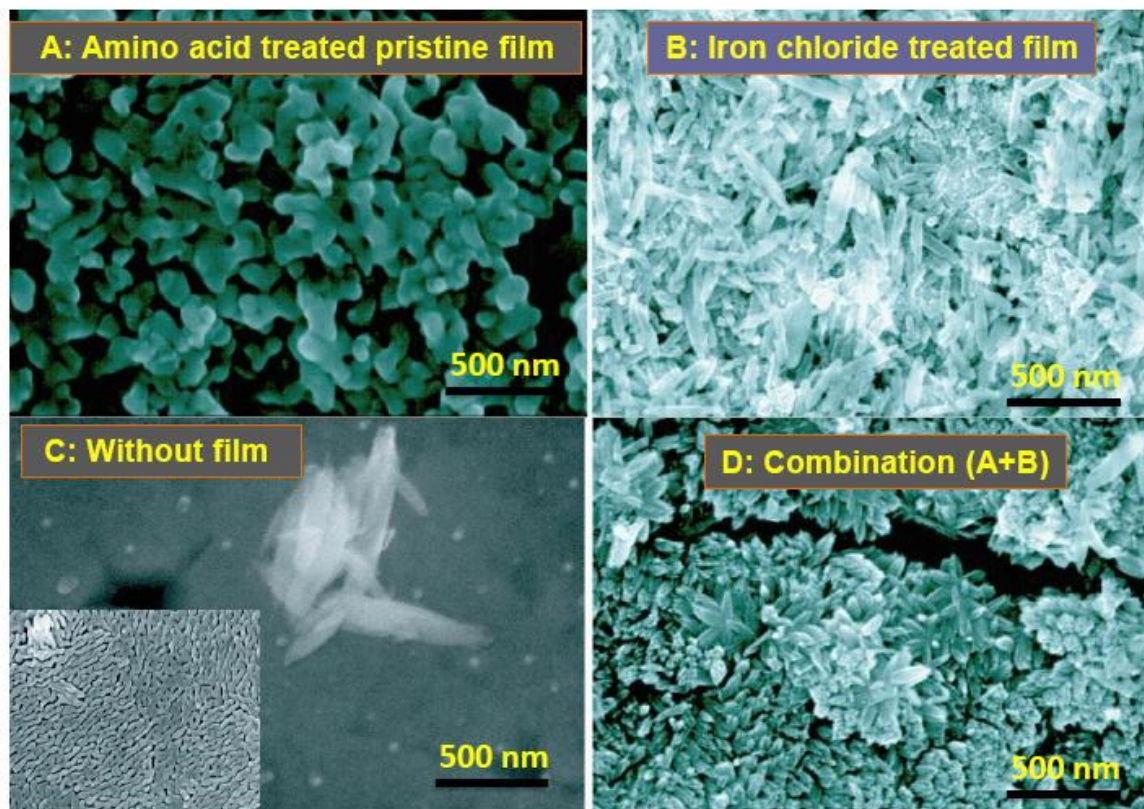


**Figure 10.10:** FESEM images A. Pristine hematite film after treatment with L –Arginine (5mmol); B. Pristine hematite film after treatment with  $\text{FeCl}_3 \cdot 6\text{H}_2\text{O}$  (5 mmol); C. Direct hydrothermal synthesis of  $\text{FeCl}_3 \cdot 6\text{H}_2\text{O}$  and L –Arginine without using hematite film (5:5 mmol) (Inset: hydrothermal treatment of hematite film with only water); D. Pristine hematite film after treatment with  $\text{FeCl}_3 \cdot 6\text{H}_2\text{O}$  and L –Arginine (5:5mmol).

In the next part of investigation, I have studied the time dependence of the morphological evolution of hydrothermally processed films with scanning electron microscopy (Figure 10.11). From this study, I found that during the early stages of hydrothermal reaction, the turf like films of nanorod already started to evolve some globular flowers. These are formed by the hierarchical assembly of individual hematite nanorod mediated by the effect of the amino acid. During the 2-18 hr. period, these structures are found to be smooth as observed from the FESEM image and with less porous character. Further on increasing the hydrothermal time, it become more rough and porous until I finally reach 48 hr.

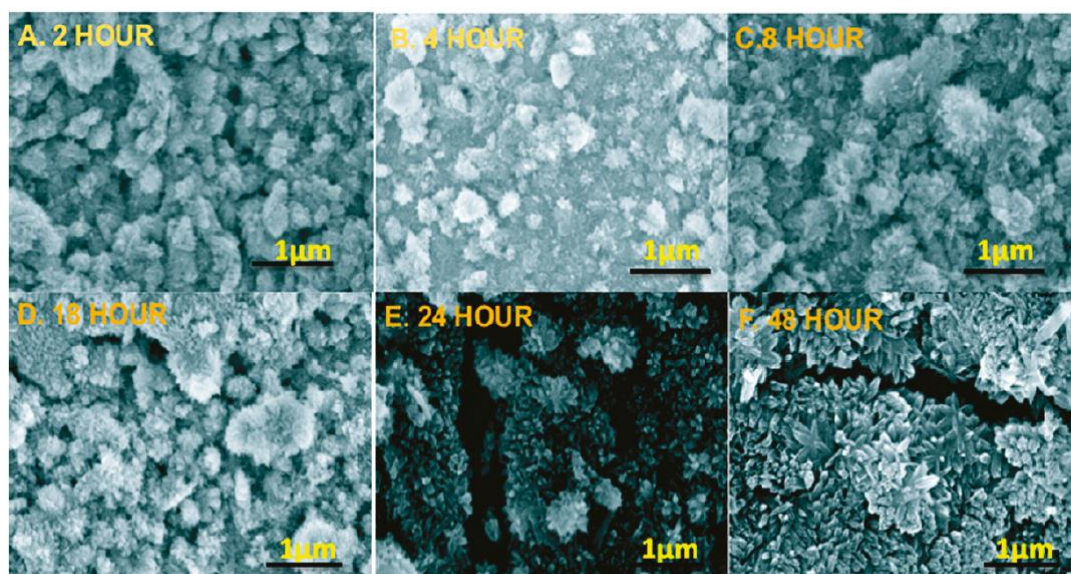
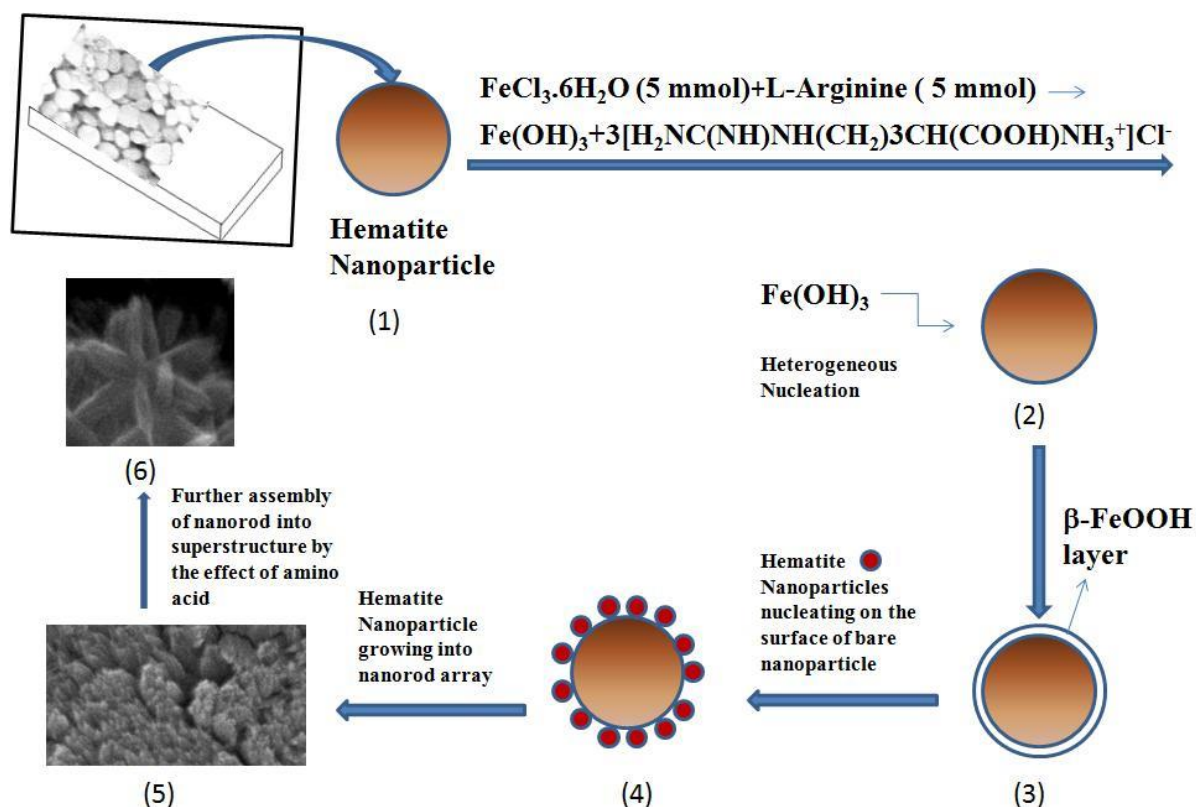


**Figure 10.11** : FESEM image of the modified films obtained after (A) 2 hr. (B) 4 hr. (C) 8 hr. (D) 18 hr. (E) 24 hr. (F) 48 hr. of hydrothermal treatment.

Finally I also illustrated a potential mechanism for the conversion process as shown in scheme 10.12. This is only a possible mechanistic pathway based on the earlier study of hierarchical assembly of  $\text{SnO}_2$  nanorod on hematite nanotubes [51]. The whole process is divided into 5 stages. The first step involves the formation of  $\text{Fe}(\text{OH})_3$  by the reaction between  $\text{FeCl}_3 \cdot 6\text{H}_2\text{O}$  and L-Arginine [24]. The side product of the reaction has also been shown on the top of the arrow. In the next step, heterogeneous nucleation of  $\text{Fe}(\text{OH})_3$  is taking place on the preexisting particle film, which is transformed initially into akaganeite phase ( $\beta\text{-FeOOH}$ ) [52] and then oxidized to hematite. Thus ultimately in step 4 hematite nanoparticle nucleated on the surface of pristine particle and it transform further into nanorod array by taking crystallographically preferred direction. Finally, flower shaped superstructures (stellate object) is formed by the self-assembly processes mediated by the amino acid. This is also supported by the specific role of amino acid as discussed above. The consequent formation of hexapod structure after prolonged hydrothermal time (48 hour) could also be triggered by the intrinsic six fold symmetry of hematite crystallite via a combination of the nanorod nucleation and competing self-assembly process of neighboring parallel nanorod [25]. In another study [53], it was proposed that when the reaction media was evaporated to half of its original volume in a period of 16 hour, the primary particle self-assembled to form large tetrahedral aggregates. Similar to this observation I have also observed the super saturation of the precursor solution evident by reaching of solution level to two third of its amount after 48 hr. of hydrothermal treatment. Because of this, structure evolution may not continue anymore and hence finally reached the hexapod structures. Next important observation is the structural evolution of free

standing



**Scheme 10.12:** Illustration of the one pot transformation process in stepwise manner.

nanoparticle after hydrothermal treatment for certain period of time (Figure S4, supporting information). I performed this experiment in order to observe the growth of cluster of nanoparticle into elongated structure. Normally, the array of nanorod could be easily seen from the FESEM image, but due to high density of the same it is difficult to observe the shape evolution of nanoparticle into rod. The detail formation mechanism will be the subject of the next study. At this moment, the unique transformation technique has been discussed with some potential scenario.

#### 10.4 Conclusions

In summary, I have developed a simple and effective hydrothermal technique for converting a pristine film of hematite into a film looks like array of nanorod with flower shape superstructures which showed enhanced photocurrent. The formation of the superstructure was greatly influenced by the presence of amino acid. It was found that the 48 hour hydrothermally treated film showed maximum photocurrent with respect to pristine and intermediate processed films. The hydrothermal treatment further affects the structure, size and shape of the nanostructure in the modified films as evidenced by XRD and TEM study. This influences the optical and surface properties of the modified films. Based on this, it was concluded that the

specific morphology along with higher surface area observed by BET measurement and tuning in the optical response of the modified hematite film favor its higher photo electrochemical activity. An important advantage of this one pot conversion method is that the performance of unique nanostructure in modified films can be directly studied for device related application. Also this technique can be applied further in enhancing the efficiency of hematite film doped with Si.

**Supporting Information Available:** The XRD pattern of different hydrothermally modified films along with expanded version of (104) and (110) peak intensities. Also, XPS survey scan, Photocurrent density results of intermediate films, FESEM images, table containing crystallite size calculation and the procedure for calculating the oxygen concentration from the number of charge collected.

## References

- [1] An, Z.; Zhang, J.; Pan, S., Yu, F. *J. Phys. Chem. C* **2009**, *113*, 8092-8096.
- [2] Wen, X. ; Wang, S. ; Ding, Y. ; Lin Wang, Z. , Yang, S. *J. Phys. Chem. B* **2005**, *109*, 215-220.
- [3] Jia, C. ; Sun, L. ; Yan, Z. ; You, L. ; Luo, F. ; Han, X. ; Pang, Y. ; Zhang, Z. ; Yan, C. *Angew.Chem.Int. Ed.* **2005**, *44*, 4328-4333.
- [4] Chueh, Y. L. ; Lai, M. W. ; Liang, Q. ; Chou, L. J.; Wang, Z. L. *Adv. Func. Mater.* **2006**, *16*, 2243-2251.
- [5] Tang, B. ; Wang, G. ; Zhou, L. ; Ge, J. ; Cui, L. *Inorg. Chem.* **2006**, *45*, 5196–5200.
- [6] Zhu, L. P.; Xiao, H.M.; Liu, X. M. ; Fu, S. Y. *J. Mater. Chem.* **2006**, *16*, 1794-1797.
- [7] Cao, M. ; Liu, T. ; Gao, S. ; Sun, G. ; Wu, X. ; Hu, C. ; Wang, Z. L. *Angew. Chem. Int. Ed.* **2005**, *44*, 4197-4201.
- [8] Vayssieres, L. *Appl.Phys.* **A2007**, *89*, 1-8.
- [9] Katsuki, H.; Komarneni, S. *J. Am. Ceram. Soc.* **2001**, *84*, 2313 – 2317.
- [10] Sun, Q. ; Lu, X. ; Liang, G. *Mater. Lett.* **2010**, *64*, 2006-2008.
- [11] Zhang, X. ; Li, Q. *Mater. Lett.* **2008**, *62*, 988-990.
- [12] Jing, Z. ; Wu, S. *Mater.Lett.* **2004**, *58*, 3637-3640.

- [13] Li, W. ; Guan, J. ; Wang, W. ; Tong, G. ; Fan, X. *Mater. Chem. Phys.* **2009**, *118*, 496-500.
- [14] Liang, M. ; Wang, S. ; Chang, Y. ; Hsiang, H. ; Huang, H. ; Tsai, M. ; Juan, W. ; Lu, S. *Ceram.Int.* **2010**, *36*, 1131-1135.
- [15] Chen, H. ; Zhao, Y. ; Yang, M. ; He, J. ; Chu, P. K. ; Zhang, J. ; Wu, S. ; *Anal. Chim. Acta* **2010**, *659*, 266-273.
- [16] Wang, W.; Yao, J. *Mater.Res. Bull.* **2010**, *45*, 1672-1678.
- [17] Diamandescu, L.; Mihaila-Tarabasanu, D.; Popescu-Pogriion, N. ; Totovina, A.; Bibicu, I. *Ceram. Int.* **1999**, *25*, 689-692.
- [18] Kandori, K.; Ishikawa, T. *J. Colloid Interf. Sci.* **2004**, *272*, 246-248.
- [19] Wu, C.; Yin, P.; Zhu, X.; Yang, C. O. ; Xie, Y. *J. Phys. Chem. B* **2006**, *110*, 17806-17812.
- [20] Zeng, S. ; Tang, K. ; Li, T. ; Liang, Z. ; Wang, D. ; Wang, Y. ; Qi, Y. ; Zhou, W. *J. Phys. Chem. C* **2008**, *112*, 4836-4843.
- [21] Gou , X. ; Wang, G. ; Kong, X. ; Wexler, D. ; Horvat, J. ; Yang, J. ; Park, J. *Chem. Eur. J.* **2008**, *14*, 5996-6002.
- [22] Vayssieres, L. ; Sathe, C. ; Butorin, S. M. ; Shuh, D. K. ; Nordgren, J. ; Guo, J. *Adv.Mater.* **2005**, *17*, 2320-2323.
- [23] Wu, S.; Cao, H.; Yin, S.; Liu, X. ; Zhang, X. *J. Phys. Chem. C* **2009**, *113*, 17893-17898.
- [24] Cao, H.; Wang, G.; Warner, J. H. ; Watt, A. A. R. *Appl.Phys.Lett.* **2008**, *92*, 013110.
- [25] Hu, W.; Zhao, Y.; Liu, Z.; Dunnill, C. W.; Gregory, D.H.; Zhu, Y. *Chem.Matter.* **2008**, *20*, 5657-5665.
- [26] Sanchez, C.; Arribart, H.; Giraud Guille, M. M. *Nature Materials* **2005**, *4*, 277 - 288
- [27] Sarikaya, M.; Tamerler, C.; Jen, A. K. Y.; Schulten, K. ; Baneyx, F. *Nature Materials* **2003**, *2*, 577 - 585.
- [28] Scriven, L. E. *Mat. Res. Soc. Symp. Proc.* **1988**, *121*, 717- 729.

[29] Deb, P. ; Basumallick, A. ; Sen, D. ; Mazumder, S. ; Nath, B. K. ; Das, D. *Phil. Mag. Letters.* **2006**, 86, 491.

[30] Cornell R. M. ; Schwertmann U. *The Iron Oxides-Structure, Properties, Reactions, Occurrence and Uses*; VCH Verlagsgesellschaft mbH: Germany, 1996.

[31] Bruce, H. *Theory of Reflectance and Emittance Spectroscopy*; Cambridge University Press, Cambridge, 1993.

[32] Baikov, M. V.; Ponyavina, A.N.; Prishivalko, A.P.; Sviridov, V.V.; Sil'vanovich, N. I. *J. Appl.Spectrosc.***1996**, 63, 297- 303.

[33] Wang, J.; White, W. B.; Adair, J. H. *J. Am.Ceram.Soc.***2005**, 88, 3449.

[34] Tauc, J.; Grigorov, R.; Vancu, A.; Optical properties and electronic structure of amorphous germanium. *Phys.Status Solidi***1966**, 15, 627.

[35] Kennedy, J. H.;Frese, K. W.;*J.Electrochem.Soc.* **1978**, 125, 709.

[36] Sivula, K.; Zboril, R.; Formal, F. L.; Robert, R. ; Weidenkaff, A. ; Tucek, J. ; Frydrych, J. ; and Gratzel, M. *J. Am. Chem. Soc.* **2010**, 132, 7436-7444.

[37] Sharma P.; Vashistha, M.; Jain, I. P. *J. Optoelectron. Adv. Mater.* **2005**,7, 2647

[38] Iribarren, A.; Castro-Rodriguez, R.; Sosa, V.; Pena, J. L. *Phys. Rev.***B1998**, 58, 1907.

[39]Patterson, A. L.;*Phys.Rev.***1939**, 56, 978–982.

[40] Fujimori, A. ; Sechi, M. ; Kimizuka, N. ; Taniguchi, M. ; Suga, S. *Phys.Rev.***B1986**, 34, 7318.

[41] Yu, X.; Cao, C. *Crystal Growth & Design***2008**, 8, 3951-3955.

[42]www. electrochem. org/meetings/scheduler/abstracts/214/0989. pdf

[43]www. siliconfareast. com/ox\_potential. htm.

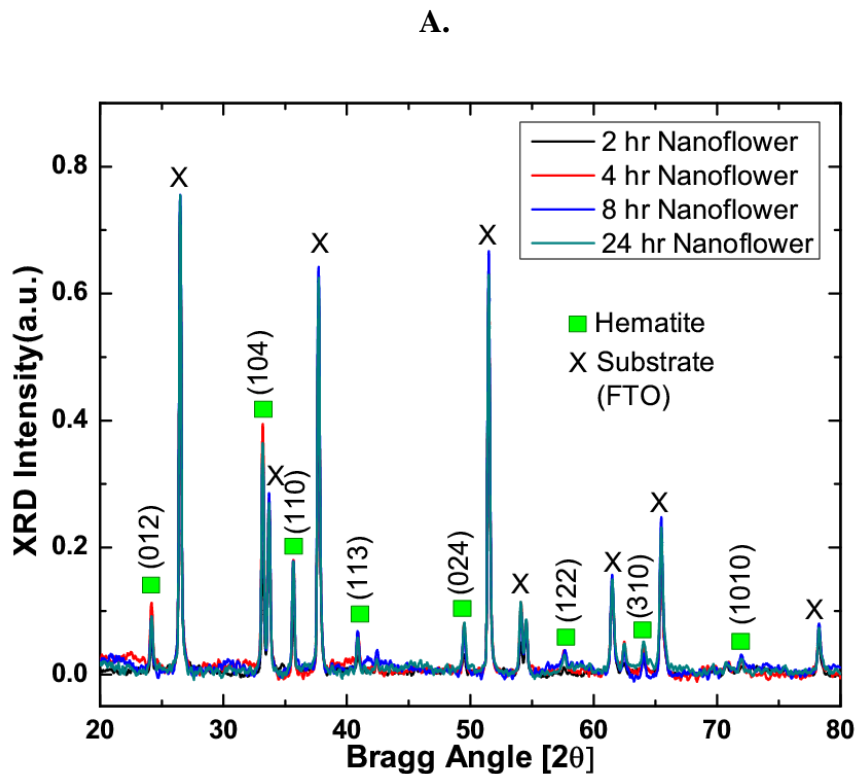
[44]Jingyu, S.; Jianshu, H.; Yanxia, C.; Xiaogang, Z. *Int. J. Electrochem. Sci.* **2007**, 2, 64 – 71.

[45] Stack, A. G.; Eggleston, C.M.; Engelhard, M. H. *J. Colloid Interf.Sci.***2004**, 274, 433– 441.

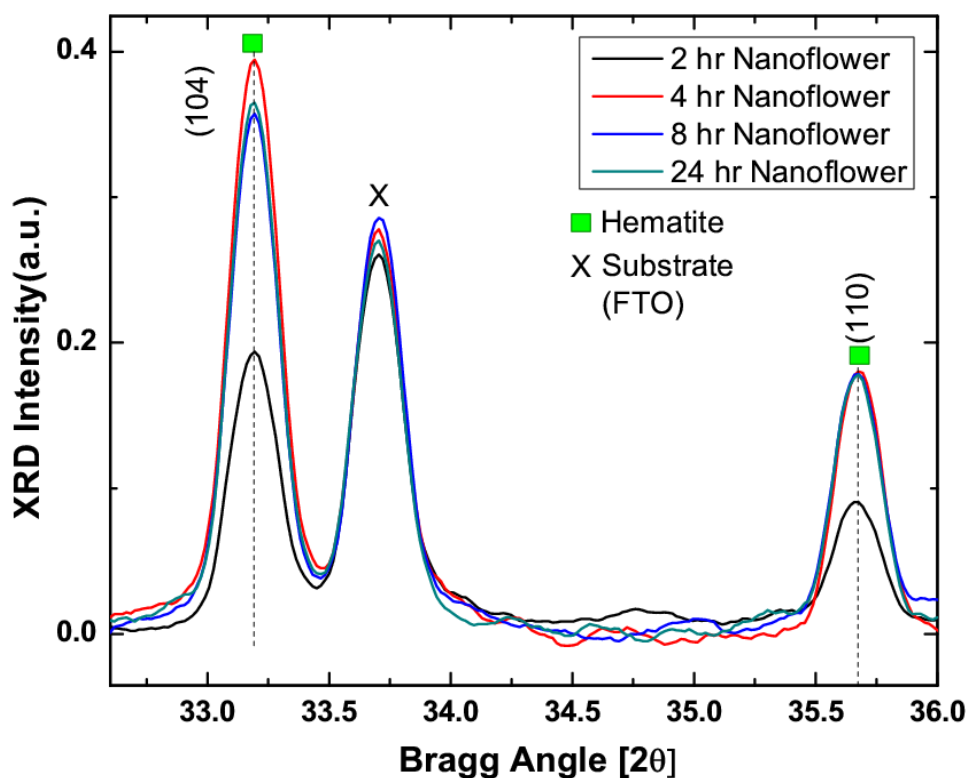
- [46] Eggleston, C. M.; Shankle, A. J. A.; Moyer, A. J.; Cesar I. ; M. Grätzel, *Aquatic Science* **2009**, 71, 151 – 159.
- [47] Orme, C. A. ; Noy, A. ; Wierzbicki, A. ; McBride, M. T. ; Grantham, M. ; Teng, H. H.; Dove, P.M.; DeYoreo, J.J.; *Nature* **2001**, 411, 775.
- [48] Zhang B.; Ye, X.; Hou, W.; Zhao, Y.; Xie, Y. *J. Phy. Chem. B* **2006**, 110, 8978 – 8985.
- [49] Lu, Q. ; Gao, F. ; Komarneni, S. *J. Am. Chem. Soc.* **2004**, 126, 54.
- [50] Barglik – chory, Ch.; Remenyi, Ch.; Strohm, H.; Müller, G.; *J. Phy. Chem. B* **2004**, 108, 7637.
- [51] Zhang, D. ; Sun, L. ; Jia, C. ; Yan, Z. ; You, L. ; Yan. C. *J. Am. Chem. Soc.* **2005**, 127, 13492-13493.
- [52] T. Nakamura and H. Kurokawa. *J. Mater. Sci.* **1995**, 30, 471
- [53] Wang, W.; Howe, J. Y.; Gu, B. *J. Phys. Chem. C* **2008**, 112, 9203 – 9208.
- [54] D. K. Bora, A. Braun, R. Erni, G. Fortunato, T. Graule, E. C. Constable, *Chem. Mater.* **2011**, 23, 2051.

Supporting Information

Figure S1: XRD profile of hydrothermally processed film for different time (A) and the expanded view of the corresponding (104) and (110) planes from hematite (B)



B.

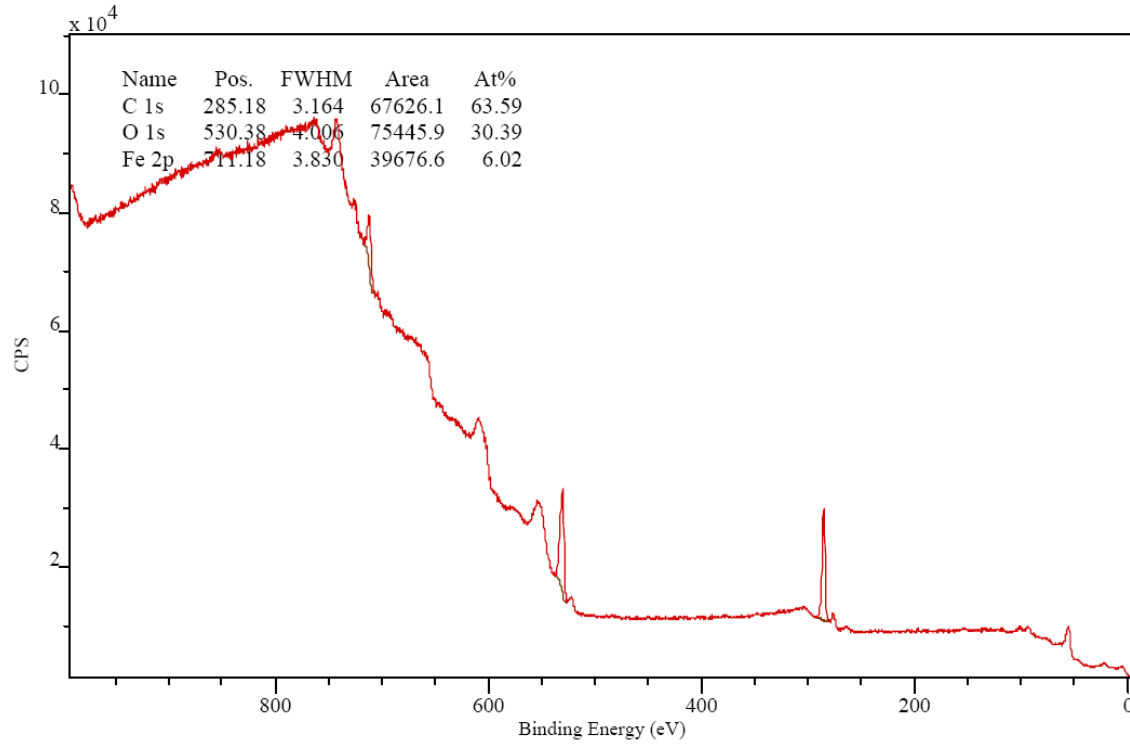


The X-ray diffraction (XRD) patterns of the nanoflower films obtained after different hydrothermal treatment time are shown in Figure S1. It has been observed that in case of nanoflowers film, the predominant peaks that can be attributed to hematite are [104] and [110]. With the increased in hydrothermal treatment time, the XRD patterns revealed that the [104] and [110] reflections gain in intensity with the change of the morphology of the film. This increase in intensity can be explained by the preferential orientation and growth direction of the nanorods along the (110) direction. Similar observations were found in the case of Si doped hematite [1] and in the case of the formation of hematite nanobelts and nanowires by thermal oxidation of iron [2]. In the case of samples doped with Si some cauliflower like structure was observed.

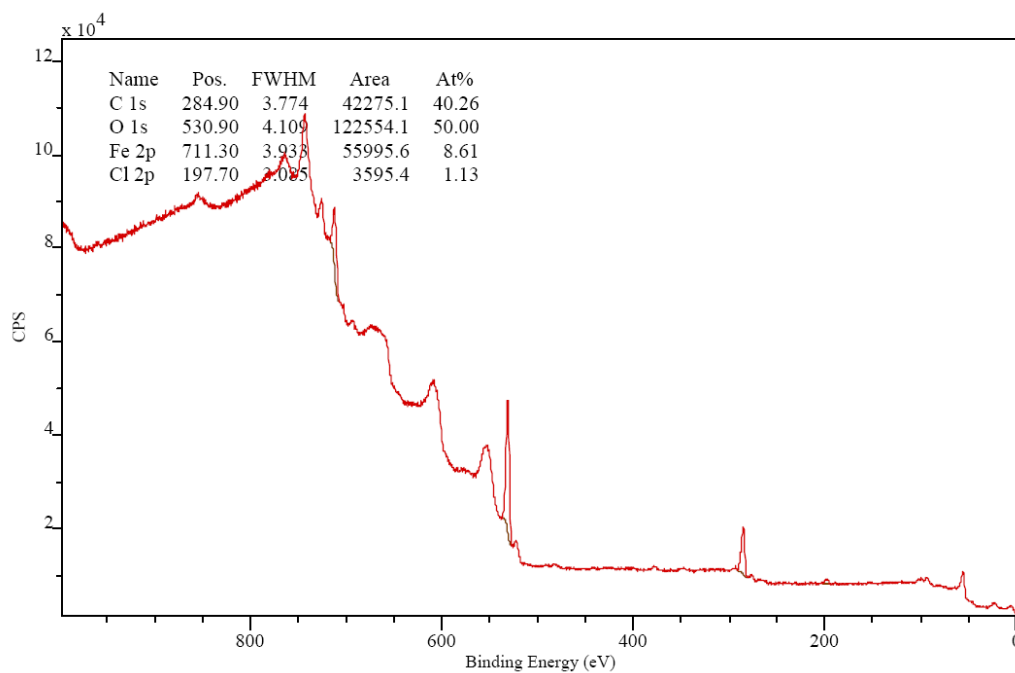
1. A. Kay, I. Cesar and M. Gratzel, *J. Am. Chem. Soc.* **2006**, *128*, 15714-15721.
2. X. Wen, S. Wang, Y. Ding, Z. L. Wang and S. Yang, *J. Phys. Chem. B.* **2005**, *109*, 215-220.

**Figure S2: XPS survey scans of pristine hematite film and hydrothermally processed film for 2 hr., 4 hr., 8 hr. and 24 hr. film [ Courtesy: Dr. G. Fortunato]**

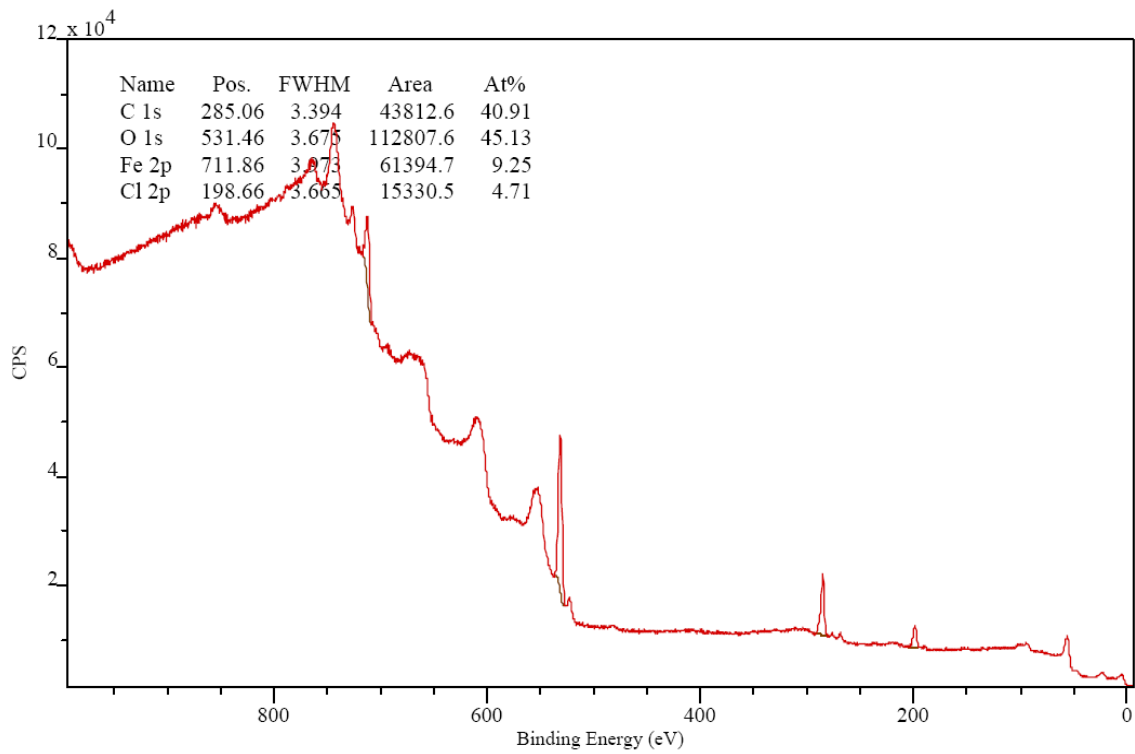
**A. Pristine hematite film**



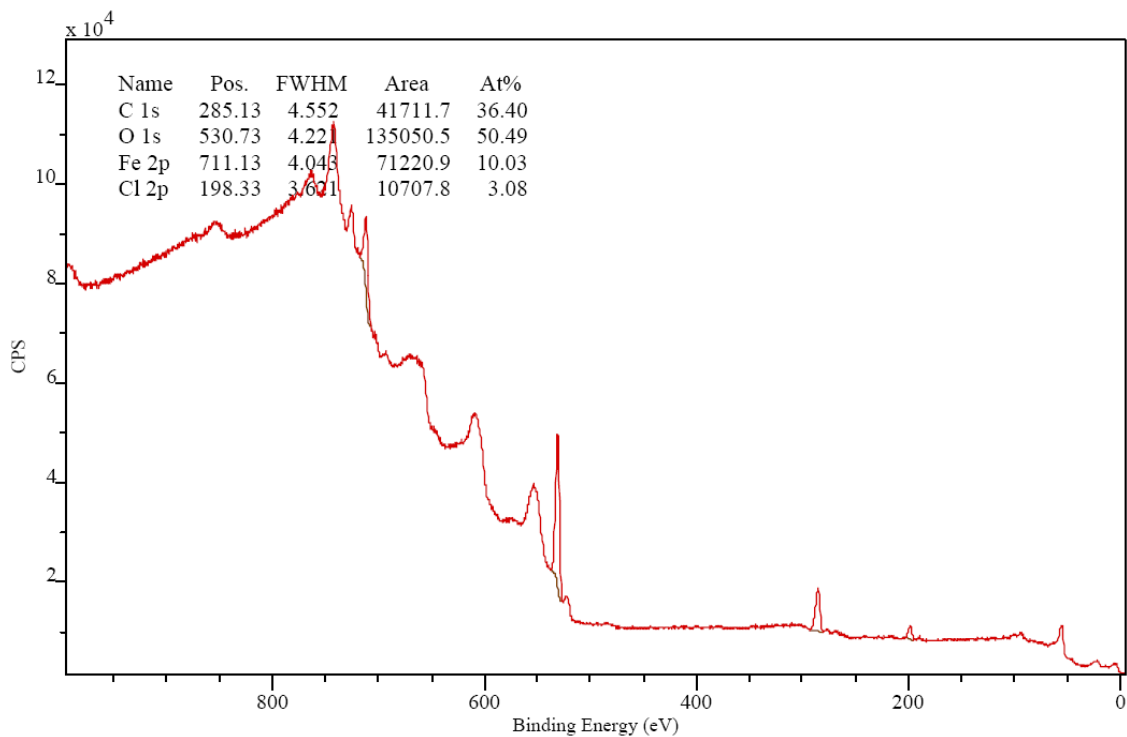
**B. 2 Hour hydrothermal treatment**



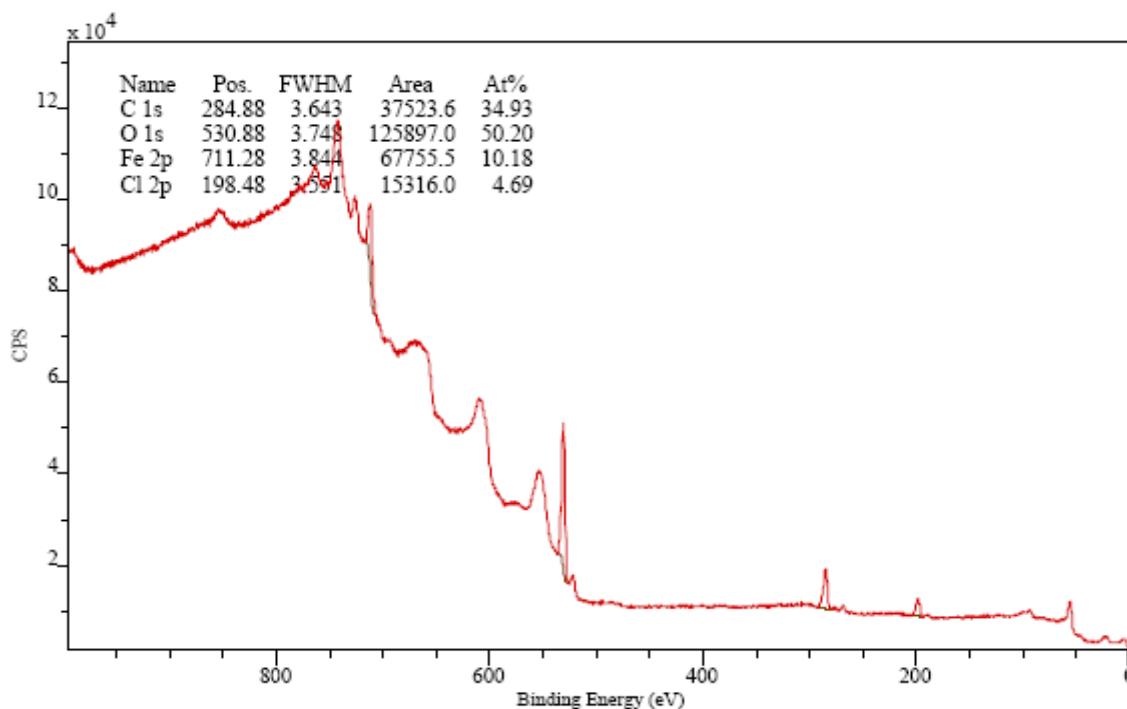
**C. 4 Hour hydrothermal treatment**



**D. 18 Hour hydrothermal treatment**



**E. 24 Hour hydrothermal treatment**



(e) 24 hour

From the XPS survey scans of the pristine films and hydrothermally processed films at different time, I have observed that the relative carbon concentration on the films decreases rapidly from 64% to below 35 % with the incremental increase in hydrothermal treatment time, while oxygen concentration remain constant. On the other hand, the relative iron concentration increases from below 6% to above 10%, and the chlorine concentration to just below 5%.

Figure S3: Photocurrent of hydrothermally treated film for 2, 4, 8, 18 and 24 hour under AM 1.5 simulated sunlight

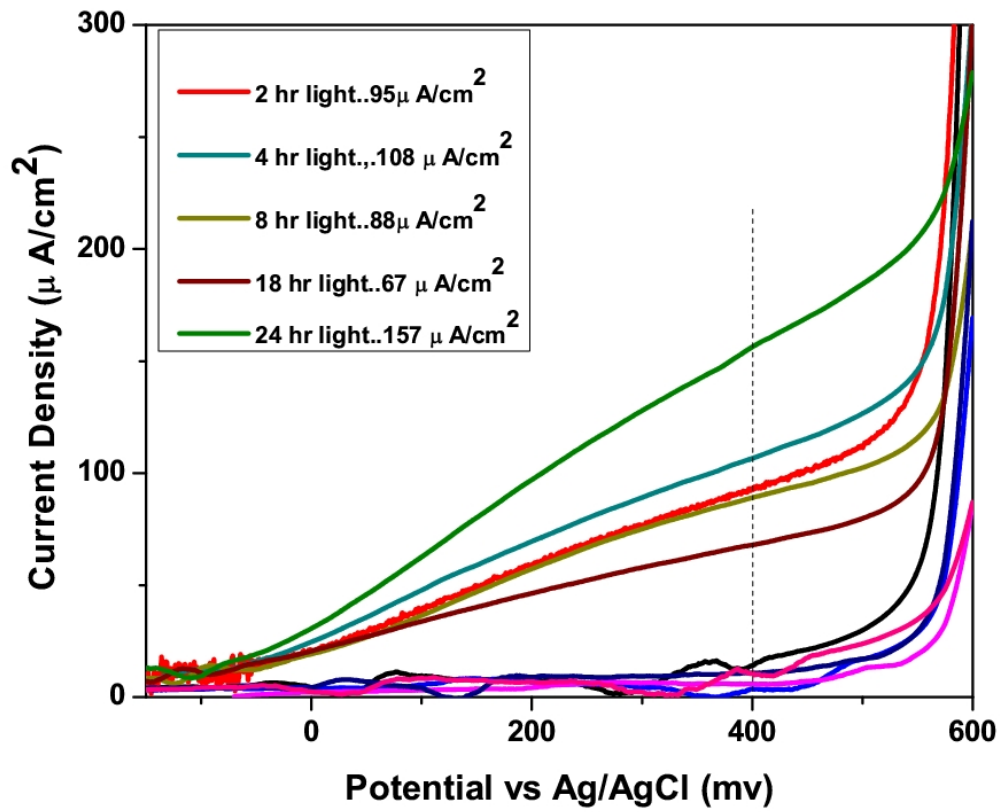
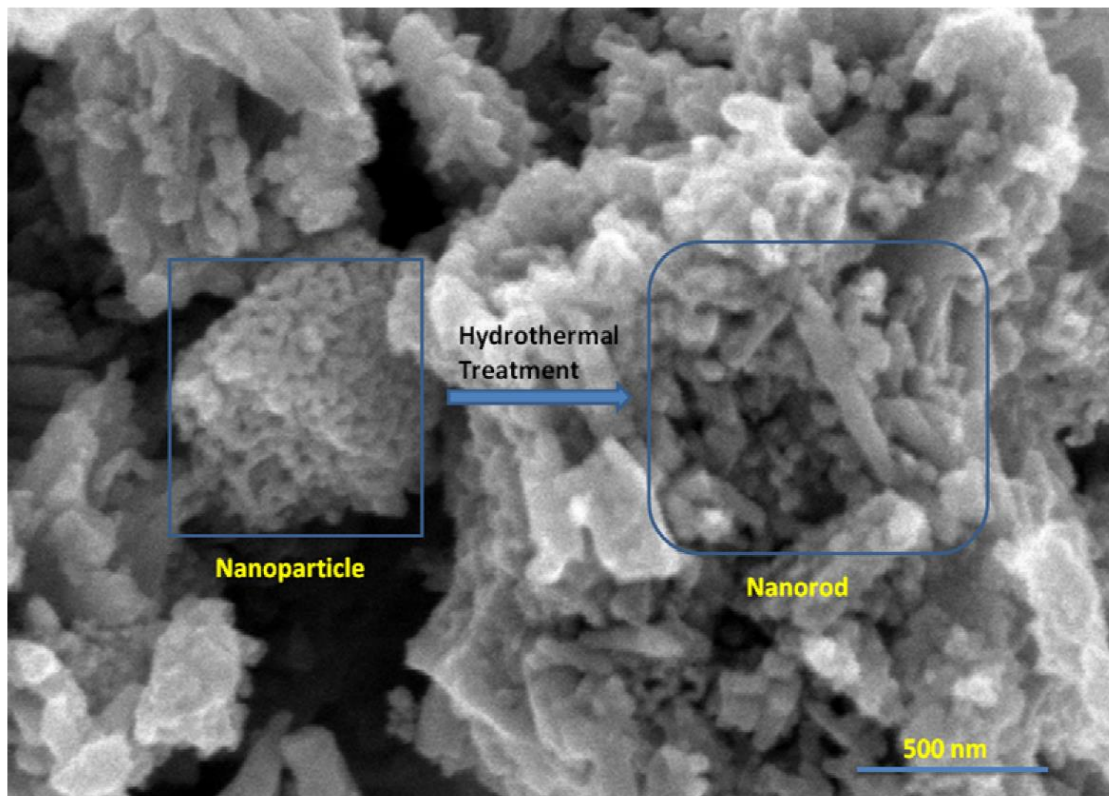
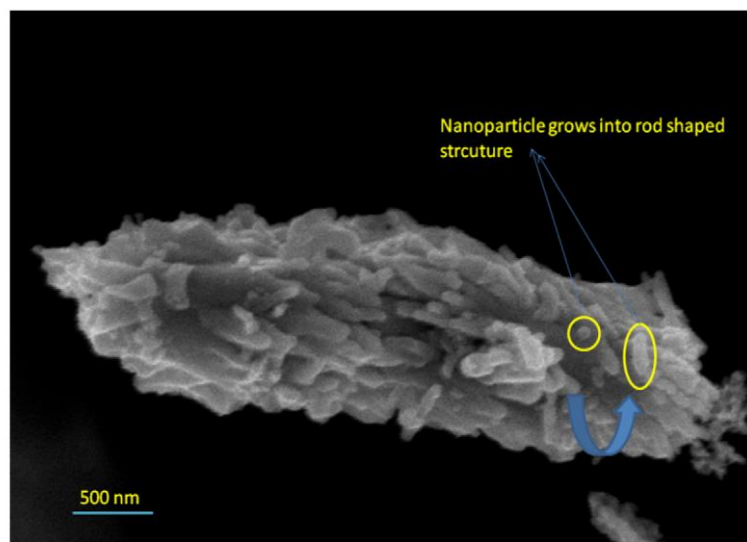


Figure S4: FESEM images of pertinent control hydrothermal experiment with free standing nanoparticle showing the transformation of nanoparticle into rod.

(a)



(b)



**Table S1: crystallite size as obtained from XRD results using Scherrer equation**

Sample	Crystallite Size
Pristine	29.3 nm
2 hour	32.6 nm
8 hour	41.5 nm
18 hour	50.9 nm
24 hour	50 nm
48 hour	51.2 nm

#### S5. Calculation of oxygen concentration or yield from collected charge during current vs. time study.

1. For the **pristine film** under light condition, I have calculated the total charge collected by integrating the current over time with the following equation

$$Q = \int_0^t Idt$$

After 60 min of chronoamperometric operation, it is = 0.12773 Coulomb.

Then I have calculated the number of moles of electrons generated by dividing it with Faraday constant (1F= 96485 C/mol) and it will be as follows:

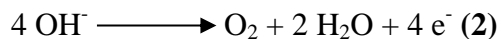
$$0.12773\text{C}/96485 \text{ C mol}^{-1} = 1.3237\mu\text{mol of electrons}$$

In the final step, I have calculated the moles of evolved oxygen.

For this calculation I have to consider the water oxidation half reaction occurred under light at the photoanode. Normally if the photoanode is in contact with an electrolyte (in this case, 1MKOH), the majority carrier electrons are driven to the back contact and eventually reduce an acceptor species to form the hydrogen via the reaction:



The minority carrier photogenerated holes flow in the opposite direction and oxidize donor species at the semiconductor liquid interface, producing oxygen through the reaction <sup>1</sup>



According to equation (2), 4 moles of electrons produce 1 mole of oxygen gas.

$$\text{Hence, } 1.3237\mu\text{mol of electrons} \times \frac{1\text{mole O}_2}{4\text{mole e}^-} = 0.331\mu\text{mol O}_2$$

From above calculation, it is evident that 1.3237  $\mu\text{mol}$  of electrons (corresponds to photocurrent) gives 0.331  $\mu\text{mol}$   $\text{O}_2$  (evolve oxygen due to water photooxidation) shows a confirmed 4:1 stoichiometric relationship between photocurrent and oxygen.

2. Similarly for **48 hour nanoflower film** under light condition after 120 min of chronoamperometric operation, the no of moles of electron will be 4.1478  $\mu\text{mol}$  of electron which gives rise to 1.0369  $\mu\text{mol}$  of oxygen.

## References

1. I.E. Paulauskas et. al. Journal of Electrochemical Society, 156(5), BB580 – B587, 2009

## Chapter 11

# **Functionalization of Nanostructured Hematite Thin Film Electrodes with the Light Harvesting Membrane Protein C- Phycocyanin yields Enhanced Photocurrent**

### **11.1 Introduction**

Inspired by the work of E. Reisner et. al. [1] my supervisor encouraged me to extend the research activity towards nanobiointerface and artificial photosynthesis. In the present work I showed how integration of light harvesting biomolecules such as C- phycocyanin on hematite is a working method to increase the photocurrent by harvesting more photons.

The low band gap energy of hematite (2.2 eV) allows the conversion of up to 40% of the incident solar radiation and thus makes it insofar suitable for photoelectrochemical cells; its abundance and environmentally benign nature make it attractive for industrial applications [2-4]. Phycocyanin is the light-harvesting protein from the phycobilisome family found in the photosynthetic blue-green algae (cyanobacteria), red algae, and the cryptomonads. It absorbs light from the red part of the visible spectrum (620 nm) and then provides a highly efficient exciton migration until the energy arrives at a photochemical reaction center through a funneling mechanism. It belongs to oligomeric proteins which use linear tetrapyrrole chromophores (phycocyanobilins) for light harvesting. The bilins are covalently attached to cysteine residues of the apoprotein by thioether bonds, and are not associated with metal ions [5]. The sensitization of hematite with a porphyrin derivate can increase performance by harvesting incident photons with higher efficiency [6]. The general viability of this route has been demonstrated recently, where phycocyanin has been used to sensitize the surface of TiO<sub>2</sub> which provides electron transfer from photo-excited phycocyanin to the conduction band of TiO<sub>2</sub>[7].

I can enhance the photocurrent from nanostructured hematite thin films by integrating the light harvesting membrane protein C-phycocyanin. This is accomplished by the immobilization of protein on the hematite surface by both electrostatic and covalent surface functionalization, involving separation by a carbohydrate polymer such as agarose with a functional imidazole carbamate in activated form. A similar strategy of covalent functionalization has been adopted for immobilizing enzyme on silica coated maghemite nanoparticles ( $\gamma$ - Fe<sub>2</sub>O<sub>3</sub>) [8]. A different set of functionalization strategy has been developed for conjugating protease enzyme on

magnetic nanoparticle [9]. Based on the same principle a nanohybrid material was fabricated by the covalent functionalization of porphyrin on carbon nanohorn for the study of photoinduced electron and energy transfer process [10]. The rationale for using surface functionalization is to stabilize the anchored protein and also to enforce lateral cross coupling between the proteins.

By this approach I expect a higher number density of immobilized proteins on the surface of hematite. This will harvest an extra portion of the light from the long wavelength region of the solar spectrum and therefore, assists in acquiring the enhanced optical properties of hematite thin film electrode which will finally yield a higher photocurrent. In the next step, different properties of the hybrid system will be studied in order to assess its effect on the final performance.

## 11.2. Experimental

*Materials:* Iron nitrate nonahydrate, oleic acid and tetrahydrofuran (THF) used in the synthesis of hematite were of reagent grade (Sigma-Aldrich). The solvent used for functionalization were anhydrous toluene and 1, 4 - dioxane, and phosphate buffered saline (PBS) was used as the coupling buffer. Films were deposited on fluorine doped tin oxide (FTO) glass (Hardford Glass Inc.). The protein used was C-phycoerythrin isolated from *Spirulina* sp. (Sigma-Aldrich, Switzerland, 99.9% purity). The linker used for the conjugation of C-phycoerythrin with hematite was 1, 1'-carbonyldiimidazole (Sigma-Aldrich, Switzerland, reagent grade 99.9% purity).

*Synthesis of hematite thin films and immobilization of C-phycoerythrin on hematite by electrostatic and covalent surface functionalization:*

Pristine hematite thin films (A) were synthesized by a previously adopted method [11]. For the synthesis of the conjugated protein-hematite system by electrostatic interaction (B) of differently charged species, hematite films were kept for 2 hours in 0.5 M phosphate buffered saline (PBS) so as to obtain a positively charged surface. PBS solution was prepared by mixing suitable amounts of NaCl,  $\text{KH}_2\text{PO}_4$  and  $\text{Na}_2\text{HPO}_4$  so as to get the requisite concentration. Further, 200  $\mu\text{l}$  solution of C - Phycoerythrin was dispersed over the hematite surface by a pipette and kept for 12 hours overnight in dark at ambient temperature. The solution was prepared by dissolving suitable amounts of C- phycoerythrin in PBS buffer to get the desired concentration. In the preparation of hematite / C-phycoerythrin conjugates by covalent cross coupling, the hematite film readily adsorbed with protein solution (B) was subjected to spin coating of an agarose layer (B1) in order to decorate the surface with free hydroxyl groups. The agarose solution was prepared by dissolving 1 mg of agarose powder in 100ml of double distilled water by heating at 60-70°C on a magnetic stirrer. After this the film was allowed to dry at room

temperature prior to CDI (carbonyl diimidazole) activation (B2). For the CDI treatment of the agarose treated protein coated hematite film (B1), first 50 mg/ml (0.3mM) of CDI was dissolved in 5 ml dioxane and agarose modified electrodes (B1) are immersed in the respective solution for 2 hours at room temperature. When the reaction was completed, the hematite/protein/agarose assembly was considered as an *activated electrode* (B2) and was rinsed 3 times with anhydrous toluene to remove excess CDI and reaction byproducts. The *activated electrode* (B2) was then treated with 0.5 M PBS solution having pH = 7.4. The pH of the coupling buffer determines the greater reactivity of the imidazole carbamate and greater coupling yields for protein. Then, activated electrodes were reacted with 200 $\mu$ M of C-Phycocyanin (B3) for 3 hr. at 37°C on a hot plate with magnetic stirrer. After the conjugation reaction, electrodes were rinsed with washing buffer (0.01M PBS), pH 7.2 to remove unbound protein molecules.

#### *Materials Characterization:*

The conjugate formation by covalent surface functionalization was studied with attenuated total reflection Fourier transformed infrared (ATR-FTIR) spectrometry. Spectra were recorded on a Bio-Rad FTS 575C instrument equipped with a mercury cadmium telluride detector and a horizontal nine reflection diamond ATR unit with KRS-5 optics (SensIR Technologies, Danbury, CT). Spectra were recorded from 400 to 4000  $\text{cm}^{-1}$  at 2  $\text{cm}^{-1}$  resolution. The phase purity of pristine and phycocyanin conjugated hematite films were further checked by x-ray diffractometry (PAN Analytical X'Pert PRO, Cu  $K\alpha$  radiation). Optical properties of the samples were studied by a UV-Vis spectrometer (Cary Scan 50). The morphology and composition of pristine and modified films were studied by FESEM (Hitachi, S 4800) equipped with an EDX detector (Oxford instruments) by using an accelerating voltage of 15 keV. The surface morphology of the pristine hematite along with the conjugated film was studied by atomic force microscopy in tapping mode, Nanosurf-AFM, (Mobile S). The optical Raman spectra were recorded with a RENISHAW® in Via Raman Microscope by using blue laser of 442 nm (exposure time 10.0 time/s, laser power 100%). For characterizing protein samples alone, I used UV excitation at 325 nm (exposure time 50.0 time/s, 4 accumulations at the 100% laser power).

#### *Photoelectrochemical Characterization:*

Photocurrent spectra were recorded with a Voltalab® potentiostat in a three electrode configuration with 1M KOH (pH=13.6) as electrolyte, Ag/AgCl/sat. KCl as reference electrode and a platinum counter electrode. In all cases, the maximum applied potential was 600 mV. The photoelectrochemical cell was custom built from PEEK plastic. Pristine hematite electrode (A) along with modified ones (B – B3) were illuminated on a 0.45  $\text{cm}^2$  area of electrolyte and a

fused silica window with a  $0.5\text{cm}^2$  circular masks, the total geometric area immersed in electrolyte was approximately  $2.6\text{ cm}^2$ . Sunlight was simulated with a filtered xenon lamp from LOT Oriel®, with the light intensity adjusted to AM 1.5. Transient photoresponse for the samples was studied by chopping the light during the chronoamperometric (current vs. time) measurement, with the working electrode kept constant at 600 mV and current measured against the time. Photocurrent action spectra were taken in a custom built IPCE set up operated by Lab View. The spectra were obtained under 300W Xe lamp connected with monochromator (LOT). The wavelength was scanned at 2nm/sec and applied voltage was 0 mV vs. SCE in the aforementioned cell. The monochromatic photocurrent of pristine hematite film vs. different wavelength (300 -700nm) was obtained by loading the power calibration data in the lab view software. This was first measured with a Si photodiode with power meter (Thor Labs) before starting the IPCE

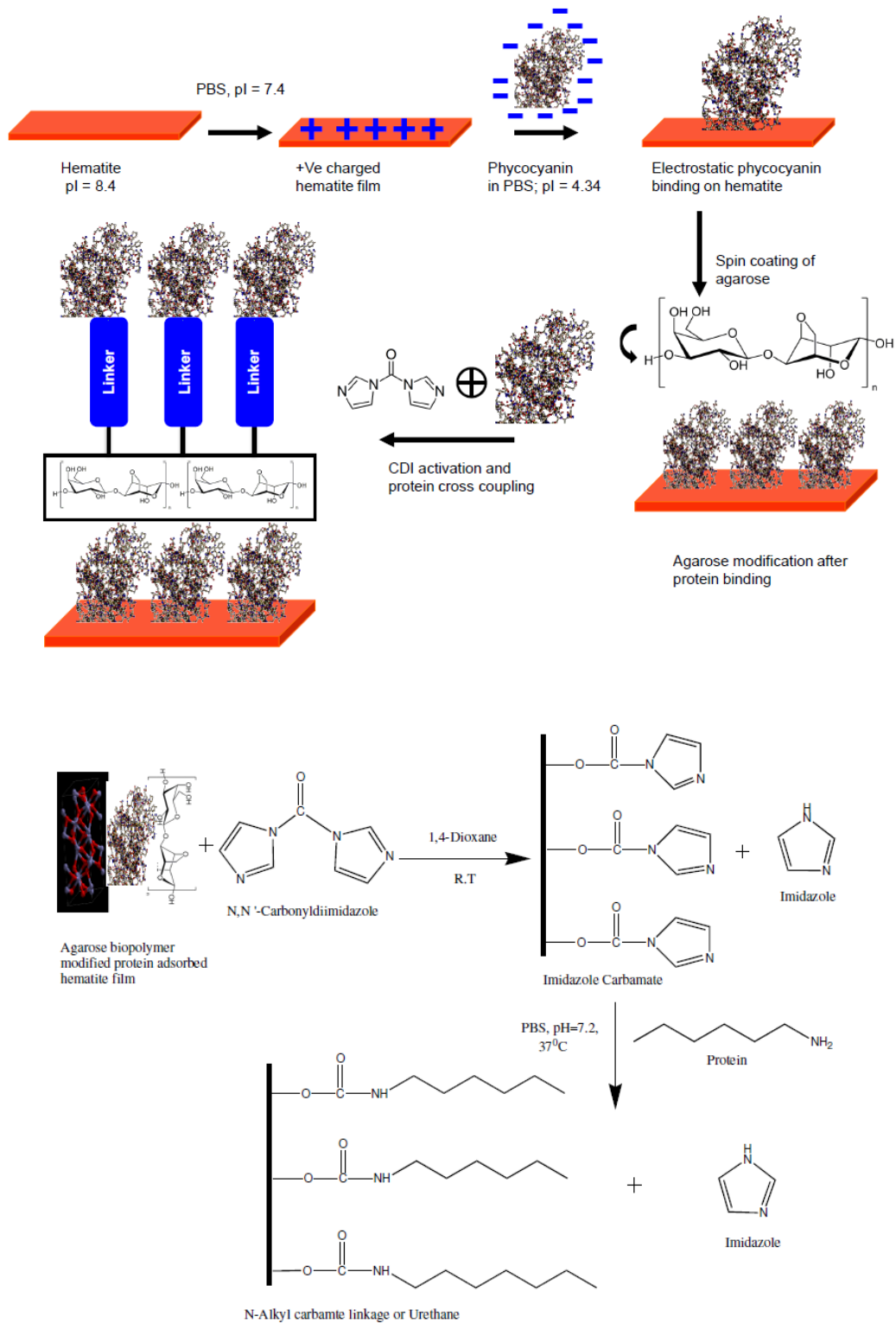
### 11.3 Results and Discussions

Before I turn to the results of current investigation, I outline in detail the basic architecture of the essential components of our system and explain their expected functionality.

#### 11.3.1 Surface functionalization of hematite thin film with C-phycoyanin protein

In the electrostatic conjugation process, the hematite surface becomes polarized as a result of pH of PBS (7.4) which is quite below that of the isoelectric point (pI) of hematite (8.4-8.5) [12]. It has been established that when the pH of the surrounding environment of a material is below the pI, then the surface of the particular material becomes positively charged, or vice versa [13]. Similarly the phycoyanin to be adsorbed on the hematite film was dissolved in PBS buffer. The pI of phycoyanin is 4.64 [14]. In this case the surface charge of the phycoyanin will be negative since the pH of the surrounding environment is higher than that of pI. Under such conditions phycoyanin will be adsorbed on the hematite by simple electrostatic interaction, and not by chemical bond. The conjugation is explained in **Scheme 11.1- A**. After this, a thin layer of agarose is spin coated onto it so that adsorbed phycoyanin on hematite can be kept under stable condition from the structural and functional point of view. This will assist in the integrity of the system upon further chemical modification. The bioprotective property of agarose, a sugar, can stabilize the phycoyanin by slowing down molecular motion of protein responsible for folding at ambient temperature [15]. In the next step, CDI reacts with the hydroxyl terminated agarose surface to create a reactive imidazole carbamate intermediate [16], which then couples with incoming amine-containing phycoyanin, finally resulting in an integrated system. CDI is an active carbonylating agent that contains two acylimidazole leaving

groups. The chemistry underlying the above conjugation process is depicted in **Scheme 11.1-B**. The active intermediate formed by the reaction of CDI with an OH<sup>-</sup> group is an imidazolyl



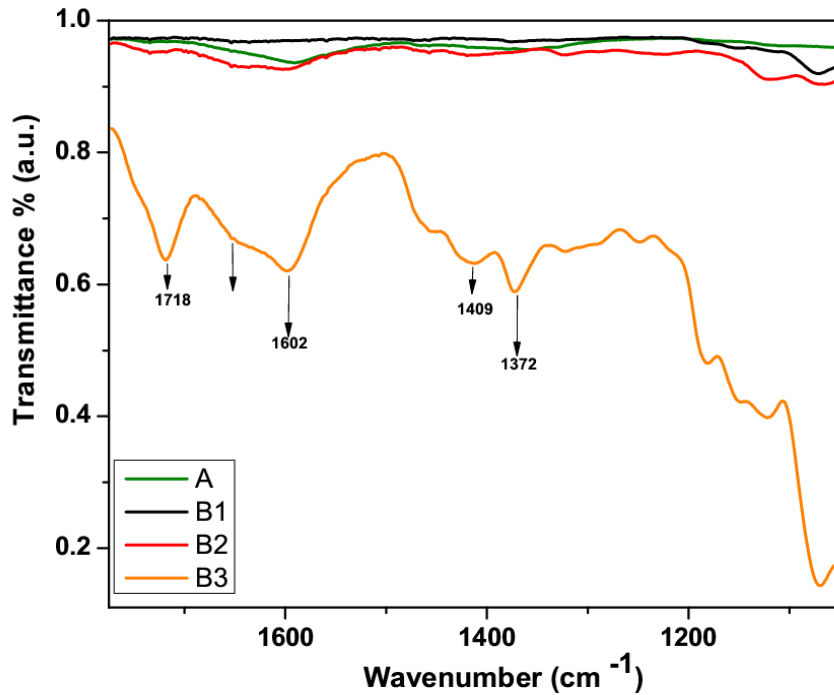
**Scheme 11.1(A)** The schematic of the conjugation strategy for the fabrication of hematite phycocyanin conjugate. **(B)** The chemistry underlying in the above conjugation process.

carbamate. Imidazole gets released on attack by amine, but the carbonyl group remains intact. In this way, hydroxyl-containing molecules can be coupled to molecules containing  $-NH_2$  functional groups with the result of a one-carbon spacer, forming stable urethane (N - alkyl carbamate) linkages. This coupling procedure has for example been adopted for an activation of agarose beads for the biospecific affinity based chromatographic isolation of serum antibodies [17]. The CDI has thus been used as a spacer arm to control the distance or separate the finally coupled protein from hematite surface. This can allow for a specific coupling of protein by avoiding steric hindrance between it and the immobilization support such as in this case with the hematite film. An ideal spacer arm should have a bifunctional group to react with both substrate and ligands and it also helps in the placing of ligands at a suitable distance from the surface of the support [18].

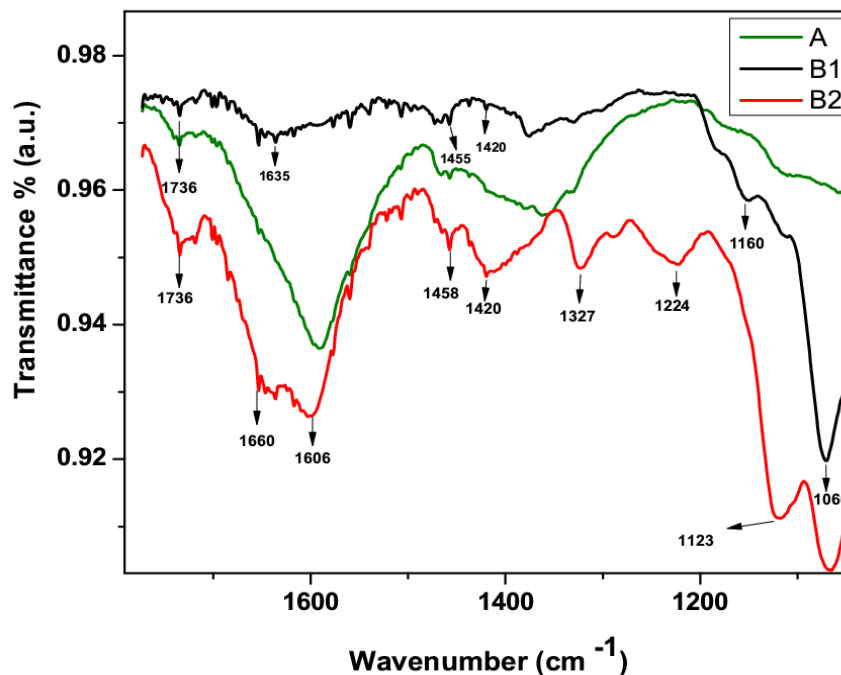
Now that I have explained the anticipated interaction of the functional components during the conjugation reaction, I present the experimental support. In order to be able to clearly correlate the structural, optical and photoelectrochemical properties with functionality, measurements have been done on the same sample after stepwise modification from pristine hematite to hematite with covalently linked protein. In order to check for the stability of the protein on the substrate surface (FTO) alone, I have carried out chronoamperometric (current vs. time) studies for 1 hour under light condition.

#### *11.3.1.1 Probing of conjugation reaction with FT-IR Spectroscopy*

The immobilization and activation of phycocyanin in the covalently coupling system is confirmed by the analysis of FTIR spectroscopy data. The FTIR spectra of all samples starting from A-B3 are shown in **Figure 11.2(I)** and (II). It is to be noted that in the case of agarose modification of the hematite film (B1), I directly spin coated agarose layer on hematite without any additional phycocyanin layer. The spectrum A in the case of pristine hematite shows an absorption band at  $1736\text{ cm}^{-1}$  corresponding to the C=O stretching of ester formed on the surface of the pristine film. The peak is prominent in all of the spectra from B1-B3 except B4. In spectrum B1, the characteristic band of the agarose structure can be seen at  $1455$  and  $1420\text{ cm}^{-1}$  which is assigned to  $-OH$  in plane bending and to  $-CH_2$  symmetric bending, respectively [18]. The next bands at  $1160$  and  $1060\text{ cm}^{-1}$  show the fingerprint of the carbohydrate cycle which corresponds to C-O-C asymmetric stretching and C - O stretching respectively. The band at  $1635\text{ cm}^{-1}$  corresponds to the OH bending mode of water absorbed on agarose. Next, in the spectrum of CDI activated film (B2) I notice an emerging band at around  $1660\text{ cm}^{-1}$ , which is assigned to C=N stretching modes of the imidazole heterocycle from the



A.



B.

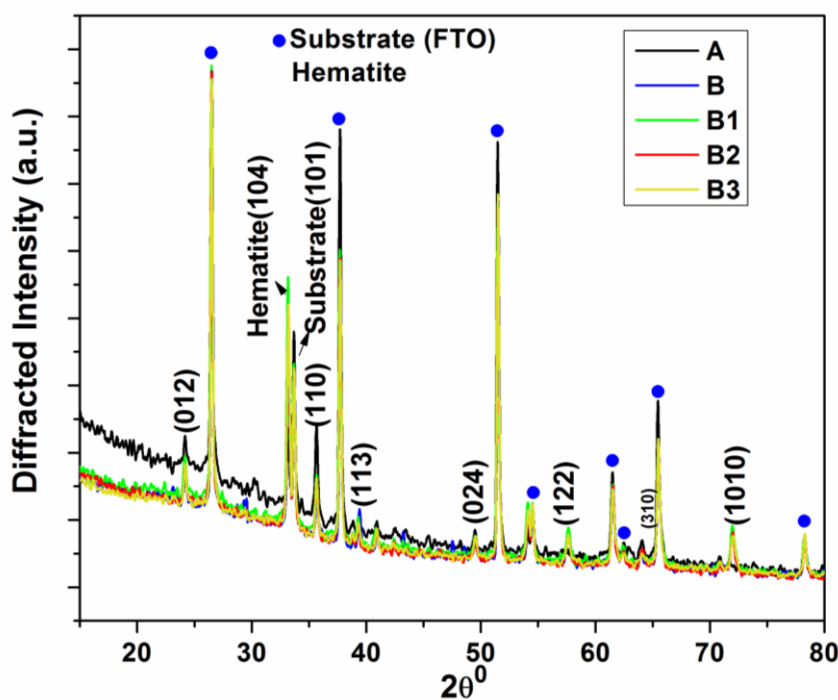
**Figure 11.2(I-II).** The FTIR spectra of Hematite – phycocyanin conjugate along with pristine, agarose modified and CDI activated films for probing the conjugation process. imidazole carbamate intermediate formed during the activation step. The absorption bands at 1606, 1458 and 1420  $\text{cm}^{-1}$  originate from the  $-\text{NH}$  bending vibration of imidazole leaving

group and  $-\text{CH}$  stretching vibration of imidazole heterocycle. The other bands at 1327, 1224 and  $1123\text{ cm}^{-1}$  originate from the C-N stretching vibration in the active intermediate. In the final spectra of the phycocyanin conjugated hematite film (B3), the absence of a peak at  $1660\text{ cm}^{-1}$  and the emergence of new bands at 1708 and  $1606\text{ cm}^{-1}$  [19, 20] corresponds to the C=O (amide I band) and -NH bending vibration. This confirms the formation of stable urethane (N-alkyl carbamate) linkages formed by the condensation reaction between the imidazole ester and amino functional group of phycocyanin protein.

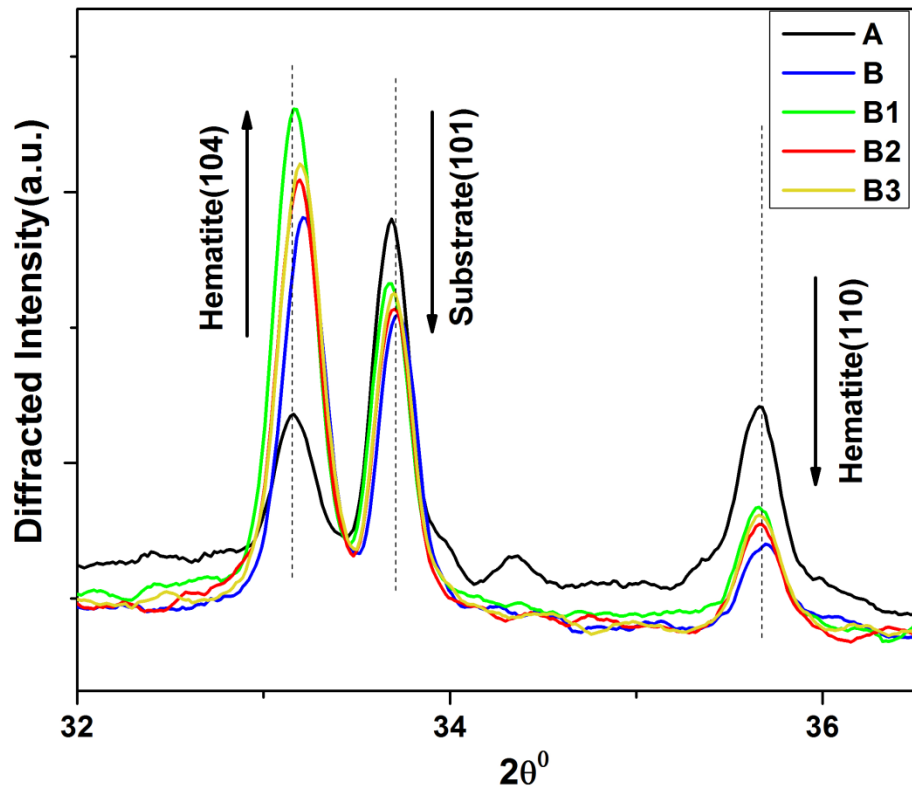
### 11. 3.2 Structural properties of hematite-phycocyanin system

In order to learn about the potential influence of the surface modification on the structural properties of hematite, I investigated the pristine hematite film and the corresponding stepwise modified films with x-ray diffraction; see Figure 11.3(I). The diffractogram of the pristine hematite film (A) shows the substrate Bragg reflection (FTO Substrate) as the most intense one. Besides these, the two prominent hematite (104) and (110) Bragg reflections are observed along with much weaker reflections corresponding to the (012), (113), (024), (122), (310) and (1010) planes. This picture is well matched by XRD results of Si doped hematite films synthesized by atmospheric pressure chemical vapor deposition [21]. The XRD of the surface modified films from B –B3 shows interesting results when I closely inspect the peak intensities of (104) and (110) reflections along with the (101) reflection from the substrate, shown in Figure 11.3(II). For the protein adsorbed film (B) I find that the (104) reflection intensity increases, whereas the (110) reflection intensity decreases in comparison to the pristine film. Upon addition of agarose (B1), the intensity reaches a maximum, and the intensity of (110) increases with respect to (B1), and again the (104) intensity decreases after CDI activation (B2), while the intensity of the (110) reflection remains same as that of (B) and (B1). Finally, upon cross-coupling of another protein molecule, it remains the same peak intensity as in case of the CDI activated film. In all cases the peaks are getting sharper, which is well justified by calculating the crystallite size. I have quantified this trend using the Scherrer equation [22] and plotted the crystallite sizes in **Figure 11.3(III)**. There I notice that the crystallite size increases from pristine (A) to phycocyanin conjugated (B3) film with the exception of the CDI modified film (B2). The growing crystallite size may be attributed to the erosion of the nanoparticle surface in the film by the organics used for the modification. Such kind of erosion phenomena is not uncommon and has been observed on protein functionalized porous silicon surfaces [23]. Due to increasing amount of organic content on the pristine hematite film, the overall thickness of the film might increase up to some extent. The erosion can have a noticeable effect on the difference in XRD peak intensity and photo absorptive ability of hematite film. For validating

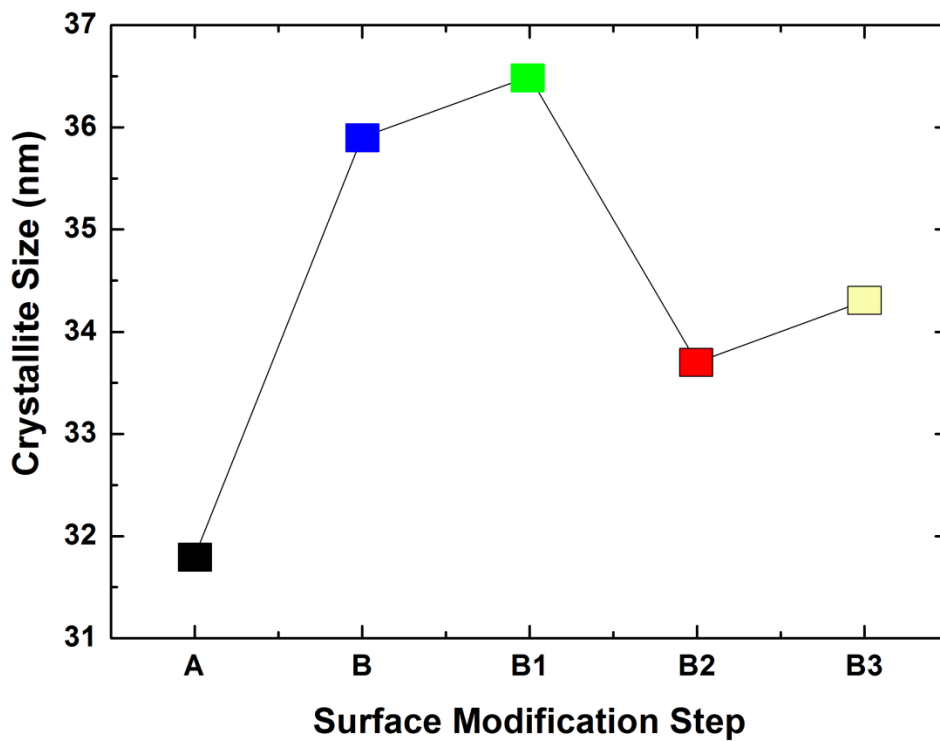
this, I look into the relative Bragg peak intensity ratio  $[I(104)/I(101)]$  from the hematite and substrate part as shown in Figure 11.3(IV). The Bragg peak ratio changes at each surface modification step. Interestingly, it remains close to unity (1.1) in both the protein adsorbed and in the cross linking step. Careful inspection of the expanded view of the (104) and (101) peak intensities from hematite and substrate, I find that the substrate peak intensity varies slightly for the films after each surface modification step. I looked into the preferential growth of the hematite crystal plane after each surface modification step. It is known that the hematite (001) plane plays an important role in the catalytic activity and electronic conductivity [24] which has further influence on the observed photocurrent. In this case, the change of the relative Bragg peak ratio  $[I(104)/I(110)]$  gives account of crystallographically preferred growth of hematite and is shown in Figure 11.3(V). By careful inspection of the trend, I find that both planes grow equally with respect to each other. This trend follows similarly to  $[I(104)/I(101)]$ , which is due to change in the overall thickness of pristine hematite film as discussed above. This means both planes grow equally in each surface modification step. This validates that there is no preferred growth of hematite crystalline lattice upon the integration of protein and also the photocurrent [see Figure 11.6] observed does not fit with the trend.



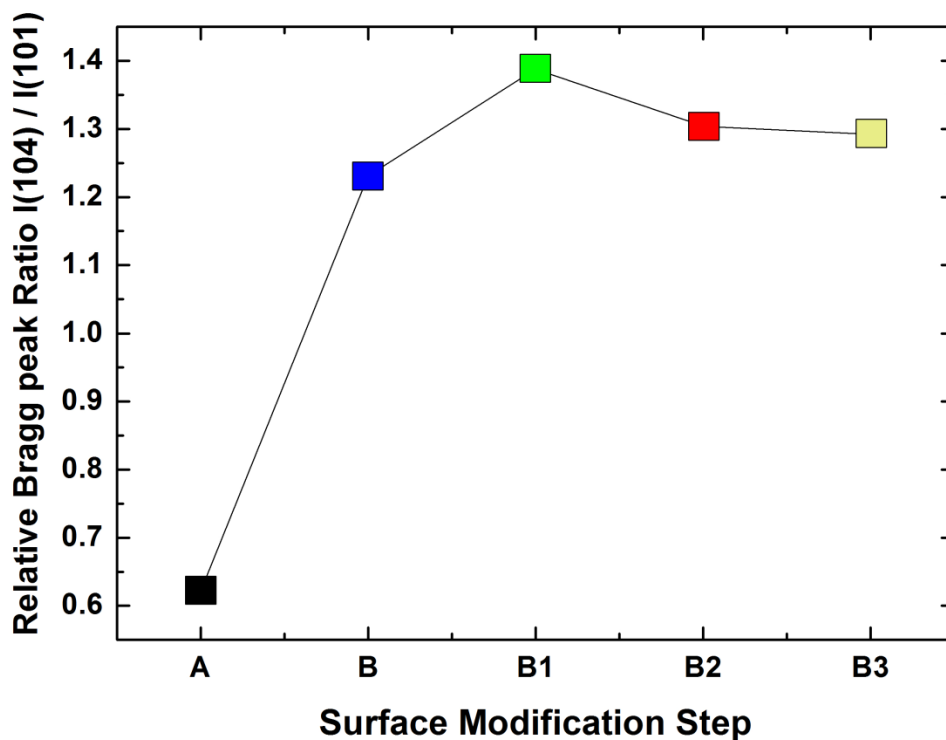
(I)



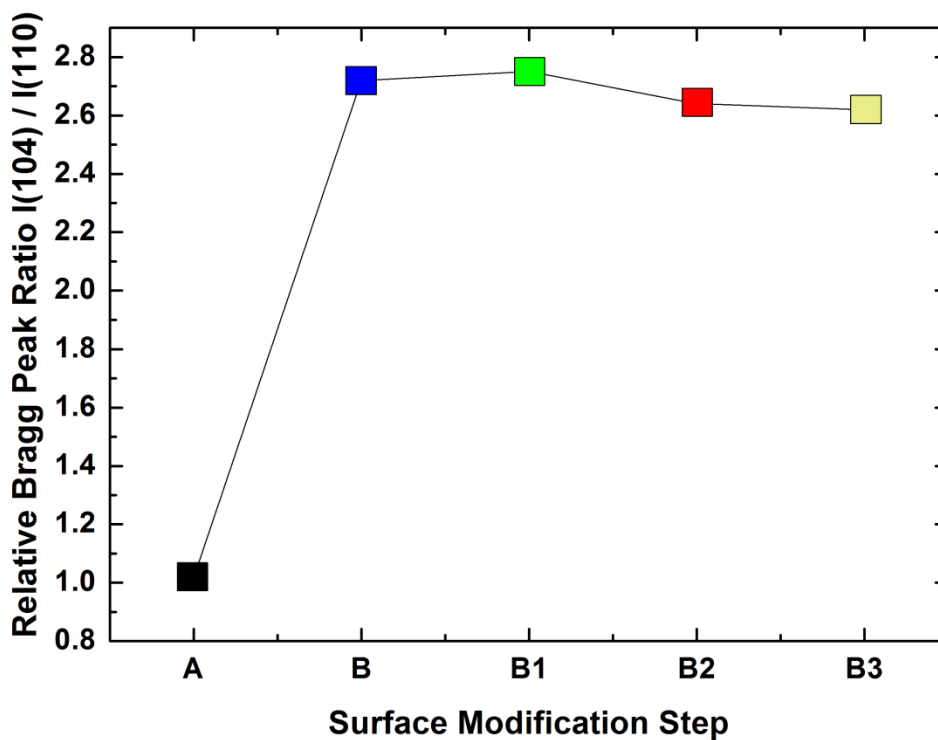
(II)



(III)



(IV)



(V)

**Figure 11.3** (I): The X-Ray Diffractogram of pristine hematite (A), Phycocyanin adsorbed on hematite (B), Agarose coated (C), CDI activated (D) and Phycocyanin conjugated (E) films. (II) Expanded view of (104) and (110) reflection along with (101) from substrate. (III)

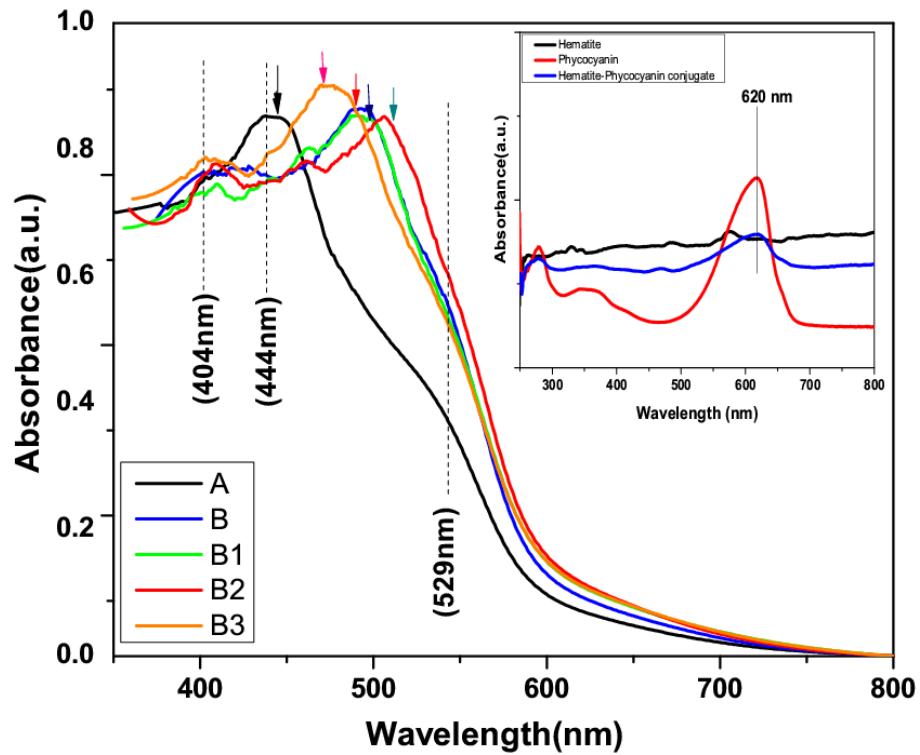
Crystallite size variation of hematite after surface modification calculated using scherrer equation. (IV) Variation in relative Bragg peak intensity ratio  $[I(104)/I(101)]$  from the hematite and substrate to see the effect of thickness. (V) Relative Bragg peak ratio  $[I(104)/I(110)]$  of hematite and its variation at each surface modification step.

### 11. 3.3 Optical properties of Hematite - Phycocyanin system

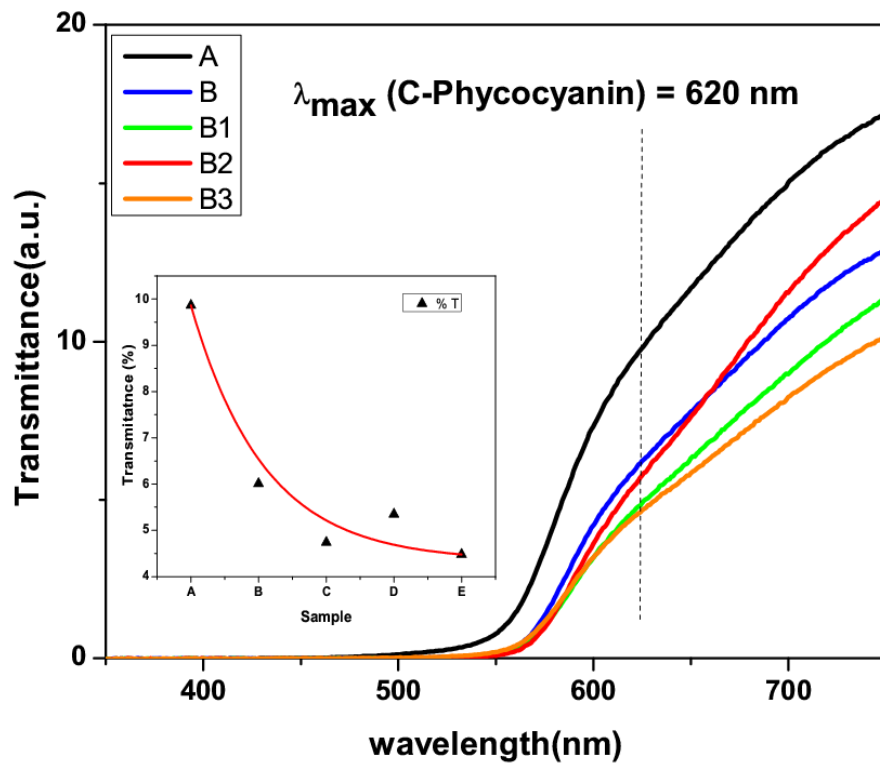
In view of the effect of the light harvesting protein (C-phycoyanin) on the optical properties of hematite, I analyze the UV-Vis spectra of pristine and other films after each surface modification step. Generally, the photocurrent obtained from hematite depends mainly on the quantity of absorbed photons which convert into electrical energy by the generation of electron-hole excitons. The anticipated enhanced photocurrent obtained in this case could be related to the light harvesting action of the protein molecule which absorbs in the red part of the visible spectrum. This means that by integrating this protein on the hematite or photoactive layer, I can increase its light absorbing properties by taking advantage of the extended region of visible wavelength. For example there are several factors which can affect the total number of photons absorbed by a solar cell active layer. These are respectively the optical absorption comparable to the solar spectrum, the absorptivity and the broadening of absorption wavelength range. In our proposed system hematite is the photoactive layer and the generation of photocurrent in this case will be enhanced only when the total number of photons absorbed by it increases. This is only possible when the absorption range and absorption peak value or the intensity increases for hematite. Therefore by anchoring the C-phycoyanin molecule on the hematite surface, the absorption peak value can be increased with a broadening of the spectral range. This was done by functionalization of the hematite surface with C-phycoyanin as described above. The absorption spectra [Figure 11.4 (I)] of all films from A-B3 reveal that the pristine hematite films (A) absorb at 404 nm, 444 nm and 545 nm respectively which corresponds to the usual band position of bulk hematite [25]. The band at 444 nm appears due to ligand field transition and 545 nm is the absorption edge of hematite. In the next step, on adsorbing protein on the hematite surface (B), the spectral broadening occurs with the 444 nm band shifted towards the longer wavelength while other band at 404 nm remains at the same position. I notice also that the intensity of the absorption edge or absorption peak value is increasing. I can attribute change of spectral weight to the interaction of absorbed protein on the hematite surface, and the enhancement in the absorption peak value occurs due to the extra portion of light absorbed by the protein. C-phycoyanin absorbs at 620 nm which is the standard absorbance wavelength supported by another study [26], and this can be seen from the inset in Figure 11.4(I). A change in the absorption maximum of phycocyanin has been observed on interacting with the

nanoparticle from the film. This change was originally proposed to be due to the perturbation of the surface charge density of the nanoparticle and the protein [27], which manifested in changing the absorption spectrum. In the next step of surface activation, on adding the agarose layer, spectrum (B1) looks the same like that of (B) with slight decrease in intensity of 444 nm band. On further treatment with CDI, the spectra of activated films (B2) change slightly with consequent increase in absorption edge peak intensity. Also the 444 nm band position shifted to longer wavelength while the intensity remains the same like that of spectra (B) and (B1). This shift towards larger wavelength can be explained with changes in the particle size. This is already evident from the crystallite calculation as shown in Figure 11.3(III), whereby I have found that crystallite size varies with preceding surface modification. It was established that the crystallite size changed with the changes in  $\text{Fe}^{3+}$ -  $\text{O}^{2-}$  distance in hematite due to temperature treatment. This resulted in a red shift of about 20 nm to the higher wavelength for absorption band due to the  $\text{Fe}^{3+}$  ligand field transition [28]. On conjugating with final phycocyanin molecule, the intensity of the 444 nm band reached maximum and again shifted to shorter wavelength. This was also due to the variation in crystallite size as stated above. A similar behavior has been observed in the photoluminescence spectra of a porous Si matrix, where a spectral shift was attributed to the erosion of the nanocrystalline Si by surface oxidation from the interacting protein [23]. The transmittance spectra [Figure 11.4 (II)] further showed the photo absorptive capability of phycocyanin molecule in the conjugated system. Hereby I have looked into the transmittance of the modified film at 620 nm where phycocyanin does absorb photons. The inset in the figure shows that the transmittance decreases strongly on going from the pristine to the phycocyanin cross linked film. This further confirms that the cross linked film absorbs more photons which is obvious by considering the maximum absorption shown at 444 nm. To give an account of the changes in the electronic structure of pristine hematite film, I have determined the energy band gap ( $E_g$ ) of the pristine film after each surface modification step [Figure 11.4 (III)]. From here I find that the band gap ranges around 2.09 - 2.12 eV, which places it in the band gap energy of hematite (1.9 - 2.2 eV) [29]. It follows the pattern as depicted in the inset of Figure 11.4(III). It slightly shifts with the modification step but stabilizes at 2.09 eV, when the agarose layer is added. From this I conclude that the surface functionalization does not effect on the electronic structure of hematite. Nevertheless, by conjugating the phycocyanin with hematite, its absorption intensity increases by the increase in the amount of photons absorbed due to light harvesting action of the C-phycocyanin molecule. This finally will enhance the photocurrent of the hematite film as observed from further analysis of the photoelectrochemical properties. A similar study has been made on the light

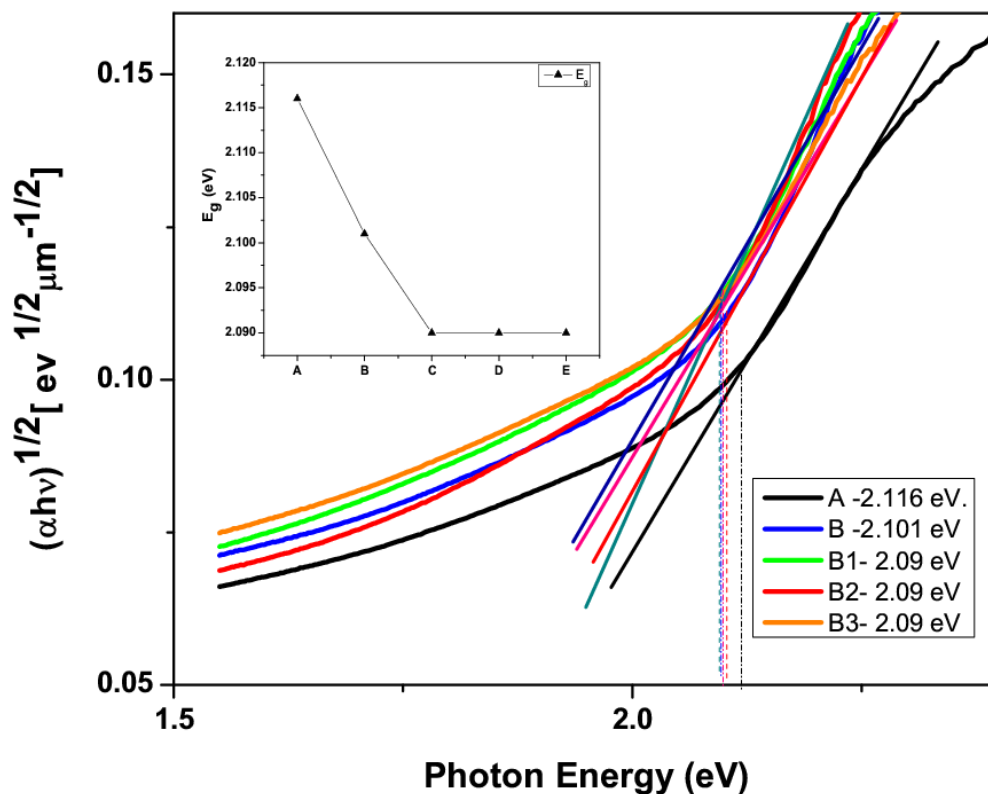
harvesting and photocurrent of a P3HT: PCBM bulk heterojunction solar cell by the contribution of Coumarin 6 using optical spectroscopy [30].



(I)



(II)



(III)

**Figure 11.4(I)** UV-VIS absorption spectra of pristine hematite (A), Phycocyanin adsorbed on hematite (B), Agarose coated (C), CDI activated (D) and Phycocyanin conjugated (E) films. Inset: the change in the absorption maximum of phycocyanin on interacting with the nanoparticle from the film.(II) transmittance spectra of films A - E. Inset: the variation of %T with surface modification step.(III) the energy band gap( $E_g$ ) of pristine film after each surface modification step in all films. Inset showing the trend in the variation of  $E_g$ .

### 11.3.4 Probing the integrity of protein structure with Raman Spectroscopy

I apply Raman spectromicroscopy to investigate the integrity of the protein structure in the finally conjugated system. The objective of this part of the study is to probe the stability of the chromophore present inside the phycocyanin protein in the conjugated system, which, as will be shown in the next section, showed a significantly enhanced photocurrent. Generally, this chromophore is responsible for the light absorption and energy transfer mechanism toward the reaction center. The corresponding Raman spectra of pristine and modified films along with spectra from the bare protein deposited on glass and on the FTO substrate are shown in Figure 11.5. The Raman spectrum of pristine hematite on FTO shows four bands at 283, 392, 488 and 607  $\text{cm}^{-1}$  with a slight shift from reference spectra [31]. The band at 488  $\text{cm}^{-1}$  is assigned to the

$A_{1g}$  mode and the remaining peaks assigned to the  $E_g$  mode [32]. The weak intensity band observed above  $600\text{ cm}^{-1}$  was mainly attributed to the presence of trace amounts of magnetite or maghemite with Raman forbidden transitions [33]. Upon addition of the agarose layer, I find that the intensities of all bands increase. This is due to the interaction of the Raman light with the density of the next incoming media. Further on activating the agarose treated hematite films with carbonyl diimidazole, a new band evolves in between  $488$  and  $607\text{ cm}^{-1}$  and the peaks from the hematite film exhibited a blue shift. This blue shift could be due to the decrease in crystallite size during the respective modification step as evident from Figure 11.3(III) and consistent with earlier studies on  $\text{TiO}_2$  powders and thin films [34]. Finally, on conjugating the phycocyanin protein with the activated film, the Raman spectrum shows a new band at around  $1610\text{ cm}^{-1}$  which fits well with the phycobilliprotein (the protein chromophore) band around  $1597\text{ cm}^{-1}$  in the Raman spectra of C - phycocyanin excited at  $488\text{ nm}$  [35]. In the spectra obtained from the bare phycocyanin on FTO and glass substrate, the band was also observed at  $1610\text{ cm}^{-1}$ .

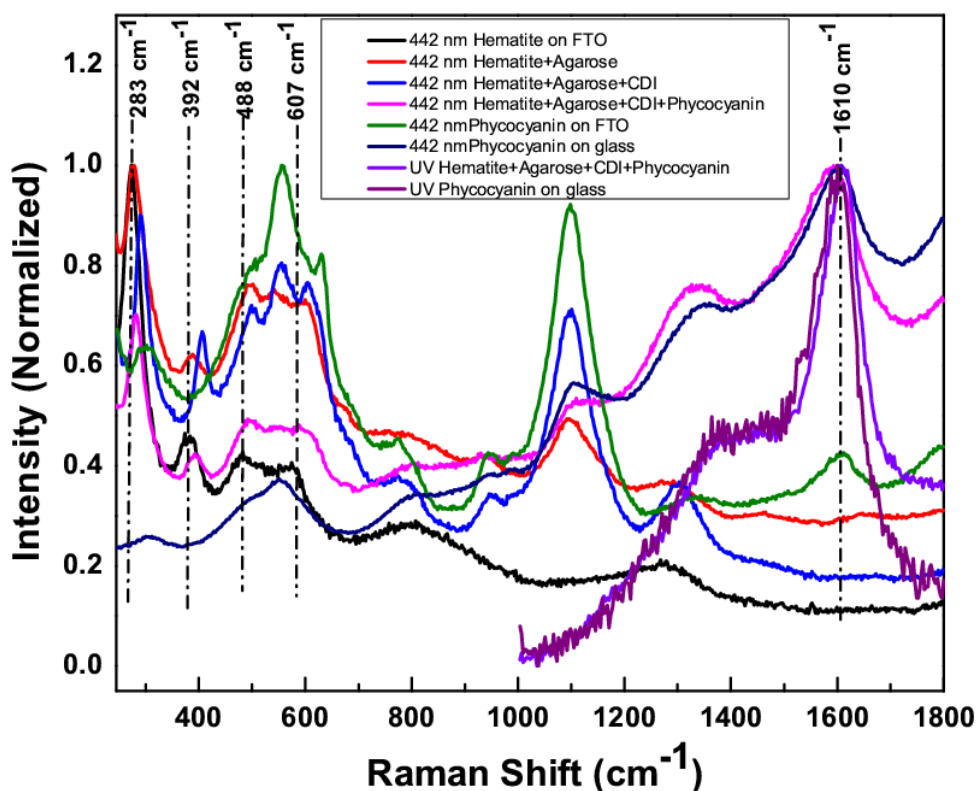


**Figure 11.5** Raman spectra of pristine and modified films along with spectra from bare protein on glass and FTO substrate excited with visible and UV light show the integrity of protein after electrochemical treatment [49].

Consideration of this scenario allows to state that the protein chromophore structure remains in stable configuration. On the other hand, if the structure gets destroyed by denaturation, then the band would gradually lose its intensity. But it remains the same as is evident from the spectra. In addition have I used UV excitation to probe the spectra of phycocyanin on glass and the protein conjugated system as shown in Figure 11.5. Since the sample contains a strong chromophore moiety or pigment, UV excitation is also preferable to visible excitation because the Raman excitation gets obscured by the fluorescence of the chromophore in the latter case. Here also I have observed the same band at  $1610\text{ cm}^{-1}$  and the intensity of the band remains same in both cases. From these discussions, I proposed that the structure of the chromophore inside the phycocyanin protein remains intact after finally conjugating over hematite surface.

### 11.3.5 Photoelectrochemical properties of hematite - phycocyanin system

The photoelectrochemical performance for the hematite–phycocyanin integrated system is obtained by sweeping the current – potential scans in 1M KOH electrolyte (pH = 13.6) in the dark and simulated solar illumination (AM 1.5) as shown in Figure 11.6 (I). Initially, the saturated photocurrent density of the pristine hematite sample (A) is  $281.40\text{ }\mu\text{A}/\text{cm}^2$ , which begins at an onset potential of -100 mV and increases until the dark current onset begins at 450 mV. After adding the first phycocyanin layer (B), the photocurrent density increases to  $420.26\text{ }\mu\text{A}/\text{cm}^2$  and remains constant on adding the agarose layer (B1). After the activation process by CDI (B2), it increases up to a value of  $458.76\text{ }\mu\text{A}/\text{cm}^2$  and finally reached  $491.53\text{ }\mu\text{A}/\text{cm}^2$  after conjugation of the next phycocyanin layer (B3) as depicted in Scheme 11.1-A. This means that after integrating the final protein molecule by covalent cross coupling I can increase the photocurrent by over  $200\text{ }\mu\text{A} / \text{cm}^2$ . I attribute this virtually two fold increases in photocurrent to the extra light absorbing capability of hematite film assisted by the light harvesting property of phycocyanin. This corresponds to the changes in the absorption spectrum of hematite-phycocyanin conjugate as discussed above. To get a clear insight into the same, I have performed IPCE studies of the pristine hematite film (A), phycocyanin adsorbed hematite film (B), agarose modified phycocyanin adsorbed hematite (B1) and conjugated film (B3) [Figure 11.7- F]. From this, it is clearly observed that the efficiency of the protein functionalized film is enhanced upon at 620 nm which is the absorption maximum of the phycocyanin molecule. Whereas the pristine hematite film does not show any enhanced efficiency at 600 - 620 nm. The inset clearly demonstrates that the photocurrent is enhanced by the functionalization of pristine hematite film by phycocyanin in both adsorbed (B) and conjugated step (B3). This clearly shows that the light absorbed by phycocyanin directly causes the increase in photocurrent. A similar rise in photocurrent efficiency was observed in the dye sensitization of

hematite nanorods, whereby an improvement of the photocurrent efficiency is reached by red shift the photocurrent onset at 750 nm with a maximum of 699 nm [36]. Besides these there may be some other factors which can enhance the photocurrent. For instance the photodynamic action of phycocyanin and the effect of carbon oxidation.

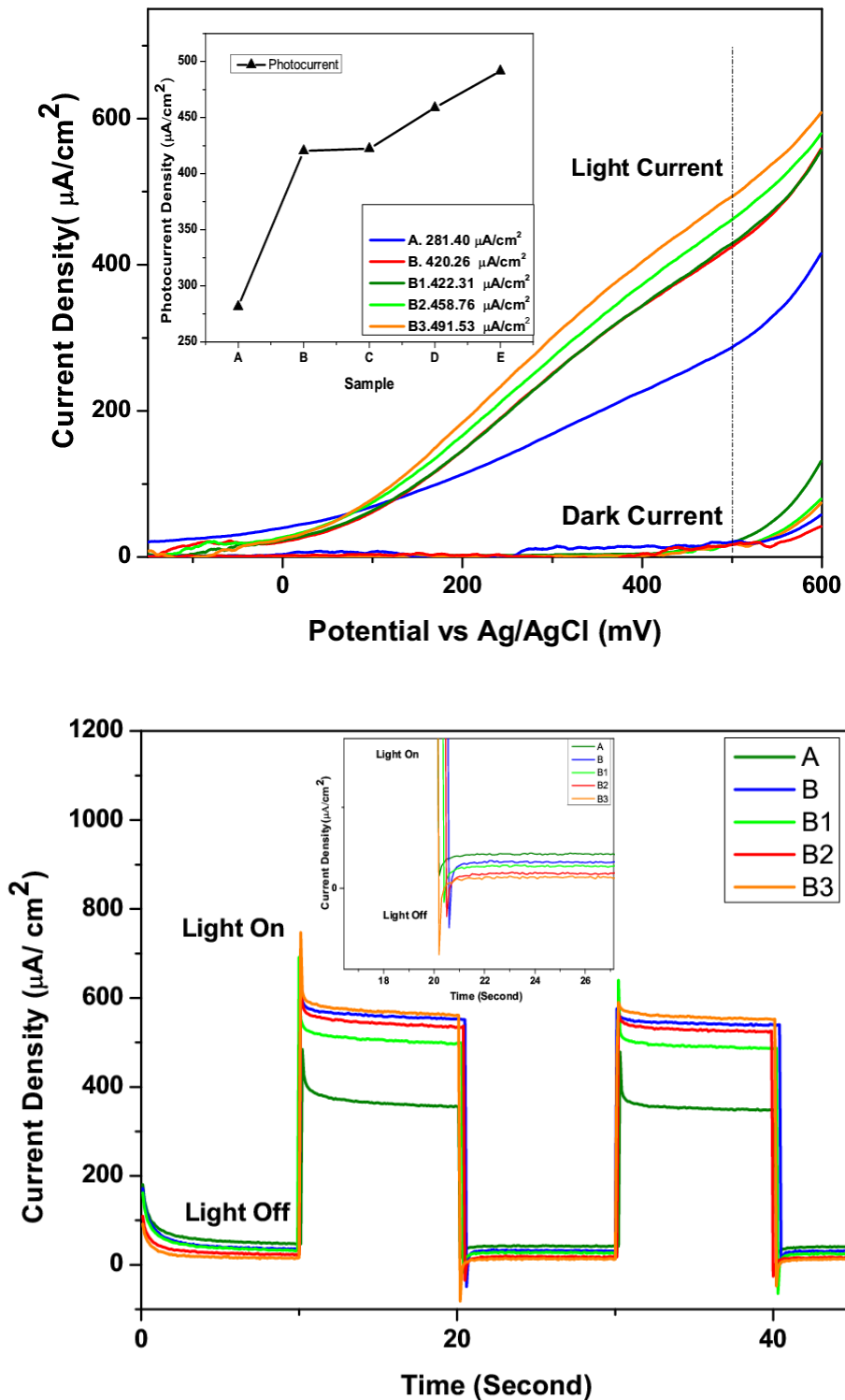


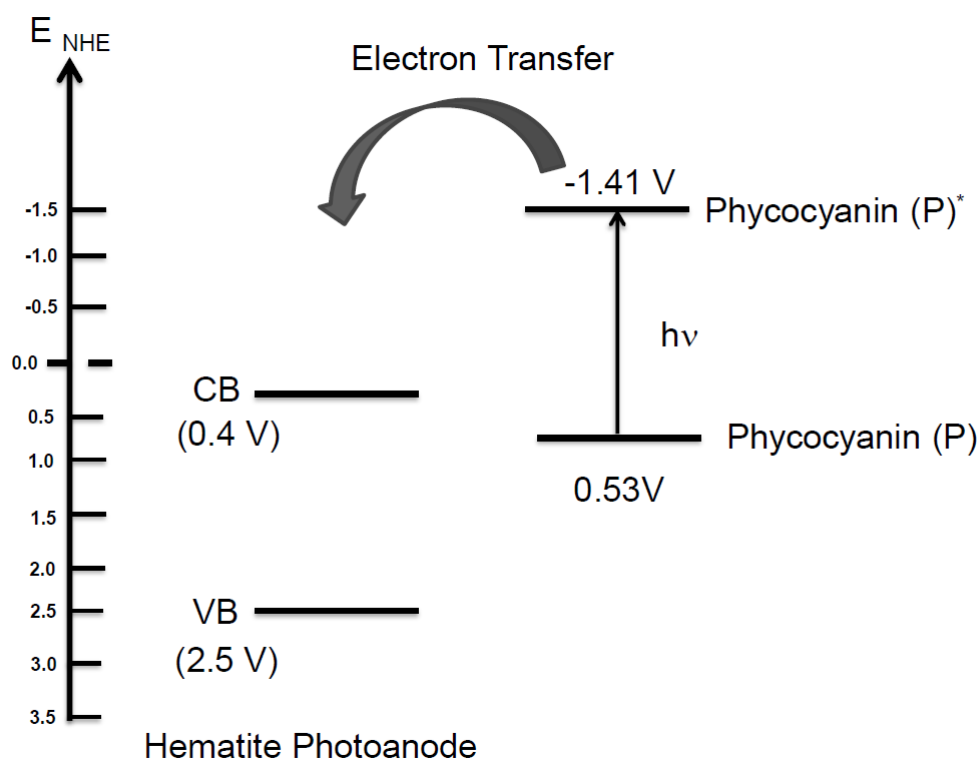
**Figure 11. 6** (I) The photocurrent measured for pristine hematite (A), Phycocyanin adsorbed on hematite (B), Agarose coated (B1), CDI activated (B2) and Phycocyanin conjugated (B3) films

in 1M KOH electrolyte (pH= 13.6) with three electrode photoelectrochemical cell under the dark and simulated solar illumination (AM 1.5 ). (II) The photocurrent transient responses of pristine hematite (A), Phycocyanin adsorbed on hematite (B), Agarose coated (B1), CDI activated (B2) and Phycocyanin conjugated (B3) films measured during chronoamperometric cycling of all electrodes.

#### *11.3.5.1 Possible factors influencing the increase in photocurrent*

Phycocyanin has a good photodynamic action for water photo-oxidation. It can interact with the water molecule (solvent) or with hematite (substrate) by a so called type I mechanism whereby it transfers charge to the solvent (electrolyte in this case) with the generation of radicals [37]. This happens only when phycocyanin gets excited with light. Photosensitized oxidations are the basis for photodynamic action. The first step of this photodynamic action is the absorption of light by a sensitizer (sens) to produce an excited state (sens<sup>\*</sup>). In this case phycocyanin acts as a sensitizer. In the presence of oxygen, two competing reactions of the excited state sensitizer can occur which is respectively Type I and Type II mechanism. Hydroxyl radical (OH<sup>•</sup>) can be generated by following mechanism when C-phycocyanin is irradiated with visible light (470 nm). It is speculated that in our case the Sens<sup>\*</sup> can either react with the hematite surface or with the electrolyte during PEC operation (Type I) or with oxygen (Type II). One important question that arises from the functionalization of the hematite is that of the charge transport across the components of the film assembly. Consequently I carried out a photocurrent transient response study [Figure 11.6(II)], which was done by chopping the light during the chronoamperometric operation of the electrode at a constant potential of 600 mV. The photocurrent of the protein adsorbed film (B) and the conjugated film (B3) are higher than the pristine film (A). On turning the light on, I obtained photocurrent transient spikes in upward direction, which then decay from a peak to a steady state (A-B3). On turning the light off after 10 seconds of illumination, the current drops towards zero and reverts back again when light is turned on. This falling photocurrent transient decay is indicative to the more rapid removal of conduction band electrons into the bulk [38] and the spike like transient response is caused by the “back reaction” or recombination of the photogenerated electrons and holes with the surface states [39]. The falling transient [40] is rationalized in terms of photogeneration of an OH<sup>•</sup> radical which acts as an electron acceptor. Assuming the charge transfer mechanism to prevail, if I carefully look into the cathodic transient spike [inset of Figure 11.6(II)] for each of the sample I find that in case of the phycocyanin cross-linked system the current decay slowly to a steady state in comparison to other samples. This has been accounted for in the energy band diagram in [7], which I adopting in scheme 11.7. The magnitude of this cathodic transient spike is quite

high in case of the protein conjugated film. It is evident that during the chopped chronoamperometric measurement, when the light is turned off,  $\text{OH}^\bullet$  at the surface continue to

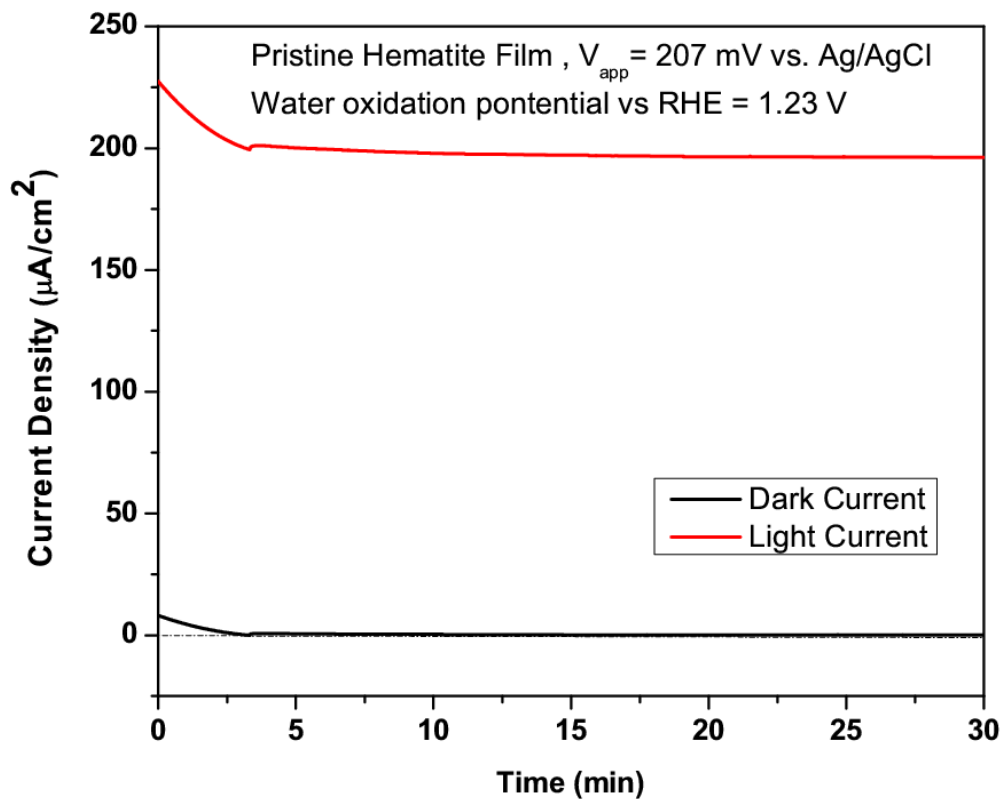


**Scheme 11.7:** Energy band diagram showing the charge transfer from excited state phycocyanin to conduction band of hematite

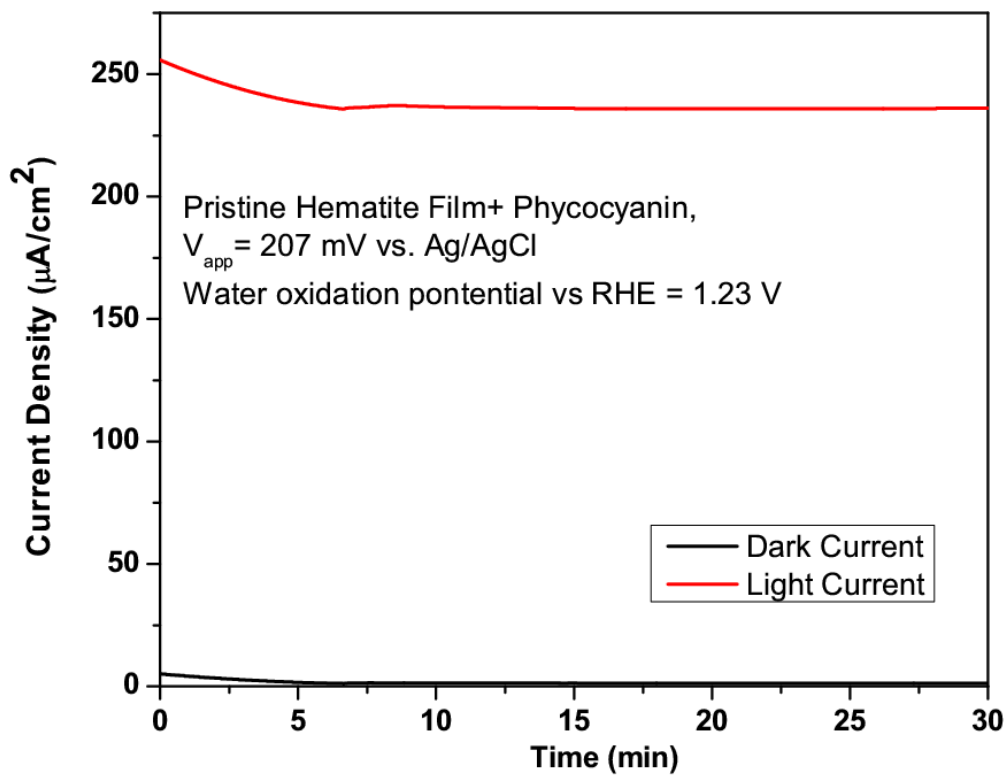
scavenge conduction band electrons and create a cathodic transient spike until the  $\text{OH}^\bullet$  is consumed. On the other hand, the current transients in the positive direction represent the accumulation of holes at the electrode / electrolyte interface under light condition. Increase in the magnitude of cathodic transient spike in the hematite-phycocyanin cross linking step as shown in inset of Figure 11.6 (II) suggests that more  $\text{OH}^\bullet$  are produced on the hematite surface due to extra photodynamic action of phycocyanin, or it takes more time to consume all the radicals by conduction band electrons. Dotan et al. recently showed the effect of hole scavenger such as  $\text{H}_2\text{O}_2$  on the photoelectrochemical properties of hematite [41]. It was found that when  $\text{H}_2\text{O}_2$  is added to the electrolyte the current transients disappear and purely faradic photocurrents are obtained. The absence of current transients suggests that no charge is accumulated at the electrode / electrolyte interface. This indicates that all charges which reach the interface are injected to the electrolyte or consumed by a very fast surface recombination.

### 11.3.5.2 Source of enhanced photocurrent in hematite – phycocyanin system

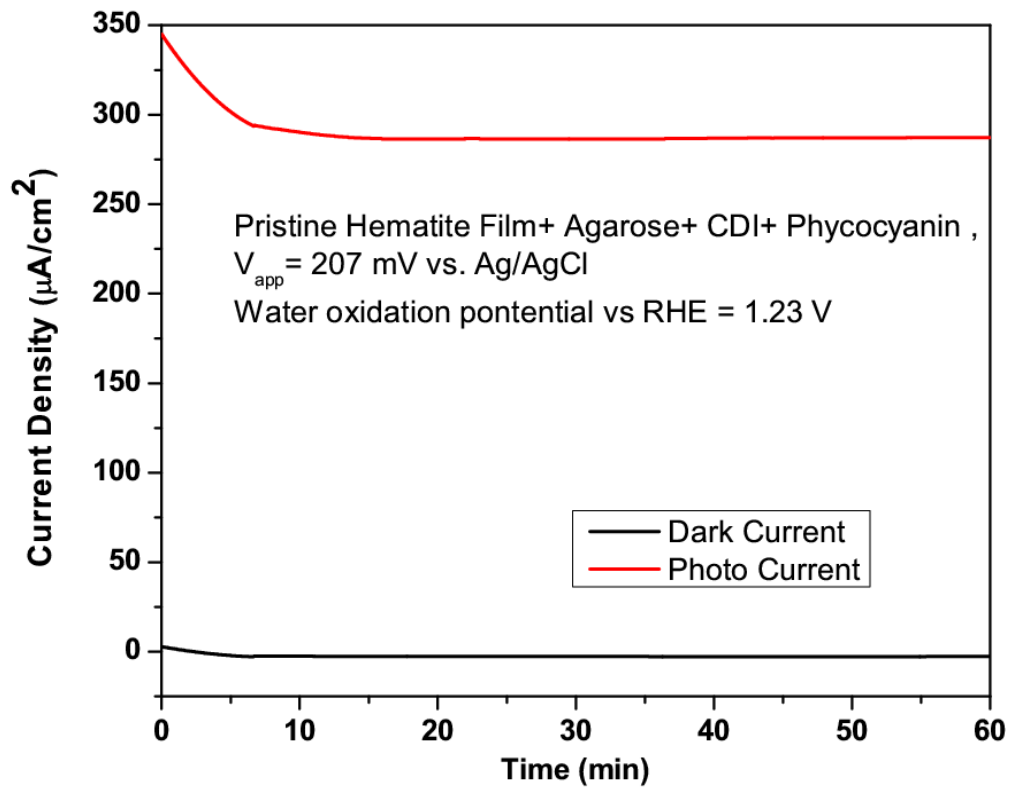
The photocurrent ideally originates from water oxidation by the photogenerated holes. Parasitic contributions may come from other oxidative processes, such as from the oxidation of organics like protein or non-converted volatile precursor components on the electrode surface, which over time may be fully consumed away. To test this, I performed long-term chronoamperometry of the hematite film (A) and the functionalized film (B and B3) at the oxidation potentials of water (207 mV, 1.23 V vs. RHE) for a suitable period of time. Here, I found reasonable stability in the photocurrent of the protein functionalized film. Upon careful analysis of the chronoamperometry results (Figure 11.8 A, B and C), I found that the dark current magnitudes are fairly low. It has been noted that during first couple of minutes, dark current decays quickly with time. I calculated the total number of moles of electrons generated after 5 minutes of each of chronoamperometric operation during dark and light experiment with a procedure described in [42]. The number of moles of electrons obtained and corresponding number of moles of evolved oxygen in each case are presented in Table 11.10. The stability of the photocurrent over time is plotted in Figure 11.8 D. I see clearly that the protein functionalized film shows sustained enhanced current as was obtained during I-V scan [Figure 11.6(I)]. I plotted the number of moles of electrons obtained during dark chronoamperometric scan after 10 min of operation for samples A, B and B3 (Figure 11.8 E). It is observed that the number of moles of electrons results from the dark oxidation of organic material decreases to a lower value over the period of time. Interestingly, in the protein conjugated hematite film (B3) this value is negligible. This clearly signifies that the enhanced photocurrent of the protein functionalized film does not originate from the oxidation of the protein itself. The origin of the enhanced photocurrent is thus from water photo-oxidation and extra light harvesting of phycocyanin at 620 nm evident from IPCE result [Figure 11.8F].



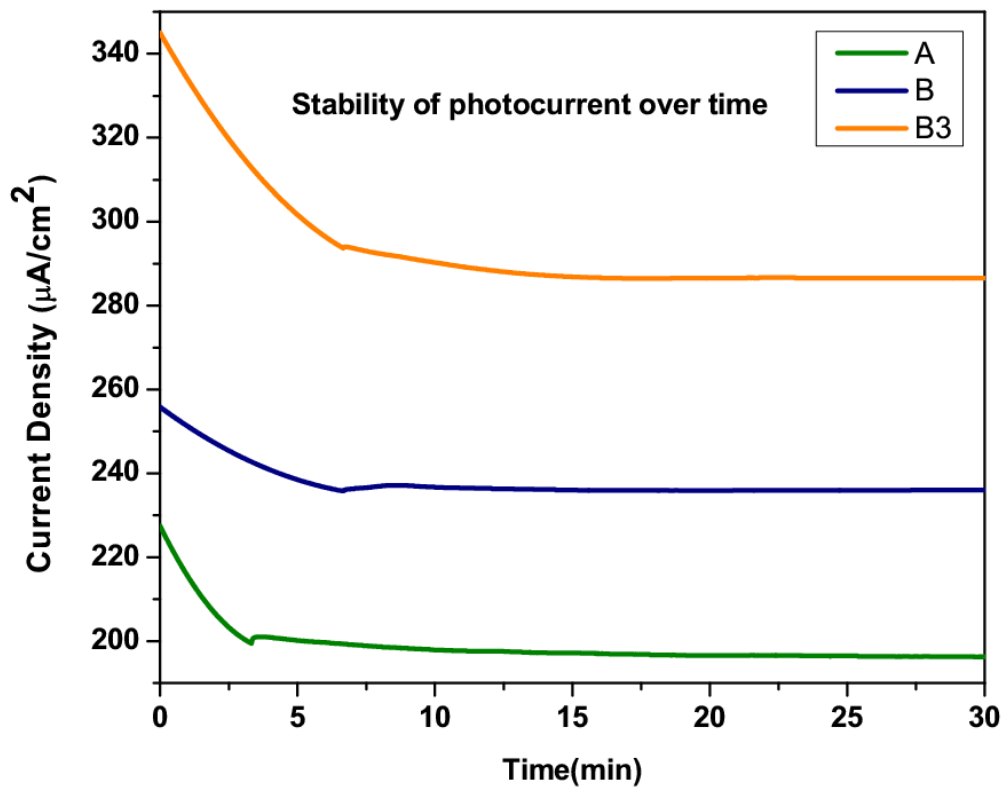
A.



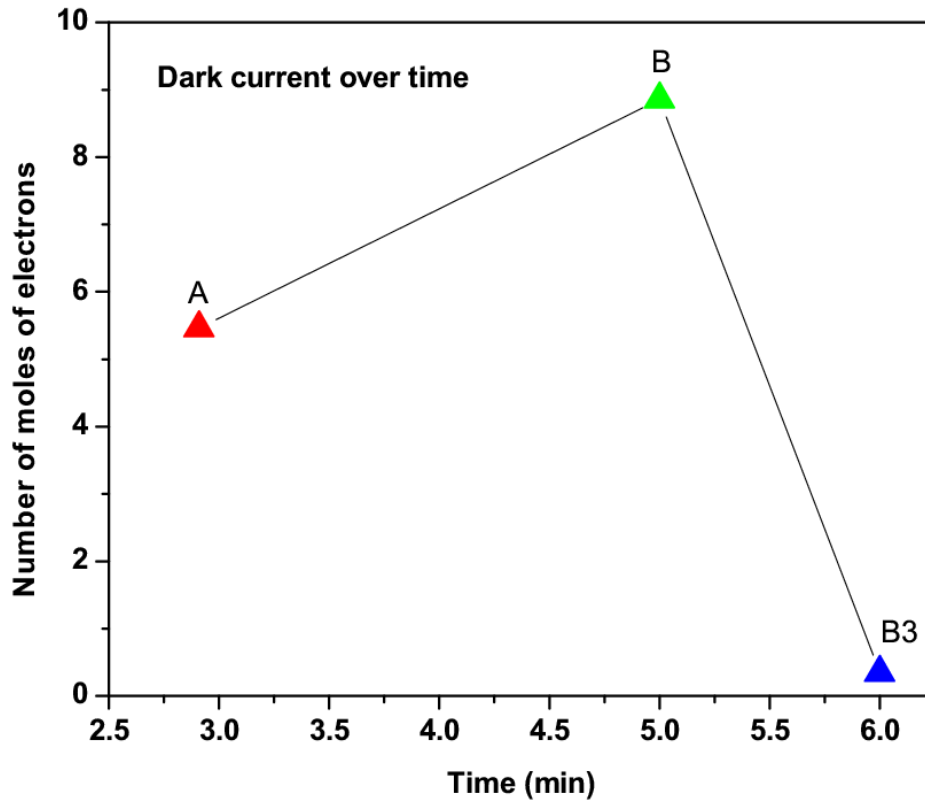
B.



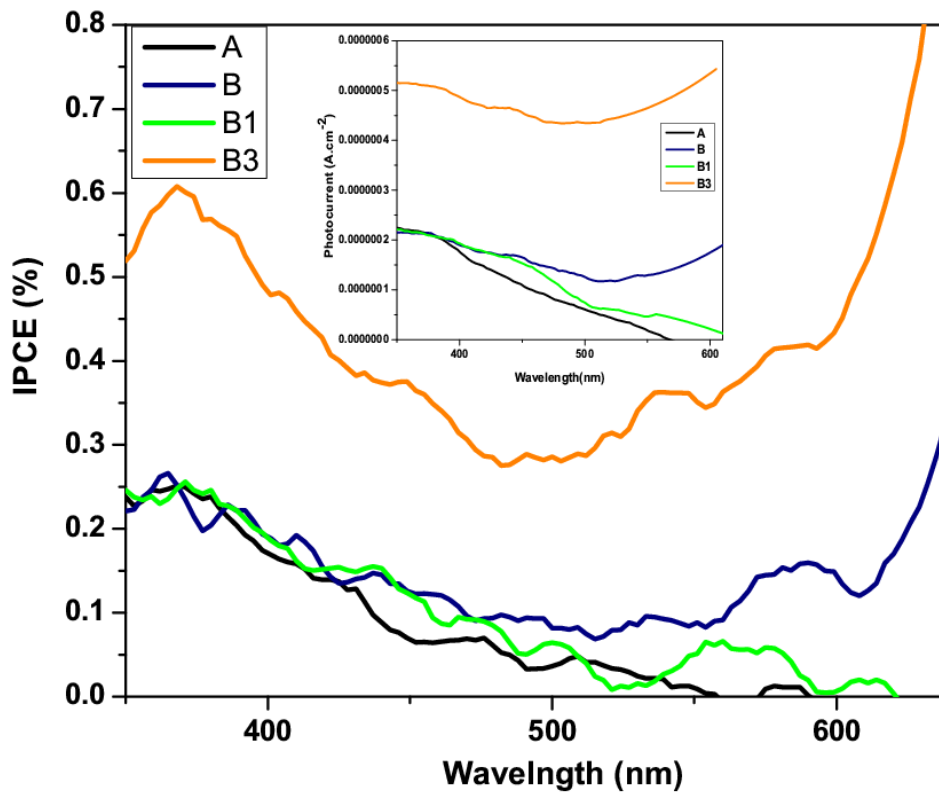
C.



D.



E.



F.

**Figure 11.8** Long-term sustainability study of the photocurrent by carrying out the chronoamperometric measurement of the hematite film (A) and the protein functionalized films (B and C) at the oxidation potentials of water (207mV, 1.23 V vs. RHE).(D) The stability of photocurrent over time for pristine and protein functionalized film. (E) Number of moles of electrons obtained during dark chronoamperometric scan after 10 min of operation for samples A, B and B3 (F) IPCE measurement of pristine hematite film(A), phycocyanin absorbed hematite film (B), Agarose modified phycocyanin adsorbed hematite(B1) an conjugated film (B2).

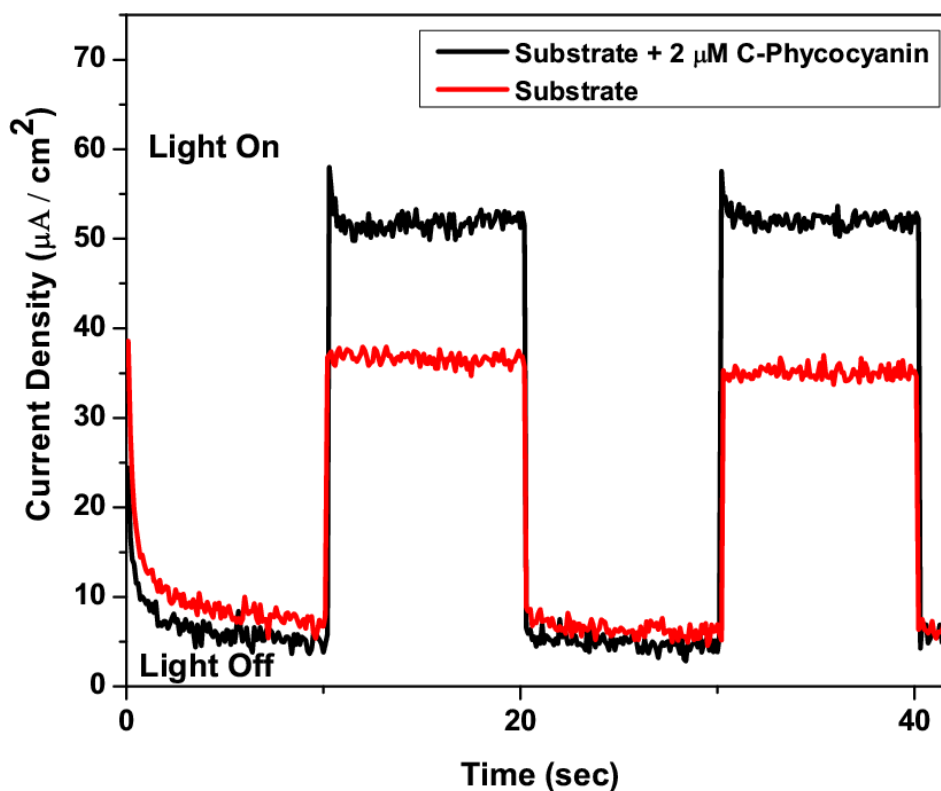
Sample	Condition	Number of moles of electrons	Number of moles of oxygen
A	Dark	9.55 n mole	2.38 n mole
	Light	3.83μ mole	0.957 μ mole
B	Dark	29.3 n mole	7.33 n mole
	Light	4.58 μ mole	1.145 μ mole
B3	Dark	42.21 n mole	10.56 n mole
	Light	5.47 μ mole	1.371 μ mole

**Table 11.9** The number of moles of electrons obtained and corresponding number of moles of evolved oxygen calculated from the chronoamperometric measurement.

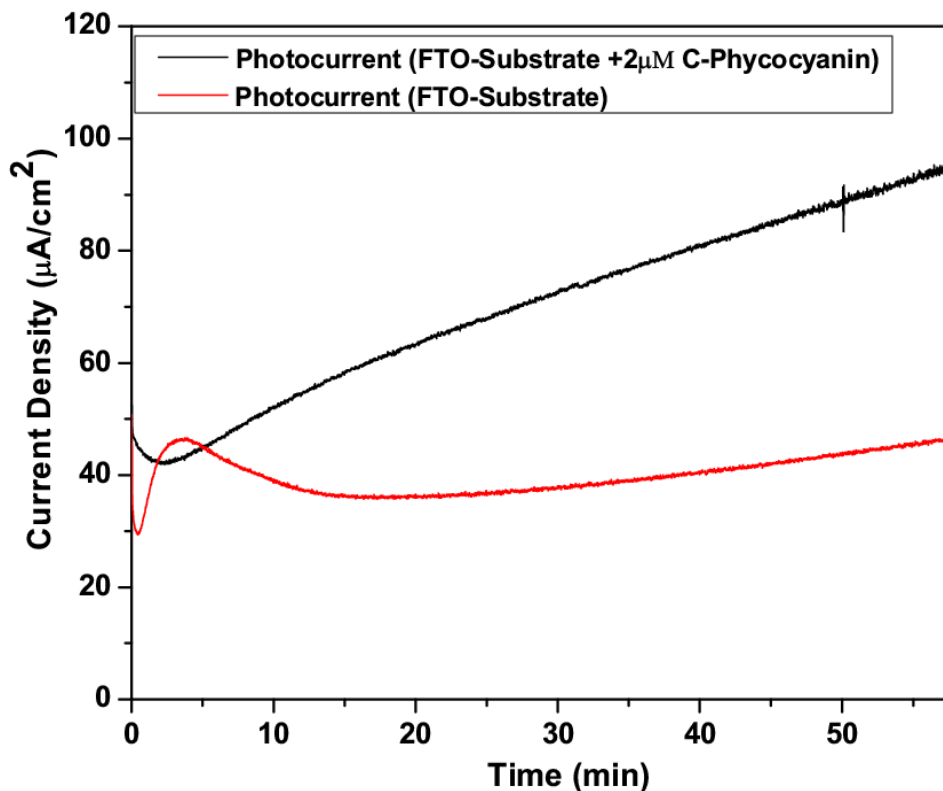
*11.3.5.3. Role of phycocyanin in enhancing the photocurrent and long term operational stability*

To investigate the individual role of phycocyanin in enhancing the photocurrent, I studied the transient photoresponse of the phycocyanin adsorbed FTO substrate and pristine FTO by applying a potential of 100 mV during chronoamperometric operation (Figure 11.10A) as a control experiment. Here, phycocyanin was first transferred to the FTO by dipping FTO into a 2 μM solution of phycocyanin. I follow for this particular case a protocol presented by Janzen and Seibert in 1980 [43], because they too worked on tin oxide substrates. Excess amount of phycocyanin solution was removed from the lower part of FTO and dried in dark. The FTO with adsorbed phycocyanin shows higher photocurrent than pristine FTO. This further validates the role of phycocyanin in enhancing photocurrent on integration of hematite electrode. Similar

observations were made on the LH1-RC complex on APS terminated ITO electrode [44]. During light-on condition I observe the photocurrent transient spike when phycocyanin is adsorbed on FTO, which is absent in case of pristine one. The reason behind the absence of any transient photocurrent spikes [45] in case of pristine FTO is due to the limitation of charge transport process by the recombination in the bulk. Sivula et al. find a similar result in case of thermal treatment of mesoporous hematite film whereby they considered the transient spike at the photocurrent onset potential [46]. The stability of phycocyanin on FTO was studied in a control experiment with chronoamperometry for one hour under light condition as shown in Figure 11.10 B. Phycocyanin shows good operational stability and has increased photocurrent in comparison to the bare FTO.



A.



B.

**Figure 11.10** (A) transient photoreponse of the phycocyanin adsorbed FTO substrate and pristine FTO during chronoamperometric cycling to evaluate the individual role of phycocyanin protein in providing extra photocurrent. (B) long term stability measurement of phycocyanin chronoamperometrically for 1 hour under light condition .

To further check the functionality of the species B after electrochemical treatment, I have recorded the absorbance spectra of species B. Figure S4 shows the difference spectrum obtained by subtracting the pristine hematite spectrum from the absorbance of species B in the wavelength range from 400 nm to 700 nm. I find a significant absorbance even after electrochemical treatment up to 600 mV. The spectral signature coincides with that from phycoerythrin [47]. This, together with comparison with the spectrum of phycocyanin 645 [5] confirms that species B has the spectral signature from phycocyanin.

With respect to scale-up and large scale production of phycocyanin-based devices, a new protein separation technique called expanded bed adsorption chromatography (EBAC) could in the future lower the cost of extraction and purification [48].

## 11.4 Conclusions

I have developed a strategy for increasing the photocurrent of a hematite thin film electrode by integrating C-phycoerythrin protein with a linker mediated covalent cross coupling technique. The hematite structure is preserved as is evident from XRD. UV spectra show increased optical absorption by harvesting more photons on finally coupling with protein. This helped further in getting an enhanced photocurrent in the chemically cross linked system in comparison to pristine hematite. Transient studies show enhanced photoresponse of the protein coupled hematite system. Enhanced cathodic transient spikes in the hematite-phycoerythrin cross linking step allowed to speculate that more OH radicals may be produced on the hematite surface due to enhanced photodynamic action of phycoerythrin. From long term sustainability studies of the functionalized photoelectrode, it has been shown that the enhanced photocurrent of the protein functionalized film does not originate from the oxidation of the protein itself. The origin of the enhanced photocurrent is indeed from water photo-oxidation and extra light harvesting action of phycoerythrin at 620 nm evident from IPCE result.

## References

- [1] Reisner, E.; Fontecilla-Camps, J. C.; Armstrong, F.A. *Chem. Commun.*, **2009**, 550–552
- [2] Duret, A.; Gratzel, M. *J. Phys. Chem. B* **2005**, *109*, 17184.
- [3] Tahir, A. A.; Upul Wijayantha, K. G.; Saremi-Yarahmadi, S.; Mazhar, M.; Mckee, V. *Chem. Mater.* **2009**, *21*, 3763.
- [4] Spray, R. L.; Choi, K.; *Chem. Mater.* **2009**, *21*, 3701.
- [5] Berns, D. S.; McColl, R. *Chem. Rev.* **1989**, *89*, 807.
- [6] Herrera, F. V.; Grez, P.; Schrebler, R.; Ballesteros, L. A.; Muñoz, E.; Cordova, R.; Altamirano, H.; Dalchiele, E. A. *J. Electrochem. Soc.*, **2010**, *157*, 302.
- [7] Kathiravan, A.; Renganathans, R. J. *Colloid Interf. Sci.* **2009**, *335*, 196.
- [8] Shukoor, M. I.; Natalio, F.; Therese, H. A.; Tahir, M. N.; Ksenofontov, V.; Panthofer, M.; Eberhardt, M.; Theato, P.; Schroder, H. C.; Muller, W. E. G.; Tremel, W. *Chem. Mater.* **2008**, *20*, 3567.
- [9] Li, D.; Teoh, W. Y.; Gooding, J. J.; Selomulya, C.; Amal, R. *Adv. Funct. Mater.* **2010**, *20*, 1767.

- [10] Pagona, G.; Sandanayaka, A. S. D.; Araki, Y.; Fan, J.; Tagmatarchis, N.; Charalambidis, G.; Coutsolelos, A. G.; Boitrel, B.; Yudasaka, M.; Iijima, S.; Ito, O. *Adv. Funct. Mater.* **2007**, *17*, 1705.
- [11] Bora, D. K.; Braun, A.; Erat, S.; Ariffin, A. K.; Löhnert, R.; Sivula, K.; Manzke, R.; Töpfer, J.; Grätzel, M.; Graule, T.; Constable, E. C. *J. Phys. Chem. C* **2011**, *115*, 5619.
- [12] Parfitt, G. D. *Pure. Appl. Chem.* **1976**, *48*, 415.
- [13] Kosmulski, M. *Chemical properties of material surfaces*, Marcel Dekker, Inc., New York, **2001**.
- [14] Adams, S. M.; Kao, O. H. W.; Berns, D. S. *Plant Physiol.* **1979**, *64*, 525.
- [15] Köper, I.; Combet, S.; Petry, W.; Bellissent-Funel, M. C. *Eur. Biophys. J.* **2008**, *37*, 739.
- [16] Hermanson, G. T. *Bioconjugate Techniques*, 2nd ed., Academic Press, United Kingdom, **2008**.
- [17] Hearn, M. T. W.; Harris, E. L.; Bethell, G. S.; Hancock, W. S.; Ayers, J. A. *J. Chromatogr.* **1981**, *218*, 509.
- [18] Zou, H.; Luo, Q.; Zhou, D. *J. Biochem. Biophys. Meth.* **2001**, *49*, 199.
- [19] Alila, S. A.; Ferraria, M.; Botelho do Rego, A. M.; Boufi, S. *Carbohydr. Polym.* **2009**, *77*, 553.
- [20] Günzler, H.; Greulich, H. *IR Spectroscopy*, Wiley-VCH, Germany, **2002**.
- [21] Kay, A.; Cesar, I.; Gratzel, M. *J. Am. Chem. Soc.* **2006**, *128*, 15714.
- [22] Patterson, A. L. *Phys. Rev.* **1939**, *56*, 978.
- [23] Tay, L.; Rowell, N. L.; Lockwood, D. J.; Boukherroub, R. *J. Vac. Sci. Technol. A* **2006**, *24*, 747.
- [24] Warschkow, O.; Ellis, D. E.; Hwang, J.; Mansourian-Hadavi, N.; Mason, T. O. *J. Am. Ceram. Soc.* **2002**, *85*, 213.
- [25] Cornell, R. M.; Schwertmann, U. *The Iron Oxides-Structure, Properties, Reactions, Occurrence and Uses*, VCH Verlagsgesellschaft mbH, Germany, **1996**.
- [26] B. Soni, B. Kalavadia, U. Trivedi, D. Madamwar, *Process Biochem.* **2006**, *41*, 2017.
- [27] Pradeep, T. *Nano: the essentials*; Tata McGraw hill, India, **2007**.

- [28] Saito, T. B. *Chem. Soc. Jpn.* **1965**, 38, 2008.
- [29] Kennedy, J. H.; Frese, K. W. *J. Electrochem. Soc.* **1978**, 125, 709.
- [30] Ismail, Y. A. M.; Soga, T.; Jimbo, T. *Sol. Energ. Mat. Sol. C.* **2010**, 94, 1406.
- [31] Grant, E. *Ann. Rev. Plant Physio.* **1981**, 32, 327.
- [32] Jubb, A. M.; Allen, H. C. *ACS Appl. Mater. Interfaces* **2010**, 2, 2804.
- [33] Chamritski, I.; Burns, G. *J. Phys. Chem. B* **2005**, 109, 4965.
- [34] Zhang, W. F.; He, Y. L.; Zhang, M. S.; Yin, Z.; Chen, Q. *J. Phys. D: Appl. Phys.* **2000**, 33, 912.
- [35] Debreczeny, M.; Gombos, Z.; Szalontai, B. *Eur. Biophys. J.* **1992**, 21, 193.
- [36] Beermann, N.; Vayssieres, L.; Lindquist, S. E.; Hegfeldt, A. *J. Electrochem. Soc.* **2000**, 147, 2456.
- [37] Zhang, S. J. Xie, J. Zhang, J. Zhao, L. Jiang, *Biochim. Biophys. Acta* 1999, 1426, 205.
- [38] Eggleston, C. M.; Shankle, A. J. A.; Moyer, A. J.; Cesar, I.; Grätzel, M. *Aqua. Sci.* **2009**, 71, 151.
- [39] Watanabe, A.; Kozuka, H. *J. Phys. Chem. B*, **2003**, 107, 12713.
- [40] Hardee, K. L.; Bard, A. J. *J. Electrochem. Soc.* **1977**, 124, 215.
- [41] Dotan, H.; Sivula, K.; Grätzel, M.; Rothschild, A.; Warren, S. C. *Energ. Environ. Sci.* **2011**, 4, 958.
- [42] Bora, D. K.; Braun, A.; Erni, R.; Fortunato, G.; Graule, T.; Constable, E. C. *Chem. Mater.* **2011**, 23, 2051.
- [43] Jenzen, A. F.; Seibert, M. *Nature* **1980**, 286, 584.
- [44] Suemori, Y.; Nagata, M.; Nakamura, Y.; Nakagawa, K.; Okuda, A.; Inagaki, J.; Shinohara, K.; Ogasawara, M.; Iida, K.; Dewa, T.; Yamashita, K.; Gardiner, A.; Cogdell, R. J.; Nango, M. *Photosynth. Res.* **2006**, 90, 17.
- [45] Sanchez, C.; Sieber, K. D.; Somorjai, G. A. *J. Electroanal. Chem.* **1988**, 252, 269.

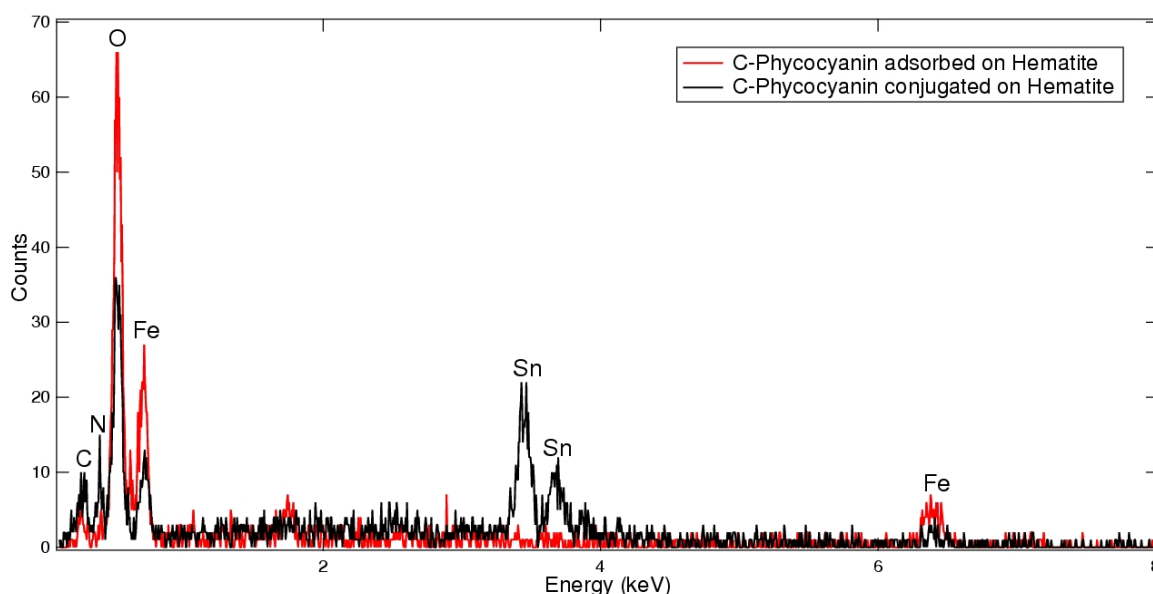
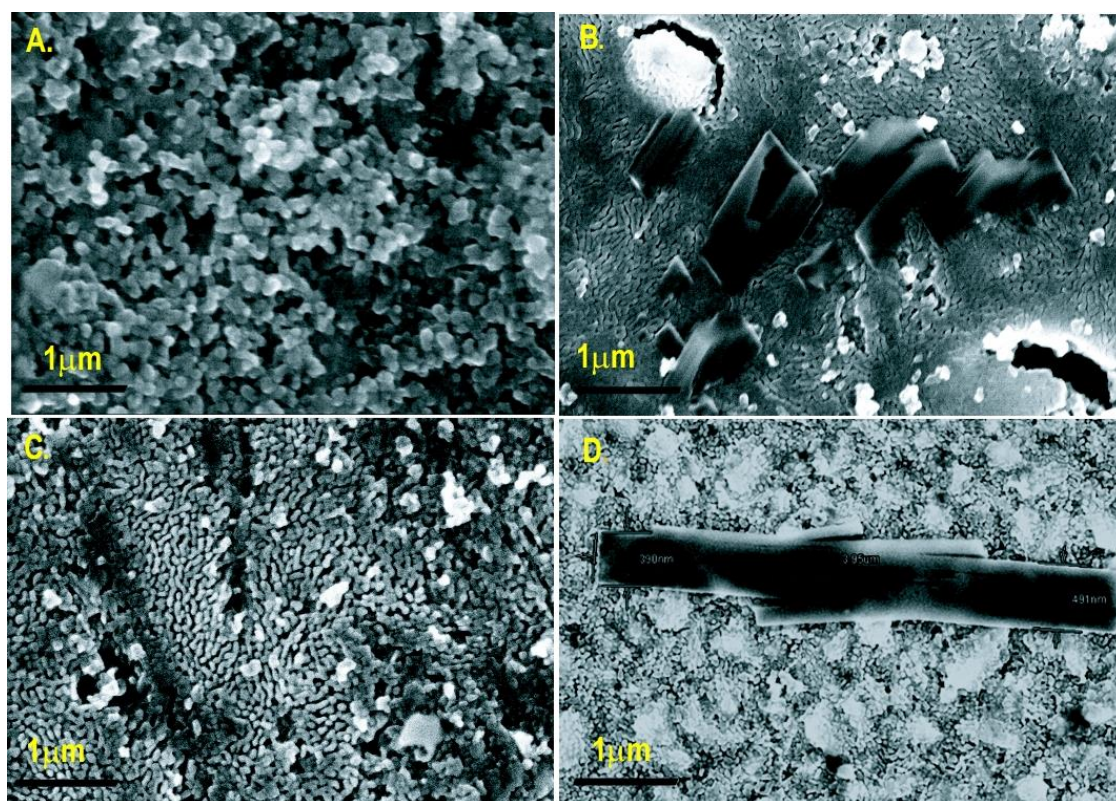
[46] Sivula, K.; Zboril, R.; Formal, F. L.; Robert, R.; Weidenkaff, A.; Tucek, J.; Frydrych, J.; Gratzel, M. *J. Am. Chem. Soc.* **2010**, *132*, 7436.

[47] Berg, J.M.; Tymoczko, J.L.; Stryer, L. *Biochemistry*. 5th edition. W.H. Freeman, New York, **2002**.

[48] Ramos, A.; Ación, F.G.; Fernández-Sevilla, J. M.; González, C. V.; Bermejo, R. *J. Chem. Technol. Biotechnol.* **2010**, *85*, 783-792.

[49] Bora, D.K.; Rozhkova, E.A.; Schrantz, K.; Wyss, P. P.; Braun, A.; Graule, T.; Constable, E.C. Functionalization of Nanostructured Hematite Thin Film Electrodes with the Light Harvesting Membrane Protein C-Phycocyanin yields Enhanced Photocurrent, *Advanced Functional Materials*, Accepted for Publication (2012).

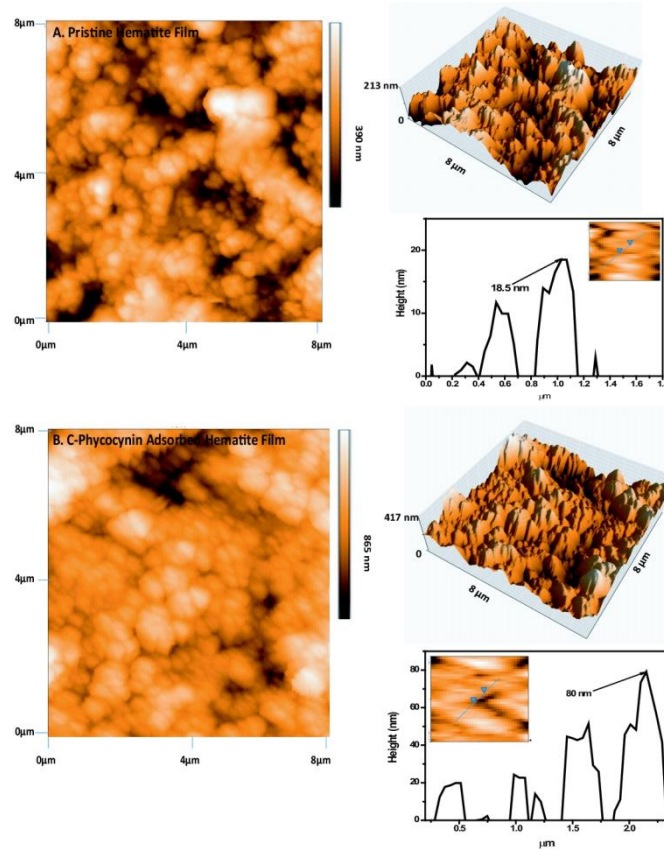
**Figure S1.** (I) FESEM images of pristine hematite (A), Phycocyanin adsorbed on hematite (B1), Agarose coated with CDI activation (B2) and Phycocyanin conjugated (B3) films. (II) Energy dispersive X ray spectroscopy (EDX) result showing the composition of protein adsorbed and conjugated films [49].



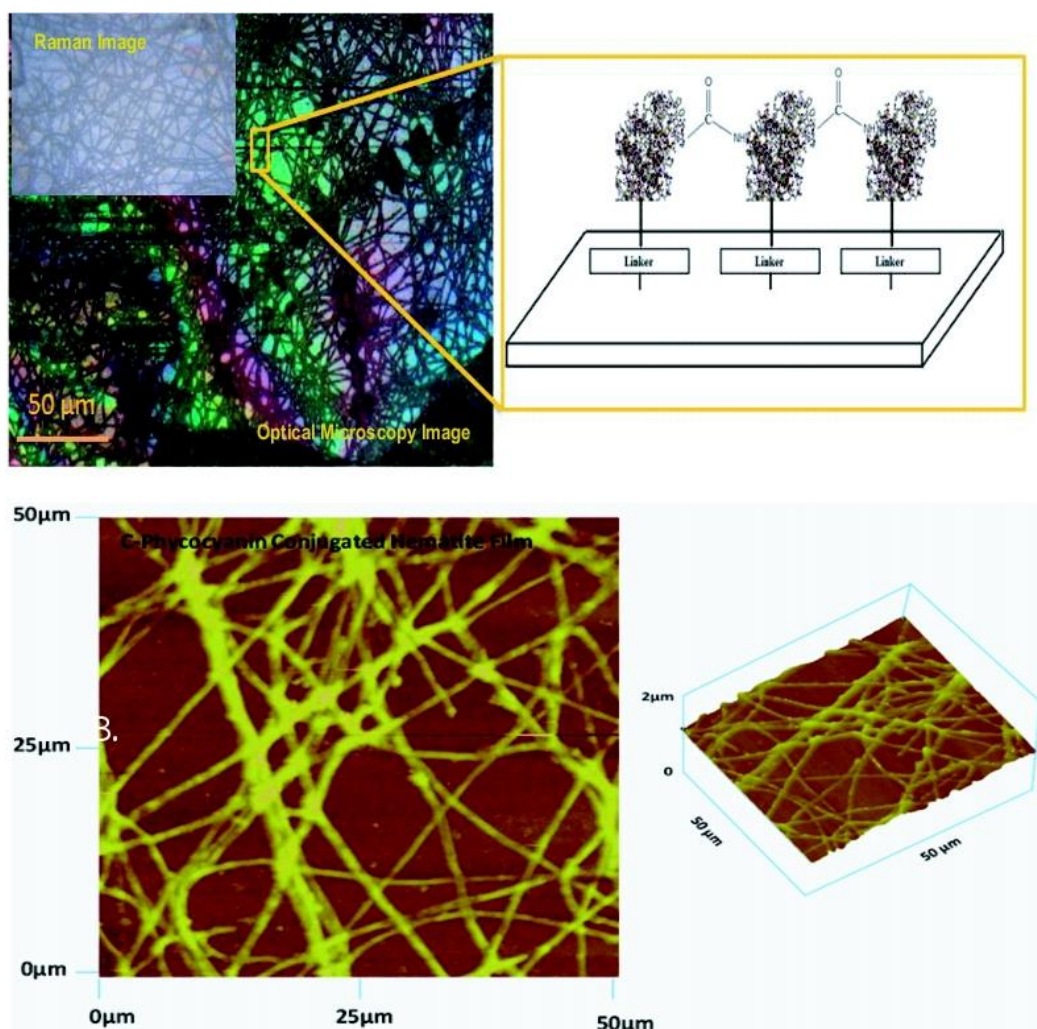
To further investigate changes in morphology and chemical composition of the nanoparticle constituting the pristine hematite film due to surface chemistry, I used scanning electron microscopy (SEM) along with energy dispersive X-Ray spectroscopy (EDX). In the SEM

image of pristine film [Figure S1(I).A], I find that the pristine hematite film has larvae shaped nanoparticle with size of 80 nm whereas, in case of phycoyanin adsorbed hematite film [Figure S1(I).B] I observe prismatic crystals of 650 nm x 130 nm size corresponds to that of rod shaped phycoyanin [44] molecule. These are not present in the pristine film. Closer inspection of the image reveals that the prisms like structures are attached to the hematite surface and stick to the nanoparticle from pristine film. On the other hand, in the chemically cross linked system, the morphology of the CDI treated agarose film [Figure S1 (I).C] contains free standing particle like feature in comparison to the pristine film. Further in the protein immobilized film [Figure S1 (I).D] again some rod like structure could be seen which manifest itself to that of electrostatically adsorbed protein on hematite film. But in this case I notice that the structure does not protrude from the surface, but is just attached to the hematite. From the EDX result [Figure S1 (II)] of both the adsorbed and conjugated protein on hematite film, besides the predominant signals (Fe, O and Sn) small traces of nitrogen has also been observed although the intensity of the nitrogen peak is quite higher in the case of chemically cross linked system. This is obvious because of the additional use of linker molecule which also contains traces of nitrogen along with protein during the covalent functionalization process. In case of protein, signal comes from the linear tetrapyrrole chromophore of phycoyanin along with a and b polypeptide subunits, covalently attached to linear tetrapyrrole chromophores [45]. The carbon comes from the use of various organics during the surface modification.

**Figure S2.** AFM images of pristine hematite film (A) and corresponding protein adsorbed film (B). Inset showing the 3D view and cross sectional height analysis [49].



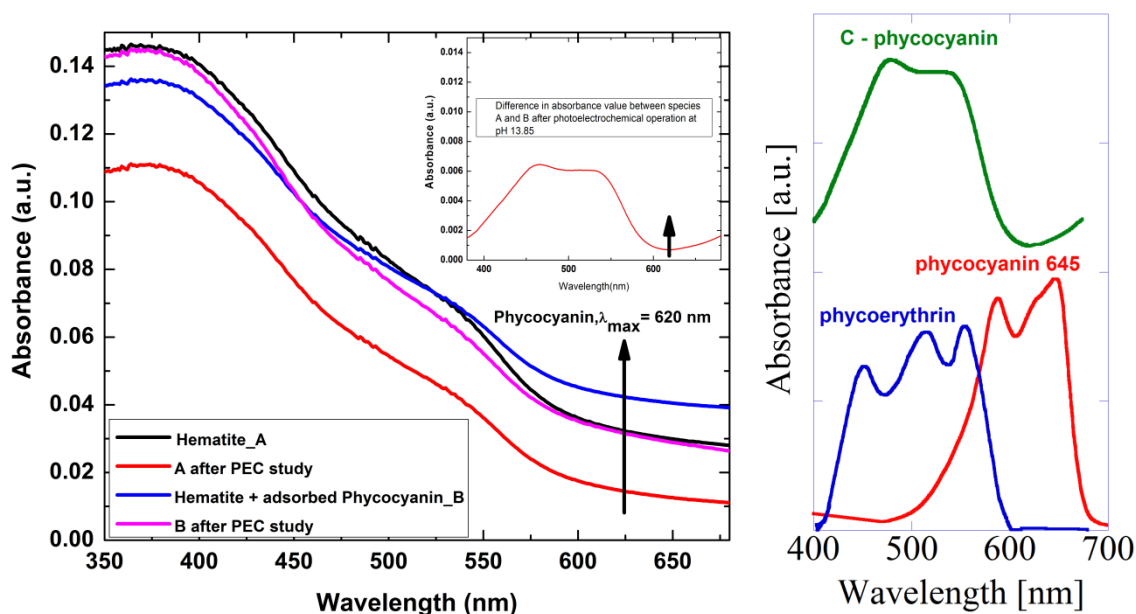
**Figure S3.** The large scan AFM image of the finally protein conjugated film(E) showing micro fibre like pattern over the hematite surface .Top images showing an optical microscopy image along with Raman image of the fibers along with depicted chemical bonding environment between two protein after CDI cross linking [49].



The surface morphology of the pristine hematite film and corresponding protein modified films has been characterized by atomic force microscopy (AFM) in tapping mode. From the cross sectional analysis of the AFM image of pristine hematite film (Figure S2.A), I find the height of the nanoparticle to be around 18.5 nm. Upon adsorbing the protein solution over the hematite film the height increases up to 80 nm as evidenced from the AFM image (Figure S2.B) of corresponding protein adsorbed film. The AFM image of the finally protein conjugated film is shown in Figure S3. Here I observe a micro fiber like pattern over the hematite surface. An optical microscopy image of the fibers has also been shown in the top of the figure. These fibers are formed due to the lateral covalent cross coupling of protein molecule as depicted in figure. It might occur due to the attack of carbonyl diimidazole molecule with the carboxyl functional group of incoming protein [29] and forming an active

intermediate, which will couple further with the amino group of protein through an amide linkage. By pointing the laser beam of the Raman spectromicroscope to one of the fibers, it is confirmed that the Raman signal originates from the phycocyanin which showed a band of  $1610\text{ cm}^{-1}$  as will be discussed in the following section. So from this investigation, I confirmed that the fiber is made of phycocyanin protein and the corresponding Raman image is also shown in the inset of Figure 6. The fibers are not present in the corresponding SEM image at  $1\text{ }\mu\text{m}$  resolution. This might get destroyed due to application of highly energetic electron beam (10 KeV) during the SEM imaging process.

**Figure S4:** left - UV-Vis absorbance spectra after photoelectrochemical treatment. – right Comparison of the UV-Vis spectrum of species B after electrochemical treatment (difference spectrum C-phycocyanin), together with spectra of phycoerythrin [64ii] and phycocyanin 645 [22, 49].



## Chapter 12

# Electrocatalytic Oxidation of Water on Hematite Surface by Hydrothermally Grown NiO Nanostructures

### 12.1 Introduction

The photoanodic behavior of hematite can be further improved by the over coating of various metal oxide [1]. The low quantum efficiency in hematite is due to electron-hole recombination via surface states. These surface states are nothing but  $\text{Fe}^{2+}$  which tends to play a significant role in the recombination process. Other metal oxide coating on the surface of hematite has been given in order to stabilize this  $\text{Fe}^{2+}$ . For instance, wide band gap material (MgO,  $\text{CaCO}_3$  and ZnO) overcoating on the surface of  $\text{TiO}_2$  nanoparticles can enhance cell efficiency. This is accomplished with the retardation of back electron transfer by the over coating material to electrolyte (retardation of charge recombination) [2]. The role of over coating process with respect to photoelectrochemical water splitting has two purposes (1) blocking the back electron transfer from photoanode to electrolyte (positive influence) to improve the performance and (2) blocking the hole transfer from photoanode to electrolyte (negative influence) to degrade the performance. The competition between the positive and negative influences of the over coating layer results in maximal performance of the photoelectrochemical cell at an optimum effective thickness of the over coating layer.

The development of such multiple band gap stacked junction electrode for photoelectrochemical storage application was date back to 1987. During that time, Licht et al. [3] for the first time demonstrated the configuration of a multiple band gap photoelectrochemical cell (MBPEC) that combines in situ electrochemical storage and solar conversion capabilities and it provides continuous output insensitive to daily variations in illumination as shown in Figure 12.1.

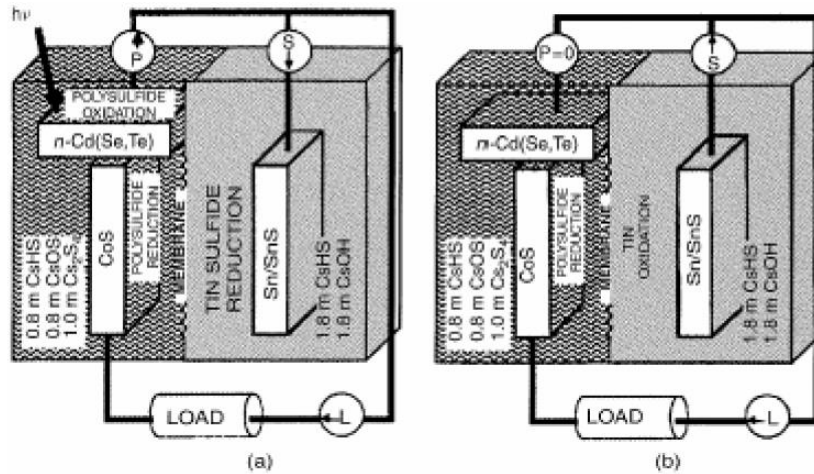


**Figure 12.1:** Schematic of a PEC cell with solar conversion and storage capabilities [3].

(a) Under light illumination (B) dark condition

It used a conversion half-cell of Cd (Se, Te)/S<sub>x</sub> and a Sn/SnS storage system, resulting in a solar cell with a continuous output. Due to low fraction of short wavelength solar spectrum, high photovoltage is generated by wide band gap solar cells but yields low photocurrent. Smaller band gap cells can use a large fraction of the incident photons, but generate lower photovoltage. Multiple band gap devices can overcome these limitations.

In MBPEC, the topmost cell absorbs (and converts) energetic photons, but it is transparent to lower energy photons. Subsequently following layers absorb lower energy photons and conversion efficiency can be enhanced. A high solar conversion and storage efficiencies have been attained with this kind of system. Following the same concept, another MBPEC [4] was developed which provides a nearly constant energy output in illumination or dark conditions as shown in Figure12.2. It consists of bipolar AlGaAs and Si and metal hydride(MH)/NiOOH storage. It is critical to minimize dark current with AlGaAs and Si which provide Ohmic contact without absorption loss and maximize cell efficiency

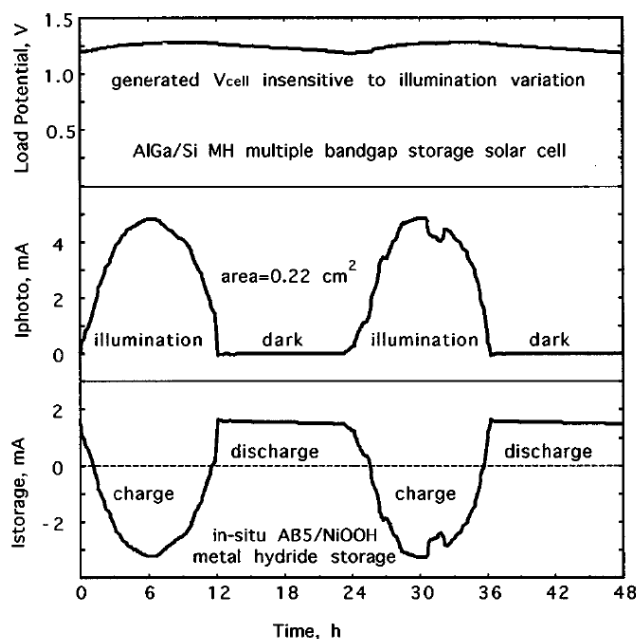


**Figure 12.2:** Two days conversion and storage characteristics of the AlGaAs/Si/MH/NiOOH MBPEC cell [4].

In a similar manner, the efficiency of hematite electrode can be increased with the over coating of wide band gap semiconductor such as NiO. It is a P - type semiconductor acts as a good oxygen evolution electrocatalyst. Semiconductor with electrocatalytic action is a promising candidate in order to make this kind of MBPEC system and these are believed to efficiently convert the electrical energy generated from sunlight into chemical bonds in fuels (hydrogen) [5]. Based on this approach, an electrodeposited composite electrode consisting of Nickel iron binary oxide electrocatalysts on semiconducting metal-oxide photoelectrodes have been developed to facilitate good oxygen evolution activity [6]. Generally, the efficiency of hematite is limited by the low conductivity and high recombination rates for the photogenerated electrons and holes as well as low electrocatalytic rate for oxygen evolution. The deposition of electrocatalyst on the surface of hematite can eliminate the high overpotential required for water oxidation reaction in a PEC cell. For example, Iron-nickel oxide catalyst can eliminate oxygen overvoltage in the electrolysis of alkaline water [7]. The largest source of energy loss in water electrolysis is the overvoltage required for the oxygen evolution reaction. The spin inversion required to produce triplet oxygen is the major source of this overvoltage. Cathodically electrodeposited Nickel oxide electrodes are available for over 100 years. It already evident that iron impurities in nickel oxide batteries facilitate the oxygen evolution reaction, which is parasitic to the battery charging process [8]. Iron impurities affected both the charge storage reaction and the oxygen evolution reaction in the thin film nickel oxide electrodes. The NiO electrode can be grown by electroplating, vacuum evaporation and sputtering. Nickel oxide has varying properties based on the synthesis process and the resulting

defect structure. Corrigan [7] used cathodic electrodeposition from nickel-nitrate/ferric-nitrate solutions to form iron-doped nickel oxide (Fe:NiO) electrodes on nickel strips. Iron coprecipitation with a few mole percent lowered the Tafel slope, resulting significant amount of oxygen evolution rates. Similar kind of electrode was also developed by reactive sputtering [8]. Electrodeposited samples have higher surface area with respect to sputtered one. Films produced by electrodeposition are often quite porous, resulting in larger effective surface area than seen in the dense, highly uniform, and continuous sputtered films. The porous film of NiO with higher surface area can also be obtained in nanostructured form with hydrothermal strategy [9-13]. Hydrothermal strategy has also been applied for coating of iron oxide nanoparticles with nickel hydroxide [14].

In the current study, my goal is to observe the electrocatalytic effect of hydrothermally deposited NiO nanostructure on the photoelectrochemical properties of hematite thin film. For the same, a multiple layered system of NiO-Hematite has been fabricated and characterized with different techniques and will be utilized to see the water splitting behavior.

## 12.2 Materials and Methods

Iron salts, oleic acid and tetrahydrofuran (THF) used in the synthesis of hematite film were of reagent grade obtained from Sigma-Aldrich. Hexamine used as capping agent for NiO nanostructure synthesis was obtained from Sigma-Aldrich, Switzerland (99.9% pure).

*Synthesis:* For the fabrication of NiO-hematite system, at first a thin monolayer of NiO was deposited on FTO substrate by dip coating of nickel fatty acid precursor and post annealing at 600°C. The annealing was done at 500 degree for 2 hour. After this 4 layer of hematite had been deposited on the NiO layer following the protocol described in chapter 6. NiO will acts as interfacial layer between FTO and hematite. The idea behind putting the interfacial layer was to minimized the recombination losses whereby NiO will acts as hole collector [16]. The top most hematite layer was again hydrothermally treated with equimolar (5:5 mmole) amount of  $\text{FeCl}_3 \cdot 6\text{H}_2\text{O}$  and Hexamine at 95°C for 8 hour to change the morphology of pristine hematite film. After this step, a coating of colloidal suspension of NiO nanoparticle have been given and the film was hydrothermally treated with  $\text{NiCl}_2 \cdot 6\text{H}_2\text{O}$  and Hexamine (5:5 mmole) for 48 hour to get the desired NiO-hematite electrode in final form.

*Characterization:* The optical properties of the NiO-hematite films were studied by UV-Vis spectrometer (Cary Scan 50). The phase composition of the pristine and modified films was examined by powder X-ray diffraction analysis (PAN analytical X'Pert PRO,  $\text{Cu K}_\alpha$  radiation). A JEOL JEM 2200 FS transmission electron microscope/STEM operating at 200 keV accelerating voltage was used for TEM analysis. Field emission scanning electron microscopy was performed on a Hitachi S-4800 model.

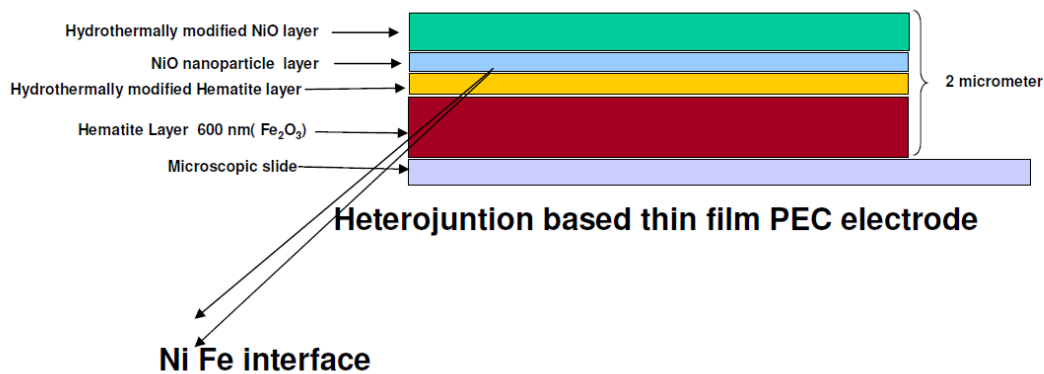
For XPS depth profile measurement, quanta 2000 XPS system have been used. The compositions of the films were determined by Elastic recoil detection analysis (ERDA). For the ERDA analysis a  $^{127}\text{I}$  beam with energy of 12 MeV was used at an incidence angle of  $18^\circ$ . The scattered recoils were identified with a time-of-flight spectrometer combined with a gas ionization chamber. The dark current and photo current was recorded with a Voltalab® potentiostat in a three electrode configuration with 1M KOH (pH=13.6) as electrolyte, Ag/AgCl/sat. KCl as reference and a platinum wire as counter electrode. The  $\text{Fe}_2\text{O}_3$  film was illuminated on a  $0.45\text{ cm}^2$  area of electrolyte through a fused silica window with a  $0.5\text{ cm}^2$  circular mask, the total geometric area immersed in electrolyte was approximately  $2.6\text{ cm}^2$ . With the help of a filtered xenon lamp from LOT Oriel®, Sunlight was simulated. The light intensity was adjusted to AM 1.5 simulated light.

*FIB Lamellae preparation:* First 100nm Platinum was deposited with electron beam at 2.7kV beam accelerating voltage. Afterwards another 1.5  $\mu\text{m}$  platinum have been deposited in a region of  $2\mu\text{m} \times 20\mu\text{m}$  by ion beam at 30kV accelerating voltage and 300pA beam current. Then two cross sections were cut with ion beam using a current of 5000pA. After that the lamellae was thinned by different currents from 3000pA-300pA to a thickness of 500nm. Due to high stress in the material two relaxing cuts on the side have been done with a beam current of 100pA. Afterwards an undercut had been performed with 300pA so that the lamellae were just fixed at 2 small points. Last but not least the lamellae was thinned down to a thickness of approximately 100nm with beam currents of 100pA and 50 pA and the last thing did was to cut the two fixation points. The lamellae have been lifted ex-situ with a glass needle and were transferred to a carbon coated copper grid.

### 12.3 Results and Discussion

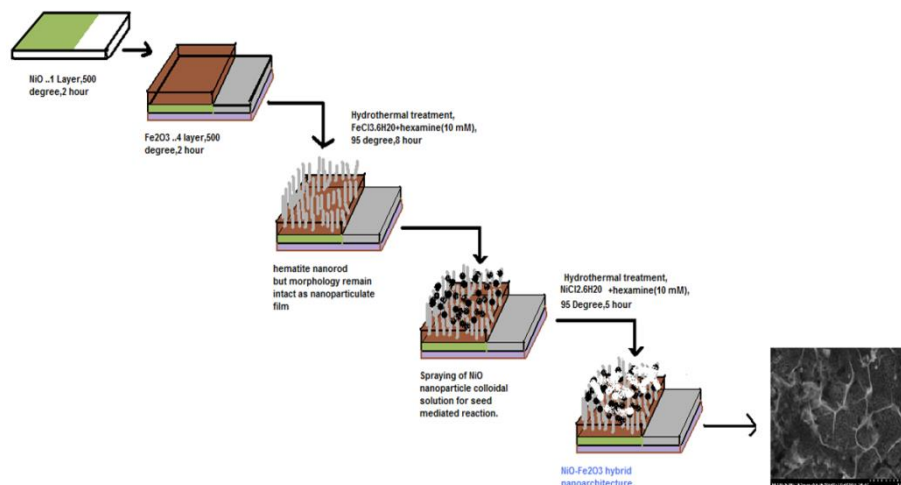
The NiO – hematite composite electrode have been fabricated with the help of hydrothermal modification of a bare pristine electrode. The architecture of the electrode as shown in Scheme 12.3. The detail synthesis process is shown in Scheme 12.4. In the first step, NiO layer have been deposited followed by the deposition of hematite layer (A). After this hydrothermal treatment have been given with iron salt ( $\text{FeCl}_3 \cdot 6\text{H}_2\text{O}$ ) and hexamine in order to get oxyhydroxide layer ( $\text{FeOOH}$ ) (A1) as shown in mechanism depicted in Scheme 12.5. NiO nanoparticle colloidal solution (B) has been sprayed on the top of hydrothermally modified hematite. The idea of putting it is to help in the seed mediated growth of NiO nanostructure after final hydrothermal modification. Finally, after step B, film has been given a final hydrothermal treatment with nickel salt ( $\text{NiCl}_2 \cdot 6\text{H}_2\text{O}$ ) and hexamine (B1). Hexamine is believed to play a role as capping agent in forming the desired nanostructures [15]. The mechanism for the formation of wall like NiO nanostructure on the top of hematite film has

been depicted in scheme 12.5. NiO along with Ni (OH)<sub>2</sub> nanostructures were formed by the seed mediated growth of pre-deposited NiO nanoparticle on the hydrothermally treated hematite film. It is believed that FeOOH layer adsorbed the NiO nanoparticle inside the porous network which formed as a result of hydrothermal treatment. This help as a formation center for NiO nanostructures. Finally, I have got a highly supersaturated solution as a result of the increasing solubility of α-Ni (OH)<sub>2</sub> nanoparticles. This solubility is increased as a result of the high temperature and pressure under hydrothermal conditions.

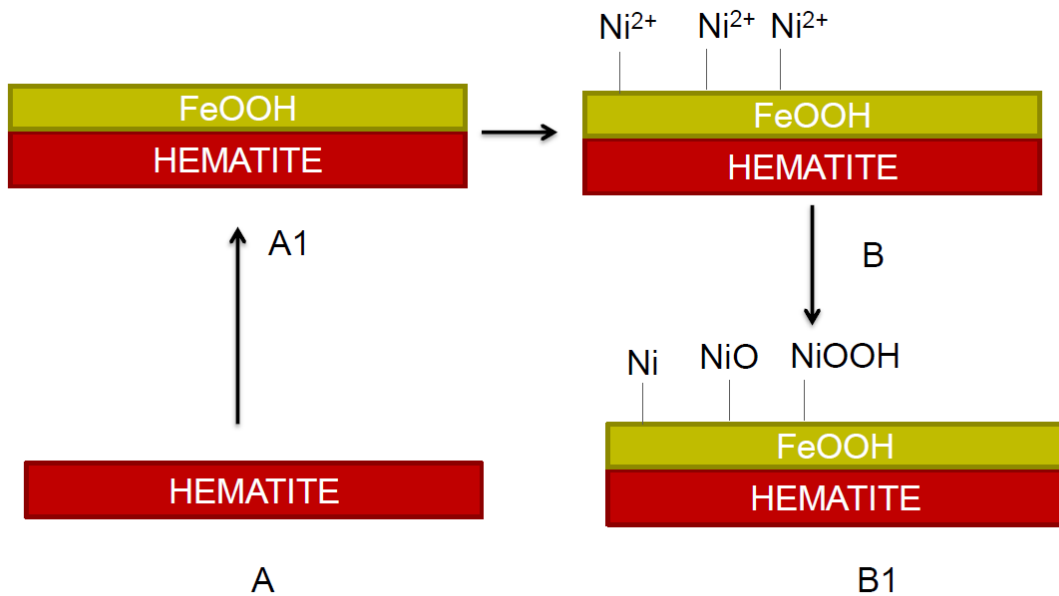


**Scheme 12.3:** Represents the architecture of NiO-hematite electrode.

The formation process of the Ni (OH)<sub>2</sub> nanostructures may be described as a sequence of dissolution, recrystallization, and oriented attachment-assisted self-assembly of predeposited nanoparticles into wall like architectures.

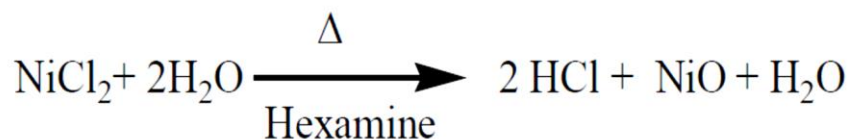
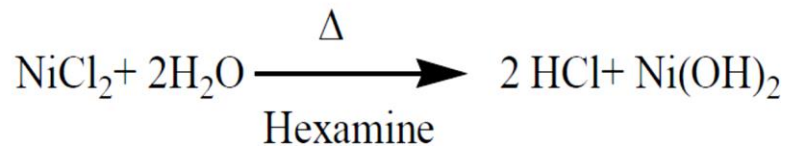


**Scheme 12.4:** Detail synthesis procedure of NiO –Hematite composite electrode.



**Scheme 12.5:** mechanism depicting the formation of NiO nanostructures on the top of hematite film.

The overall reaction process involves the transformation of nickel chloride to clusters of nickel oxide in the presence of water and air oxygen. The deposited film has disordered Ni(OH)<sub>2</sub> structure or nanocrystalline NiO structure according to the following reactions:



### 12. 3.1 Optical Properties of NiO-hematite electrode:

The UV-Vis transmittance spectra of NiO – hematite electrode is as shown in Figure 12.6(A). From the optical spectra, I can clearly see the differences in the optical properties of hematite film modified hydrothermally. For instance, after the final step, the film B1 absorb from 550 nm which is just before the absorption edge of hematite. This is accomplished when NiO nanostructure is over coated on the top of hematite. It is to be mentioned here that during

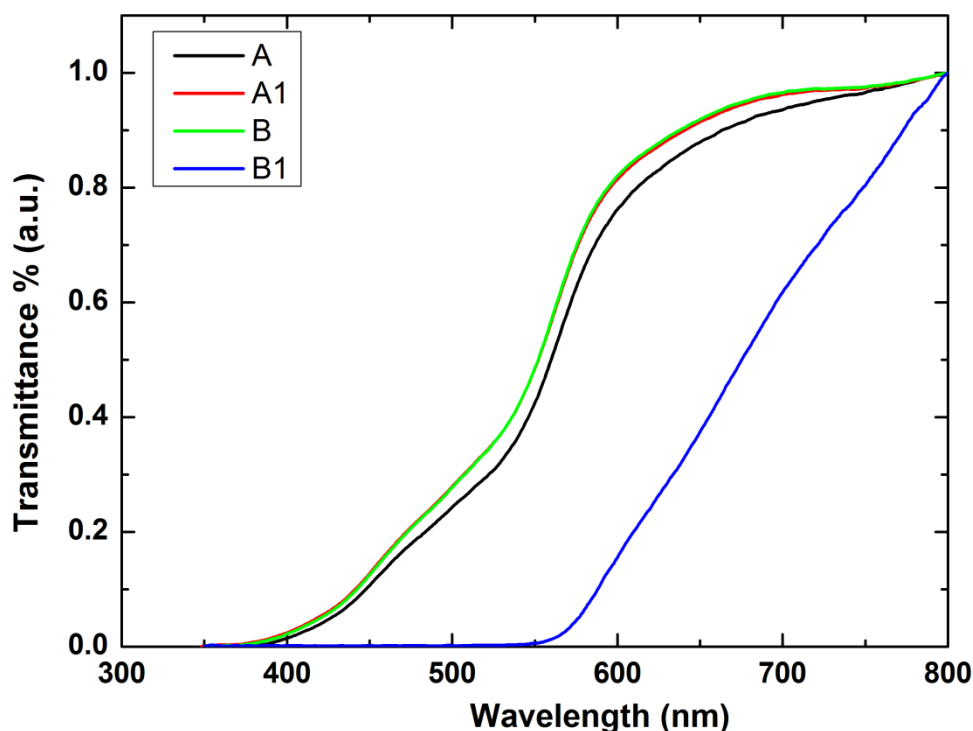


**Figure 12.6 (A):** UV-Vis transmittance spectra of NiO-hematite electrode.

hydrothermal modification, NiO is grown by the oxidation of NiOOH layer and the oxidized form or NiO absorbs light throughout the visible region of the spectrum. This optical transition is assigned to band to band transition involving charge transfer between oxygen and higher valence nickel atoms. In case of film A, A1 and B; I can see that there is no significant change in the absorption edge of hematite. Also from the band gap calculation [see Figure 12.6 (B)] I have found that hematite have its usual band gap at 1.9 eV even after modification. Here I applied Tauc methodology for an indirect transition in case of hematite. It is also noted that during the hydrothermal modification, subtle amount of nickel hydroxide gets formed along with NiO. From earlier study [24], it has been found that the oxidized form of nickel hydroxide absorbs throughout the visible range with maximum absorption occurring in the blue portion of the spectrum.

On the other hand, in case of finally obtained NiO hematite film, I have calculated the band gap for NiO by considering the direct transition. Here I have plotted  $(\alpha h\nu)^2$  versus photon energy [Figure 12.6 (C)], where  $\alpha$  the absorption coefficient and  $h\nu$  is the energy in eV. The X axis intercept of the plot is then taken as an optical band gap. This yields a value of around 3.4 eV. The calculated band gap is different from bulk special flowerlike nanoporous structure

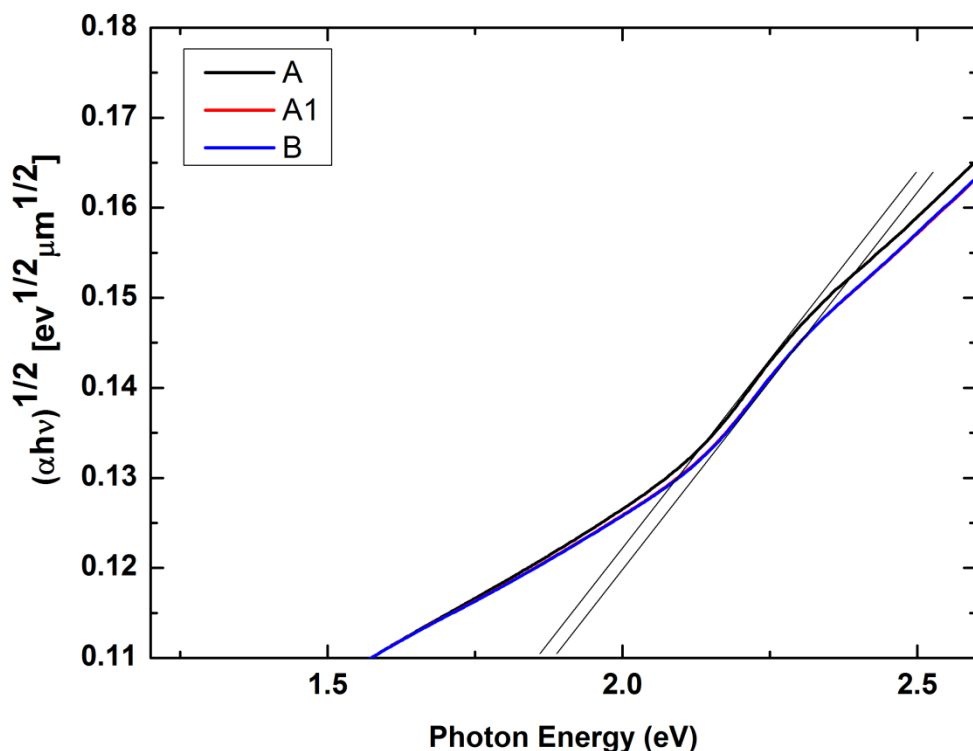


**Figure 12.6 (B):** Evaluation of optical band gap using Tauc plot for indirect transition.

and is due to decrease in grain size of NiO and the interaction between connected building blocks which give rise to quantum size effect [21]. NiO shows a strong anodic electrochromic effect, as it changes color from transparent to brown-black upon application of positive potentials. This effect is caused by oxidation of Ni atoms located at the NiO / electrolyte interface. The discussion will be followed in the photoelectrochemical properties [17]. This dramatic change in optical properties is due to changes in the electronic properties of nickel hydroxide which occur upon oxidation/reduction. In addition, electronic properties are also likely to strongly affect the kinetic behavior of nickel hydroxide electrodes and thus affect the coloration / bleaching processes in electrochromic films [18]

### 12. 3.2 Structural properties of NiO- Hematite electrode:

The structural properties of NiO – hematite electrode were studied with XRD. From XRD result as shown in Figure 12.7, it is evident that the film B1 (NiO-hematite) shows diffraction peaks corresponding to hematite, substrate (FTO) and NiO respectively. However, the peaks due to NiO are consistent with its cubic structure. The presence of multiple NiO peaks further validates the polycrystalline nature of the hydrothermally obtained NiO hematite film. The polycrystalline nature is supported by other reports dealing with the thin film NiO<sub>x</sub>

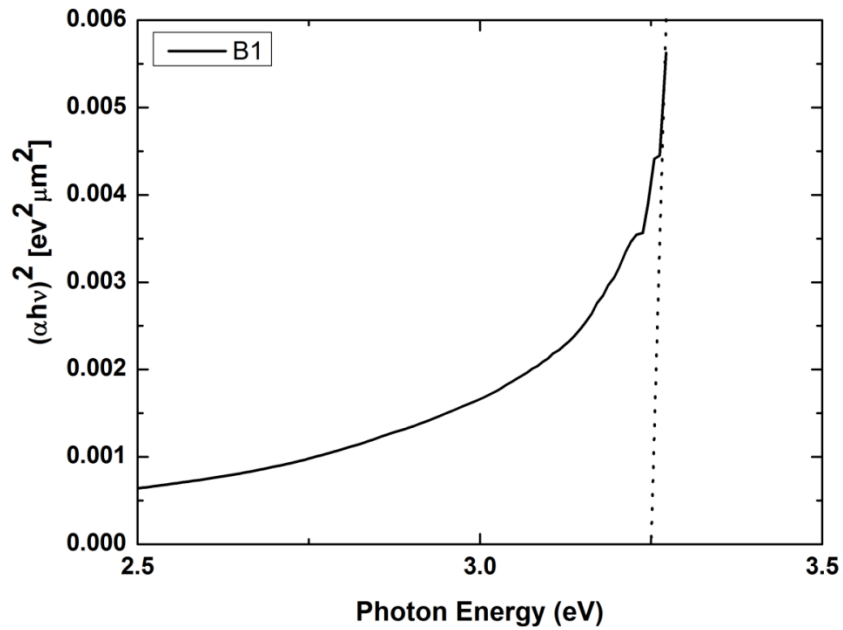


**Figure 12.6(C):** Evaluation of optical band gap for NiO - hematite electrode using Trauc plot for direct transition.

fabricated by sputtering [19]. The diffraction peak obtained at  $2\theta = 37.28^\circ$  and  $43.33^\circ$  are attributed to the diffractions from (111) and (200) planes of the cubic NiO lattice and the preferential growth is along (200) plane. The intensity of these peaks in the diffraction pattern is found to increase with annealing temperature [20] and might be due to the enhanced oxidation kinetics and improvement in crystallinity.

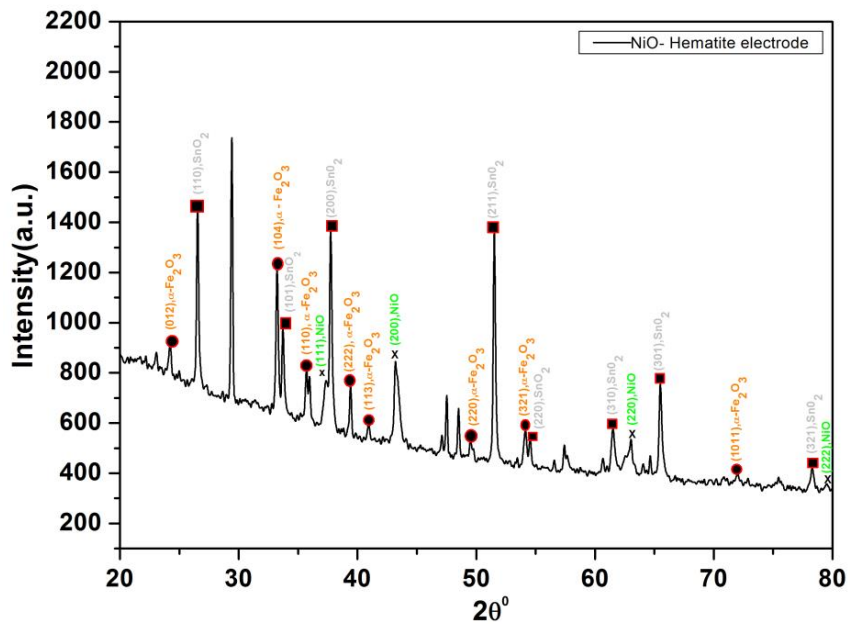
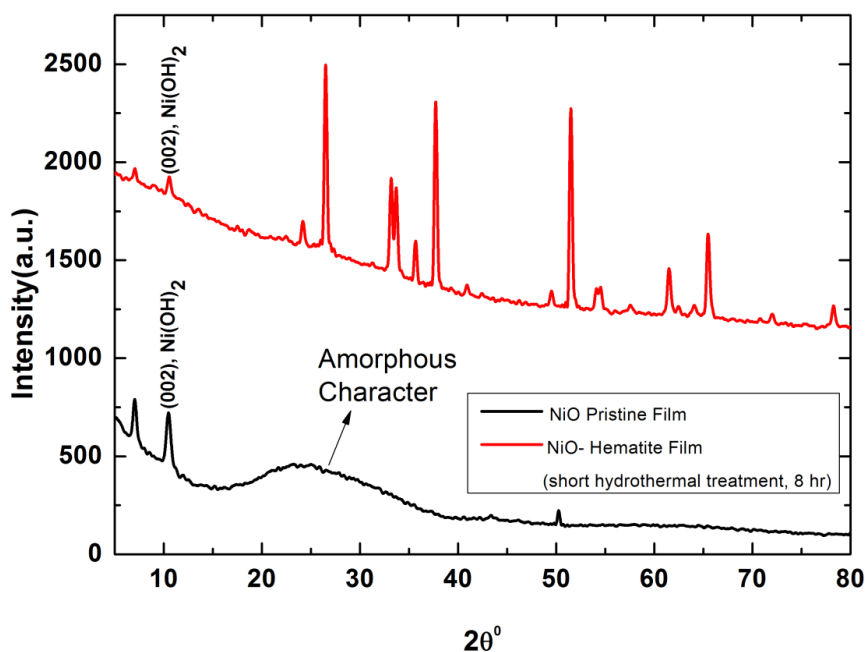


**Figure 12.7: (A)** XRD pattern of NiO – Hematite electrode.



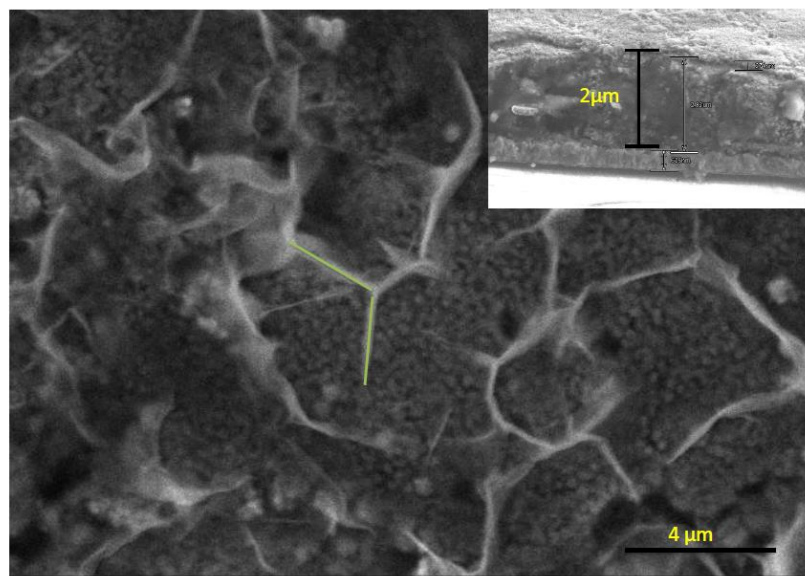
(B) XRD pattern of NiO- Hematite film synthesized for short hydrothermal treatment showing the presence of Ni (OH)<sub>2</sub>.

On the other hand, the NiO - hematite film synthesized for shorter hydrothermal duration (8 hour) did not show the diffraction peak corresponding to (200) planes, whereas a new peak arises at lower Bragg angle as shown in figure 12.7 (B). On comparing this with standard card JCPDF No. 41-1424, it is assigned to the diffraction peak corresponding to (001) plane from Ni (OH)<sub>2</sub>. All other diffraction peaks could be clearly indexed to the monoclinic phase  $\alpha$ -Ni (OH)<sub>2</sub> with lattice constants of  $a = 7.89$ ,  $b = 2.96$ ,  $c = 16.63$  Å, and  $\beta = 91$  [12]. Nickel hydroxide is considered as layered double hydroxide (LDH), of which there are two polymorphs, namely the  $\alpha$ - and  $\beta$ -phases [21]. Both phases supposed to be crystallized by c- axis stacking of the Ni (OH)<sub>2</sub> layers in the hexagonal system with the brucite-type structure. The main difference between the  $\alpha$ - and  $\beta$ -Ni (OH)<sub>2</sub> phases arises when other ions or molecules are present between the stacking layers along the c axis.  $\alpha$ -Ni (OH)<sub>2</sub> structure consists of stacked Ni(OH)<sub>2-x</sub> layers intercalated with various anions (e.g., carbonate, nitrate, sulfate, etc.) or interlayer space containing water molecules to maintain the overall charge neutrality.

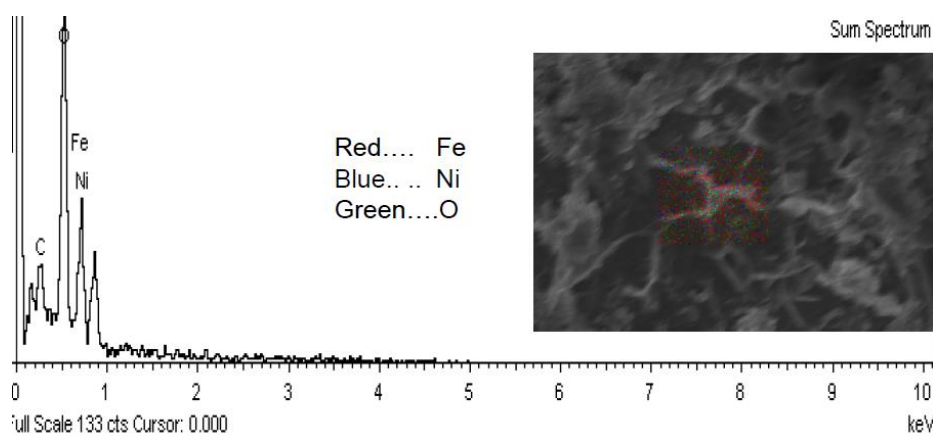
### 12. 3.3 Morphology investigation of NiO - Hematite electrode

The detail morphology study of the NiO - Hematite electrode has been studied with FESEM. From the corresponding SEM image, some wall like structure has been observed on the surface of hematite thin film. If I carefully look into Figure 12.8 A, the nanostructures standing vertically on the surface of hematite film and form a regular pattern. The porous nature of hematite film can also be observed along with this wall like nanostructures. The total thickness of the film was 2  $\mu\text{m}$  as observed with the cross sectional view in FESEM. The composition of

the electrode has been studied with EDX mapping [Figure 12.8 B]. The mapping shows the presence of Ni (blue), Fe (red) and O (green). Also from EDX pattern, I can easily distinguish between Fe and Ni element from the energy position. The high resolution FESEM image further shows the structure of wall like feature as shown in Figure 12.9. The structure doesn't seem to have porous character as that of pristine hematite film, on which it was formed due to hydrothermal modification. These are aligned on hematite film and interconnected with each other resulting in the formation of extended network architectures. By using nullaginite ( $\text{Ni}_2(\text{OH})_2\text{CO}_3$ ) as precursor, similar type of porous NiO nanowall arrays on conductive substrate was obtained [11].



A.



B.

**Figure 12.8:** A. FESEM Image represents the morphology of electrode. B. EDX Mapping shows the presence of Fe and Ni elements along with Oxygen.

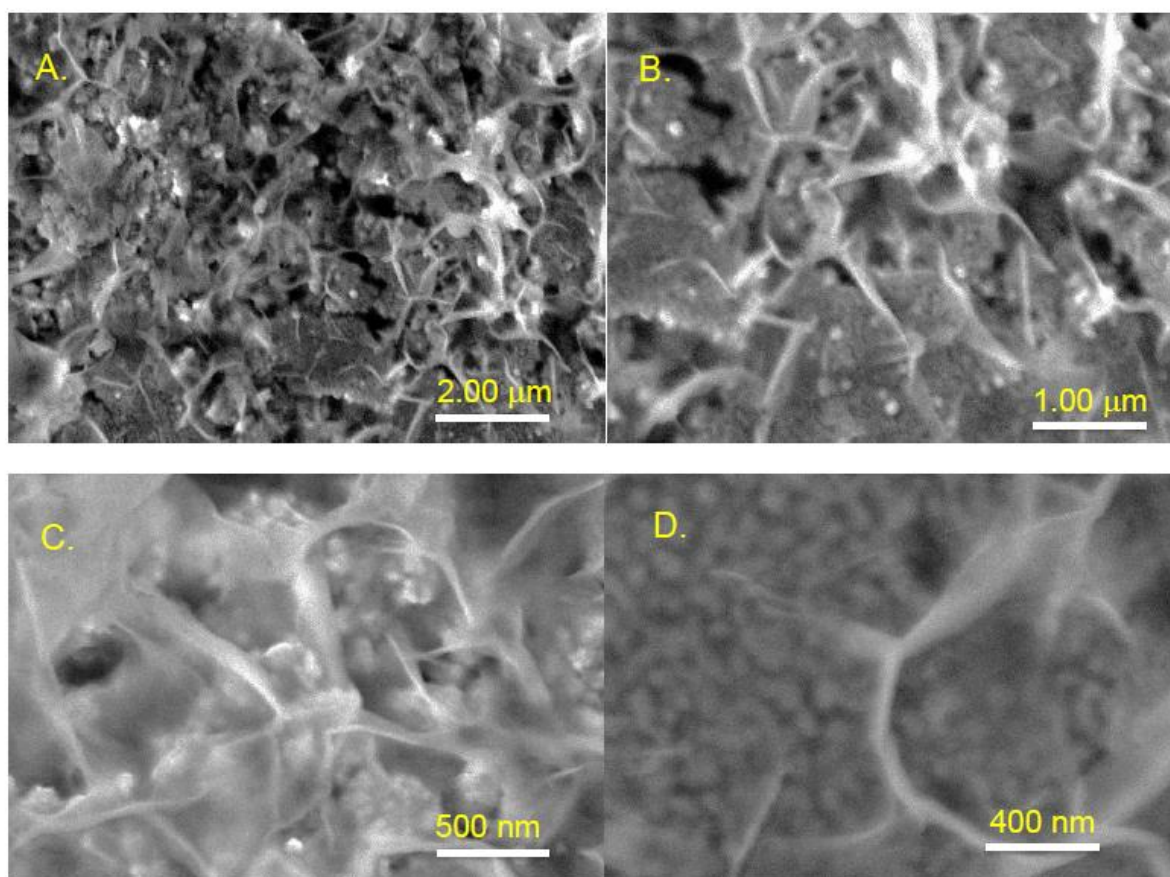


**Figure 12.9:** From SEM Image at higher resolution, some wall like nanostructure has been observed on hematite surface.

To get more in depth understanding of the morphology of nanostructure and its interfacial structure, transmission electron microscopy has been done. Figure 12.10 shows the microscopic investigation of representative cross section of NiO – Hematite electrode prepared with Focused Ion Beam epitaxy (FIB). Figure 12.10.A shows the prepared FIB lamellae and its cross sectional morphology has been taken with the low resolution TEM mode (B). From the high annular angular bright and dark field imaging (C and E), I can distinguish between hematite and NiO nanocrystalline grains and it has been found that NiO nanocrystallite diffuse across the layer of hematite. This further validate that the prepared electrode don't have definite interfacial boundary. It acting like a composite system. From the bright field image, the porous network of the electrode can be seen along with fibrillar morphology or channels between the columns of crystallites. Each fibril is not a single crystallite but randomly oriented one stacking upon each other [22]. The wall like nanostructure formed only on the top surface which is expected to play role in the electrocatalytic oxidation of water. Figure 12.10.D represents the

selected area electron diffraction pattern (SAED) of the NiO- hematite electrode with the formation of rings clearly signified the polycrystalline nature of the electrode.

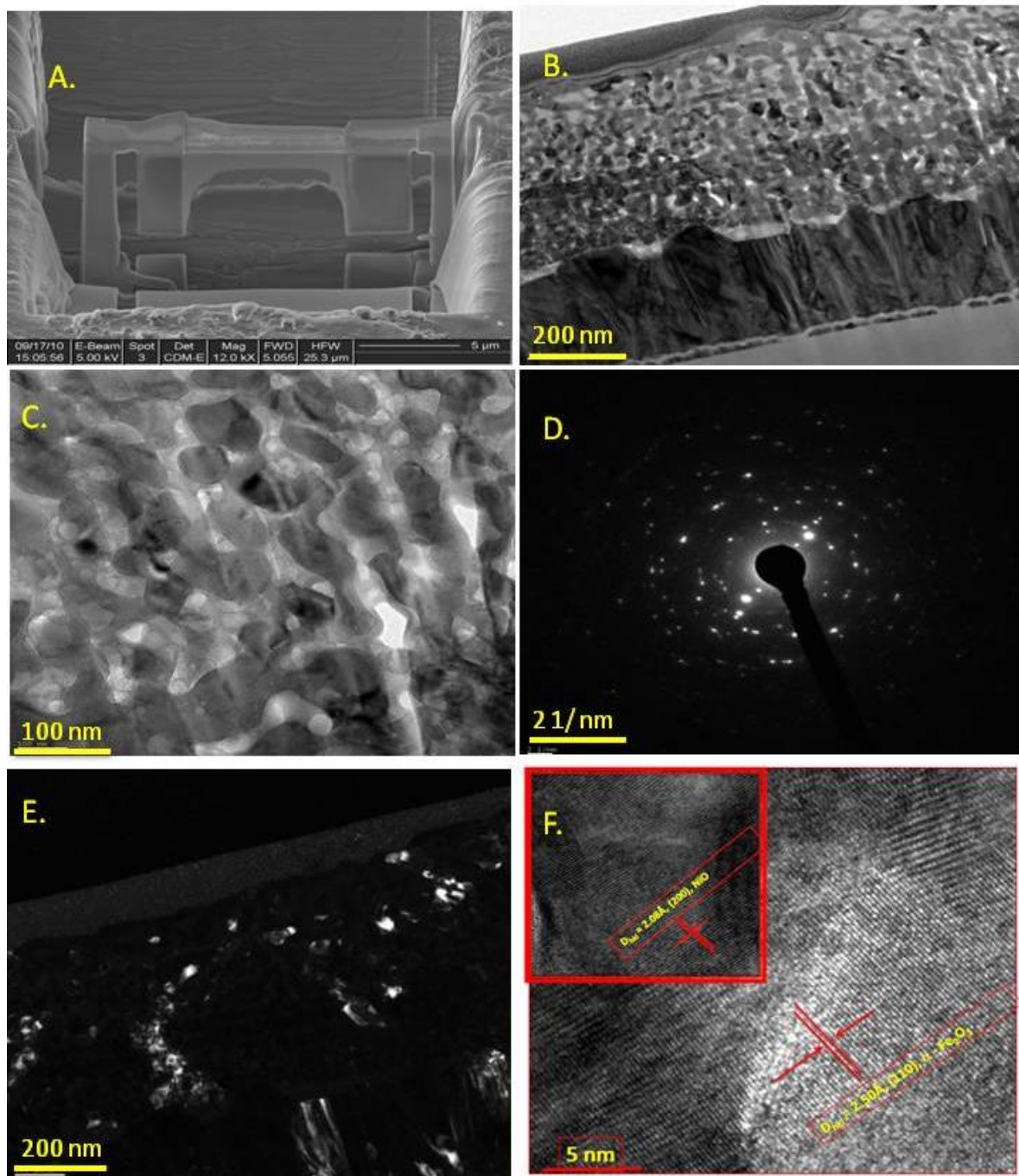


**Figure 12.10:** A. FIB Lamellae of NiO - Hematite Electrode; B. TEM Image of cross section of the electrode; C. Bright field image; D. SAED pattern showed the polycrystalline nature of the electrode; E. Dark field image showed the presence of NiO grain; F. HRTEM image showing the lattice fringes of hematite nanocrystallite and NiO corresponding to (110) and (200) plane.

[Courtesy: Dr.Magdalena Parlinska, Electron Microscopy Center, EMPA, Dübendorf]

Figure 12.10 F shows the lattice fringes of hematite nanocrystallite and NiO corresponding to (110) and (200) plane. A two-dimensional (2D) lattice with spacing of 0.20 nm, which corresponds to the separation between the (200) planes of cubic NiO (Fm3m,  $a = 4.168 \text{ \AA}$ ). This indicates the thermal decomposition of  $\text{Ni(OH)}_2$  to a NiO phase upon electron-beam irradiation under high vacuum conditions [12]. The presence of NiO and hematite crystalline plane further signified that the electrode consists of NiO and hematite nanocrystallite form in distributed form. To further quantify this distribution in nanoregime, EDX mapping of NiO - Hematite electrode was taken in STEM mode as shown in Figure 12.11 A. The frame in the STEM image has been taken in order to make drift correction and the EDX map was taken from this frame (spectrum image). The RGB map as shown in Figure 12.11 B, clearly represent the Ni signal in blue and the Fe signal in red.

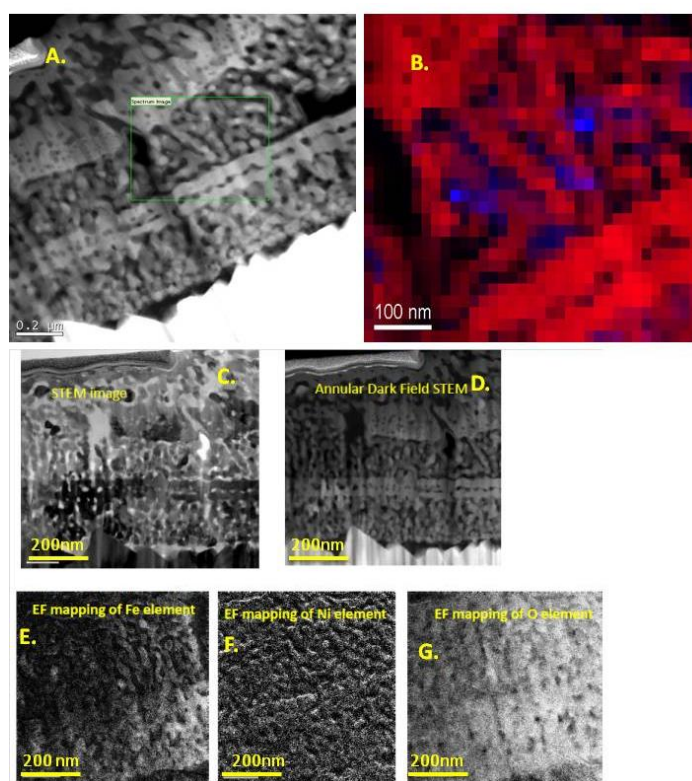


**Figure 12.11:** A. Area showing the EDX mapping region in the TEM cross section of NiO-hematite electrode. B. EDX mapping shows the presence of Ni (blue) along with Fe (red). C. STEM imaging of cross section of NiO - hematite electrode. D. Annular dark field STEM imaging for the energy filtered mapping of different elements present in the electrode. E, F, G: EF mapping showing the distribution of Fe, Ni and O elements. [Courtesy: Dr. Rolf Erni and Dr. Magdalena Parlinska, Electron Microscopy Center, EMPA, Dübendorf]

Annular bright field and dark field STEM images [Figure 12.11: C-D] have been taken to elucidate the distribution of Fe, Ni and O element with the help of energy filtered mapping.

Figure 12.11: E-G showed the energy filtered mapping of Fe, Ni and O element. From the EF mapping I have found that Ni is distributed along with iron down to the substrate (FTO).

### 12. 3. 4 Surface and Interfacial compositional analysis of NiO - Hematite electrode

The electrocatalytic action of NiO nanostructure has a profound influence on the final photoelectrochemical performance of NiO - Hematite electrode. The presence of NiO on the very top surface of the electrode (10nm) is therefore very important from the functionality point of view. In order to quantify the amount of Ni element on the very top surface, ERDA spectrum has been taken. The ERDA spectra of each of the samples (A, A1, B, B1) are shown in Figure 12.12 (A) and (B). The mass spectra for the Ni and Fe standard are nicely separated and allowing us to fit the Ni/Fe ratio in unknown samples. From the two dimensional ERDA raw data, it has been observed that Ni is detectable on Fe surface for the treated NiO on hematite. This further clarify the presence of clear Ni signal on the very top surface, which helps in getting very high current density as will be discussed in photoelectrochemical properties. The mass spectra have been produced from the 2 D raw data for the topmost 10 nm of the samples. The spectra are then fitted by a mixture of the Fe and Ni standard spectra which yields the Ni/(Ni+Fe) ratio. If we carefully look at the respective mass spectrum of hydrothermally treated hematite film (A1) and NiO dispersed on hematite (B), we obtained Ni/(Ni+Fe) ratio as 3 at. % and  $(7 \pm 3)$  at % respectively. This ratio increases to  $(75 \pm 5)$  at. % on the long term hydrothermal treatment of NiO dispersed hematite electrode for 48 hour. This led to the conclusion that the long term hydrothermal after treatment modifies the very surface of the hematite film by the deposition of NiO nanostructure.

2-dimensional ERDA raw data (velocity versus Energy)



**Figure 12.12:** (A) Two Dimensional ERDA raw data

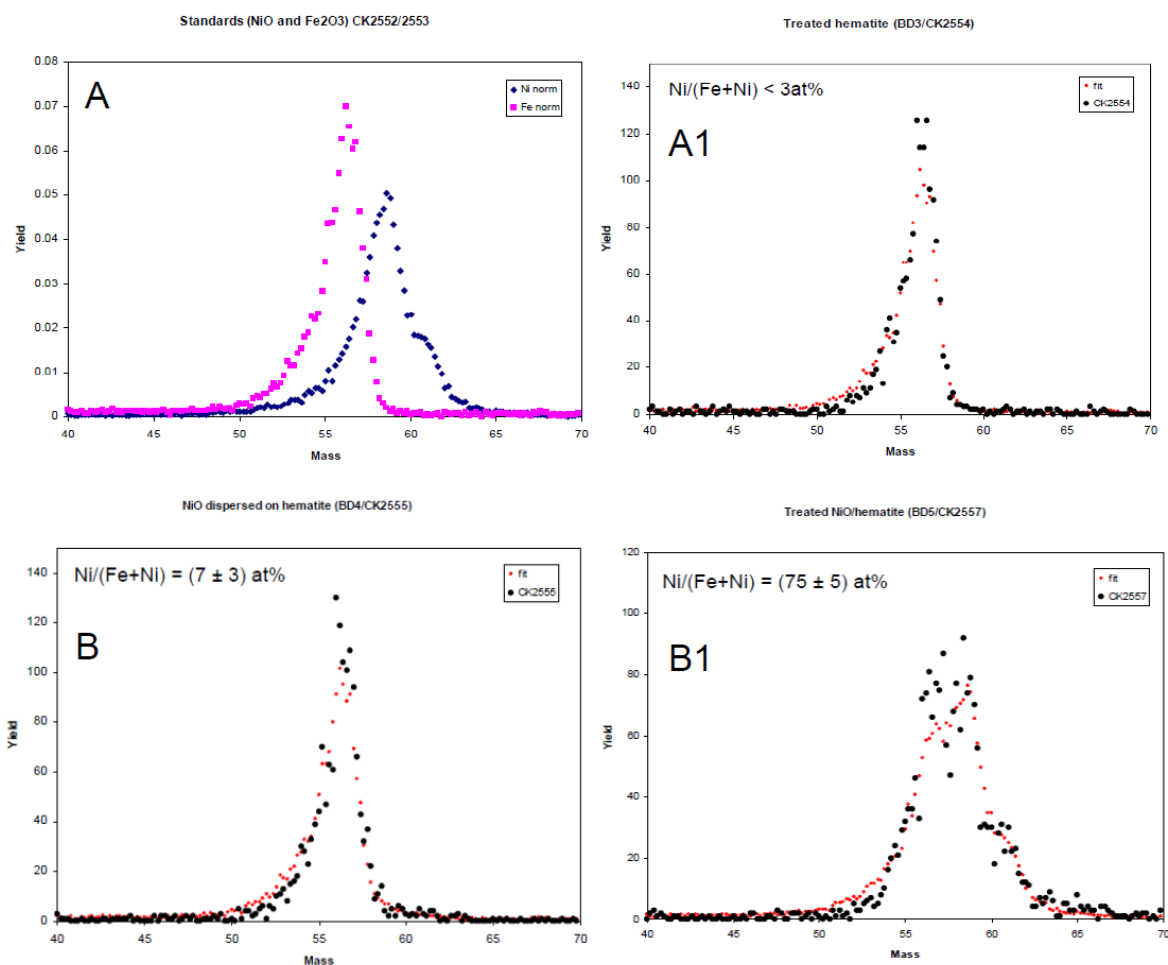


**Figure 12.12:** (B) ERDA mass spectrum showed the higher content of Ni on very top surface at 10 nm depth in case of long term hydrothermally treated NiO dispersed on hematite.[Dr. Max Doebli, Ion Beam Physics, ETH Zürich]

To get more knowledge of the chemical identity of the species present inside the film, XPS depth profiling technique has been applied. It provides the most quantitative data for depth profiling of NiO- Hematite electrode compared to other characterization techniques. X-ray photoelectron spectroscopy (XPS) depth profiling is the most suitable technique to probe the concentration versus depth as it has very good depth resolution and quantitative ability. It has been used to characterize the depth profile of other organic materials in an inorganic matrix [23]. Before doing the XPS depth profiling of the NiO - hematite electrode, survey scan [Figure 12.13.A] has been performed and it has been found that the atomic % of carbon is higher. This carbon content comes from the precursor material (hexamine) used during the hydrothermal after treatment. Also the atomic % of Ni is just 4.2% which is quite different from the ERDA data obtained for 10 nm of the film. On the other hand, during the survey scan, the atomic composition was probed at an attenuation depth of 40 nm. XPS depth profile was performed at two different region of NiO – Hematite electrode and the results are shown in Figure 12.13(B-

C). From the result obtained I observed that Nickel can infiltrate all the way to a depth of 40 nm and it supports the energy filtered TEM mapping data. In both the sputtered regions the atomic concentration increases. Whereas, in case of Fe and O, the concentration varies not in a distinct fashion. This time, no proper justification can be made for the abrupt variation in the concentration of Fe and O elements.

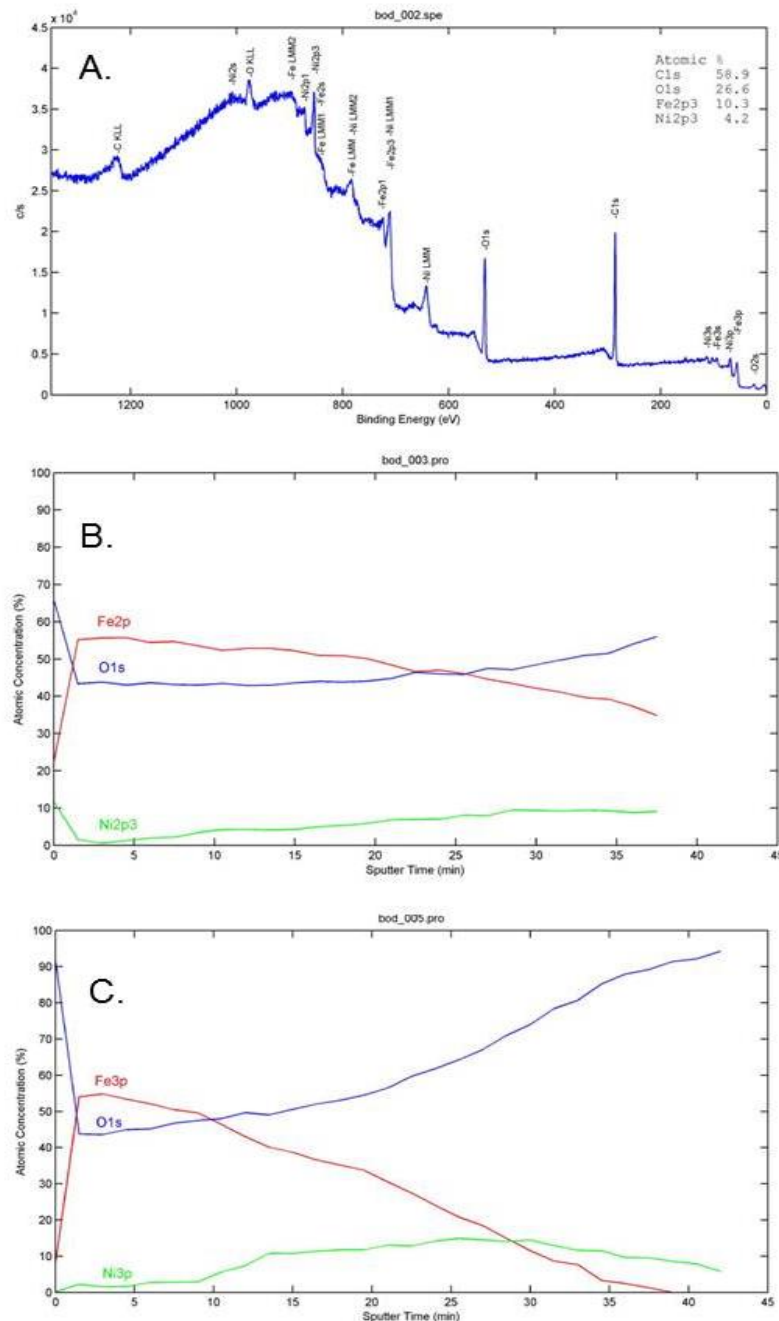
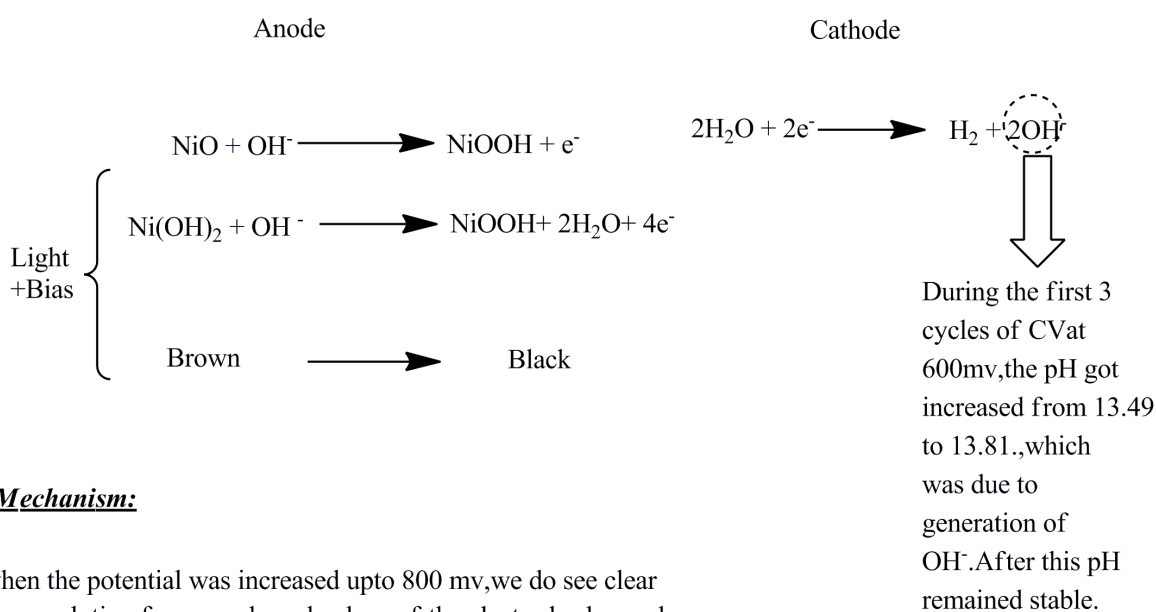


**Figure 12.13:** A. XPS survey scan showing the atomic content of Fe, Ni and O. B. XPS depth profile analysis of region 1 showing the atomic distribution of Fe and Ni element across the interface of NiO – Hematite electrode. C. XPS depth profile analysis of different region of NiO – Hematite electrode. [Courtesy: Dr. Ulrich Müller]

### 12.3.5 Photoelectrochemical study of NiO- Hematite electrode

Figure 12.14: A. shows the results of cyclic voltammetry (CV) of NiO –Hematite electrode. This was taken in 1 M KOH at a sweep rate of  $30 \text{ mV}\cdot\text{sec}^{-1}$  in both dark and A.M 1.5 illuminated light conditions. In the light condition, I did not get the usual trend of photocurrent. Still there is little difference in the CV under both dark and light condition. The voltmmogram changes with the number of cycles and it gives rise to a saturated anodic current density of  $15 \text{ mA} / \text{cm}^2$  with good gas evolution on electrode surface. An increase in anodic and cathodic current has been seen and which confirms the oxidation and reduction of species with time. This generally happens as a result of the increase in surface area of the electrode owing to the corrosion caused by the electrolyte [22]. The inset of Figure 12.14 B shows the photocurrent density of pristine hematite film which is around  $100 \mu\text{A} / \text{cm}^2$ . On comparing this photocurrent with that of NiO-Hematite film, 15 fold increase was obtained and at the water splitting potential (1.23 V) the current is found to be  $7.2 \text{ mA} / \text{cm}^2$ . The anodic current obtained during the cyclic voltammetry of NiO - Hematite electrode is due to oxidation of nickel hydroxide at 0.4 V vs. Ag / AgCl. The anodic photocurrent observe at more positive potential arises from the oxidized form. Cathodic photocurrent was obtained at water splitting potential as shown in Figure 12.15 A. From the chronoamperometric study [Figure 12.15: C], I can clearly see that at the oxidation potential of nickel hydroxide, the current decays in slow manner in comparison to other potential window. It is to be noted that the amount of current density depend strictly on the applied potential. The transient photoresponse at an applied potential from 100-300 mV is shown in Figure 12.15 D. Illuminating the film results in sharp anodic spike which rapidly decays, leaving a small anodic photocurrent. Blocking the light causes a cathodic spike which decays to a cathodic photocurrent. The electrode reaction drive by the cathodic photocurrent is presumably the same as that driven by the dark current, the reduction of water by conduction band electrons. The possible reason for the transientsbehavior includes double-layer effects, acceleration of surface redox reactions, and the excitation of midgap states. Also they result from the buildup and decay of the concentration of photogenerated carriers in the film. The dynamics of the local carrier concentrations will depend on the diffusion and recombination rates of both holes and electrons [24]. Transient photocurrent spikes have been previously observed in iron oxide [25]. These transient photocurrents have been explained either on the basis of back reactions between photogenerated intermediates and conduction band electrons or in terms of midgap surface states.

One important observation is the change in color of the electrode as a result of the applied bias. This electrochromic behavior is very well known in NiO and Ni(OH)<sub>2</sub> electrode [9, 22]. It can be initiated by the applied overpotential when the samples have been subjected to 10 cycles in KOH. The samples were colored with the anodic bias of 660 mV vs. Ag/AgCl reference electrode and again at the cathodic bias of -600mV it gets bleached. The color change of NiO is due to NiOOH color centers formed as a result of anodic reaction and caused the material to darken in considerable manner. These NiOOH color centers can be removed by reversing the polarity of the bias and the NiO return to the transparent or bleached state.



**Mechanism:**

when the potential was increased upto 800 mv, we do see clear gas evolution from anode and colour of the electrode changed from brown to black. From this we can say that Ni(OH)<sub>2</sub> oxidized to NiOOH.

**Scheme 12.14:** Mechanism depicting the origin of color transformation.

The color changing phenomenon of NiO- Hematite electrode is shown in scheme 12.14. Hereby it is to be noted that NiO gets oxidized to nickel oxyhydroxide (NiOOH). It has also been suggested that the electrochromic properties arise owing to a small quantity of nickel hydroxide which is present along with NiO. The electrochromic reaction of nickel hydroxide is a reversible redox reaction in which the reduced form is nearly transparent while the oxidized form is a dark brown. This change in optical properties is due to changes in the electronic properties of nickel hydroxide which occur upon oxidation/reduction. Knowledge of the electronic properties of both the oxidized and reduced phases is important for complete understanding of the system [24].

Clear gas evolution has been observed on the surface of NiO - Hematite electrode [Figure 12.15: F]. The nature of the gas was not validated during the study due to the technical constraint.

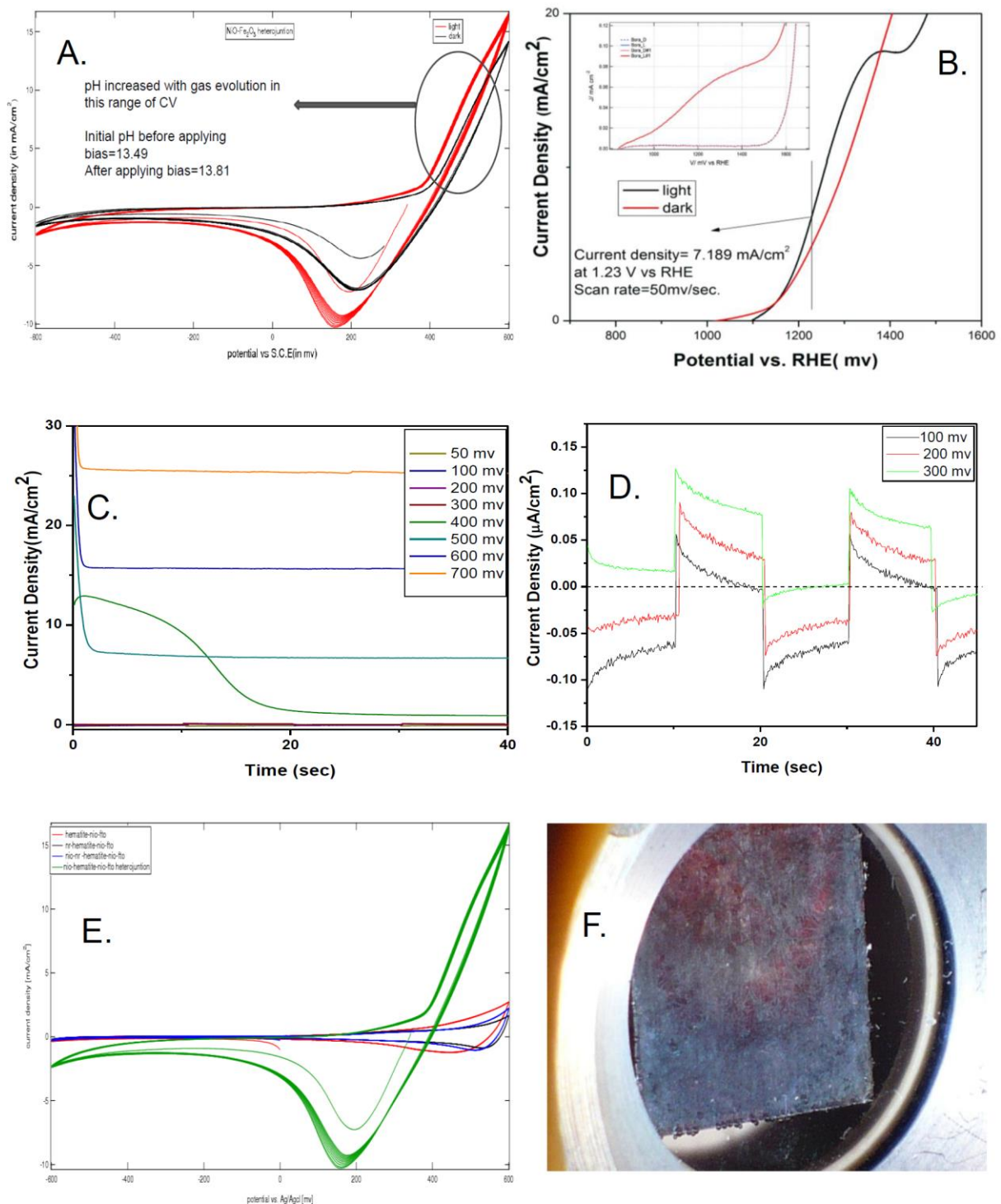


**Figure 12.15:** A. Cyclic Voltammogram of NiO- Hematite electrode showing around 15 mA/cm<sup>2</sup> dark current. B. Comparison of the photocurrent density of hybrid electrode with pristine hematite electrode. C. Chronoamperometric study of NiO - Hematite electrode D. Photocurrent transient vs. time for NiO – hematite electrode at 100, 200 and 300 mV respectively. E. Comparison of cyclic voltammogram of samples (A, A1, B, B1) G. Significant gas evolution was observed on the surface of electrode. The exact nature of gas need to be further confirmed with gas chromatography.

Finally on comparing the cyclic voltammogram of each sample obtained after modification step [Figure 12.15: E], I have found that the redox current of the sample B1 was higher. It is due to the increase in the surface area of the electrode caused by hydrothermal deposition of NiO nanostructure on top of hematite.

#### 12.4 Conclusion

A composite electrode made of NiO and Hematite nanocrystallite have been developed with hydrothermal strategy. From the optical property study, it has been found that the modified electrode strongly absorb in visible region at 550 nm with different optical behavior. The XRD study validated the presence of NiO phases along with hematite. The morphology of the electrode looks like some wall like feature formed in regular fashion. The composition of the electrode has been studied with TEM EDX and STEM energy filtered mapping. From both the study, I have found that Ni is distributed along the hematite layer down to the FTO substrate. Since the electrode showed good surface electrocatalytic behavior, an ERDA analysis has been performed which showed that the very top surface of the electrode (10 nm) have good atomic percentage of nickel. The TEM result has further been correlated with XPS depth profiling study and it is found that nickel diffuses across the hematite film. From the photoelectrochemical investigation, the photoanodic current density was found to be  $15 \text{ mA} / \text{cm}^2$  which is 15 fold higher than that of pristine hematite film. The system also showed good gas evolution but the nature of the gas has not been finalized during this study. The high current density obtained in case of NiO - hematite electrode is suggested to be due to redox activity of NiO and nickel hydroxide present on the surface of hematite. The system also showed good electrochromic behavior due to formation of NiOOH color centers.

## References

- [1] Kishi, T.; Aritsuka, M. *Surface and Coating Technology*, **1988**, *34*, 345 - 353.
- [2] Bae, S.; Shin, H.; Kim, J. Y.; Jung, H. S.; Hong, K. S. *J. Phys. Chem. C* **2008**, *112*, 9937-9942.
- [3] Licht, S.; Hodes, G.; Tenne, R.; Manassen, J.; *Nature* **1987**, *326*, 863 - 864.
- [4] Licht, S.; Wang, B.; Soga, T.; Umeno, M. *Appl. Phys. Lett.* **1999**, *74*, 4055-4057.
- [5] Helm, M. L.; Stewart M. P.; Bullock R. M.; DuBois M. R.; DuBois D. L. *Science* **2011**, *333*, 863 - 6.
- [6] Kleiman-Shwarscstein, A.; Hu, Y.; Stucky, G. D.; McFarland, E. W.; *Electrochem. Commun.* **2009**, *11*, 1150-1153.
- [7] Merrill, M. D.; Dougherty, R. C. *J. Phys. Chem. C* **2008**, *112*, 3655-3666.
- [8] Corrigan, D. A. *J. Electrochem. Soc. Electrochemical Science and Technology*. **1987**, *134*, 377-384.
- [9] Miller, E. L.; Rocheleau, R. E. *J. Electrochem. Soc.* **1997**, *144*, 3072-77.
- [9] Yang, D.; Wang, R.; He, M.; Zhang, J.; Liu, Z. *J. Phys. Chem. B* **2005**, *109*, 7654-7658.
- [10] Ni, X.; Zhang, Y.; Tian, D.; Zheng, H.; Wang, X. *J. Cryst. Growth* **2007**, *306*, 418-421.
- [11] Zhu, J.; Jiang, J.; Liu, J.; Ding, R.; Ding, H.; Feng, Y.; Wie, G.; Huang, X. *J. Solid Stat. Chem.* **2011**, *184*, 578-583.
- [12] Dong, L.; Chu, Y.; Sun, W. *Chem. Eur. J.* **2008**, *14*, 5064-5072.
- [13] Liang, Z.; Zhu, Y.; Hu, Y. *J. Phys. Chem. B* **2004**, *108*, 3488 - 3491.
- [14] Xiang, L.; Yin, Y. P.; Jin, Y. *Mater. Lett.* **2005**, *59*, 2223-2228.
- [15] Samanta, P. K.; Patra, S. K.; Chaudhuri, P. R. *Physica E* **2009**, *41*, 664-667.
- [16] Irwin, M. D.; Buchholz, D. B.; Hains, A. W.; Chang, R. B. H.; Marks, T. J. *PNAS*, **2008**, *105*, 2783-2787.
- [17] Boschloo, G.; Hagfeldt, A. *J. Phys. Chem. B* **2001**, *105*, 3039-3044.
- [18] Carpenter, M. K.; Conell, R. S.; Corrigan, D. A. *Solar Energy Mat.* **1987**, *16*, 333.
- [19] Wruck, D.; Dixon, M.; Rubin, M.; Bogy, S. *J. Vac. Sci. Technol. A*. **1991**, *9*, 2170.
- [20] Sasi, B.; Gopchandran, K. G. *Nanotechnology* **2007**, *18*, 115613.
- [21] Oliva, P.; Leonardi, J.; Laurent, J. F.; Delmas, C.; Braconnier, J. J.; Figlarz, M.; Fievet, F. *J. Power Sources* **1982**, *8*, 229.
- [22] Agrawal, A.; Habibi, H. R.; Agarwal, R. K.; Cronin, J. P.; Roberts, D. M.; Caron-Popowich, R.; Lampert, C. M. *Thin solid films* **1992**, *221*, 239-253.

- [23] Ding, I.; Tétreault, N.; Brillet, J.; Hardin, B. E.; Smith, E. H.; Rosenthal, S. J.; Sauvage, F.; Gratzel, M.; McGehee, M. D. *Adv. Funct. Mater.* **2009**, *19*, 1–6.
- [24] Carpenter, M. K.; Corrigan, D. A. *J. Electrochem. Soc.* **1989**, *136*, 1022 – 1026.
- [25] Hardee, K. L.; Bard, A. J. *J. Electrochem. Soc.* **1977**, *124*, 215.

## Conclusion and Future Outlook

Hematite nanostructures are successfully synthesized and applied for photocatalytic as well as photoelectrochemical application. The system showed good photocatalytic behavior in the degradation of organic acid which make it suitable for further synthesizing hematite thin film on FTO substrate. Pristine hematite film prepared by the thermal decomposition of fatty acid precursor showed good photocurrent of around  $250 \mu\text{A}/\text{cm}^2$  without any additional doping. It is worthwhile to mention that following the adopted dip coating strategy and special precursor development, a reasonable photocurrent density is achieved which is quite higher than the hematite films obtained with different strategy. The electronic structure of a photoelectrochemically treated hematite film showed extra energy transition in the NEXAFS spectra further helps in understanding the oxidation of hematite surface with applied bias. One major success of this thesis study is the prediction of electron – hole pair formation with soft X-ray absorption spectroscopy in a working photoelectrode using the specially developed liquid cell. The result obtained is the first of its kind in photoelectrochemistry research area. No doubt this will provide new set of information in understanding the photoelectrochemical process. Besides these, the development of hematite based hybrid nanostructure provides another alternative way to change the photoelectrochemical properties of hematite electrode. A very simple and cost effective method was developed which can transform the morphology of hematite into flower form. This helps in increasing the photocurrent and opens up new vistas in the research topic. Based on the bioinspired design, a novel hybrid electrode made up of hematite and C- Phycocyanin protein was developed in order to increase the photocurrent. Finally a hydrothermally prepared NiO- Hematite electrode showed high current density of  $15 \mu\text{A}/\text{cm}^2$ .

The future outlook of this thesis study can be extended to understand the origin of enhanced photocurrent obtained in hematite based hybrid nanostructures. One can utilize this synthesis strategy (as described for hematite based hybrid nanostructures) for improving the efficiency of good photoelectrode. For instance Si- Hematite film synthesized by dip coating of TEOS modified precursor showed current density of around  $1\text{mA}/\text{cm}^2$ . If I adopt the same modification strategy for getting hybrid nanostructures, the photocurrent density of Si- Hematite film can be improved upto several orders of magnitude as shown in figure C-7 in appendix A.

Appendix A : Hematite Nanoflower Optimization

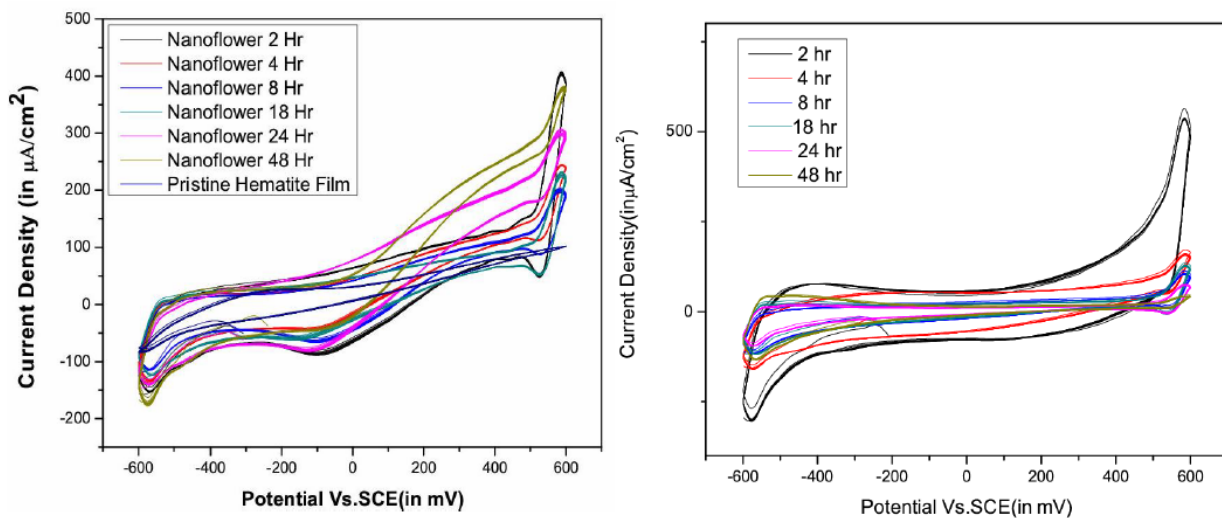


**Figure C-1:** Cyclic Voltammetric investigation of hematite nanoflower obtained by the hydrothermal treatment of hematite films for different duration of time.

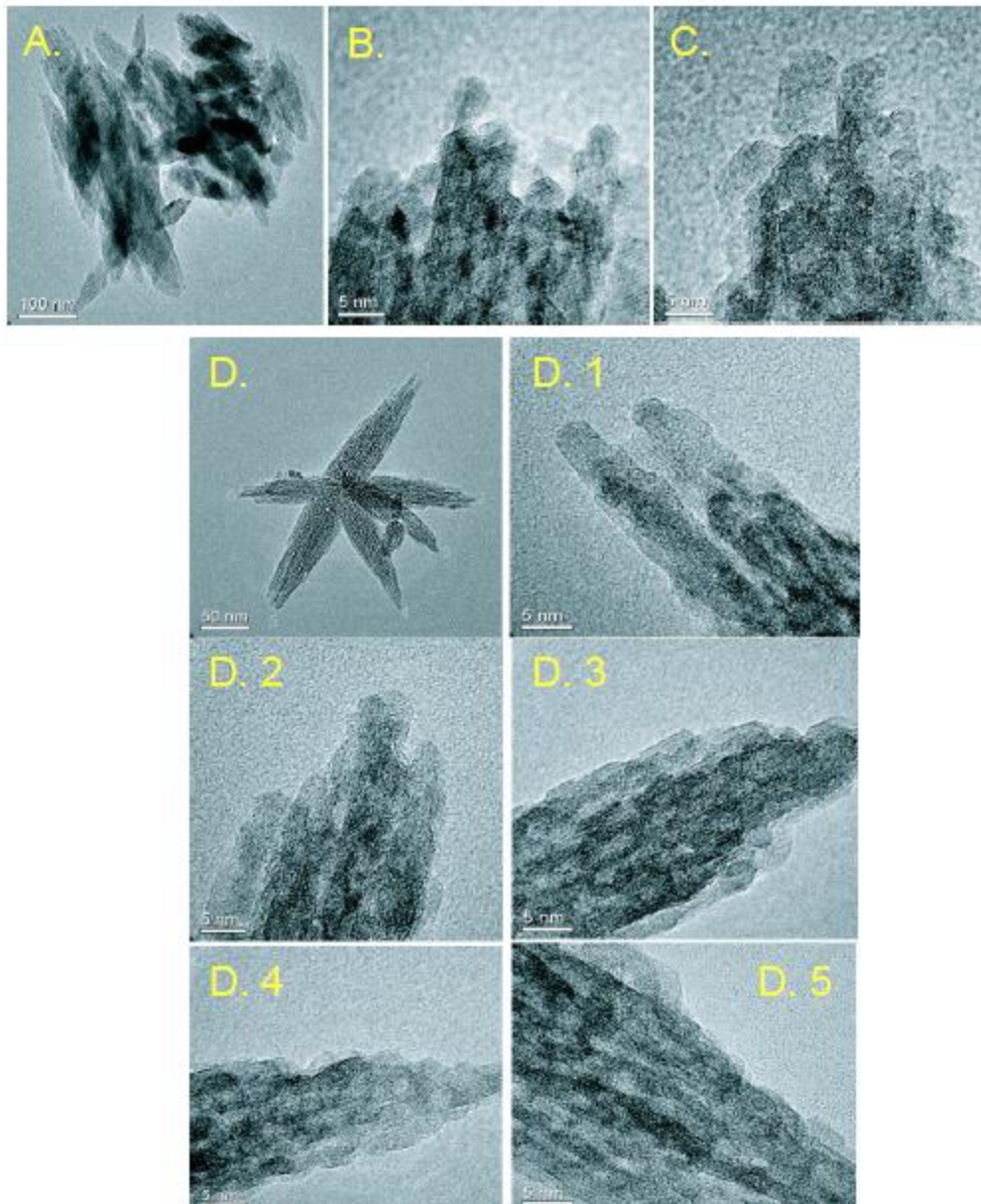


**Figure C-2:** A. Transmission electron micrograph of bundles of hematite nanoflowers. B-C. represents the HRTEM images of hematite nanoflower. D. Low resolution TEM image of single hematite nanoflower. D1-D5. HRTEM images of each arm of the nanoflower showing the growth along crystallographically preferred direction. [ Courtesy: Dr. Rolf Erni]

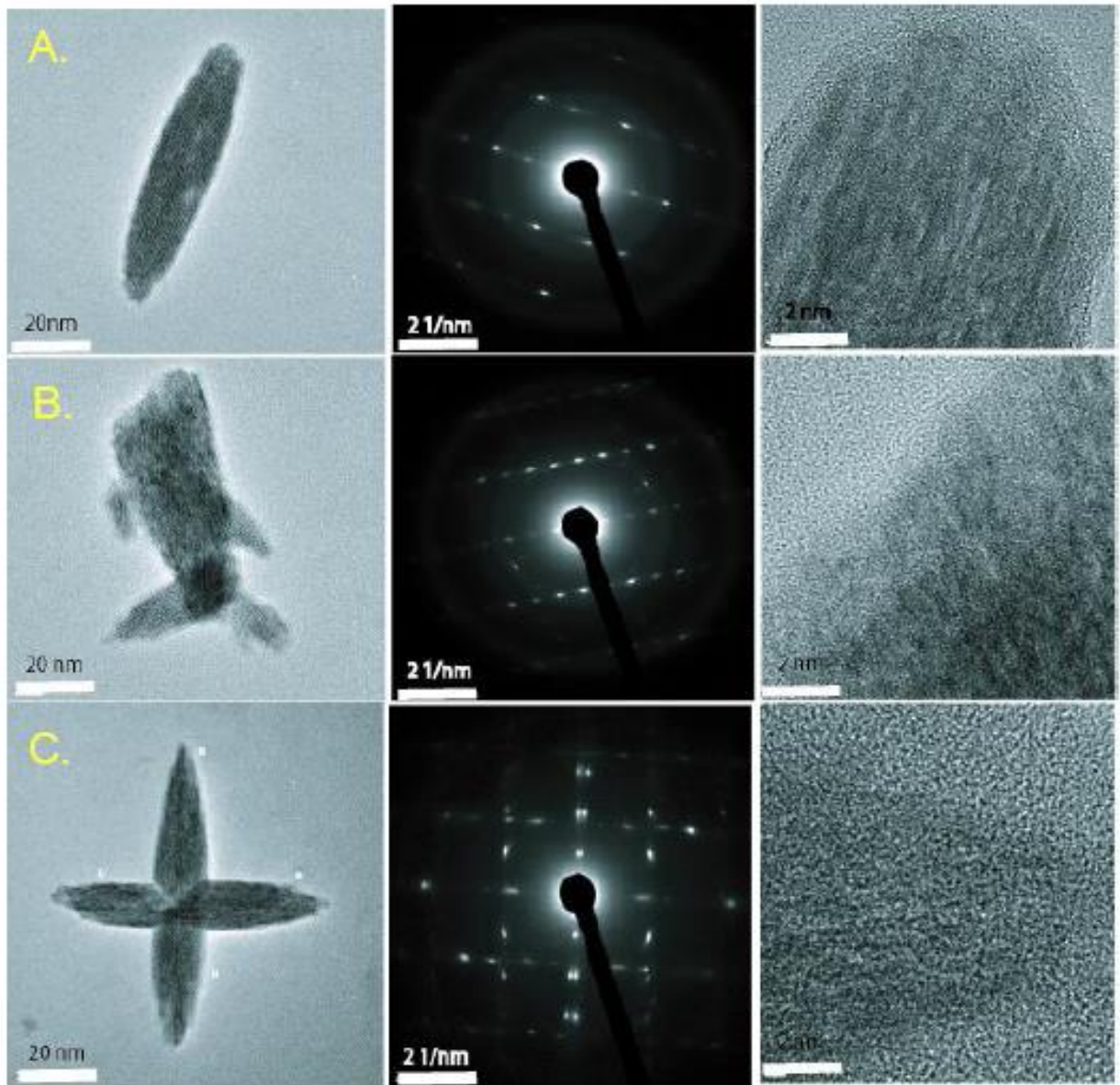


**Figure C-3:** **A.** Left- Low resolution TEM imaging of single hematite nanorod; center-selected area electron diffraction pattern; Right- HRTEM imaging of hematite nanorod. **B.** Left- Low resolution TEM imaging of partially developed hematite nanoflower; center- selected area electron diffraction pattern: right- HRTEM imaging **C.** - Low resolution TEM imaging of fully developed hematite nanoflower; Centre- selected area electron diffraction pattern; right- HRTEM imaging showing the wellaligned lattice fringes.[ Courtesy: Dr. Rolf Erni]

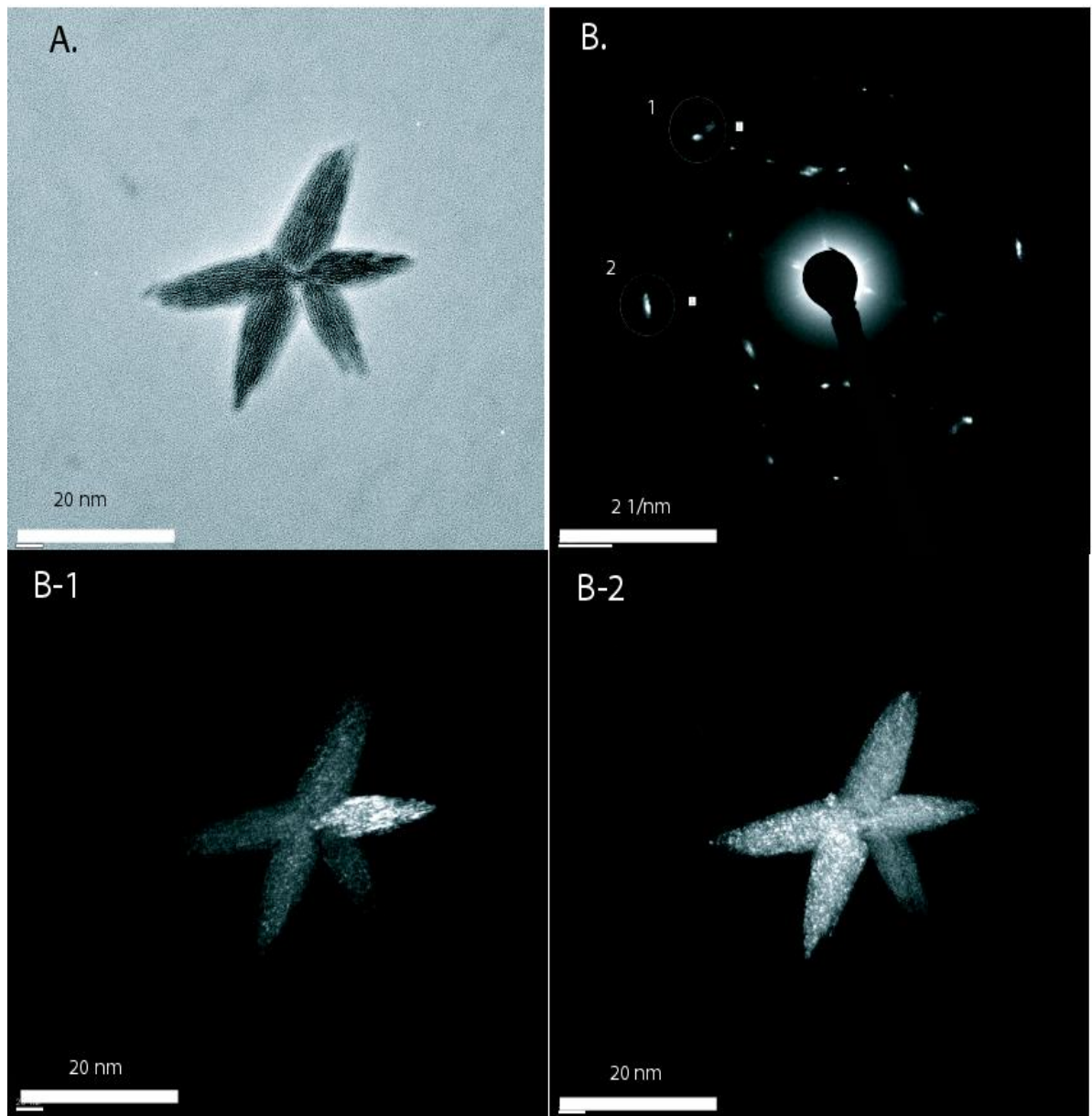


**Figure C-4:** **A.** Low resolution TEM imaging of pentapod shaped hematite nanoflower.**B.** Selected area electron diffraction pattern showing the overlapping of diffracted spot (1 and 2).**B1-B2.** HAADF (high-angle annular dark-field imaging) imaging showing the origin of diffracted spot 1 and 2. [ Courtesy: Dr. Rolf Erni]

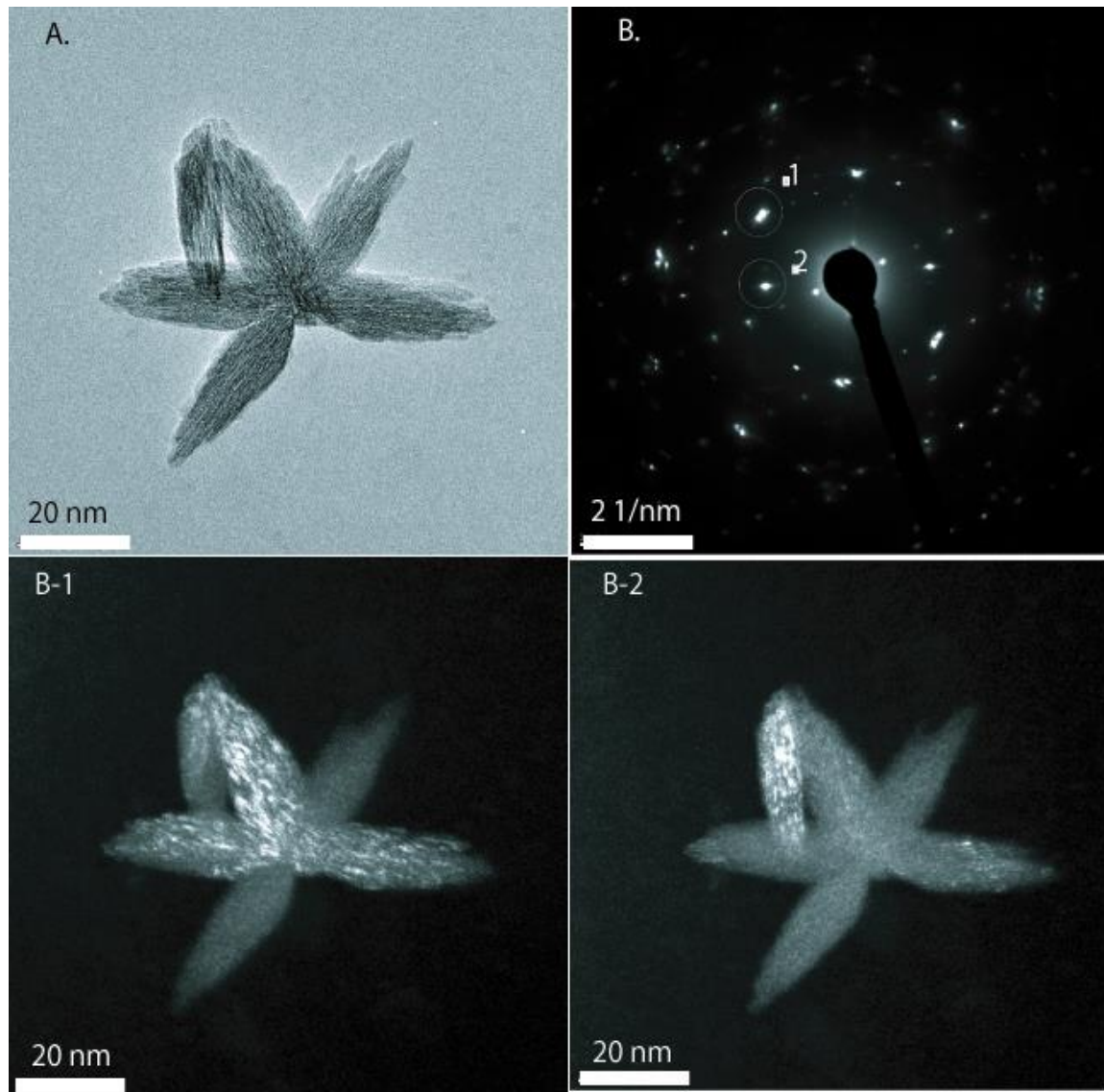


**Figure C-5:**A. Low resolution TEM imaging of pentapod shaped hematite nanoflower.**B.** Selected area electron diffraction pattern showing the overlapping of diffracted spot (1 and 2).**B1-B2.** HAADF (high-angle annular dark-field imaging) imaging showing the origin of diffracted spot 1 and 2.[ Courtesy: Dr. Rolf Erni]



**Figure C-6:** STEM tomography of hematite nano flower showing the two dimensional geometry. [Courtesy: Dr. Rolf Erni, Mr. Daniel Schreier, Dr. Magdalena Parlinska, Electron Microscopy Center, EMPA]

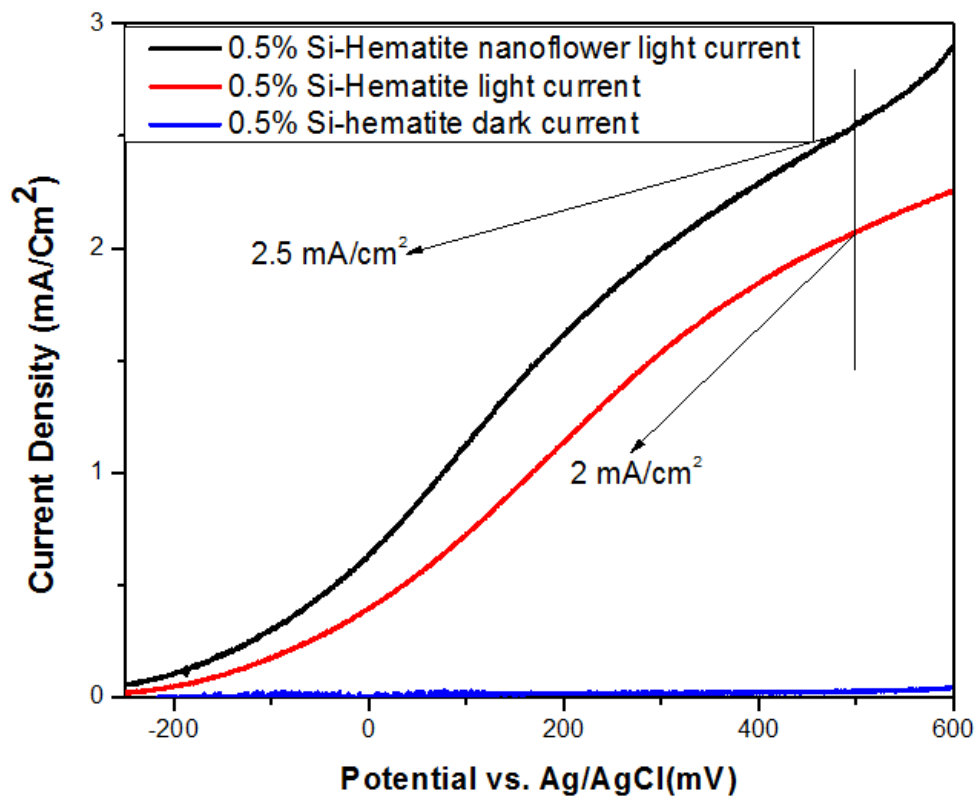
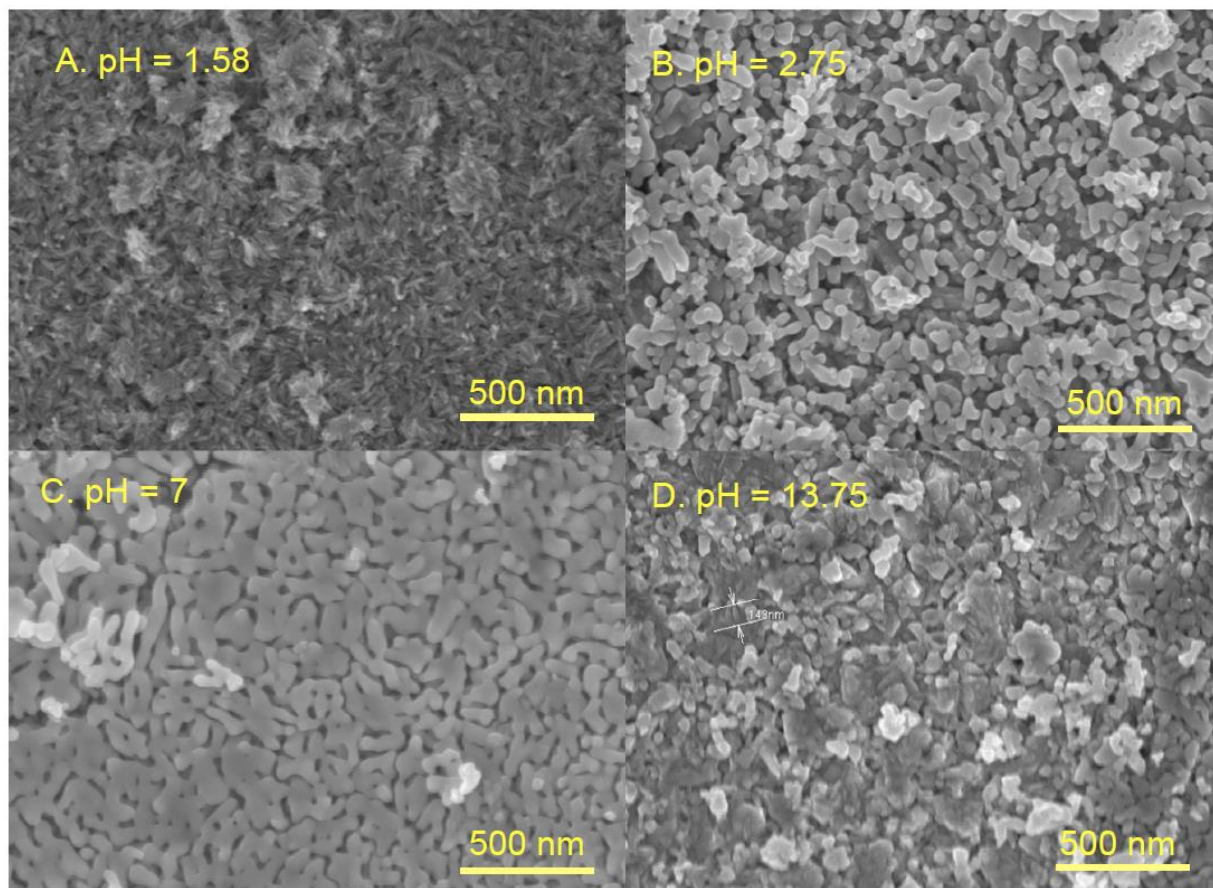


Figure C-7: Photocurrent density of hydrothermally treated silicon doped hematite film.

Table C-8: pH dependent study -Formation of nanoflowers on 0.5% Si hematite

pH	Flower formation
1.58	Yes (no hexapod, $118 \pm 102$ nm)
2.75	No
7.00	No
13.75	Yes (Under basic condition, not homogeneous)  Remark: The original nanoparticle from the pristine film does not turn into flower shaped morphology)

**Figure C-9:** FESEM imaging shows the morphology of hematite nanoflowers obtained at different pH of the precursor solution.



**Experiment:** To study the effect of hydrothermal treatment temperature on the formation of hematite nanoflowers.

**Results:** from electron microscopy results, I have found that the pristine film shows some small nanoparticle on the surface after hydrothermal treatment for 15 min at 50°C. These particles have a size of 25 nm (which fits with the concept of nucleation of nanoparticle on the surface of pristine hematite thin film).

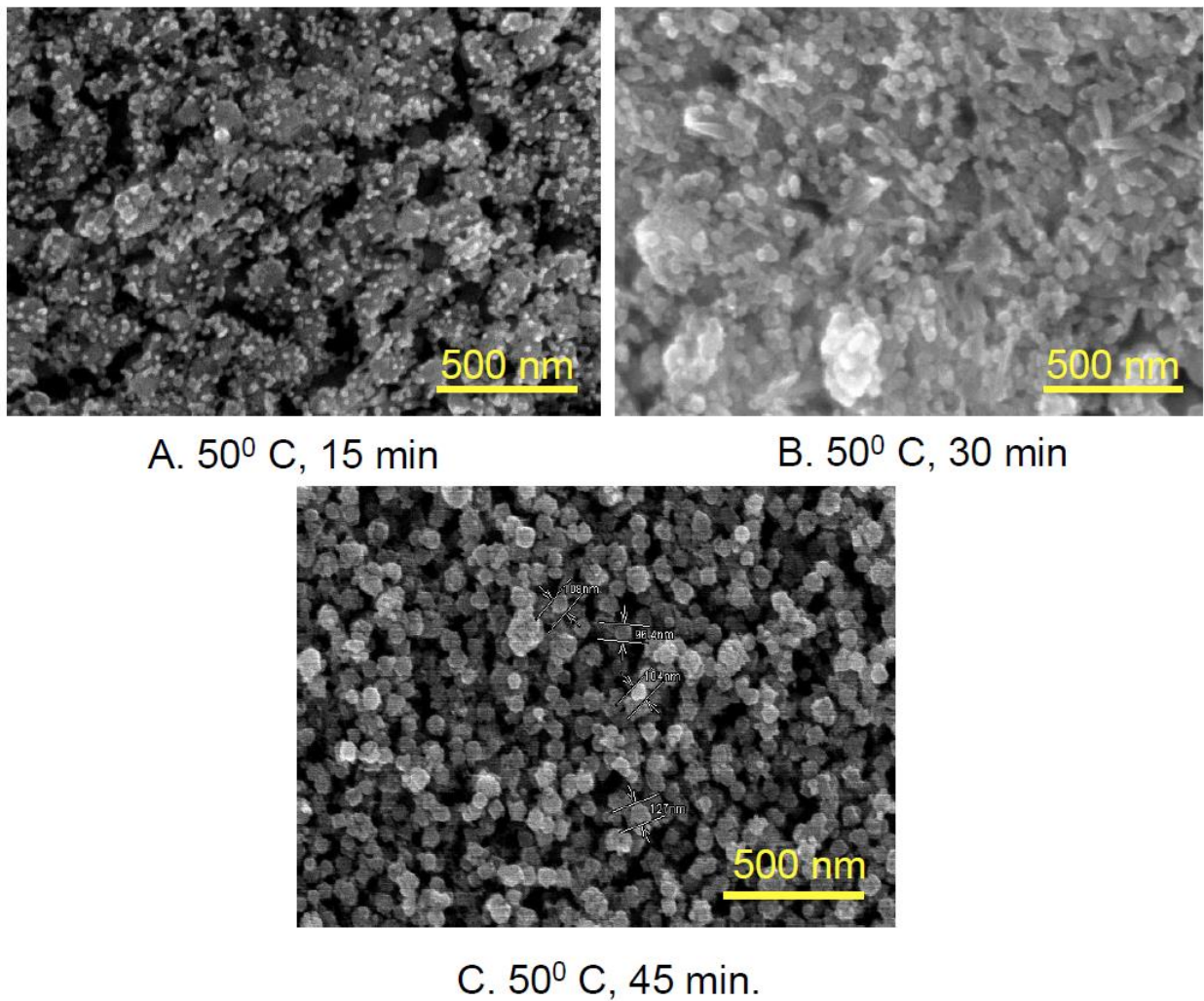


**Figure C-10:**FESEM showing the morphology evolution with respect to time.

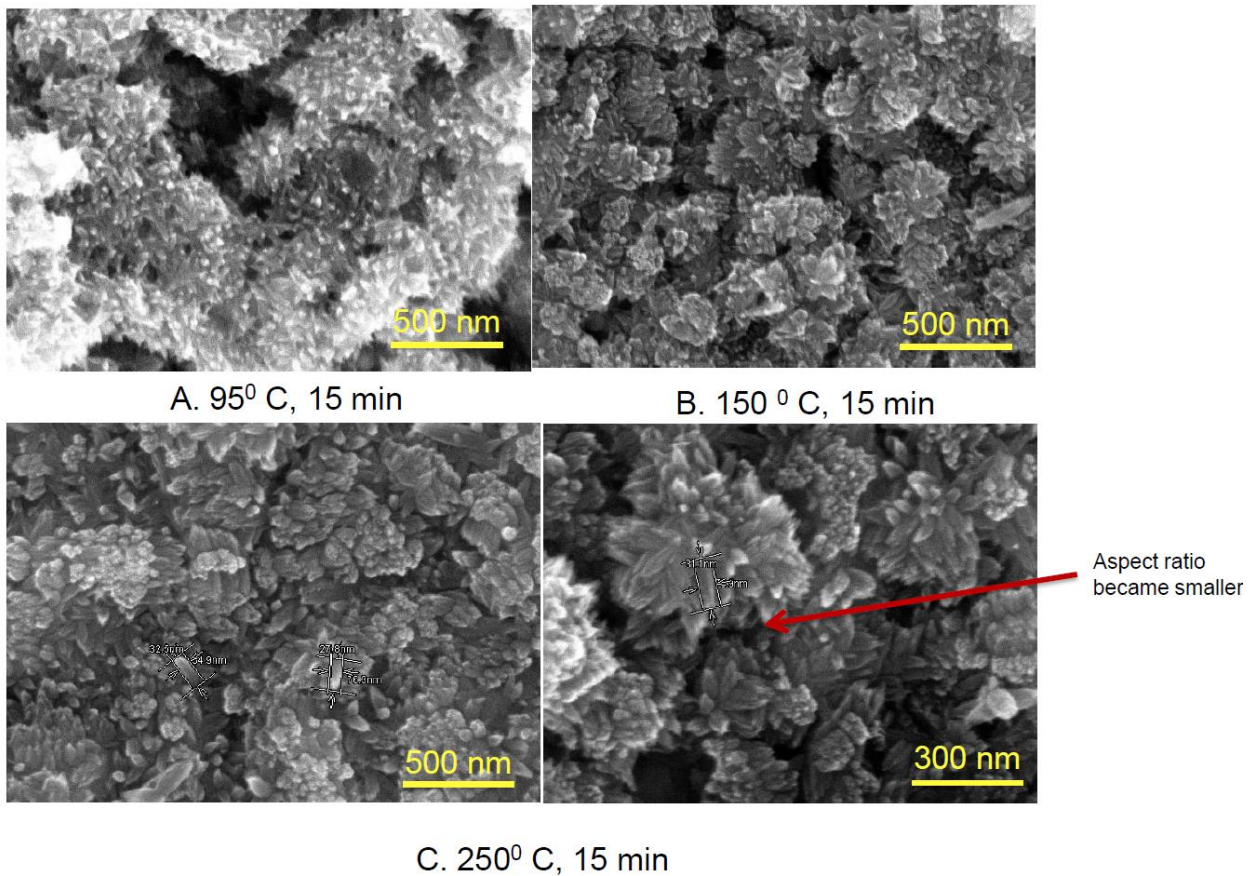
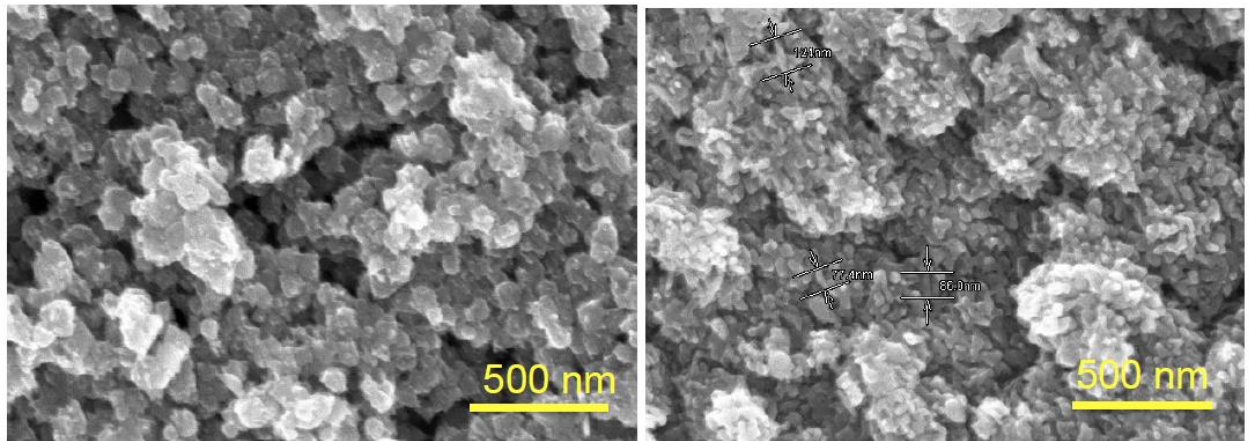


**Figure C-11:** Effect of hydrothermal treatment temperature on the growth of nanoflower.

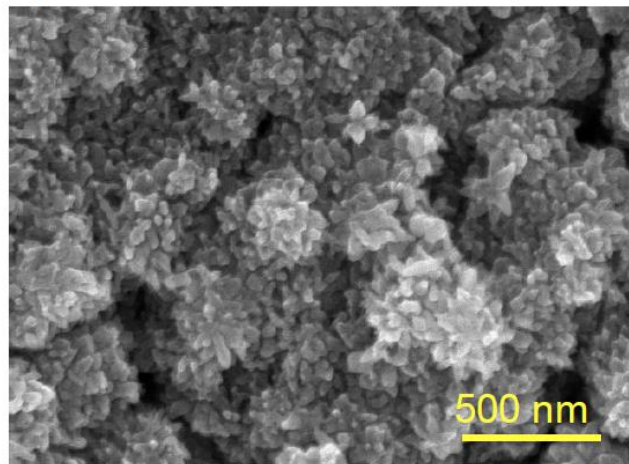
**Remark:**

1. The original pristine film shows dissolution behavior.
2. Time evolution experiment has to be done on 50<sup>0</sup>C treated films (0 – 60 min). Each sample will be monitored after 15 min by FESEM.
3. Again on 95<sup>0</sup>C sample, nanoflower form quite fast in comparison to 50<sup>0</sup>C sample. The sample was given a hydrothermal treatment of 15 min.
4. 150<sup>0</sup>C shows also same behaviors but flowers are quite rough in comparison to 95<sup>0</sup>C.
5. 250<sup>0</sup>C shows the formation of nanoflower just after 5 min
6. Temperature has a profound influence on the rate of dissolution and recrystallization process.



A. 95<sup>0</sup> C, 15 min, post annealed

B. 150<sup>0</sup> C, 15 min, post annealed



C. 250<sup>0</sup> C, 15 min, post annealed

**Figure C-12:** Effect of post heat treatment temperature on the morphology of nanoflower.

**Experiment:** To see the effect of concentration and time on the growth of nanoflower by keeping fixed temperature at 150°C

**Materials needed:**

1. Pristine hematite film ...1 mmole (hydrothermal precursor concentration)
2. Do.....2.5 mmole
3. Do.....5 mmole
4. Do.....10 mmole

**Parameters:** Time = 10, 20 and 30 min, Temperature = 250°C

**Results:** From FESEM study, it was found that temperature and concentration plays a critical role in forming the nanoflower. It has been found that 5 mmole gives the best nanoflower. Also the rod constituting the flowers has smaller size within 45-60nm. In case of photocurrent, 5 mmole samples give good performance.

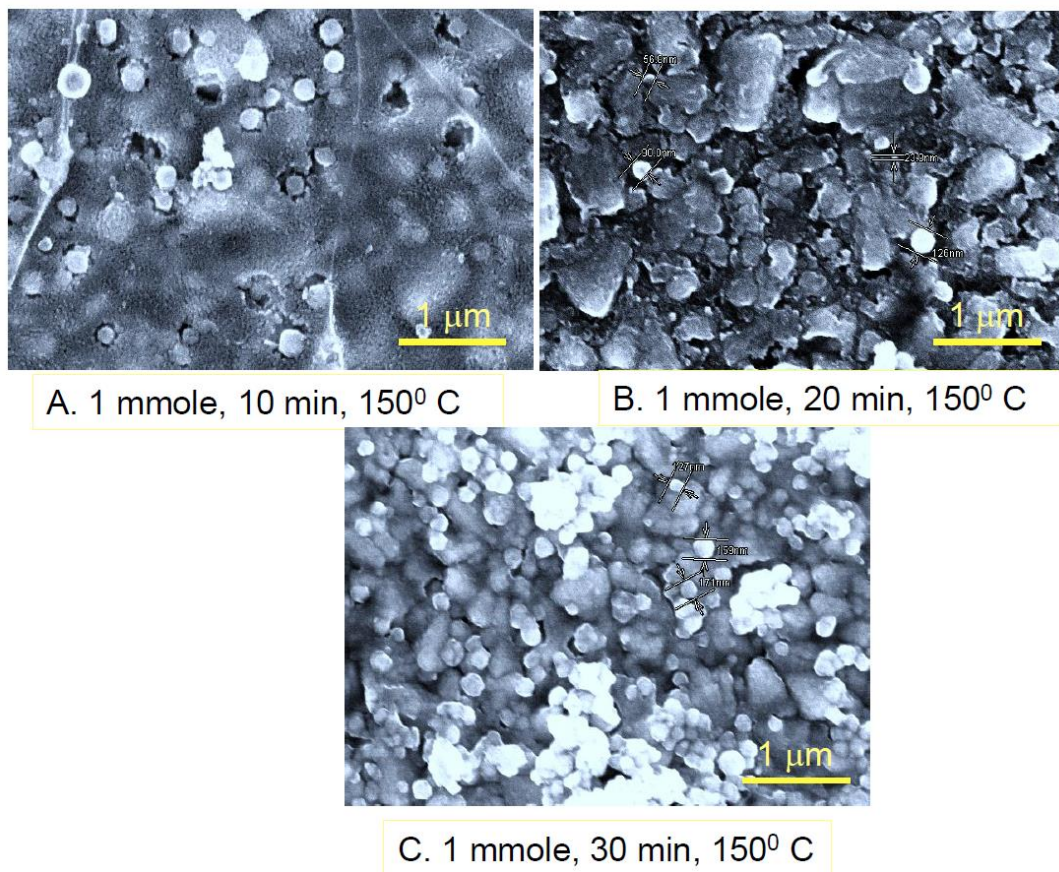
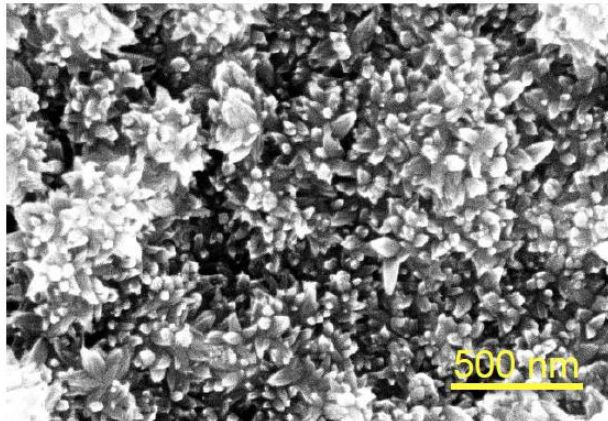
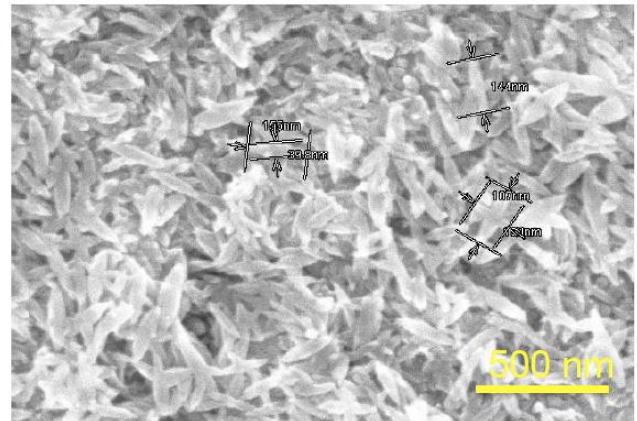


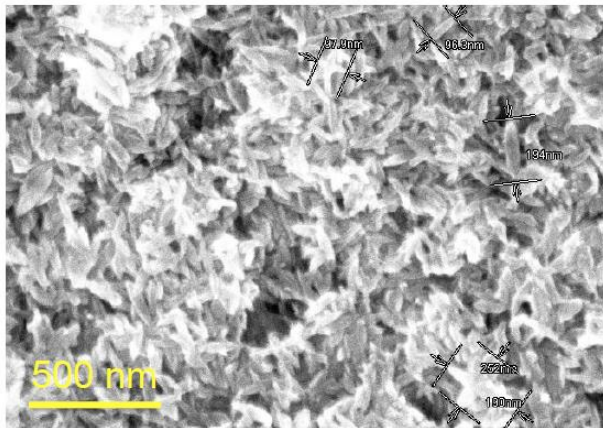
**Figure C-13:** FESEM image of nanflower grown for different time evolution at fixed temperature and concentration (1mmole).



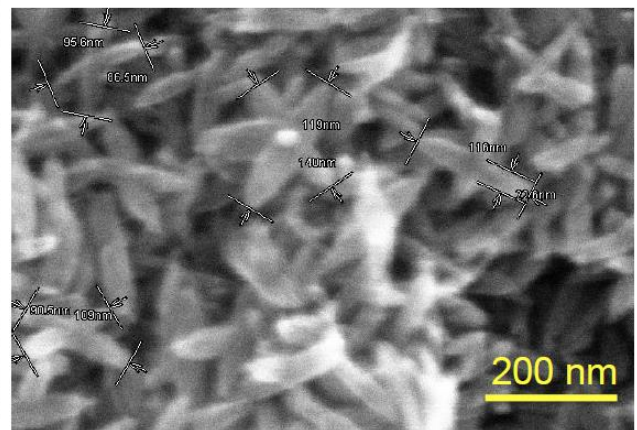
A. 10 mmole, 10 min, 150<sup>0</sup> C



B. 10 mmole, 20 min, 150<sup>0</sup> C



C. 10 mmole, 30 min, 150<sup>0</sup> C



D. 10 mmole, 40 min, 150<sup>0</sup> C

**Figure C-14:** FESEM image of nanflower grown for different time evolution at fixed temperature and concentration (10 mmole).

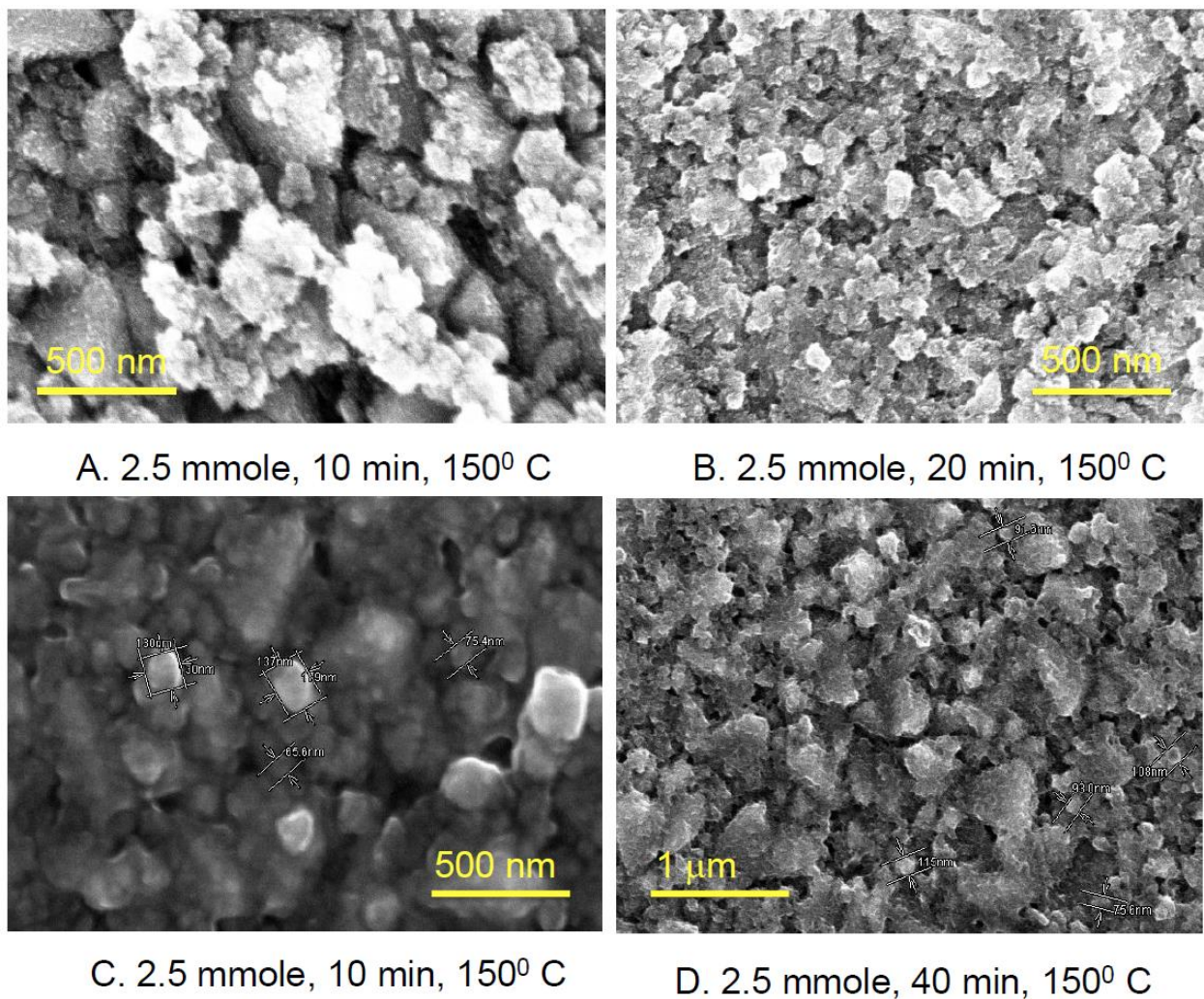


**Figure C-15:** FESEM image of nanoflower grown for different time evolution at fixed temperature and concentration (2.5 mmole).

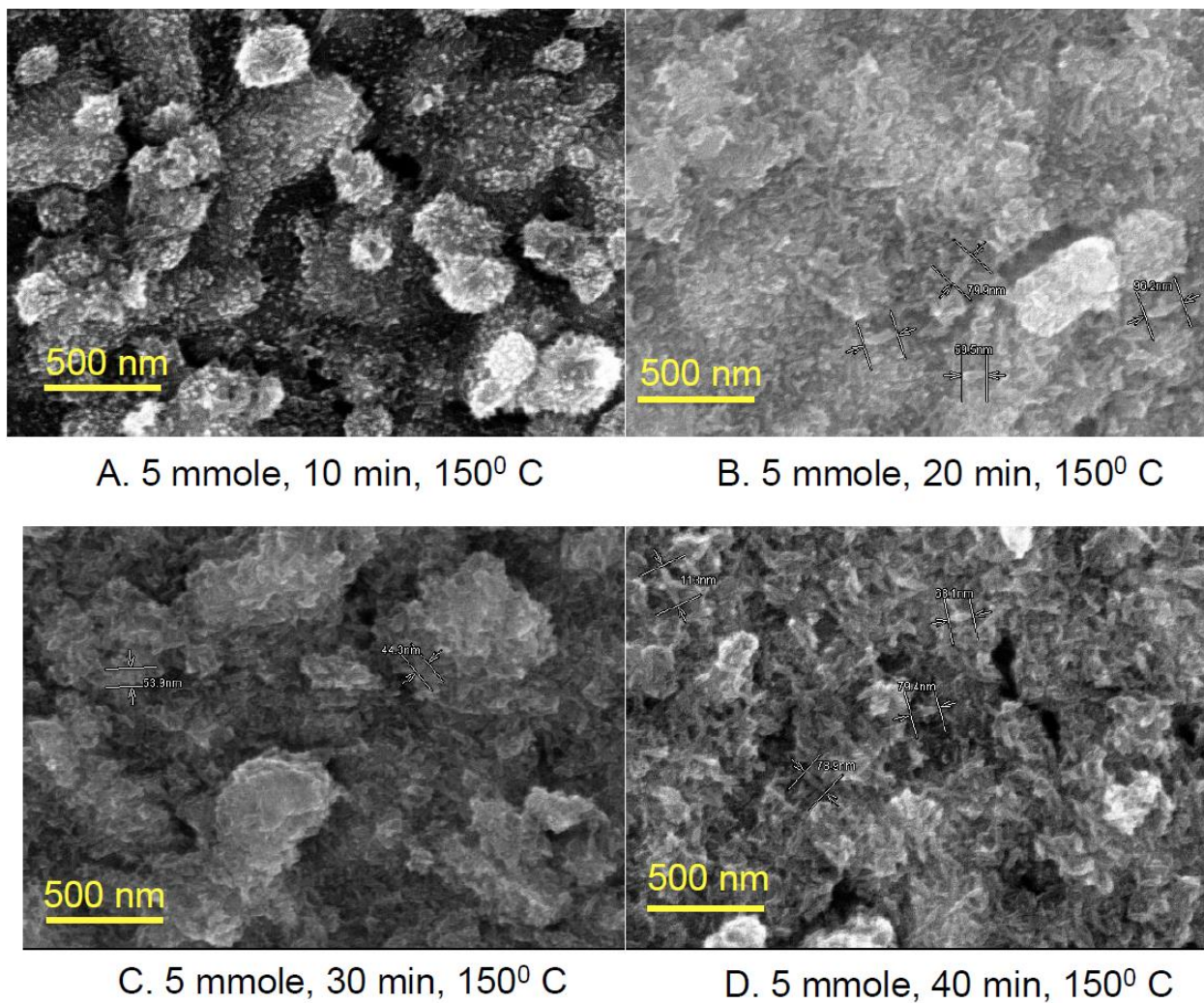


**Figure C-16:** FESEM image of nanoflower grown for different time evolution at fixed temperature and concentration (5 mmole).

**Type of measurement:** AFM, topography and Scanning Kelvin Probe Microscopy

**Samples:** hematite pristine, pristine hematite smoothed, hydrothermal treated hematite (24 hours), hydrothermal treated hematite smoothed.

- **Pristine hematite/ bright area**

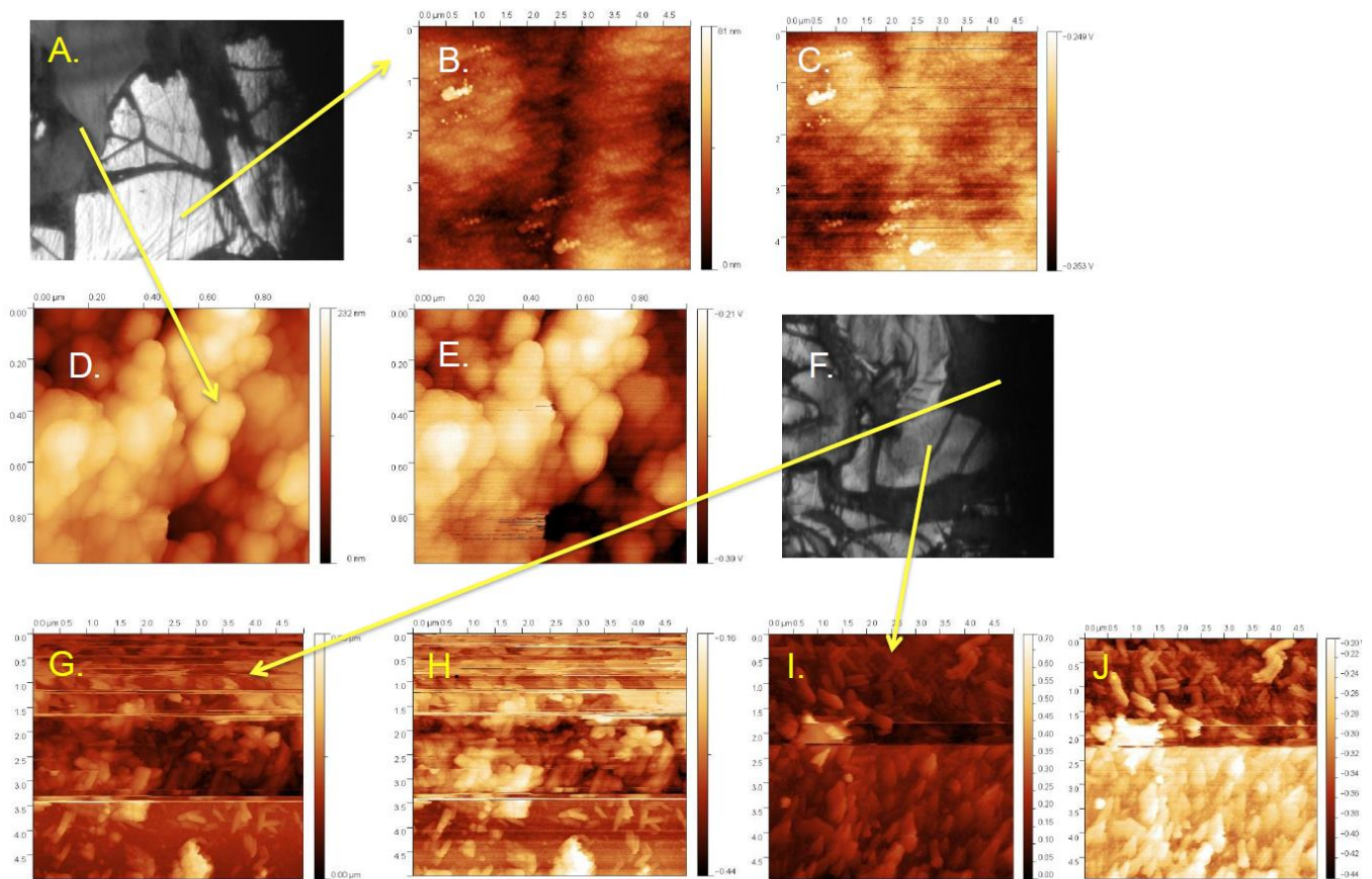


**Figure C-17:** A. Optical image of the ‘bright smooth part’; B. Topography of the smooth bright area; C. potential of the bright area; D. Topography of the pristine/grey area; E. Potential of the pristine/grey area; F. Optical image of the hydrothermally treated sample/bright area; G. Topography of the hydrothermally treated bright area; H. Potential of the hydrothermally treated bright area; I. Topography of the hydrothermally treated bright area; J. Potential of the hydrothermally treated bright area

## Appendix B

### Optimized parameter for the fabrication of NiO – hematite electrode

To get into a detail look into the change in structure, optical, morphology and Photoelectrochemical behavior of nanostructured NiO–hematite multilayer system, effect of different process parameters was studied. For it, 10 different sets of NiO-hematite system has been synthesized by varying the number of deposited hematite layer on 3 systems S-1, S-2, S-3 respectively. After this 6 sets of normal pristine hematite film were fabricated by taking the optimized layer thickness and no of dip coated layer without having NiO interfacial layer. Samples (S-1 to S-3) were hydrothermally treated with equimolar concentration of (10mM)  $\text{Fe}_2(\text{NO}_3)_3 \cdot 9\text{H}_2\text{O}$  and Hexamine for 8 hour. Samples S-3 to S-8 was subjected to different hydrothermal processing time and precursor concentration. Also samples S-9 to S-10 was treated with L-arginine instead of Hexamine along with different processing time. All the processing parameters were tabulated as shown below:

samples	NiO layer	Hematite Layer	Precursor Conc. Iron salt+hexamine (A)	Processing time	NiO Nano layer	Precursor conc. Ni salt+hexamine (B)	Processing time	Colour change After running cyclic voltammogram
1	1	1	10mmole	8Hr.	x	10 mmole	24hr.	
2	1	2	10 mmole	8Hr.	x	10 mmole	24hr	
3	1	4	10 mmole	8Hr.	1	10 mmole	24hr	
4	1	4	10 mmole	8hr	1	10 mmole	24hr	No CV, control sample for XRD, XPS.
5	X	4	1 mmole	1hr	1	1 mmole	4hr	
6	X	4	1 mmole	4Hr.	1	1 mmole	24hr.	
7	X	4	5 mmole	1Hr.	x	5 mmole	4hr	
8	X	4	5 mmole	4Hr.	x	5 mmole	24hr	
9	X	4	10 mmole	1hr	1	10 mmole	4Hr.	
10	X	4	10 mmole (L-arginine)	4Hr.	1	10 mmole	24Hr.	

Figure D-1: Morphology of S 1-A to S 10-A

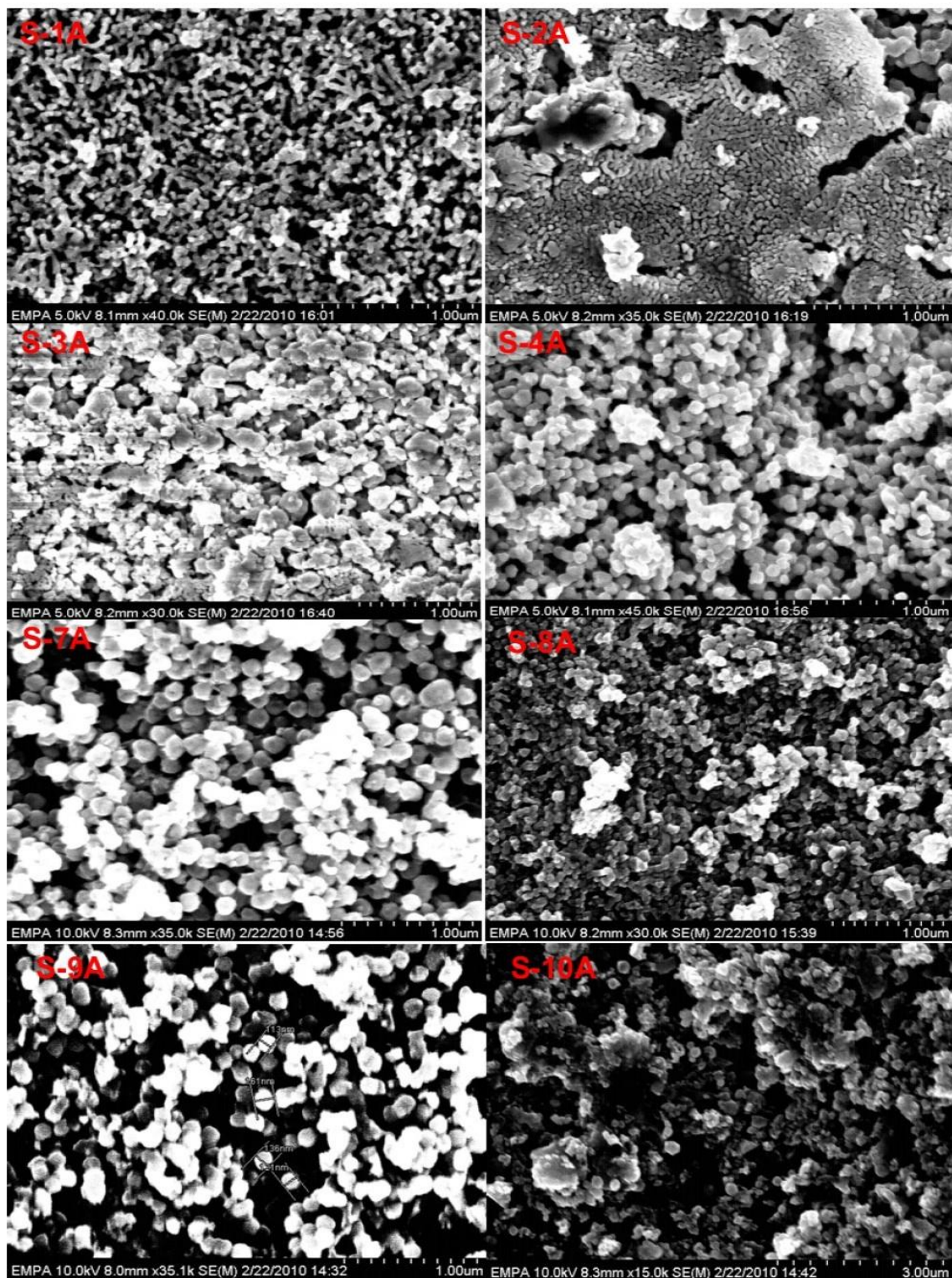
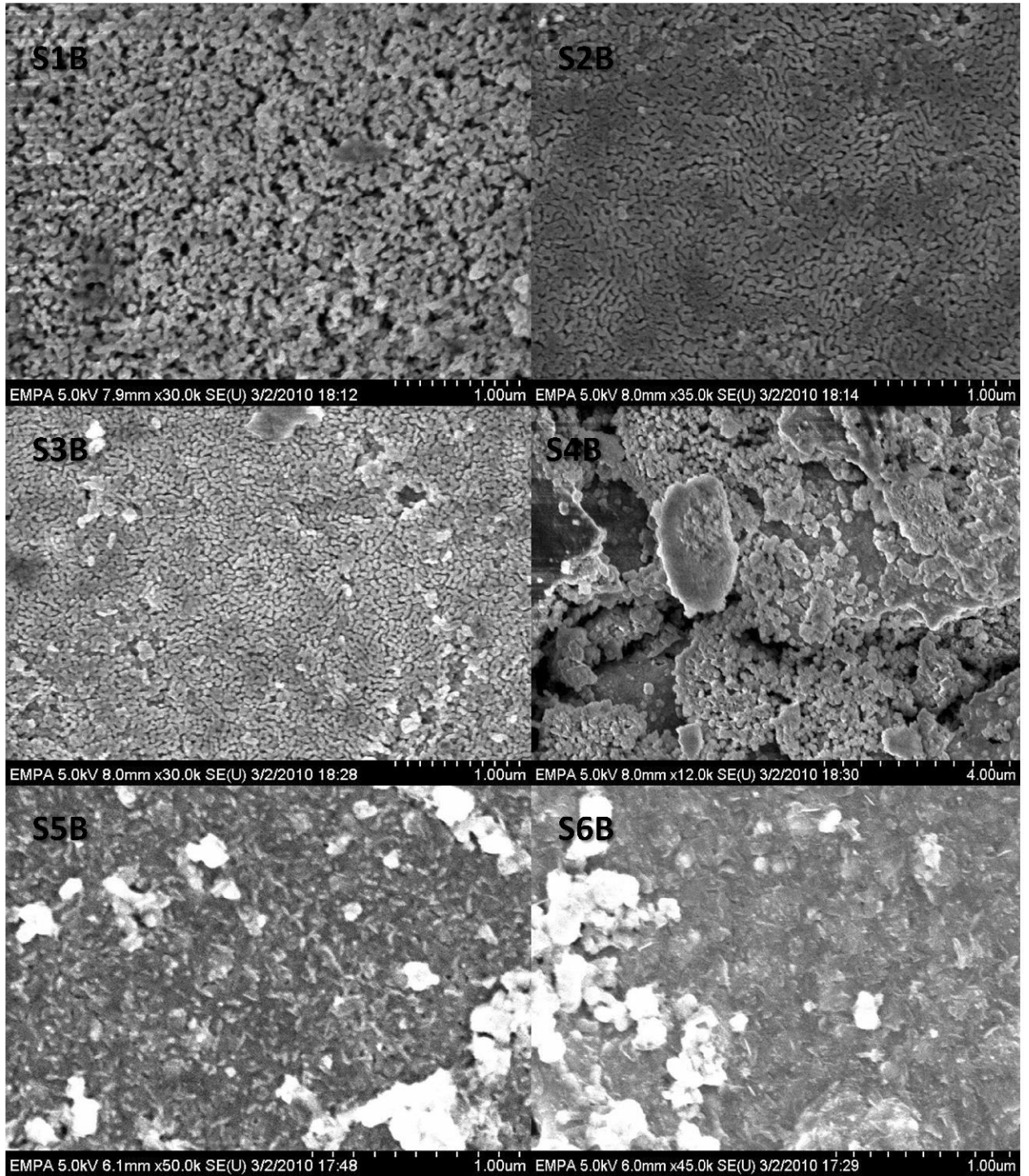


Figure D - 2: Morphology of S 2-A to S 6-B



## Publication List

1. Debajeet K. Bora, Artur Braun, Selma Erat, Ahmad K. Ariffin, Romy Löhnert, Kevin Sivula, Recardo Manzke, Jörg Töpfer, Michael Grätzel, Thomas Graule and Edwin C. Constable, **Evolution of an oxygen NEXAFS transition in the upper Hubbard band in  $\alpha$ -Fe<sub>2</sub>O<sub>3</sub> upon electrochemical oxidation**, *J. Phys. Chem. C*, 2011, 115 (13), pp 5619–5625.
2. Debajeet K. Bora, Artur Braun, Rolf Erni, Giuseppino Fortunato, Thomas Graule and Edwin C. Constable, **Hydrothermal Treatment of a Hematite Film Leads to Highly Oriented Faceted Nanostructures with Enhanced Photocurrents**, *Chem. Mater.*, 2011, 23 (8), pp 2051–2061.
3. Debajeet K. Bora, Elena A. Rozhkova, Krisztina Schrantz, Pradeep P. Wyss, Artur Braun, Thomas Graule and Edwin C. Constable, **Functionalization of Nanostructured Hematite Thin Film Electrodes with the Light Harvesting Membrane Protein C-Phycocyanin yields Enhanced Photocurrent**, *Advanced Functional Materials*, Accepted for Publication (2011).
4. Debajeet K. Bora, A. Braun, S. Erat, O. Safonova, E. C. Constable and T. Graule, **Evolution of structural properties of iron oxide nanoparticles during temperature treatment from 250°C – 900°C: X-ray diffraction and Fe K-shell pre-edge x-ray absorption study**. *Current Applied Physics*, Accepted for Publication. (2011).
5. A. Braun, D.K. Bora, K. Sivula, L. Zhang, T. Graule, J. Guo, M. Grätzel, E. Constable, **Direct observation of light generated electron holes in hematite during the photoelectrochemical water splitting process**, submitted to *Nature Chemistry*, 2012.

## Curriculum Vitae

---

**Debajeet K. Bora,**  
Laboratory for High Performance Ceramics  
Empa  
Swiss Federal Laboratories for Material Science and Technology

Überlandstrasse 129  
8600 Dübendorf  
Switzerland  
Tel +41 58 765 4967

---

### Current Research Summary

- **EMPA and University of Basel, Switzerland (2009 – present)**

Mentor: Dr. Artur Braun and Thesis Advisor: Prof. Edwin C. Constable.

*Synthesis of metal oxide based hybrid system in the form of thin film electrode for photo electrochemical hydrogen generation. Study has been done to elucidate different properties of the system which could affect the final performance. A new defect state in the electrochemically treated hematite thin film has been uncovered with the help of NEXAFS spectroscopy technique. Besides these electrode with enhanced photocurrent been developed by hydrothermally converting the morphology of hematite nanostructures into hexapod like super- structures. A similar rise in photocurrent has been observed on surface functionalization of hematite surface with cyanobacterial light harvesting protein. In a further attempt a novel multiband gap electrode is developed, where Isurprisingly could get dark current of 20 mA / cm<sup>2</sup> upon light exposure. The system showed good gas evolution both in the light and dark condition. An in – situ ATR-FTIR study was also conducted to see the adsorption and photocatalytic behavior of hematite nanoparticle for the degradation of organic compound. Another study dealing with the effect of oxidation state of hematite on photocatalytic properties is currently going with the help of Fe – L edge NEXAFS spectroscopy.*

### Education

- PhD in Nanosciences, Department of Chemistry, University of Basel (Joint Affiliation with Laboratory for High Performance Ceramics, EMPA), Switzerland. 2012
- M.Sc in Nanoscience & Technology (2005 – 2007). Tezpur University, India.
- Diploma in Bioinformatics. (2003 – 2005). Bioinformatics Institute of India, Noida, India
- B.Sc in Chemistry (honors). (2000 – 2004). Govt. Science College (Affiliated to Dibrugarh University), India.

### Graduate Research Skills

- **Synthesis skills:** Hematite nanoparticles and thin films by non - aqueous synthetic chemistry, surface functionalization of hematite thin films with light harvesting protein, fabrication of multi band gap heterogeneous thin film by hydrothermal route, hydrothermal modification of hematite thin film into nanostructures for enhanced energy efficiency, fabrication of microstructure as co – catalyst for water photo oxidation chemistry.
- **Analytical skills:** UV-Vis Spectroscopy, Fluorescence Spectroscopy, FESEM with EDX, HRTEM, XRD, XPS with depth profiling, BET, Synchrotron based hard and soft x ray spectroscopy \* ( XAS, NEXAFS and PES for electronic structure study), ATR – FTIR for in situ photo degradation study, particle size analyzer, profilometer, AFM (environmental, Kelvin probe),

photoelectrochemical workstation (cyclic voltammetry, chronoamperometry, transient photocurrent and IPCE), STEM tomography, Electron beam induced current measurement, light scattering set up, Z- scan experiment for photonic investigation, Gas chromatography.

- **Software and programming skills:** Origin 8.5, Igor Pro 6, KaleidaGraph 4.0, Win XAS, Chem Draw, Pan Analytical XRD analysis, Ubuntu, Windows vista and 7, C and C ++ programming.

### **Awards and Credentials**

- 1000 Euro travel grant from COST office (Through European Science Foundation).
- 1000 CHF as a Swiss graduate student support grant from CCMX.
- Chaired a session in the MRS Spring Meeting, 2010, 5-9 th April, San Francisco, USA.

### **Membership of Professional Organization**

American Chemical Society, American Physical Society, Material Research Society, Swiss Physical Society.

### **References**

**Dr. Artur Braun**, Physicist  
Head, Principle and Fundamentals Group  
for High Performance Ceramics  
EMPA-Swiss Federal Laboratories for  
Material Science and Technology  
Überlandstrasse 129, CH-8600  
Dübendorf, Switzerland  
Phone: +41 44 823 4850  
E-mail: [artur.braun@empa.ch](mailto:artur.braun@empa.ch)

**Prof. Dr. Edwin C. Constable**  
Department of Chemistry Laboratory  
University of Basel  
Spitalstrasse 51, CH-4056  
Basel, Switzerland  
Phone: +41 61 2671001  
E-Mail: [edwin.constable@unibas.ch](mailto:edwin.constable@unibas.ch)